PLANETOLOGIE

A MODEL OF THE CRUSTAL MAGNETIC FIELD OF MARS

ACHIM MORSCHHAUSER

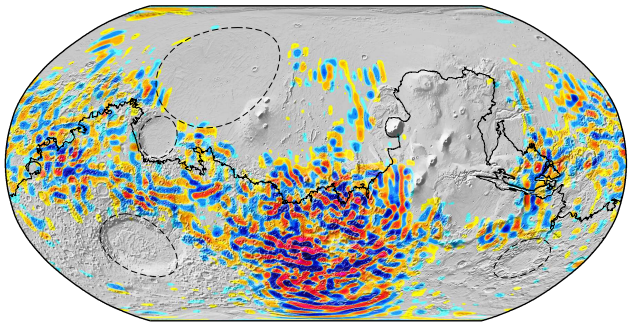

Inaugural-Dissertation zur Erlangung des Doktorgrades der Naturwissenschaften im Fachbereich Geowissenschaften der Mathematisch-Naturwissenschaftlichen Fakultät der Westfälischen Wilhelms-Universität Münster

vorgelegt von
Achim Morschhauser
aus Wiesensteig

- März 2016-

Achim Morschhauser: *A model of the crustal magnetic field of Mars,* Dissertation © März 2016

Dekan:	Prof. Dr. Hans Kerp
Erster Gutachter:	Prof. Dr. Tilman Spohn
Zweiter Gutachter:	Dr. Vincent Lesur
Weiterer Prüfer:	Prof. Dr. Harald Hiesinger
Weiterer Prüfer:	Prof. Dr. Michael Becken

Tag der mündlichen Prüfung: 29.06.2016

I MAY NOT HAVE GONE WHERE I INTENDED TO GO, BUT I THINK I HAVE ENDED UP WHERE I NEEDED TO BE.

— Douglas Adams —

ABSTRACT

The true nature of the Martian magnetic field remained undiscovered until Mars Global Surveyor (MGS) arrived at Mars in 1997. This satellite discovered strong magnetic fields of crustal origin[1], which exceed their terrestrial counterparts by about an order of magnitude. Along with this discovery, many new questions related to the Martian magnetic field were raised, and many of these remain unanswered. Here, we will derive, present, and analyze a model of the crustal magnetic field of Mars which is based on the MGS data set, and which was designed to contribute to answer these questions. For this purpose, it is important that the model is stable when downward-continued to the surface and that the highest feasible model resolution is achieved. In order to meet these requirements, the model was expanded up to spherical harmonic (SH) degree and order 110, and several numerical and mathematical techniques have been applied during data inversion: First, temporal variabilities and non-crustal field contributions in the data that lead to unrealistically strong magnetic fields in the model were handled by additionally minimizing a measure of field complexity at surface altitude. This minimization was performed with an iteratively reweighted least squares (IRLS) algorithm which approaches an L1 norm (absolute measure) for the minimization. As compared to an L2 norm (least-squares measure), this norm allows for a better representation of strong localized magnetic anomalies which are present on Mars. Second, a modified Huber norm was used. In this way, the obtained model approaches the maximum likelihood solution of the normally distributed part of the data. At the same time, the negative influence of data outliers is significantly reduced without completely disregarding them. Third, the mapping phase orbit (MPO) data were weighted based on a statistical analysis of the data. As a result, spatial and temporal inhomogeneities in the variances of the data noise could be considered in a self-consistent way. Finally, static external fields were handled by including a description of external day- and nightside fields.

The resulting model reproduces all known characteristics of the Martian crustal magnetic field and agrees well with other published models. In addition, it is characterized by its rich level of detail, its low level of noise, and its robustness when downward-continued to the surface.

We used our model to address several of the open questions related to the crustal magnetic field of Mars. The timing of the core dynamo was investigated by analyzing the magnetic signature, topography, geology, and

1 The term crustal origin refers to the natural remanent magnetization (NRM) of solid rocks. On Mars as well as on Earth, these rocks are mainly located in the crust [Wasilewski and Mayhew, 1992; Lewis and Simons, 2012; Vervelidou and Thébault, 2015]. Still, we acknowledge that the lithospheric mantle might be magnetized as well [Arkani-Hamed, 2003; Ferré et al., 2014].

gravity of several ancient highland volcanoes. From this analysis, we conclude that no known volcano on Mars possesses a magnetic field signature which indicates strong thermoremanent magnetization (TRM). Interestingly, earlier studies suggested that the core dynamo was active during the formation of the highland volcano Apollinaris Patera, which was emplaced at about 3.8 Gyr ago. In contrast, we argue that its magnetic signature is better compatible with thermal demagnetization, and that the Martian core dynamo was extinct by the end of the Noachian (3.8 Gyr ago, Michael [2013]). Furthermore, the magnetic signatures of impact basins were considered to study the timing of the dynamo shutdown. For large craters of more than 1000 km in diameter, the obtained results are in accordance with previous studies and suggest a dynamo shutdown in the Noachian at about 4.1 Gyr ago. Moreover, the magnetic field signature at surface altitude was used to study craters in Terra Sabaea with crater diameters down to 150 km, which was previously hampered by the coalescence effect. Overall, the magnetic signatures of most of the studied craters support a dynamo shutdown at about 4.1 Gyr ago, in accordance with the results that we obtained for the highland volcanoes. In order to determine the strength of magnetization of the Martian crust, we applied the method of Gubbins et al. [2011] to our model of the crustal magnetic field[2]. As a result, it was found that at least a magnetization of 20 A/m is necessary to explain the strongest fields on Mars if a 40 km thick magnetized layer is assumed. Finally, it was demonstrated that the presented model of the crustal magnetic field is able to resolve previously undiscovered isolated anomalies. Such isolated anomalies may be used to study the crustal magnetization and to determine Martian paleopole positions. In addition, the model resolution and covariance matrices can be used to estimate uncertainties of paleopole positions, and such estimates are largely missing in the current literature.

This work is divided into parts and chapters, and the first part starts with an overview of the current knowledge of the Martian magnetic field (Ch. 1) which is followed by a discussion of the open questions related to the crustal magnetic field of Mars (Ch. 2). The second part introduces the MGS mission (Ch. 3) and its obtained magnetic field data (Ch. 4). In the third part, an introduction to linear inversion is given (Ch. 5) before these principles are applied to Mars (Ch. 6). The resulting model of the crustal magnetic field is presented in the fourth part where its basic properties (Ch. 7), its residuals to the data (Ch. 8), and its comparison to other models (Ch. 9) are discussed. In the last part of this work, some of the previously mentioned open questions will be addressed with the help of the derived model of the crustal magnetic field. Namely, these questions include the timing of the Martian core dynamo (Ch. 10), the magnetization of the Martian crust (Ch. 11), and the location of isolated anomalies which will help to derive paleopole positions (Ch. 12).

2 Foteini Vervelidou made a significant contribution to this part of the thesis.

PUBLICATIONS

A part of this work has appeared in the Journal of Geophysical Research:

A. Morschhauser, V. Lesur, and M. Grott. A spherical harmonic model of the lithospheric magnetic field of Mars. *J. Geophys. Res.*, 119:1162–1188, June 2014. doi: 10.1002/2013JE004555.

DANKSAGUNG

Ganz besonders und zuallererst danke ich meinen Eltern und meiner Familie. Ohne ihre ständige und bedingungslose Unterstützung hätte ich diese Arbeit nicht schreiben können.

ACKNOWLEDGMENTS

First and most of all, I thank my parents and my family. This work could not have been written without their unconditioned and steady support.

I thank Matthias Grott for his continuous advice and support. He always had a fast and critical mind when discussing details of my work. As well, he helped to put this thesis into context with his broad knowledge in planetary science. Equally, I thank Vincent Lesur for many discussions at the blackboard, his clear advice, and for teaching me the details of linear inversion. Further, I thank Tilman Spohn for being my doctoral advisor as well as Doris Breuer for all her support and for creating a comfortable, open and productive working atmosphere.

I am grateful for my office mate Tina Rückriemen, with whom I shared many wonderful lunch breaks and many interesting discussions. Also, she always had an open ear for my troubles and frustrations. I thank my colleagues at the German Aerospace Centre and at the German Research Centre for Geosciences who supported me in various ways. In particular, I want to thank Alexander Hölscher, Christian Althaus, Dennis Höning, Alexander Jordan, Martin Knapmeyer, Martina Krüger, Matthieu Laneuville, Jürgen Matzka, Wladimir Neumann, Lena Noack, Ina Plesa, Martin Rother, Frank Sohl, Vlada Stamenković, Gregor Steinbrügge, Claudia Stolle, Nicola Tosi, Foteini Vervelidou, and Frank Wagner.

I thank all the friends who helped me to relax, made delicious food, and were sympathetic during busy and stressful times. Namely, I want to mention Anna, Ben, Iulia, Laurel, Martina, Peter, Renaud, and my flatmates Anja, Anna, Benno, Frank, Gudrun, Hanna, Irina, Kathrin, Nina, Noémie, Sabine and Wiebke. Particularly, I thank Angie for her encouragement and for her support when I had to sacrifice another and another weekend to finish this work.

Finally, I want to thank NASA for financing the MGS mission, the German Research Foundation (Deutsche Forschungsgemeinschaft) for their financial support within SPP1488, Paul Wessel and Walter H.F. Smith for providing their great Generic Mapping Tools, as well as André Miede for providing his template `classicthesis` for LaTeX which was used to typeset this thesis.

CONTENTS

LIST OF FIGURES

LIST OF TABLES

ACRONYMS

AB Aerobraking phase 37, 46
CMB Core-mantle boundary 16
CMM Continuous magnetization model [Whaler and Purucker, 2005] . . 9
CRM Chemical remanent magnetization 21
ESD Equivalent source dipole 8
ER Electron reflectometer 38
GSFC Goddard Space Flight Centre 38
IAU International Astronomical Union 68
IRLS Iteratively reweighted least squares 61
FGM Fluxgate magnetometer 39
FMGG Fluxgate Magnetometer Mars (FGM on Phobos 1 and 2) 4
HGA High-gain antenna 42
IMF Interplanetary magnetic field 90
MAG Fluxgate magnetometers on MGS 38
MAGMA Magnetic Fields near Mars (FGM on Phobos 1 and 2) 4
MAGSAT Magnetic Field Satellite 5
MAVEN Mars Atmosphere and Volatile Evolution 163
MD Multi domain 21
MGS Mars Global Surveyor 4, 37
ML Mauersberger-Lowes [Mauersberger, 1956; Lowes, 1966] 94

Part I

MARS MAGNETIC FIELD

The long way of discovering the nature of Mars' magnetic field will be described in the first chapter of this part. This long way was marked by failed missions in the early days of spaceflight, and culminated in the discovery of the crustal magnetic field of Mars by MGS. This crustal field was described by different models, which will be reviewed here, and I will provide arguments why another such model is needed. Subsequently, open questions related to the Martian magnetic field will be presented in the second chapter, and I will comment on how this work may contribute to answer some of these questions.

1 OVERVIEW

The current knowledge on the Martian magnetic field relies on space missions that were equipped with magnetometers. These missions and their data are summarized here, ranging from Mars 1 in the sixties to Mars Global Surveyor (MGS) in the late nineties. Based on these data, the global characteristics of the crustal magnetic field will be discussed. Then, published models of the crustal magnetic field will be presented before a justification for a new model of the crustal magnetic field is given.

1.1 MAGNETIC FIELD DATA

With the beginning of the Space Age, ambitious plans were made to reach for the planet Mars at every biennial opportunity. Early as this, many missions were equipped with magnetometers to characterize the magnetic fields in interplanetary space and around the planets. The first attempt to reach for Mars was made by the Soviet Union with the launch of the twins Mars-1M A/B (or Marsnik 1/2) on October 10th[1] and 14th, 1960. Unfortunately, both of these missions failed due to problems with the launcher [Perminov, 1999]. Out of the other seven Soviet attempts in the sixties, only Mars 1 and Zond 3 were successful. These probes approached Mars at distances of 195000 km (June 19th, 1963), and 1500 km (Aug. 6th, 1965), respectively, but returned no scientific data due to loss of communication. Likewise, the United States (U.S.) National Aeronautics and Space Administration (NASA) failed to reach Mars in the early sixties as no capable launcher was available. However, NASA eventually succeeded on July 14th, 1965, with the fly-by of Mariner[2] 4 at a distance of 9850 km. Mariner 4 carried a helium vector magnetometer which registered significant magnetic field fluctuations 22 minutes after its closest encounter, at 14700 km from the center of Mars. Assuming that these fluctuations were related to the Martian bow shock, Smith et al. [1965] concluded that the Martian dipole moment cannot exceed $30 \cdot 10^{-4}$ the Earth's dipole moment. Later, the same data were reanalyzed, and a respective value of $\leqslant 21 \cdot 10^{-4}$ was obtained [Dryer and Heckman, 1967]. Regrettably, the following successful flyby missions Mariner 6 and 7 (1969) did not carry any magnetometers [Snyder and Moroz, 1992].

1 This attempt was reported by the Administrator of NASA, but Soviet scientists who were involved in the Soviet Space Program report that they had no knowledge of this attempt.

2 Mariner 4 was the replacement for the lost Mariner 3 mission.

A new era began in 1971, when the Soviets inserted Mars 2 and 3 in highly elliptical orbits with relatively low periapsides of 1380 km and 1530 km, respectively. Both missions carried vector fluxgate magnetometers (FGMs) and provided evidence for magnetic field fluctuations that are indicative for bow shock and magnetopause crossings [Dolginov et al., 1973]. Hence, Dolginov et al. [1973] concluded that Mars may possess an internal dipolar field with a magnetic moment of $2.4 \cdot 10^{19}$ Am^2, corresponding to $30 \cdot 10^{-4}$ the Earth's dipole moment of 1970, and in good agreement with the Mariner 4 results. Later on, these results were confirmed by Mars 5 which crossed the Martian magnetotail in 1973 at a periapsis of 1755 km [Dolginov et al., 1976; Dolginov, 1978]. However, a re-analysis of the Mars 3 and 5 data suggested that the observed magnetic field fluctuations are not typical of an intrinsic field and that the Martian magnetosphere was never penetrated by these spacecraft (S/C) [Russell, 1978a]. Rather, the observed bow shock and related magnetic fields may be explained by the interaction of the solar wind with the Martian ionosphere. With this interpretation, Russell [1978b] obtained an upper limit of $2 \cdot 10^{17}$ Am^2 for Mars' dipole moment, corresponding to $25 \cdot 10^{-6}$ that of the Earth. As well, this result is supported by theoretical simulations which reproduce the Mars 3 observations [Russell et al., 1984].

On July 7 and 12, 1988, the Soviet missions Phobos 1 and 2 became the next S/C[3] to carry magnetometers (FMGG[4] and MAGMA[5]) and several plasma instruments to Mars. Communication to Phobos 1 was lost, but Phobos 2 orbited Mars with a periapsis of 827 km for three months before communication was lost as well. The new data were not supporting an intrinsic dipolar field [Riedler et al., 1989, 1991], but such a field could not definitely be ruled out [Riedler et al., 1989; Dolginov and Zhuzgov, 1991]. In particular, co-rotating features of the magnetic field were interpreted as evidence for an intrinsic Martian field [Moehlmann et al., 1991]. Alternatively, it was suggested that these features may be explained by a locally magnetized crust [Curtis and Ness, 1988; Leweling and Spohn, 1997].

The dispute whether Mars possesses a core dynamo field was not resolved until 1997, when MGS, a downgraded version of the lost Mars Observer mission, was the first mission to reach Mars after a gap of 21 years. MGS was launched on November 7, 1996 and operated in Martian orbit from 1997 to 2006. It was equipped with two vector FGMs (MAG) and an electron reflectometer (ER) [Acuña et al., 2001]. During its early aerobraking phase (AB) and science phase orbit (SPO), MGS sampled the Martian magnetic field down to a periapsis of 80 km. At low altitudes below 200 km, this orbit resulted mainly in dayside data with sparse global coverage [Acuña et al., 1999]. On March 9, 1999, MGS entered the final mapping phase or-

3 The U.S. Viking landers in 1975 did not carry magnetometers.
4 Fluxgate Magnetometer Mars (FMGG): Build by D. Möhlmann, German Democratic Republic.
5 Magnetic Fields near Mars (MAGMA): Build by W. Riedler, Austria.

bit (MPO) which was almost perfectly circular. During this mission phase, a vast amount of data were collected which provide dense global coverage during day- and nighttime at a nearly constant altitude of around 400 km.

1.2 GENERAL PROPERTIES OF MARS' MAGNETIC FIELD

Earliest results based on MGS AB/SPO data indicated that Mars does not possess a relevant large-scale magnetic field originating in an active core dynamo. In particular, Acuña et al. [1998] constrained the dipole moment to less than $2 \cdot 10^{17}\,\mathrm{Am}^2$, in agreement with the interpretation of Mars 3 and 5 data by Russell [1978b]. Instead, strong crustal anomalies with an estimated magnetization of $1.6 \cdot 10^{16}\,\mathrm{Am}^2$ were discovered in old Noachian[6] terrain at the boundary of Arabia Terra and Acidalia Planitia[7] [Acuña et al., 1998; Ness et al., 1999]. In Fig. 1.1, the complete MAG AB/SPO magnetic field data are shown along with the dichotomy boundary[8] (thick black line). For the most part of this map, magnetic sources correlate with older, topographically elevated southern crust [Acuña et al., 1999]. For instance, the strongest field intensities (F) with up to 1600 nT at 100 km altitude are observed over Terra Sirenum (TS) and Terra Cimmeria (TC) in the Noachian highlands between 120°E and 210°E [Acuña et al., 1999]. As an exception, a region largely devoid of fields is observed between 80°W/80°E and south of 30°S [Arkani-Hamed and Boutin, 2012b]. Vice versa, magnetic fields are observed in the northern lowlands near Amazonis Planitia, near Arcadia Planitia, and near the north pole [Acuña et al., 1999; Hood and Zakharian, 2001]. Other prominent features of the Martian crustal field include elongated anomalies with alternating polarity in TS/TC [Connerney et al., 1999] as well as the lack of measurable fields above the large impact basins (Hellas, Argyre, Isidis, and Utopia, marked by dashed lines in Fig. 1.1) and the volcanic provinces of Tharsis and Elysium [Acuña et al., 1999].

As compared to the AB/SPO data, the MPO data have the advantages of a constant observation altitude and less noise due to the dense global coverage on the nightside. Similar to Fig. 1.1, the MPO nighttime data are presented in Fig. 1.2, and the previous observations can be confirmed. Moreover, the maximum of the vertically down (Z) component reaches ~220 nT at 400 km altitude, corresponding to ~20 times the strongest terrestrial fields of crustal origin as observed by the Magnetic Field Satellite (MAGSAT) at a similar altitude [Langel et al., 1982; Acuña et al., 2001]. Further, Acuña et al. [2001] have shown that the MPO data allow for a dipole moment of $< 2 \cdot 10^{17}\,\mathrm{Am}^2$ only, which may be completely explained by the crustal field.

6 Based on crater-size frequency distributions, different epochs have been defined for Mars. The oldest epoch is the Noachian, followed by the Hesperian and Amazonian. In order to convert these epochs to absolute ages, theoretical models have been used along with the radiometric record of the moon [Hartmann and Neukum, 2001; Michael, 2013].

7 Please refer to Fig. A.1 for an overview of regions and geologic features on Mars.

8 The dichotomy boundary separates the topographically elevated southern highlands from the northern lowlands (Sec. 2.4).

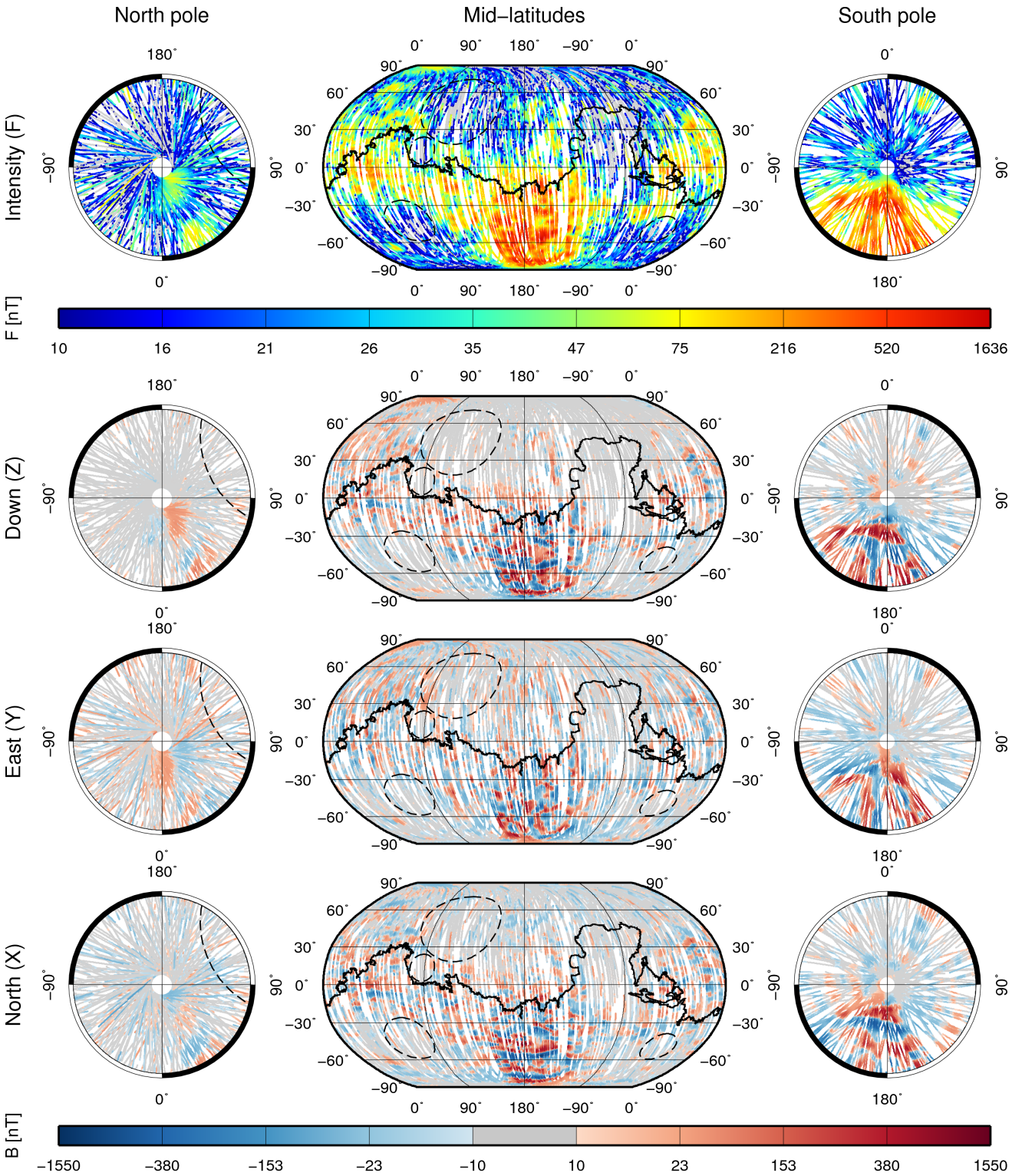

Figure 1.1. Magnetic field of Mars as measured by MGS during the AB and SPO at altitudes of 80 km – 200 km. From bottom to top, the horizontally north (X), east (Y), and vertically down (Z) components as well as the field intensity (F) are shown. Also, the topographic dichotomy as defined by the 0 m MOLA isoline is indicated by the black solid line, and major impact basins are indicated by black dashed circles (from left to right: Hellas, Isidis, Utopis, Argyre).

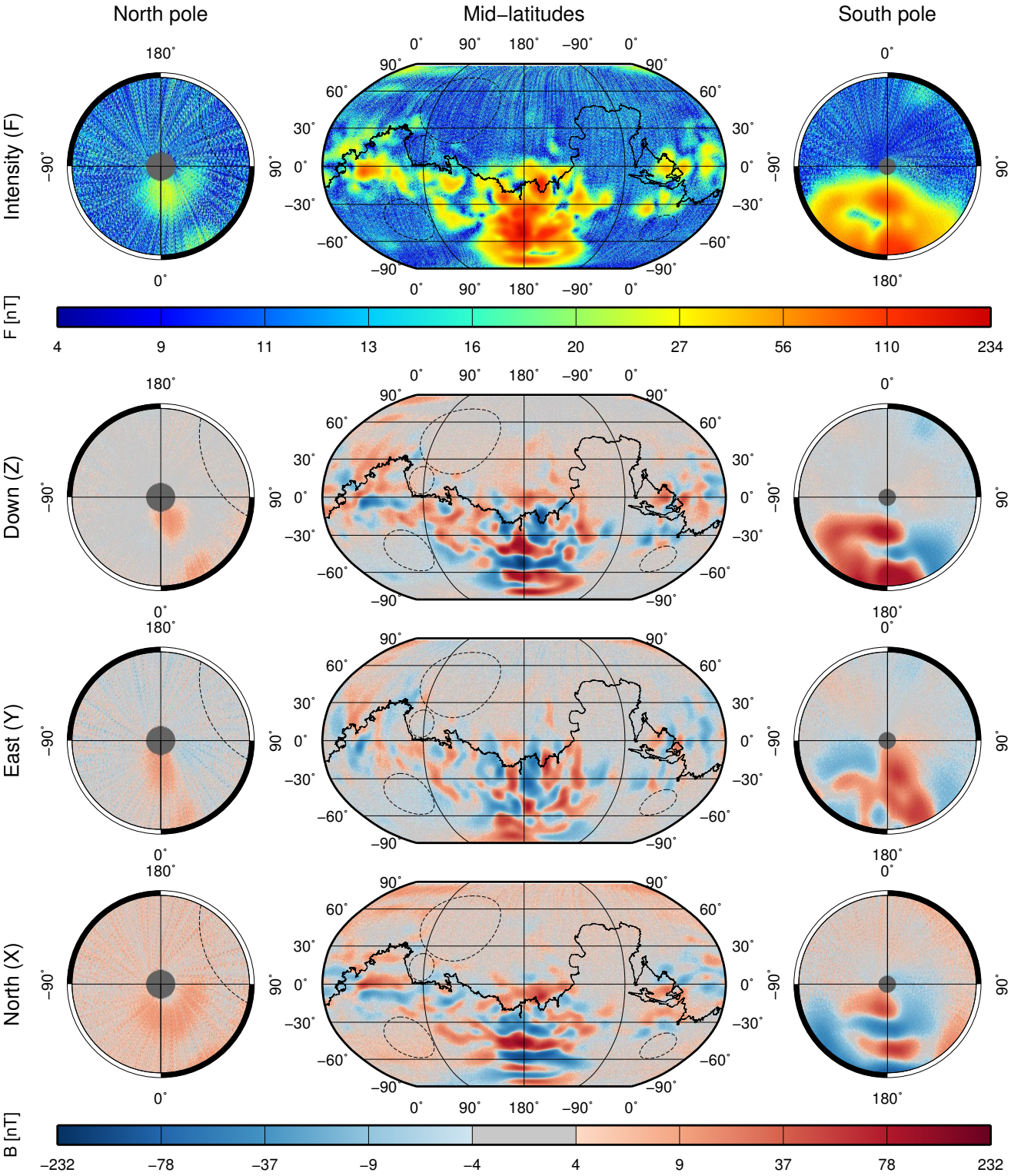

Figure 1.2. Magnetic field of Mars as measured by MGS during the MPO at an altitude of 400 km. From bottom to top, the horizontally north (X), east (Y), and vertically down (Z) components as well as the field intensity (F) are shown. Furthermore, the topographic dichotomy as defined by the 0 m MOLA isoline is indicated by the black solid line, and major impact basins are indicated by black dashed circles (from left to right: Hellas, Isidis, Utopis, Argyre).

1.3 MODELS OF THE CRUSTAL MAGNETIC FIELD

For the following two major reasons, models of the crustal magnetic field are an important and powerful tool when interpreting magnetic field data: First, non-crustal field contributions[9] in these models can be minimized, for example by including a description of the external field [Olsen et al., 2010a]. Second, such models provide a physically consistent description of the crustal magnetic field. Hence, they allow to downward-continue the field to any altitude within the limits of the data quality, within the achieved model robustness and resolution, and within the validity of the underlying physical assumptions (e.g. in source-free regions, Sec. 6.1). In this way, it is easier to interpret magnetic anomalies as compared to using the raw data, which were obtained from different altitudes. Moreover, the altitude of observation determines the footprint of the data points and acts as a high-pass filter, eliminating shorter wavelengths at higher altitudes [Purucker et al., 2000; Connerney et al., 2004, 2005]. Thus, anomalies of smaller scale may be revealed when a model is evaluated at lower altitudes.

Published models of the crustal magnetic field can be grouped according to the underlying data set and the chosen representation of the crustal field (Tab. 1.1). Early models used the AB/SPO data set, whereas later models used the MPO data set, or a combination of both. The chosen representation of the crustal field either consists of a set of equivalent source dipoles (ESDs) located in the crust, a continuous magnetization model (CMM), or an expansion of the scalar magnetic field potential in terms of spherical harmonic (SH) functions. In principle, the SH and ESD representations can be transformed into each other [Arkani-Hamed, 2002c; Lesur, 2006]. However, an infinite maximum SH degree and order must be used (ESD $\rightarrow$ SH) or assumptions on the location of the sources (SH $\rightarrow$ ESD) must be made. A summary of all published models of the crustal magnetic field is given in Tab. 1.1, and a detailed description of these models is presented below.

EQUIVALENT SOURCE DIPOLES Models of the crustal magnetic field that are based on ESDs describe the observed field in terms of a linear combination of the field contributions from single dipoles which are distributed within the planetary crust [Mayhew, 1979]. Without additional constraints, an infinite number of ESD distributions correctly describe the data [Runcorn, 1975; Parker et al., 1987; Lesur and Jackson, 2000; Gubbins et al., 2011]. For example, such constraints may include the additional minimization of the root mean square (RMS) magnetization amplitude [Whaler and Purucker, 2005; Langlais et al., 2004], or a fixed direction of magnetization [Purucker et al., 2000]. With regard to the resolution, an ESD model contains spectral information of infinitely small wavelengths. These short wavelengths are particularly sensible to external field contributions in satellite data, and cannot be fully controlled with an ESD model. What is more, the physi-

9 Such non-crustal fields may originate in the ionosphere, magnetosphere, or the S/C itself.

cal rock magnetization is continuous in space and cannot consistently be described by ESDs. In particular, the localized signature of the individual ESDs must be smoothed when an ESD model is downward-continued below a critical altitude which roughly corresponds to the dipole spacing. This can be achieved by expressing the ESD model in a truncated series of SH functions [Langlais et al., 2004].

The first published ESD model of the Martian crustal magnetic field was presented by Purucker et al. [2000]. This model was derived from the vertically down (Z) component of binned AB/SPO data with altitudes below 200 km. Further, it is based on 11550 radially oriented ESDs located on the mean surface of Mars with a mean dipole spacing of 111 km. This model was updated by Langlais et al. [2004], who used a combination of the AB/SPO and the MPO data. Also, they used all vector components to simultaneously solve for the magnetization directions and intensities (F) of 4840 dipoles with a mean dipole spacing of 173 km. The newest version of this model was presented by Langlais et al. [2010] who included a higher resolution of 130 km, the ER data [Lillis et al., 2008a], and an updated data selection scheme. Another ESD model was published by Chiao et al. [2006] who implemented a wavelet transform which allows for independently regularizing different spatial wavelengths.

A slightly different description of the crustal field was used by Whaler and Purucker [2005] who provided a CMM. In this case, the magnetization is described as a linear combination of the Green's functions relating the magnetization to the observed field for each of the data points [Parker et al., 1987; Whaler and Langel, 1996; Whaler and Purucker, 2005]. However, this model is based on the AB/SPO/MPO data set of Cain et al. [2003], thus not containing any data beyond 2003.

SPHERICAL HARMONICS In spherical geometry, the SH functions solve the Laplace equation (Eq. 6.3) which describes the scalar magnetic potential V in a source-free region. Moreover, the SH functions form a complete basis, allowing for a consistent downward-continuation of the scalar potential and the crustal field to any altitude within the source-free region. Still, the resolution of models based on SH functions is limited by the degree and order at which the SH expansion is truncated. As compared to ESD models, no assumptions on the number, size, and location of the sources have to be made. However, localized solutions require more sophisticated basis functions, which may be expressed as a linear combination of SH functions [Wieczorek and Simons, 2005; Simons et al., 2006; Lesur, 2006; Thébault et al., 2006].

The first published SH model of the Martian crustal magnetic field is based on all three vector components of the binned AB/SPO data set of Purucker et al. [2000] [Arkani-Hamed, 2001b]. This model is expanded up to SH degree and order 60. Subsequently, it was truncated at SH degree and order 50 as non-crustal signals leak into the model and become dominant

Table 1.1. Overview of published models of the crustal magnetic field of Mars.

REFERENCE	DATA SET	NUMBER OF DATA[a]	COMPO-NENTS	METHOD (RESOLUTION)	COMMENT
Purucker et al. [2000]	• AB/SPO (Complete) • $h < 200\,km$[b] • Binned & Averaged ($1° \times 1° \times 10\,km$ bins)	40546	Z	ESD 11550 dipoles 111 km spacing	• "Quick-look data" • Only radial dipoles used • standard deviation (STD) of binned data as data weights
Connerney et al. [2001]	• MPO nighttime • March, 1999 - August, 2000 • 1° along-track averaging • Subsequently Binned & Median (360×180 bins)	N/A	X,Y,Z	N/A	• Visual map from binned data • No lithospheric field model
Arkani-Hamed [2001b] Arkani-Hamed [2002a]	• Purucker et al. [2000]	40546	X,Y,Z	SH $L_{max} = 60$[c] $L_{trunc} = 50$[d]	
Arkani-Hamed [2002b]	• Purucker et al. [2000] • MPO nighttime • Binned & Averaged ($0.5° \times 0.5° \times 10\,km$ bins) • Outliers removed ($> 2\sigma$)[e]	40546 274000	X,Y,Z X,Y,Z	SH $L_{max} = 60$[c] $L_{trunc} = 50$[d]	• Covariance analysis of separate low-/high-altitude models
Cain et al. [2003]	• AB/SPO (Complete) • $h < 200\,km$[b] • MPO nighttime • March, 1999 - March, 2000 • MPO data selected to fill remaining data gaps	~ 65000 ~ 45000	X,Y,Z X,Y,Z	SH $L_{max} = 90$[c]	• STD of residuals as data weights • Selected data set provides a uniform data density on a $5° \times 5°$ grid
Arkani-Hamed [2004a]	• MPO nighttime • Binned & Averaged ($0.5° \times 0.5°$ bins) • Outliers removed ($> 2\sigma$)[e]	>233840[f]	Z	SH $L_{max} = 90$[c] $L_{trunc} = 62$[d]	• Covariance analysis of two temporally separated data sets
Arkani-Hamed [2004b]	• MPO nighttime • Binned & Averaged ($0.25° \times 0.25°$ bins) • Outliers removed ($> 2\sigma$)[e]	N/A	Z	SH $L_{max} = 90$[c] $L_{trunc} = 50$[d]	• Covariance analysis of two temporally separated data sets

REFERENCE	DATA SET	NUMBER OF DATA[a]	COMPO-NENTS	METHOD (RESOLUTION)	COMMENT
Langlais et al. [2004]	• AB day/nighttime / SPO nighttime • $h < 350$ km[b] • Binned & Averaged ($1° \times 1° \times 10$ km bins) • Outliers removed ($\Delta Z > 50$ nT relative to Purucker et al. [2000]) • MPO nighttime • Binned & Averaged ($1° \times 1° \times 10$ km bins) • Outliers removed ($\Delta Z > 50$ nT relative to Purucker et al. [2000])	75380 103996	X,Y,Z X,Y,Z	ESD 4840 dipoles 173 km spacing	• STD of bins as data weights
Whaler and Purucker [2005]	• Cain et al. [2003]	111274	X,Y,Z	CMM Continuous	• Same weights as Cain et al. [2003]
Chiao et al. [2006]	• Cain et al. [2003]	111274	X,Y,Z	ESD 10242 nodes	• Multiresolution analysis (Wavelet basis) • Linear interpolation between model nodes
Lillis et al. [2010b]	• MPO nighttime • 1999 - 2006	N/A	X,Y,Z	ESD & SH $L_{max} = 90$[c] $L_{trunc} = 51$[d]	• ESD from data on adjacent tracks • Subsequently transformed to SH using a $2° \times 1°$ grid
Langlais et al. [2010]	• AB day/nighttime / SPO nighttime • $h < 350$ km[b] • MPO nighttime • ER	~120000 N/A $\sim 2.3 \cdot 10^6$	X,Y,Z X,Y,Z F	ESD 130 km spacing	• In preparation for final publication (B. Langlais, pers. comm., 2014)
Olsen et al. [2010a]	• MPO nighttime • March, 1999 - November, 1999	~ 50000	X,Y,Z	SH $L_{max} = 40$[c] $Lext = 20$[g] $Ltor = 20$[h]	• External, internal, and toroidal fields modeled • A similar model was developed for the dayside

[a] The number of data used to derive the model. This is not equal to the initial number of used data , i.e. before data selection and possibly averaging.
[b] h is altitude above the surface.
[c] The maximum SH degree and order of the model of the crustal field.
[d] The SH degree and order at which the solution was truncated.
[e] For each bin, outliers have been rejected which deviate by more than the given number of STD σ from the mean in the respective bin.
[f] Over 90% of their 360×720 data bins were filled.
[g] The maximum SH degree and order of the model of the external field.
[g] The maximum SH degree and order of the model of the toroidal field.

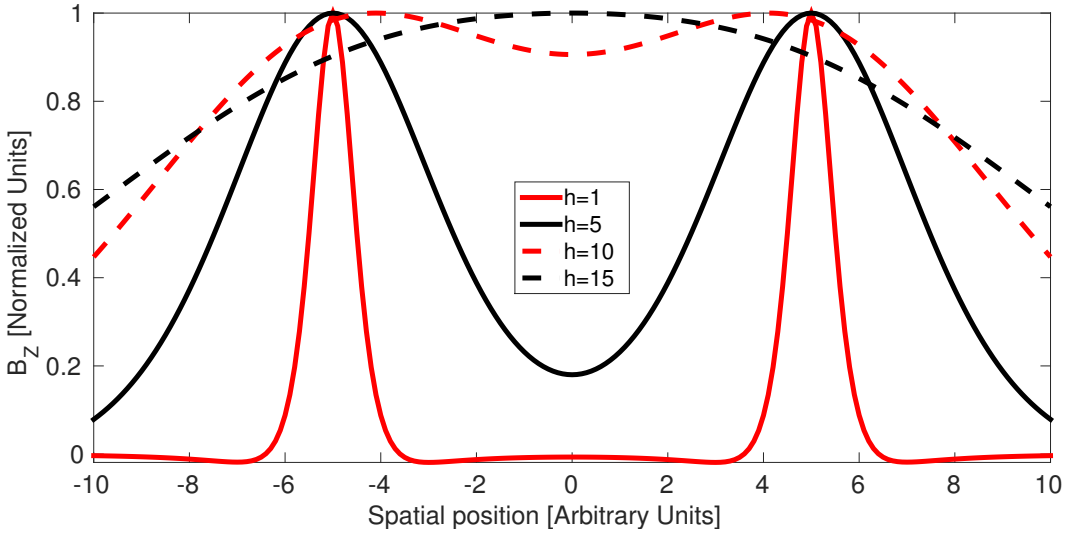

Figure 1.3. Normalized vertically down (Z) magnetic field component of two radially oriented dipoles at different observation altitudes h (arbitrary units). The source dipoles are separated by a distance of 10 arbitrary units. For altitudes higher than the dipole separation (i.e. $h \geqslant 10$), the signal of the individual dipoles smears, and eventually becomes indistinguishable.

for higher SH degrees. Later, Arkani-Hamed [2001b] averaged the covarying SH coefficients [Arkani-Hamed et al., 1994] of their first model [Arkani-Hamed, 2001b] and a new model which is based on binned MPO vector data. The resulting model is expanded up to degree and order 65, and subsequently truncated at degree and order 50. However, Cain et al. [2003] showed that such a truncation is insufficient to represent the AB/SPO data. In other words, contributions from smaller wavelengths contain valuable information, even though "the statistical significance of the highest-degree individual terms is low" [Cain et al., 2003]. Consequently, Cain et al. [2003] presented a model that is expanded up to SH degree and order 90. This model was obtained from mainly AB/SPO data, and the MPO data were used to fill data gaps. As well, the two latest SH models [Arkani-Hamed, 2004a,b] are expanded up to degree and order 90, but have been truncated at SH degrees and orders 62 and 50, respectively. Again, these models were derived by covariance analysis [Arkani-Hamed et al., 1994] of two temporally separated MPO data sets. In addition, contributions from non-crustal fields were minimized by using only the vertically down (Z) field component, which is least contaminated by noise [Arkani-Hamed, 2004a]. In the latest SH model, Lillis et al. [2010b] applied along-track filtering to remove external fields. In particular, they first removed external fields by fitting adjacent tracks using ESDs, and subsequently converted this solution to a SH basis. However, Thébault et al. [2012] have shown that this approach also removes a part of the crustal field.

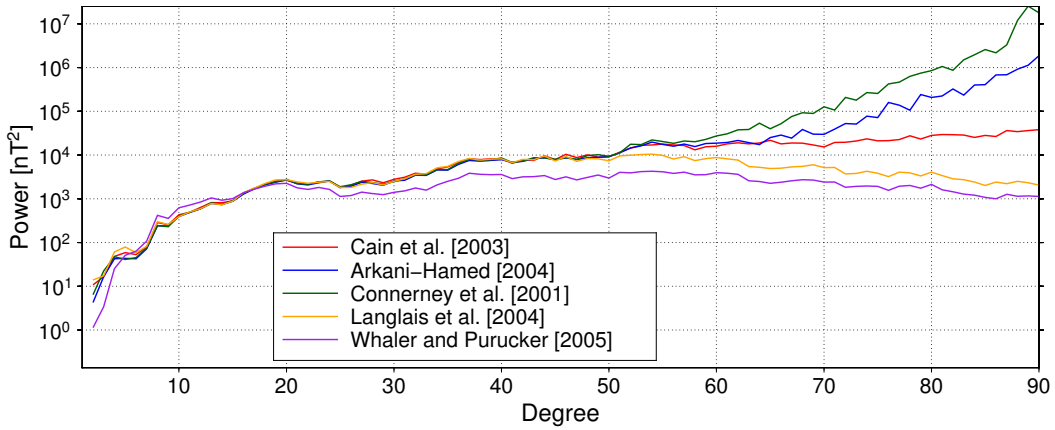

Figure 1.4. The ML power spectrum describes the averaged power for each SH degree [Mauersberger, 1956; Lowes, 1966] and is shown at a radius of 3393.5 km for different published models.

1.4 LIMITS OF PUBLISHED MODELS

Models of the crustal magnetic field help to reduce the influence of non-crustal signals in the data, to project the data on a single altitude, and to investigate the field down to surface altitude. Yet, the quality of the data may severely restrict the resolution and robustness of such models. As an example, the normalized vertically down (Z) component of the field produced by two radially oriented dipoles is shown in Fig. 1.3 at different observation altitudes (arbitrary units). For altitudes larger than the dipole separation ($d = 10$), the signal of the two dipoles merges and a single global maximum is observed at their average position. Hence, it appears that the maximum achievable resolution is limited by the observation altitude [Arkani-Hamed, 2002b; Mayhew, 1979]. However, this is not completely true, as the signature of the two dipoles is still present in the signal. Rather, this signature eventually falls below the noise level when a certain altitude is exceeded. Vice versa, leakage of noise into the model will result in large correlated anomalies [Lesur et al., 2013] and in an exponential increase of power above a certain SH degree of the Mauersberger-Lowes (ML) power spectrum[10] (Fig. 1.4). Hence, the resolution is limited by the wavelength where noise starts to become significant in the data at orbit altitude [Connerney et al., 2004].

Ideally, a model of the crustal magnetic field extracts all possible information from the data and reduces the influence of non-crustal signals at the same time. For this purpose, the model can either be truncated at the SH degree where non-crustal fields start to reach the signal intensity [Arkani-Hamed, 2001b, 2002b, 2004a,b; Lillis et al., 2010a], or it can be regularized by suppressing strong correlated anomalies [Purucker et al., 2000; Langlais

10 The Mauersberger-Lowes (ML) power spectrum is defined as the average power on a spherical surface in dependence of the SH degree [Mauersberger, 1956; Lowes, 1966].

et al., 2004; Whaler and Purucker, 2005; Chiao et al., 2006; Langlais et al., 2010]. Still, both of these methods have their drawbacks. In the first case, a significant part of the signal may be missed, in particular for low-altitude data [Cain et al., 2003]. In the second case, the regularization may not only remove noise, but also damp the actual signal of the crustal field. An additional way to reduce non-crustal fields is to remove noisy data a priori. For example, only nighttime data may be selected [Cain et al., 2003], only the least-contaminated vertically down (Z) component may be selected [Purucker et al., 2000; Arkani-Hamed, 2004a,b], or individual data may be removed when they are incompatible with the other data. In particular, such data tracks may be identified by their deviation from the mean [Arkani-Hamed, 2001b; Arkani-Hamed and Boutin, 2004], or by comparison to a previous model [Langlais et al., 2004]. However, even the noisiest data contain useful information, and should ideally be considered in an appropriate way.

Here, a model of the crustal magnetic field will be presented which is robust and, at the same time, possesses a high resolution. This was achieved with the help of several techniques. First of all, the model has been expanded up to degree and order 110, sufficient to fit most of the variations in the AB/SPO data. Second, leakage of non-crustal fields is minimized by approaching an L1 norm for regularization (Sec. 6.4). In this way, strong crustal field gradients, as they are present on Mars, will be better supported than if an L2 norm is used. Further, MPO daytime data and three AB/SPO tracks with location errors (c.f. Sec. 4.2) have been rejected. Else, less weight is given to noisy data without ignoring them (Sec. 6.3). Overall, the presented model is well suited to help in answering some of the unresolved questions which will be described in the next chapter.

2 OPEN QUESTIONS

The origin of the Martian magnetic field was finally revealed with Mars Global Surveyor (MGS) magnetic field data. At the same time, new questions arose, and many of these are still under debate. Here, I will summarize these questions, and I will outline how this work may contribute to answer them.

2.1 TIMING OF THE CORE DYNAMO

MGS magnetic field data unambiguously revealed that the Martian magnetic field is of crustal origin, and that no significant core dynamo exists today. For this reason, it is assumed that the observed crustal field originates from natural remanent magnetization (NRM) which was acquired when an internal core dynamo was active [Acuña et al., 1998]. Still, the cessation time of this dynamo is unknown. In particular, an early cessation in the Noachian at around $4.0 - 4.1$ Gyr b.p. is suggested by the apparently demagnetized major impact basins such as Hellas, Isidis, Argyre, and Utopia[1] [Acuña et al., 1999; Mohit and Arkani-Hamed, 2004; Lillis et al., 2008] as well as by the magnetic signatures of smaller craters down to 300 km in diameter [Lillis et al., 2013a]. Further, the largest volcanic provinces, namely Tharsis and Elysium, which were in place at around $3.5 - 3.7$ Gyr ago[2] [Phillips, 2001; Werner, 2009], appear to be demagnetized [Acuña et al., 1999; Arkani-Hamed, 2004b; Johnson and Phillips, 2005]. Alternatively, the Martian core dynamo may have ceased in the Hesperian, later than 3.7 Gyr ago. This hypotheses is supported by the observation of strong magnetic fields above regions of Noachian and Hesperian crust [Milbury and Schubert, 2010], the observation of Hesperian-aged paleopoles near the geographic poles [Milbury et al., 2012], and positive magnetic anomalies over the volcanic edifices of Apollinaris Patera and Hadriaca Patera[3] [Lillis et al., 2006; Langlais and Purucker, 2007; Hood et al., 2010]. Another possibility was proposed by Schubert et al. [2000] who argued that the dynamo may have started only after the formation of Tharsis and the large impact basins. Also, a late onset of the core dynamo at around $50 - 100$ Myr after the formation of Mars is in agreement with the large field-free region in the southern high-

1 Please refer to Fig. A.1 for an overview of regions on Mars.

2 From an analysis of valley networks, Phillips [2001] concluded that the main load of Tharsis was in place by the end of the Noachian, probably before Hellas formed. Also, crater-counting on the flanks and calderas of the Tharsis Montes and in the Elysium province suggest that they were largely in place at around 3.5 Gyr ago [Werner, 2009].

3 These volcanoes were active about 3.9 Gyr – 3.3 Gyr ago [Williams et al., 2008; Werner, 2009].

lands (Figs. 1.1 and 1.2) [Arkani-Hamed, 2012; Arkani-Hamed and Boutin, 2012a]. However, all of these scenarios have been criticized. For example, large impact basins may always appear demagnetized[4] [Solomon et al., 2005]. As well, the interpretation of the magnetization of volcanic features is ambiguous [Lillis et al., 2006], and the inferred surface age might not be representative for the time of (de)magnetization [Johnson and Phillips, 2005].

The timing of the Martian core dynamo has deep implications on the thermal and chemical evolution of Mars [Stevenson, 2001; Connerney et al., 2004; Breuer et al., 2010]. In the case of an early core dynamo shut down (~4.1 Gyr ago), the most probable energy source to power the dynamo would have been thermal convection which requires a superadiabatic heat flux of $5-19\,\mathrm{mW/m^2}$ at the core-mantle boundary (CMB) [Nimmo and Stevenson, 2000; Breuer and Spohn, 2003]. Such a heat flux may either be provided by a superheated core, which needs to be rich in sulfur (>14 wt.% S) in order to prevent inner core formation [Stevenson et al., 1983; Schubert and Spohn, 1990; Hauck and Phillips, 2002; Breuer and Spohn, 2003, 2006; Williams and Nimmo, 2004], or an early regime of plate-tectonics [Nimmo and Stevenson, 2000; Breuer and Spohn, 2003]. Alternatively, the dynamo may have been chemically powered by solidification of the inner core [Stevenson, 2001]. However, such a dynamo can only be stopped by completely freezing the iron core, or by one or several large impacts[5]. In addition, some unorthodox alternatives to explain the Martian core dynamo have been suggested. These scenarios include the excitation of the dynamo by tidal forces [Arkani-Hamed et al., 2008; Arkani-Hamed, 2009] from an hypothetical ancient Martian companion [Arkani-Hamed, 2005b], by precession [Tilgner, 2005], or by a growing inner core in the Fe-snow regime [Stewart et al., 2007].

The presented model of the crustal magnetic field of Mars will help to constrain the timing of the Martian core dynamo by reanalyzing the magnetic signature of volcanoes (Sec. 10.1) and by investigating the magnetic signature of impact craters with diameters down to 195 km (Sec. 10.2). In contrast to previous studies (e.g., Lillis et al. [2013a]; Langlais and Purucker [2007]), the predicted field at surface altitude instead of the field at orbit altitudes will be used.

4 Solomon et al. [2005] argue that large basins will be preferred sites of hydrothermal alteration, mainly due to their topographic setting and availability of enhanced heat. Due to this hydrothermal activity, the magnetization within the craters will decay faster and eventually be erased. For further arguments, see footnote on p. 142.

5 Impacts might stop a core dynamo through the deposition of heat in the mantle [Roberts et al., 2009] and stable thermal stratification of the core [Arkani-Hamed and Olson, 2010; Arkani-Hamed, 2010, 2012; Roberts and Arkani-Hamed, 2014]. On the other hand, a large impact may also trigger a dynamo by heat transportation to the core through sinking iron droplets [Reese and Solomatov, 2010]

2.2 MAGNETIZATION OF THE MARTIAN CRUST

The exact distribution of magnetization cannot be inferred from magnetic field measurements alone. The reason is the fundamental non-uniqueness in the mathematical relationship between magnetization and magnetic field. In other words, an infinite number of magnetization distributions result in exactly the same magnetic field topology [Runcorn, 1975; Parker et al., 1987; Lesur and Jackson, 2000; Gubbins et al., 2011]. Nevertheless, additional knowledge of the sources or the magnetization distribution reduces the number of possible solutions. Hence, several attempts to investigate the magnetization of the Martian crust have been made, which are grouped in Tab. 2.1 according to the applied additional constraints (column "Method"). In this table, empty cells should be read as containing the content of the cell above.

A unique magnetization solution is obtained if the exact shape and size of a uniformly magnetized body is known. However, such information is not available for Mars. Still, gravity data[6], isolated magnetic field anomalies, or geologic structures which are causally related to a magnetic anomaly, may allow to constrain the location of the source. Studies with the source location and/or size as a constraint are labeled "Source geometry" in the third column ("Method") of Tab. 2.1. Many of these studies were primarily designed to obtain paleopole positions and use single dipoles as a source (Sec. 2.5). In this case, the resulting dipole moment $\mathbf{m}$ can be transformed to an equivalent magnetization[7] $\mathbf{M} = N\mathbf{m}/V$ (N is the number of elementary dipoles in the volume V), if assumptions on the source body shape and thickness (fifth column) are made[8]. Another method to estimate rock magnetization is to minimize the required total magnetization (labeled "minimum magnetization" in Tab. 2.1). This approach was implemented by most of the models describing the crustal magnetic field which are based on equivalent source dipoles (ESDs) (Sec. 1.3). Similarly, Parker [2003] obtained a hard lower limit for magnetization by calculating the minimum magnetization required to explain individual magnetic field measurements. Further, the magnetization can be constrained by fixing the direction of magnetization (labeled "Fixed orientation" in Tab. 2.1). For example, the remanent magnetization of the crust may be restricted to the direction of the ancient core dynamo field lines. For Mars, this field topology is unknown, but might be inferred from paleopole positions if a dipolar field is assumed [Arkani-Hamed, 2002c]. Else, an arbitrary direction might be imposed on magnetization [Purucker et al., 2000].

6 Note that gravity data suffers from the same non-uniqueness as magnetic field data. Nevertheless, it is useful when investigating vertically averaged density contrasts.

7 Here, the term "magnetization" is equivalent to "dipole moment per unit volume" with units of A/m. For a more detailed discussion of units in geomagnetism refer to Butler [1992, p. 12ff.].

8 Still, a forward model using this equivalent volume magnetization with the assumed body shape will not exactly reproduce the field of the respective single dipole.

Table 2.1. Overview of crustal magnetizations which have been obtained for Mars. Empty cells should be read as containing the content of the cell above.

REFERENCE	METHOD	LOCATION	SOURCE[a]	EQUIV. LAYER THICKNESS [KM][b]	MAGNETIZATION[7] [A/M]
Acuña et al. [1998]	Source geometry	Arabia Terra	Single dipole	100[c]	16
Connerney et al. [1999]		Terra Cimmeria (TC) / Terra Sirenum (TS)	Several sources 30 km deep, 200 km wide and infinitely long in E-W direction	30	20
Sprenke and Baker [2000]			Several sources 30 km deep, 100 km wide and infinitely long in E-W direction	30	9.8[d] 0-70 [20] [e]
Nimmo and Gilmore [2001]			400 km stripe	10 100	40 5
Hood et al. [2007]			41 Surface disk(s)	30	5-58 [17] [e]
Frawley and Taylor [2004]		TS	Polygonal prism	20	16 / 23
Quesnel et al. [2007]			Single dipole	31/55/58[f]	143/54/32
Hood and Zakharian [2001]		Planum Boreum / Acidalia Planitia	Surface disk	100	0.4-0.9
Arkani-Hamed [2001a]		Various locations (mainly highlands)	Elliptical prism	10	9-15
Arkani-Hamed and Boutin [2004]			Elliptical prism	10	13-42
Hood et al. [2005]			Surface disk(s)	50	2-15

To be continued on next page.

Table 2.1. Overview of crustal magnetizations obtained for Mars.
- Continued from previous page. -

REFERENCE	METHOD	LOCATION	SOURCE[a]	EQUIV. LAYER THICKNESS [KM][b]	MAGNETIZATION[7] [A/M]
Langlais and Purucker [2007]	Source geometry	Apollinaris Patera	Multiple dipoles	40	0.2-10.1
Hood et al. [2010]			Surface disk(s)	50	2.8 - 3.8
Arkani-Hamed [2002c]	Fixed orientation	Global	Continuous (SH functions)	50	$\leqslant$35
Purucker et al. [2000]	Minimum Magnetization & Fixed orientation		Multiple dipoles (ESD)	40	-22 - 17
Langlais et al. [2004]	Minimum Magnetization			50	$\pm$12
Whaler and Purucker [2005]			Continuous (Green functions)	50	$\pm$ 20
Parker [2003]		TC / TS	Continuous (Elementary dipoles)	50	4.76
Hood et al. [2010]		Lucus Planum		3	16

[a] Equivalent source that has been used to model the observed field.
[b] Thickness of the equivalent layer that has been used to constrain the magnetization.
[c] Cube with 100 km side length.
[d] All sources with uniform magnetization
[e] Sources with variable magnetization. Mean is given in brackets.
[f] Sphere tangent to the surface with center at dipole depths of given value.

All of these methods require the thickness of the magnetized layer in order to estimate the volume rock magnetization. Again, this thickness cannot be constrained from magnetic field data alone, and additional assumptions on the magnetization are required. For instance, the thickness of the magnetized layer can be estimated from a comparison of the observed and a theoretical power spectrum. With this method, Voorhies [2008] and Voorhies et al. [2002] obtained a magnetic layer thickness of 47.8 ± 8.4 km

and 46.7 ± 6.8 km, respectively, depending on the assumptions regarding the sources. More recently, Lewis and Simons [2012] locally resolved magnetization thicknesses by combining Slepian functions[9] with the approach of Voorhies [2008]. As a result, thicknesses of $0 - 57.3$ km were obtained, with an average of 26 km, which correlate with crustal thickness estimates [Lewis and Simons, 2012]. Hence, most of the remanently magnetized rocks are indeed located within the crust. The maximum thickness of the magnetized layer can also be estimated from the Curie depth[10] of the most relevant magnetic minerals (for an overview of magnetic minerals and their inferred Curie depths please refer to Tab. 2.2). For this purpose, the ancient Martian heat flow must be estimated in order to obtain the minimum Curie depth since the acquisition of thermoremanent magnetization (TRM). Such an estimate may be obtained either from thermal evolution models (e.g., Hauck and Phillips [2002]; Breuer and Spohn [2003]; Morschhauser et al. [2011]) or the elastic thickness of the lithosphere [Ruiz et al., 2006; Ruiz, 2009]. With this method, the estimated maximum thicknesses of the magnetized layer range from < 20 km to 100 km. A third method to estimate the magnetization thickness was proposed by Nimmo and Gilmore [2001] who suggested that this thickness is equivalent to the typical excavation depth of unmagnetized craters. In their study, they observed weak fields over impact basins larger than 500 km in diameter. From a comparison with the dimensions of terrestrial craters, they inferred a magnetized layer thickness of $10 - 100$ km, with a favored value of $30 - 40$ km. However, their study might have suffered from using the noisy raw data at satellite altitude.

The model of the crustal magnetic field of Mars as presented in this thesis will help to better constrain the magnetization of the Martian crust. In particular, the minimum required magnetization will be calculated from the SH coefficients of the presented model (Ch. 11).

2.3 MAGNETIC MINERALS

The Martian magnetic field is dominated by its crustal field. In other words, the major sources of the planetary magnetic field consist of magnetized ferro- and ferrimagnetic minerals[11] within the crust. These minerals have the ability to acquire stable remanent magnetization when they are

9 Slepian functions are based on a linear combination of spherical harmonic (SH) functions in a way to maximize their spectral power in any specified spatial region [Simons et al., 2006].

10 The Curie depth describes the depth at which the Curie temperature is reached. Further, the Curie temperature is the temperature above which ferromagnetic minerals become paramagnetic (Sec. 2.2).

11 In ferromagnetic minerals, all magnetic moments are aligned in the same direction to the applied field. In ferrimagnetic minerals, different sublattices of atoms can have their magnetic moments aligned parallel or antiparallel to the applied field. For both contributions having the same strength, the respective minerals are called antiferromagnetic.

temporally exposed to an external field[12]. In the following, they will be called "magnetic minerals". Among these, FeTi-oxides such as titanohematites and titanomagnetites are the most probable carriers of magnetization on Mars. In addition, pyrrhotites may play an important role. In general, these minerals can occur either in single domain (SD) or multi domain (MD). MD minerals consist of large grains, where domain walls separate several magnetic domains. These domains are magnetized in different directions, whereas the elementary magnetic moments of an individual domain are aligned in the same direction. In contrast, SD minerals consist of smaller grains with a single magnetization direction. For these minerals, the saturation isothermal remanent magnetization (SIRM)[13] and the geologic remanence stability[14] are stronger.

To magnetize a mineral with its SIRM, the applied external field must be much stronger than the field of typical core dynamos on terrestrial planets[15]. Still, strong NRM may be acquired from a core dynamo field by the following mechanisms:

- THERMOREMANENT MAGNETIZATION (TRM) When cooled from above their Curie temperature T_C, magnetic minerals will acquire stable TRM. If cooled from lower temperatures, magnetic minerals will acquire partial thermoremanent magnetization (pTRM) of lower remanence. In any case, the remanence will usually be stronger with slower cooling.

- CHEMICAL REMANENT MAGNETIZATION (CRM) When magnetic minerals form or crystallize, they may obtain CRM.

- SHOCK REMANENT MAGNETIZATION (SRM) When magnetic minerals are shocked with transient peak pressures of several GPa, they may acquire SRM. This process is usually related to impacts.

As well, these mechanisms may be responsible for demagnetization, if no ambient field is present.

In the following, the most important properties of some magnetic minerals will be presented. As well, arguments for and against their presence on Mars and their ability to explain the required strong magnetization on Mars will be given.

12 Diamagnetic and paramagnetic minerals loose their magnetization as soon as the magnetizing field is removed. In particular, all minerals have diamagnetic properties and acquire induced magnetization in the opposite direction to the applied field. In addition, a smaller group of so-called paramagnetic minerals exists which acquire a much stronger magnetization in the direction of the applied field. On Earth, these minerals play an important role when studying the crustal field, as the core dynamo represents a strong magnetizing field.

13 The SIRM is the maximum achievable remanent magnetization .

14 Remanent magnetization is not stable due to thermal movements of magnetic spins and will decay over time, depending on temperature. This phenomenon is called viscous decay.

15 Among the terrestrial planets and moons, an active core dynamo is observed on the Earth, Mercury, and Ganymede.

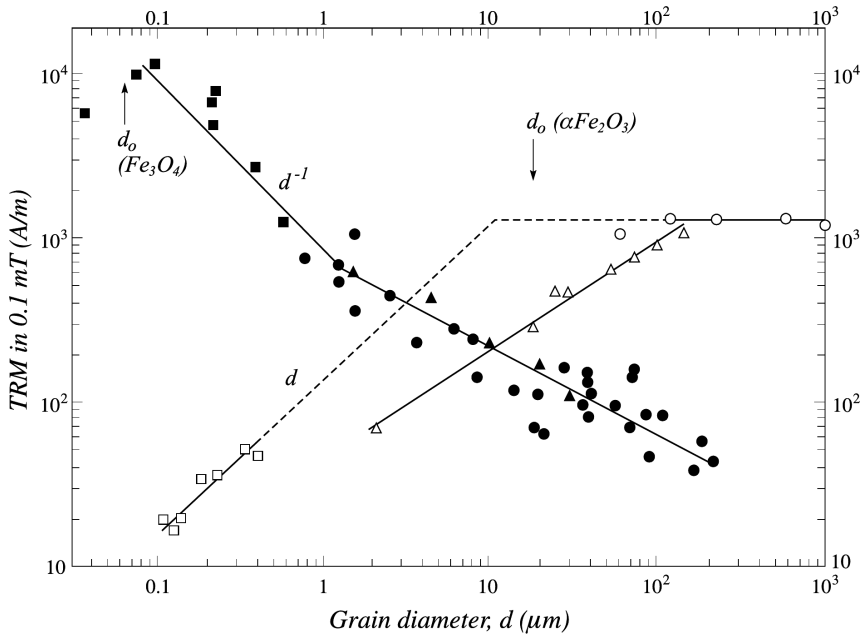

Figure 2.1. The dependence of TRM on grain size is shown for different minerals. The shape of the symbols refers to the corresponding study as referenced in Dunlop and Arkani-Hamed [2005]. Further, filled symbols and the thick solid line refer to magnetite, and other symbols and lines refer to hematite (Fig. 3 of Dunlop and Arkani-Hamed [2005], Copyright 2005 by the American Geophysical Union, reprinted with kind permission from publisher John Wiley & Sons Ltd.).

TITANOMAGNETITES Titanomagnetites ($Fe_{3-x}Ti_nO_4$, $0 \leqslant n \leqslant 1$) belong to the group of Fe-Ti oxides. The respective endmembers are magnetite (Fe_3O_4, $n = 0$) and ulvöspinel (Fe_2TiO_4, $n = 1$). Titanomagnetites crystallize in the inverse spinel structure where cations occupy two different sublattices[16] of opposite magnetization. Pure magnetite is ferrimagnetic, and ulvöspinel is antiferromagnetic[17] [Butler, 1992, p. 20off.]. Further, the Néel temperature[18] T_N and the SIRM M_s decrease almost linearly with increasing Ti-concentration x. Particularly, $T_N = 580°\,C$ and $M_s = 480\,kA/m$ for magnetite [Butler, 1992; Nagata, 1961], whereas ulvöspinel has a Néel temperature of T_N =-153°C and a very low SIRM . Hence, ulvöspinel is paramagnetic within the crust of terrestrial planets, and not relevant for remanent crustal magnetization.

As illustrated in Fig. 2.1 (Fig. 3 of Dunlop and Arkani-Hamed [2005]), the efficiency of TRM critically depends on grain size for magnetite (filled

16 Sublattice A is in tetrahedral coordination, with four cations surrounding one oxygen anion, whereas sublattice B is in octahedral coordination, with eight cations surrounding one oxygen anion [Butler, 1992, p. 21].

17 Titanium atoms replace ferric iron in one sublattice and balance the magnetic moments between the two sublattices.

18 The Néel temperature is the temperature above which antiferromagnetic coupling disappears and these minerals become paramagnetic. For antiferro- and ferrimagnetic minerals, the Néel temperature is identical to the Curie temperature.

symbols and thick solid line). In more detail, TRM is about two orders of magnitude stronger in SD-sized grains as compared to MD-sized grains (Fig. 2.1 and Tab. 2.2). In addition, the long-term stability of TRM is weak for magnetite with grain sizes above the pseudo single domain (PSD)[19] grain size range [Butler, 1992]. For these reasons, MD magnetite is an unlikely candidate for carrying magnetic remanence on Mars [Connerney et al., 2001; Dunlop and Arkani-Hamed, 2005]. SD magnetite, on the other hand, is a potent carrier of TRM. In particular, its high Curie temperature allows for a magnetized crust of up to 50 km in thickness and its strong SIRM requires a rock concentration of only 0.3 vol.% to explain the strongest observed fields on Mars [Dunlop and Arkani-Hamed, 2005].

As a drawback, SD-sized minerals may not be present in intrusive sills and dikes, as their formation requires fast cooling rates [Butler, 1992]. Still, Arkani-Hamed [2005a] suggested that a large volume of crust may contain SD-sized magnetite when this crust resulted from successive extrusive eruptions. Alternatively, SD-sized magnetite may form by exsolution from pyroxene [Feinberg et al., 2004], by oxidation of olivine [Gunnlaugsson et al., 2006], by thermal decomposition of siderite [Scott and Fuller, 2004], by serpentinization [Quesnel et al., 2009], or by oxyexsolution[20] [Dunlop and Arkani-Hamed, 2005].

Amongst the Martian meteorites, SD magnetite has been discovered in the Noachian-aged ALH84001 [Thomas-Keprta et al., 2001; Weiss et al., 2002; Antretter et al., 2003]. As well, SD- and PSD-sized titanomagnetites have been discovered in the Amazonian-aged[21] (e.g., Nyquist et al. [2001]) Shergottite, Nakhlite, and Chassignite meteorites (SNCs) [Cisowski, 1986; Kletetschka et al., 2000b; Rochette et al., 2001, 2005; Funaki et al., 2009; Gattacceca et al., 2013, 2014]. However, the magnetic properties of these younger rocks may differ from those of the Noachian crust where the strongest magnetic fields are observed (Sec. 1.2).

TITANOHEMATITES Titanohematites ($Fe_{2-n}Ti_nO_3$, $0 \leqslant n \leqslant 1$) also belong to the group of Fe-Ti oxides, but they are more oxidized as compared to titanomagnetites. What is more, the respective endmembers ilmenite ($FeTiO_3$, $n = 1$) and hematite (Fe_2O_3, $n = 0$) are found in an antiferromagnetic configuration. However, the magnetic spins of subsequent crystal layers in hematite are not exactly antiparallel to each other, if the Morin transition temperature of 252 K (-21°C) is exceeded [Schroeer and Nininger, 1967]. This misalignment results in canted antiferromagnetism and a small SIRM of $M_s = 2\,kA/m$ [Butler, 1992, p. 23]. With regard to

19 PSD-sized grains contain a small number of domains but behave similar to SD grains. For magnetite, their typical grain size is $d < 15\,\mu m$ [Winklhofer et al., 1997].

20 Oxyexsolution is a combination of deuteric oxidation, which results in an increased ratio of ferrous to ferric iron [Butler, 1992, p27f.], and the exsolution of smaller sized Ti-rich and -poor endmembers when cooling through temperatures of 200°C to 700°C [Butler, 1992, p. 26f.].

21 Note, however, that Pb isotope ages for Shergottites give $4.1 - 4.3$ Gyr [Bouvier et al., 2009].

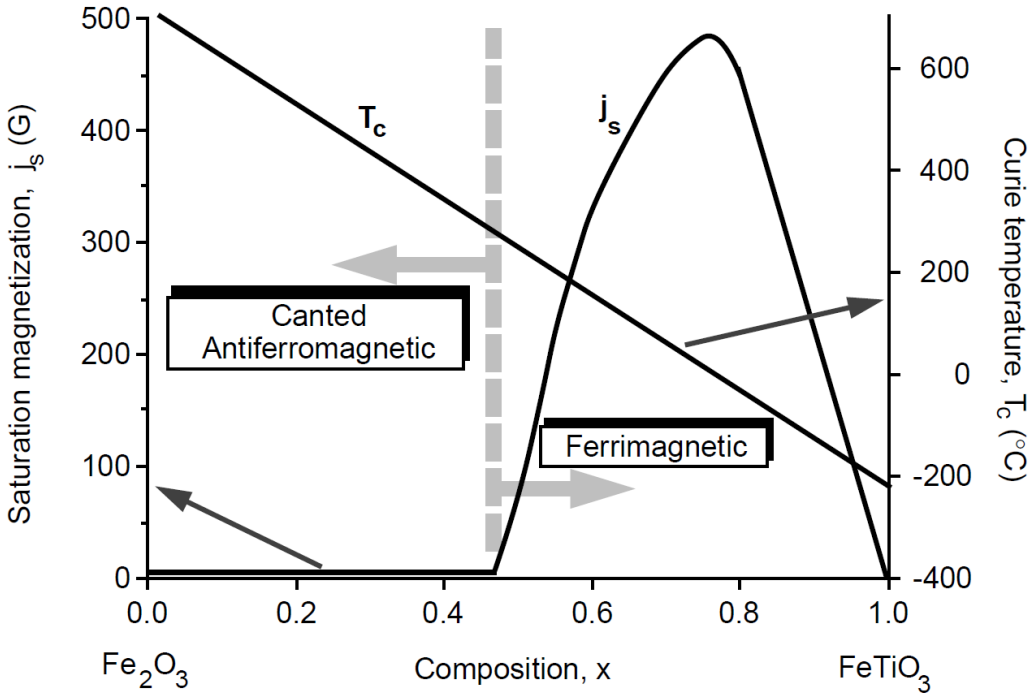

Figure 2.2. SIRM (here: saturation magnetization) M_s (here: j_s) and Néel (Curie) temperature T_N (here: T_C) for titanohematites in dependence of Ti-content n (here: Composition, x) (Fig. 2.10 of Butler [1992], reprinted with permission of Robert F. Butler.).

the Néel (Curie) temperature of Ti-hematites, an almost linear increase is observed with decreasing Ti-content n (Fig. 2.2, Fig. 2.10 of [Butler, 1992]). Especially, the Néel temperatures of the endmembers hematite and ilmenite are given by T_N =675°C and T_N =-218°C, respectively. Therefore, hematite is ferrimagnetic whereas ilmenite is paramagnetic in the lower layers of the Martian crust. With regard to the SIRM (M_s), Fig. 2.2 reveals a more complex behavior in dependence of the Ti-content. Particularly, M_s peaks at $M_s \approx 50\,\mathrm{kA/m}$ for a Ti-content of $0.6 < n < 0.8$, whereas $M_s = 2\,\mathrm{kA/m}$ if $n < 0.5$, i.e. if titanohematite is in the canted antiferromagnetic configuration [Butler, 1992, p. 23ff.].

Despite its relatively low SIRM, hematite has some interesting properties. First, its TRM increases with increasing grain size, as illustrated by the dashed line and open symbols in Fig. 2.1 [Kletetschka et al., 2000a; Dunlop and Kletetschka, 2001]. Second, TRM of MD hematite almost saturates in fields comparable to the expected Martian core dynamo [Kletetschka et al., 2000c,b]. Third, its Néel temperature allows for a magnetized layer of 60 km in thickness [Dunlop and Arkani-Hamed, 2005].

Crystalline hematite with MD-sized grains of $> 10 - 15\,\mu\mathrm{m}$ was discovered in infrared spectra[22] of the Martian surface at Sinus Meridiani [Chris-

22 Obtained by the thermal emission spectrometer (TES) on MGS.

tensen et al., 2000]. Later, the rover Opportunity[23] identified hematite in millimeter-sized spherules[24] in this region [Christensen et al., 2004; Klingelhöfer et al., 2004]. However, the hematite-rich layer in Terra Meridiani may be only a few hundred meters thick [Christensen and Ruff, 2004], and hematite has not yet been discovered in Martian meteorites [Connerney et al., 2001; Rochette et al., 2005].

HEMATITE-ILMENITE LAMELLAE On Earth, strong and stable NRM of $4 - 36\,A/m$ has been observed in rocks with titanohematites of intermediate Ti concentrations [McEnroe and Brown, 2000; McEnroe et al., 2000, 2001a,b, 2002; Dyar et al., 2004; McCammon et al., 2009]. These rocks consist of exsolved hematite or ilmenite lamellae (e.g., McEnroe et al. [2002]) with a Curie temperature comparable to that of hematite [Robinson et al., 2002; McEnroe et al., 2002; Dyar et al., 2004]. The observed strong NRM in these rocks may either be explained by contact layers of the host mineral (hematite or ilmenite) and its exsolved counterpart [Robinson et al., 2002; McEnroe et al., 2002; Robinson et al., 2004], or may simply result from MD hematite [Kletetschka et al., 2002]. In the first case, NRM is acquired through CRM during exsolution of the lamellae. In the second case, NRM is acquired earlier through TRM. Overall, hematite-ilmenite lamellae are an interesting candidate for strong crustal NRM on Mars. Still, they have been discovered neither on Mars nor in SNCs [Yu and Gee, 2005].

MAGHEMITE Maghemite is a low-temperature oxidation product of magnetite. It is chemically equivalent to hematite, but organized in the same spinel structure as magnetite. Maghemite is metastable, and irreversibly changes to hematite at temperatures of 300°C-500°C [Butler, 1992, p. 28f.]. Also, maghemite may acquire TRM with a similar efficiency as MD hematite [Özdemir and O'Reilly, 1982; Dunlop and Özdemir, 1997], but with a stronger SIRM of $42\,kA/m$ [Butler, 1992, p. 29].

Maghemite has been detected along with PSD magnetite in the 2.1 Gyr old [Humayun et al., 2013] Martian meteorite NWA7034[25] [Gattacceca et al., 2014]. The mineralogy of this meteorite may explain a several kilometer thick layer with magnetizations of up to $120\,A/m$ [Gattacceca et al., 2014].

PYRRHOTITE Pyrrhotite (Fe_7S_8 to Fe_9S_{10}) is ferrimagnetic and usually crystallizes in a monoclinic crystal structure [Butler, 1992, p. 29]. Its Néel temperature is T_N =320°C with a SIRM of $M_S = 130\,kA/m$ [Butler, 1992, p. 29]. Pyrrhotite has been discovered in many Martian meteorites [Rochette et al., 2001, 2005; Weiss et al., 2002] but may easily be demagnetized by im-

23 A major reason to land Opportunity in Terra Meridiani was the discovery of surface hematite (TES) as its formation may be related to the presence of liquid water [Christensen et al., 2000; Hynek et al., 2002].

24 Also known as "blueberries" [Moore, 2004].

25 Northwest Africa 7034 (NWA7034) was discovered in the Sahara desert in 2011.

Table 2.2. Some important magnetic minerals and their properties[a].

MINERAL	GRAIN SIZE [μM]	FORMULA	T_C [°C]	D_C [KM]	SIRM [KA/M]	TRM [KA/M]
SD magnetite	$< 0.05 - 0.084$ [1] < 0.1 [2] < 0.6 [3]	Fe_3O_4	580 [2,4]	50 [5,2] 30 [6] 90 [7] >32 [8]	480 [2,4]	2-25 [1]
MD magnetite	> 20 [3]	Fe_3O_4	580 [2,10]	c.f. SD magnetite	480 [4]	0.03-0.2 [1]
SD hematite	2-15 [2]	Fe_2O_3	675-680 [2,4]	c.f. MD hematite	≈ 2.5 [2]	0.01-0.9 [1]
MD hematite	> 15 [1]	Fe_2O_3	675-680 [2,4]	70 [5] 60 [2] 100 [7] >37 [8]	2 [10] ≈ 2.5 [2]	0.12-2.5 [1]
SD maghemite	< 0.06 [3]	Fe_2O_3	– –[b]	c.f. MD hematite	42 [4]	c.f. MD hematite [1]
SD pyrrhotite	< 1.6 [1,3]	$Fe_{1-x}S$ $x<0.13$	210-320 [2,3]	20 [2] 55 [7] <20 [8]	≈ 100 [2]	1-9 [1]
MD pyrrhotite	c.f. SD pyrrhotite	$Fe_{1-x}S$ $x<0.13$	210-320 [2,3]	c.f. SD pyrrhotite	130 [4]	0.2-0.5 [1]
Hematite-ilmenite lamellae		Fe_2O_3-$FeTiO_3$	530-650 [9]	– –	55 [9]	1.2 [10]

[a] Grain size indicates the critical grain size for the respective domain (SD or MD), and formula gives the chemical composition. T_C is the Curie temperature, and D_C the minimal Curie depth since magnetization in the Martian crust. Further, the SIRM and the TRM are given. For TRM, an ambient field of 50 μT has been assumed, which is comparable to the present terrestrial core dynamo.
[b] Transforms to hematite at 300-500°C [Butler, 1992].

References: [1] Kletetschka et al. [2000a] and ref. therein [2] Dunlop and Arkani-Hamed [2005] and ref. therein [3] Clark [1997] [4] Butler [1992] [5] Nimmo and Gilmore [2001] [6] Hood et al. [2005] [7] Arkani-Hamed [2005a] [8] Ruiz et al. [2006] [9] Robinson et al. [2002]. [10] McEnroe et al. [2002].

Table 2.3. Overview of minerals that have been suggested as source candidates for the crustal magnetic field on Mars. For each mineral, arguments for and against its presence on Mars and its capability to provide strong magnetization are given.

MINERAL	POSITIVE	NEGATIVE
SD magnetite	• Strongest TRM • 30-90 km magnetized layer • Important magnetic carrier in SNCs	• Difficult to form with slow, intrusive cooling
MD magnetite	• 30-90 km magnetized layer	• Low TRM • Weak TRM long-term stability
SD hematite	• 40-100 km magnetized layer • Low viscous decay	• Weak TRM
MD hematite	• 40-100 km magnetized layer • Strong TRM • Very efficient TRM • Detected on the surface of Terra Meridiani • Low viscous decay	• Less stable than SD hematite • Not detected in SNCs
SD pyrrhotite	• Strong TRM • Important magnetic carrier in SNCs	• 20-60 km magnetized thickness • Easily demagnetized by impacts • Strong viscous decay
Hematite-ilmenite lamellae	• Strong TRM • 40-100 km magnetized layer • Stable TRM • Low viscous decay	• Not detected on Mars or SNCs

pacts. In more detail, half of its TRM is lost when shocked to 1 GPa and all of its TRM is lost when shocked to $1.6 - 3$ GPa [Vaughan and Tossell, 1973; Rochette et al., 2003]. For pyrrhotite, mineral concentrations of $2 - 4$ wt.% are required in order to explain the observed Martian anomalies [Dunlop and Arkani-Hamed, 2005].

In summary, no conclusive evidence is found on the question of the dominant carrier of magnetization on Mars. In particular, the most important magnetic properties of all candidate minerals (Tab. 2.2) imply advantages as well as drawbacks concerning their ability to explain the strong magnetic fields on Mars (Tab. 2.3). In addition, the mineralogy of most SNCs cannot explain these strong fields if they were magnetized in a field of similar strength as Earth's main field. As long as no selected samples from the Martian crust are to be returned, only further restrictions on the required magnetization and magnetic layer thickness may therefore provide information on the dominant carriers of the remanent magnetization of the Martian crust. Such restrictions may be obtained with the help of the presented model of the crustal magnetic field of Mars, as outlined in Ch. 11.

2.4 MAGNETIC DICHOTOMY

The hemispheric dichotomy is one of the most prominent features on Mars and its origin remains a key question in understanding the early evolution of this planet [McGill and Squyres, 1991; Watters et al., 2007]. This dichotomy refers to the differences of the relatively smooth and flat northern lowlands and the heavily cratered southern highlands (e.g., Watters et al. [2007]). In particular, these differences are reflected in the topography (e.g., Smith et al. [1998]), the crustal thickness [Neumann et al., 2004], and the surface composition [Bandfield, 2000]. Early on, it was speculated that the dichotomy may also be reflected in the crustal magnetic field [Leweling and Spohn, 1997], which was eventually confirmed with MGS data [Acuña et al., 1998]. Hence, an improved understanding of the characteristics and the origin of the magnetic anomalies on Mars may help to understand the origin of its hemispheric dichotomy.

As one scenario to explain the hemispheric distribution of strong magnetic fields on Mars, an asymmetric core field has been suggested, which in turn requires an asymmetric heat-flux at the CMB [Stanley et al., 2008; Amit et al., 2011; Dietrich and Wicht, 2013]. Such an asymmetric heat-flux may either be triggered by a degree-one convection pattern in the mantle[26] [Zhong and Zuber, 2001; Roberts and Zhong, 2006; Keller and Tackley, 2009; Yoshida and Kageyama, 2006] or a large impact[27] [Roberts et al., 2009]. However, Dietrich and Wicht [2013] have noted that an asymmetric core dynamo may lead to frequent magnetic pole reversals at intervals of 10 kyr and hence fail to explain the observed strong magnetization.

Alternatively, the processes responsible for (de)magnetization of the Martian crust could have been asymmetric. For example, a low degree mantle convection pattern could have concentrated TRM in one hemisphere [Harrison and Grimm, 2002; Roberts and Zhong, 2007; Reese and Solomatov, 2010; Citron and Zhong, 2012]. As well, a giant impact such as Borealis[28] could have demagnetized any preexisting magnetic field in the northern lowlands [Nimmo et al., 2008]. In addition, the energy of such an impact can accumulate at the antipode of the impact location where it may demagnetize crust through shock and thermal effects. This scenario is in agreement with the

26 This degree-one convection pattern is achieved by introducing a viscosity jump in the mantle, resulting either from an asthenosphere with low viscosity, mineral phase transitions, a transition from diffusion to dislocation creep, or a residue layer from a magma ocean [Roberts and Zhong, 2006].

27 Note that one giant [Wilhelms and Squyres, 1984; Andrews-Hanna et al., 2008; Marinova et al., 2008] or several large impacts [Frey and Schultz, 1988] could also be responsible for the topographic dichotomy, the cessation of the magnetic dynamo [Roberts et al., 2009] trough deposition of heat in the mantle, or the start of the magnetic dynamo, if heat transportation to the core through sinking iron droplets is considered [Reese and Solomatov, 2010].

28 It was suggested that the hypothetical Borealis impact created the topographic dichotomy and that the corresponding impact basin includes the whole northern lowlands [Wilhelms and Squyres, 1984; Andrews-Hanna et al., 2008; Marinova et al., 2008].

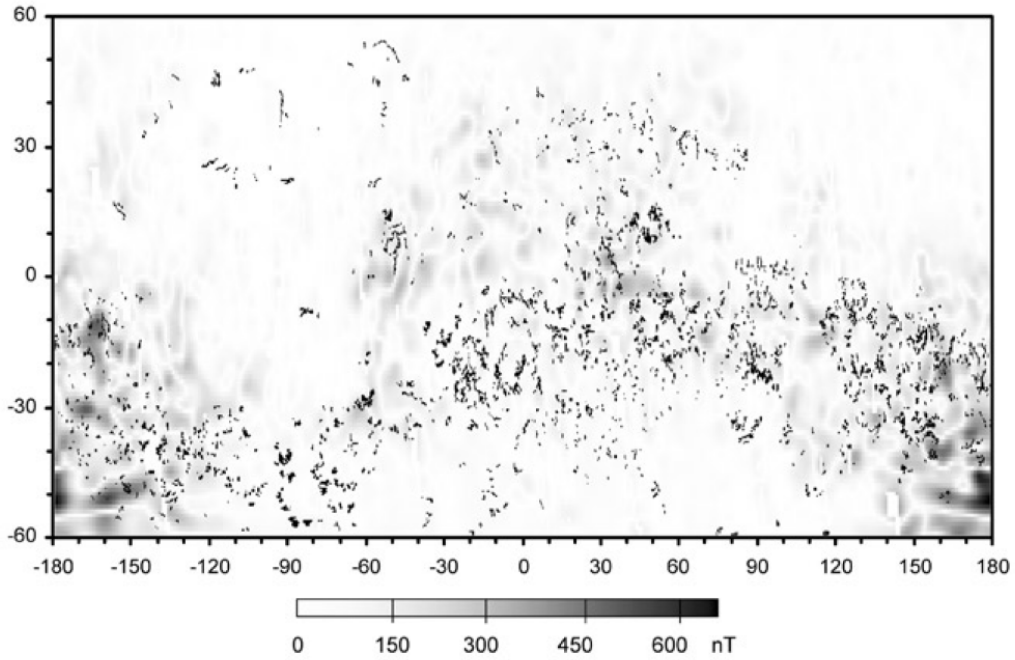

Figure 2.3. Absolute values of the vertically down (Z) magnetic field component at 200 km altitude from the ESD model of Purucker et al. [2000] are shown along with the location of the valley networks as mapped by Kieffer [1981] (Fig. 10 of Harrison and Grimm [2002]), Copyright 2002 by the American Geophysical Union, reprinted with kind permission from publisher John Wiley & Sons Ltd.).

observation of a low-field region in the southern hemisphere [Nimmo et al., 2008]. However, a very large impact may as well demagnetize the complete Martian crust by thermal blanketing through the deposition of impact ejecta and by shock demagnetization through secondary craters [Citron and Zhong, 2012].

Also, spatially inhomogeneous chemical conditions could have regionally favored the occurrence of highly magnetic crust. For example, the presence of water can advance the formation of magnetite by serpentinization [Hood et al., 2005; Quesnel et al., 2009; Chassefière et al., 2013], or by hydrothermal exsolution from siderite[29] [Griffith and Shock, 1995; Scott and Fuller, 2004]. As well, pyrrhotite can form under hydrothermal conditions [Hood et al., 2005; Rochette, 2006; Hood et al., 2010]. Additionally, the presence of water can increase the cooling rate of magmatic intrusions, and therefore lead to the formation of SD mineral grains [Hood et al., 2007]. Indeed, the location of valley networks and phyllosilicates, which are indicative for the presence of water, appear to be correlated with regions of strong magnetic anomalies on Mars (Fig. 2.3, Fig. 10 of Harrison and Grimm [2002]) [Jakosky and Phillips, 2001; Harrison and Grimm, 2002; Hood et al., 2005, 2010]. Still, it

29 Siderite is composed of iron(II) carbonate, i.e. $FeCO_3$, and can be decomposed to SD magnetite by thermal decomposition and exsolution.

remains to be explained why the presence of water and hydrothermal alteration should have been restricted to these regions. As one possibility, a giant mantle plume (see above) may have resulted in a regional heat source which regionally allowed to melt ground ice [Harrison and Grimm, 2002]. Another possibility is related to paleopole estimates (Sec. 2.5), which suggest that valley networks and strong magnetic anomalies were located near the equator before true polar wander may have occurred [Hood et al., 2005]. Alternatively, hydrothermal alteration may have occurred globally, but the formation of magnetite may have been less effective in the lowlands [Scott and Fuller, 2004]. However, it has been criticized that efficient hydrothermal circulation is required to magnetize large quantities of crust [Dunlop and Arkani-Hamed, 2005]. As well, Rochette [2006] noted that hydrothermally formed magnetic minerals are not uniformly magnetized on Earth [Rochette, 2006].

An additional aspect was raised by Rochette [2006] who argued that weaker magnetization will result if magmatic intrusions cool faster than the core dynamo reverses its polarity. Faster cooling rates, in turn, may result from aqueous erosion of insulating regolith, from regional differences in heat flow by a low degree convection pattern, or from differences in crustal thickness [Rochette, 2006].

To summarize, none of these scenarios is favored to explain the magnetic and topographic dichotomy. Still, a better knowledge of the crustal magnetic field along with an improved understanding of the formation of valley networks, of the presence of magnetic minerals, and of the location of paleopoles (see next section) can help to further constrain the history and origin of the Martian dichotomy.

2.5 PALEOPOLES

The Martian paleomagnetic dipole may not have been aligned with the current rotational axis. Namely, true polar wander may have occurred due to the emplacement of the massive Tharsis rise and the subsequent reorientation of the planet's rotational axis. Moreover, apparent polar wander may have occurred in an early phase of plate tectonics on Mars. As well, the core field may have changed with time, resulting in different paleomagnetic dipole locations, and even pole reversals.

As for magnetization (Sec. 2.2), the determination of paleopole positions is possible only with additional information, as an infinite number of magnetization solutions correctly describe the resulting magnetic field [Runcorn, 1975; Parker et al., 1987; Lesur and Jackson, 2000; Gubbins et al., 2011]. Further, the robustness of the estimated paleopole positions significantly depends on the type of available additional information. In the most unambiguous case, the magnetization direction of a rock with known spatial orientation and location is available. However, such information is missing for SNCs. Still, the paleopole may be estimated from modeling a

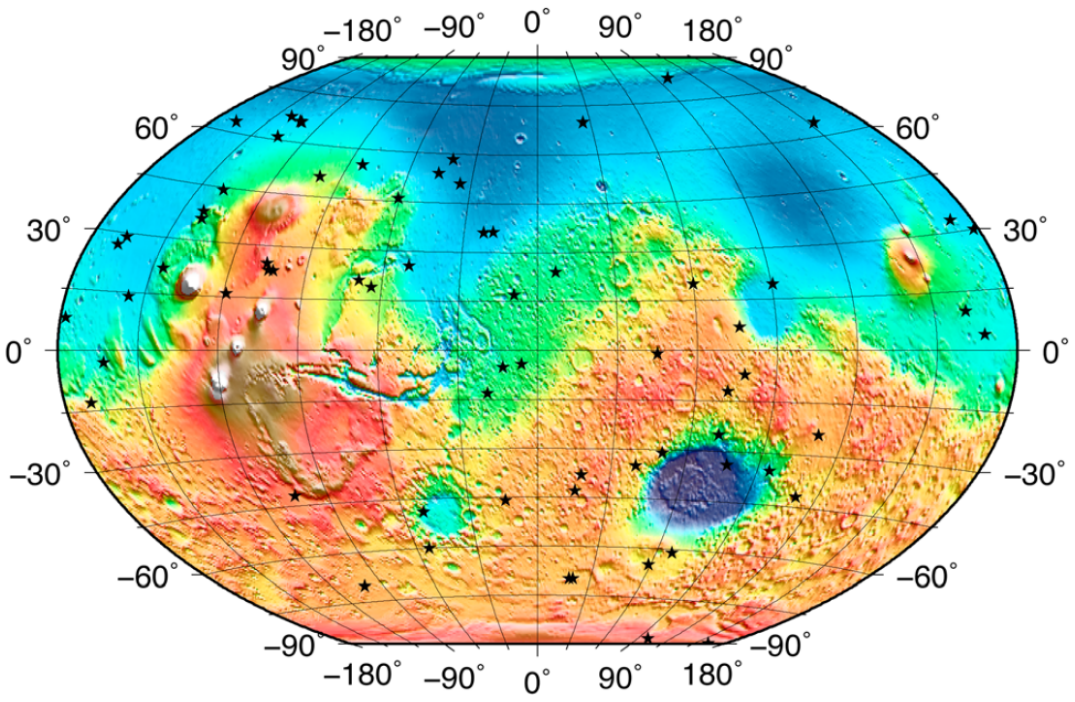

Figure 2.4. Magnetic north paleopole positions are shown as obtained from several published studies (Fig. 8 of Milbury et al. [2012], Copyright 2012 by the American Geophysical Union, reprinted with kind permission from publisher John Wiley & Sons Ltd.).

magnetic field anomaly of known source location and geometry. These, in turn, may be constrained from seismic or gravity data. On Mars, only gravimetric satellite data of low resolution is available. This data was used by Milbury et al. [2012] to infer the source location of magnetic anomalies. Alternatively, the source location of a magnetic anomaly can be constrained if it is associated with a known geological structure. In this way, Langlais and Purucker [2007] and Hood et al. [2010] estimated paleopole positions from the magnetic anomaly associated with the Apollinaris Patera volcano. For the most part, however, the observed strong magnetic anomalies cannot be related to any particular geologic setting. Then, an isolated anomaly which is undisturbed from any surrounding fields may still be used to estimate paleopole positions [Arkani-Hamed, 2001a; Hood and Zakharian, 2001; Arkani-Hamed and Boutin, 2004; Frawley and Taylor, 2004; Hood et al., 2005; Boutin and Arkani-Hamed, 2006; Hood et al., 2007; Quesnel et al., 2007]. In the worst case, an arbitrary source geometry [Sprenke and Baker, 2000] or global characteristics of the observed magnetic field [Sprenke, 2005; Kobayashi and Sprenke, 2010; Milbury and Schubert, 2010] are used to infer paleopole positions. Then, the obtained results may greatly depend on the assumptions and should not be over interpreted.

Most published estimates of the magnetic north paleopole positions are shown in Fig. 2.4 (Fig. 8 of Milbury et al. [2012]). To begin, these paleopoles are scattered over both hemispheres. Consequently, pole reversals of

the ancient Martian core dynamo must have occurred (e.g., Arkani-Hamed [2001a]) and such pole reversals are also suggested by numerical dynamo simulations [Wicht and Tilgner, 2010]. What is more, the locations of these paleopoles vary greatly, possibly due to different assumptions on the location and geometry of the magnetic sources (e.g., Frawley and Taylor [2004] [30]) or due to differences in the used data sets and their processing (e.g., Hood et al. [2007] [31]). In addition, deviations of the ancient core dynamo field from a purely dipolar field may introduce scatter in paleopole estimates. Still, most studies agree that paleopoles cluster at low latitudes near the Tharsis rise. For instance, Arkani-Hamed and colleagues propose that paleopoles cluster within 30° of 25°N/230°E [Arkani-Hamed, 2001a; Arkani-Hamed and Boutin, 2004; Boutin and Arkani-Hamed, 2006]. Similarly, Hood et al. [2005, 2007] found a mean paleopole position of 34±10°N/202±58°E. As a result, it was suggested that true polar wander occurred on Mars (e.g., Boutin and Arkani-Hamed [2006]). In comparison, estimates of true polar wander based on the emplacement of the Tharsis rise range from less than 18° [Willemann, 1984] to larger than 25° [Melosh, 1980; Spada et al., 1996; Sprenke et al., 2005].

Overall, reliable estimates of the inherent uncertainties of paleopole estimates are crucial to understand if polar wander truly occurred on Mars. Yet, such information is largely missing in published studies, with the exception of the work by Hood and colleagues [Hood and Zakharian, 2001; Hood et al., 2005, 2007, 2010][32]. With reference to this thesis, such estimates may be provided by analyzing the covariance (Sec. 7.4) and resolution matrices (Sec. 7.5) of the presented model of the crustal magnetic field of Mars. Further, the increased resolution of the presented model allows to identify new isolated anomalies on Mars (Sec. 12).

2.6 MAGNETIC LINEATIONS - PLATE TECTONICS ?

As of today, Mars is in the stagnant lid regime of mantle convection (e.g., Hauck and Phillips [2002]; Breuer and Spohn [2003]; Morschhauser et al. [2011]). In this regime, the crust and lithosphere consist of a single stagnant plate. For this reason, heat transport trough the lithosphere is limited

30 In Frawley and Taylor [2004] and Arkani-Hamed [2001a], an identical anomaly is investigated. However, the results of these studies differ significantly. According to Frawley and Taylor [2004], different assumptions on the source geometry may lead to this discrepancy. In particular, Frawley and Taylor [2004] use a single dipole as source geometry whereas Arkani-Hamed [2001a] uses two vertically oriented dipolar sources as source geometry.

31 Hood et al. [2007] and Frawley and Taylor [2004] investigated the same anomalies and obtained inconsistent results. According to Hood et al. [2007], differences in the used data sets and their processing may be responsible for this discrepancy. In particular, Hood et al. [2007] give an example where differently processed data show significantly different relative maxima above the same anomaly.

32 Hood and colleagues estimated error ellipses with semimajor axes of 5-30° from an analysis of the residual root mean square (RMS) between the data and their model.

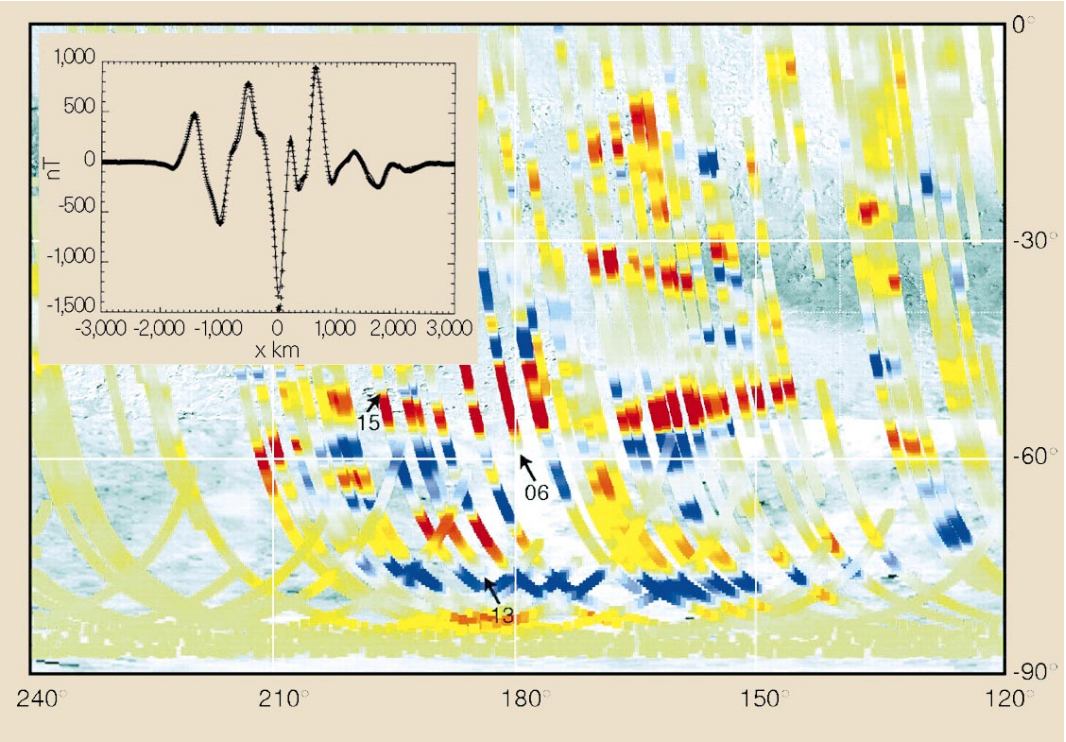

Figure 2.5. The vertically down (Z) component of the magnetic field from AB/SPO data is shown over TC/TS where elongated anomalies are visible. In the inlet (upper left corner), a selected track shows the magnetic field of alternating sign, which has been interpreted in terms of seafloor spreading. The shown profile corresponds to the track labeled 15, and the label denotes the center ($x = 0$ km of the track (Fig. 1 of McKenzie [1999], originally published as Figs. 1 and 2 of Connerney et al. [1999]. Reprinted with permission from AAAS).

by heat conduction. In contrast, early Mars may have been in the plate tectonics regime of mantle convection [Sleep, 1994][33]. In this regime, the crust and lithosphere consist of several dynamic plates. Hence, heat transport through the crust and lithosphere is dominated by more effective heat transport by convection.

Wegener [1912] suggested the basic ideas of plate tectonics about a century ago. Still, the necessary conditions for the occurrence of plate tectonics are not fully understood. To our understanding, plate tectonics is operating on Earth only, where elongated magnetic anomalies associated with seafloor spreading and magnetic pole reversals provided evidence for this mode of heat transport [Vine and Matthews, 1963]. On Mars, similar elongated anomalies have been discovered in TC and TS (c.f. Fig. 2.5). However, these anomalies are much larger than on Earth and extend to over 2000 km in the east-west direction when observed at MGS orbit altitudes [Acuña et al., 1999; Connerney et al., 1999; Purucker et al., 2000].

33 Sleep [1994] argued that the topographic dichotomy is the relic of an ancient subduction zone.

An early episode of plate tectonics on Mars has deep implications on the evolution of this planet [Nimmo and Stevenson, 2000; Breuer and Spohn, 2003]. Hence, the interpretation of the elongated magnetic anomalies has been discussed since their discovery by MGS. On one hand, Connerney et al. [1999] successfully fit fluxgate magnetometers on MGS (MAG) AB data to infinitely elongated stripes of alternating magnetizations. Therefore, they argued that these anomalies formed by magnetic pole reversals and seafloor spreading in a regime of plate tectonics. Similarly, Fairén et al. [2002] interpreted these anomalies as the result of collisional plates. Later, Connerney et al. [2005] identified further signs of plate tectonics in Terra Meridiani using MGS mapping phase orbit (MPO) magnetic field data. On the other hand, the interpretation of the observed linear magnetic field anomalies as a relic of plate tectonics has been criticized for several reasons. First, the magnetic declinations obtained by Connerney et al. [1999] are not compatible with seafloor spreading [Harrison, 2000; Sprenke and Baker, 2000]. Furthermore, their obtained magnetizations lack the necessary symmetry [McKenzie, 1999]. Also, Sprenke and Baker [2000] have argued that these elongated anomalies do not necessarily imply formation by plate tectonics. Second, the strong intensity and large spatial extent of the observed stripes require a homogeneously magnetized crust of 30 km thickness [Albee, 2000] which had to form and cool faster than pole reversals occurred [Albee, 2000; Nimmo and Stevenson, 2000].

Alternative explanations for the formation of these anomalies have been suggested. Namely, these elongated anomalies may have formed by a moving locus of dike intrusions [Nimmo, 2000], by magnetization in a global dipole field and subsequent local demagnetization [Sprenke and Baker, 2000], by uniform magnetization and subsequent periodic folding [Connerney et al., 1999], by chemical remanent magnetization in banded zones of hydrochemical alteration [Connerney et al., 1999], or by hot spots under a drifting lithosphere [Kobayashi and Sprenke, 2010][34]. In addition, the elongated magnetic anomalies may consist of individual, more localized magnetic sources [Arkani-Hamed, 2001b; Hood et al., 2007; Jurdy and Stefanick, 2009; Ravat, 2011].

In summary, the origin of the most intense magnetic features on Mars remains disputed. The presented model of the Martian crustal magnetic field may help to improve our understanding of these elongated anomalies. In particular, the model's higher resolution and its ability to predict the magnetic field at the surface altitude may be valuable for this purpose.

34 Kobayashi and Sprenke [2010] suggest that "tidal force on the early lithosphere by former satellites [...] may have pulled the lithosphere". Accordingly, a fixed hot spot may have produced elongated magnetic anomalies on a drifting lithosphere.

Part II

DATA

The presented model of the crustal magnetic field is based on the MGS data set which will be described in this part of the thesis. The first chapter of this part contains a description of the mission phases, the magnetic field sensors, and the NASA data processing and calibration. In the second chapter, I will present the data selection process and the derivation of appropriate data weights.

3

MGS - MISSION AND INSTRUMENTS

This chapter begins with an overview of the main mission phases of the orbiting satellite Mars Global Surveyor (MGS). Then, the electron reflectometer (ER) data will be discussed shortly. Finally, I will describe the working principle of the fluxgate magnetometers on MGS (MAG) as well as the data calibration, the data pre-processing, and the removal of spacecraft (S/C) magnetic fields as done by the National Aeronautics and Space Administration (NASA).

3.1 OVERVIEW OF MISSION PHASES

Albee et al. [2001] presented an overview of the MGS mission which is shown in Fig. 3.1 (c.f. Fig. 2 in Albee et al. [2001]). In detail, the MGS spacecraft operated for almost a decade (1997-2006) in Martian orbit. It was launched on November 7, 1996 from Cape Canaveral Air Force Station, Florida, and was captured into a highly elliptical Martian orbit on September 11, 1997. The initial aerobraking phase (AB-1) started with a low periapsis of 262.9 km and an apoapsis of 54026 km. Subsequently, these were lowered with the help of atmospheric drag using the solar panels. However, a damper failure during solar panel deployment did not allow the S/C to dip as deep into the atmosphere as initially planned. Hence, periapsides of only 115 to 175 km could be achieved during the aerobraking phase (AB), resulting in a delay of the initial AB schedule by one Earth year. From March 27, 1998, to September 23, 1998, the aerobraking operation was halted for 373 elliptical 175×17800 km orbits with the purpose of obtaining a sun-synchronous 2 am/2 pm orbit. This mission phase is named science phase orbit (SPO-1 and SPO-2), as most scientific instruments were turned on. It was followed by a second aerobraking phase (AB-2), further lowering the apoapsis down to 450 km. Eventually, MGS reached its final mapping phase orbit (MPO) on March 9, 1999. This final orbit was sun-synchronous, passing the equator at 2 am/2 pm local time with a polar inclination of $i = 92.96^\circ$ and with altitudes ranging from 368 to 438 km above the Martian surface [Albee et al., 2001].

As will be discussed below, the AB/SPO and MPO data sets have complementary strengths and weaknesses. Hence, it is necessary to combine these data in order to obtain dense global coverage and the best possible resolution for models of the crustal magnetic field of Mars [Arkani-Hamed, 2002b; Cain et al., 2003; Langlais et al., 2004].

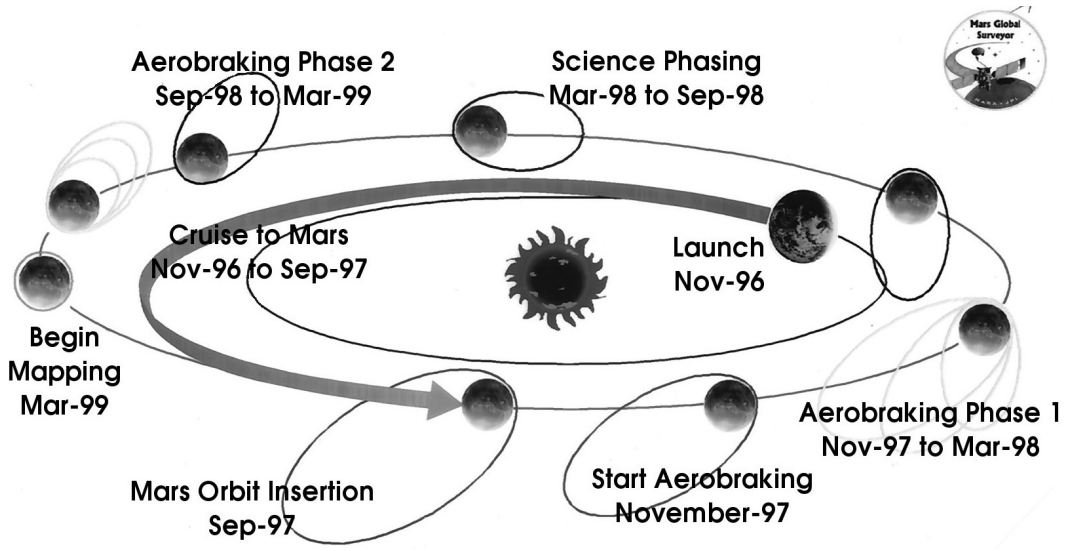

Figure 3.1. Schematic overview of the launch, cruise, and main mission phases of the MGS mission (Fig. 2 of Albee et al. [2001], Copyright 2001 by the American Geophysical Union, reprinted with kind permission from publisher John Wiley & Sons Ltd.).

3.2 THE ELECTRON REFLECTOMETER (ER)

The electron reflectometer (ER) measures the energy and angular distribution of 10 eV to 20 keV electrons [Mitchell et al., 2001]. In combination with the vector magnetic field measured by MAG, the magnetic field intensity at lower altitudes can be estimated from these electron energy spectra if the crustal magnetic field is connected to the interplanetary magnetic field (IMF) (open field lines). On Mars, this altitude corresponds to $170-185$ km above the surface[1] [Lillis, 2004; Lillis et al., 2008b]. Further, the ER was not continuously operating during the early mission phases (AB/SPO) due to concerns about high voltage arcing in the dense atmosphere (R. Lillis, personal communication, 2014), but operated continuously during MPO.

The most recent ER map was released by Lillis et al. [2008a] and is shown in Fig. 3.2 (Fig. 4 of Lillis et al. [2008a]). In this work, this ER map will be used to validate some predictions of the presented model (Ch. 10 and 12).

3.3 THE FLUXGATE MAGNETOMETER (MAG)

MGS was equipped with two triaxial FGMs (MAG). These instruments provided data during all mission phases with only a few data gaps. The MAG was built at the Goddard Space Flight Centre (GSFC)[2] with heritage from the failed Mars Observer Mission. The MGS magnetometers were able to

1 On Mars, the ER measures the magnetic field intensity (F) at the altitude where electrons are absorbed into the atmosphere.

2 Principal investigator (PI): Mario H. Acuña

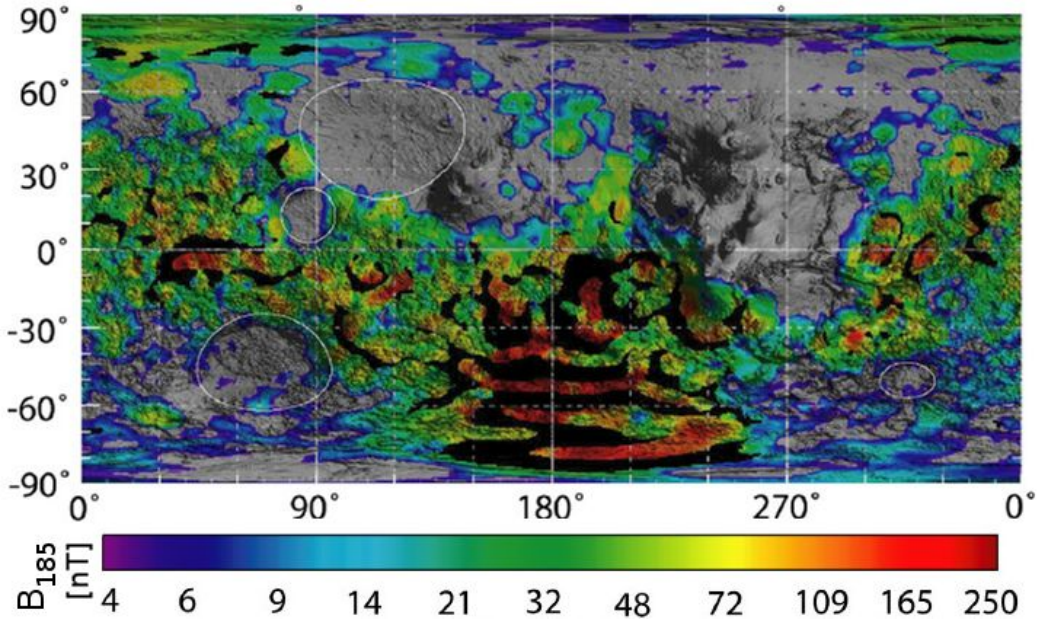

Figure 3.2. A map of the binned and averaged ER data is shown which reflects reflects the magnetic field intensity at 185 km [Lillis et al., 2008a]. Black areas represent closed magnetic field lines where data are missing. White ellipses represent the largest impact basins on Mars (from left to right: Hellas, Isidis, Utopia, and Argyre) (Fig. 4 of Lillis et al. [2008a], reprinted with permission from Elsevier Inc. via RightsLink.).

measure ambient fields from ±4 to ±65536 nT with a sampling rate of up to 32 Hz. Depending on telemetry rate, the S/C transmitted averaged values every 0.75, 1.50 and 3.00 s. Moreover, the orthogonality of the MAG sensing coils (see below) was calibrated at the GSFC and is known to an accuracy of better than 0.2°. Concerning the alignment of the MAG sensors with respect to the S/C reference coordinate system, the team at GSFC estimated a maximum error of 1° [Acuña et al., 2001]. In addition, the S/C generated magnetic fields can easily disturb the fluxgate sensors. Therefore, the MAG sensors were attached to the tips of the solar panels at about 5 m from the S/C main body. Further, the solar panels were designed to be magnetically clean [Acuña et al., 2001].

A FGM is sensitive to the magnetic field along each of its three orthogonal axes. On MGS, a ring-core FGM was used [Acuña et al., 1992], and a schematic setup of such an instrument is shown in the top row of Fig. 3.3. In detail, the driving coil (blue) is directly wrapped around a ring-shaped core (brown and green) of molybdenum permalloy with high magnetic susceptibility X_c. Now, the driving coil (blue) is driven by a periodic voltage U_d of frequency f_0. In consequence, a magnetic field $\mathbf{H}_d$ (black arrows) is generated by the driving coil and the core is magnetized with $\mathbf{M} = X_c \mathbf{H}_d$. Overall, the total magnetic field is then given by $\mathbf{B}_d = \mu_0(\mathbf{H}_d + \mathbf{M}) = \mu_c \mathbf{H}_d$ where μ_0 is the vacuum permeability and $\mu_c = \mu_0(1 + X_c)$. The sensing coil

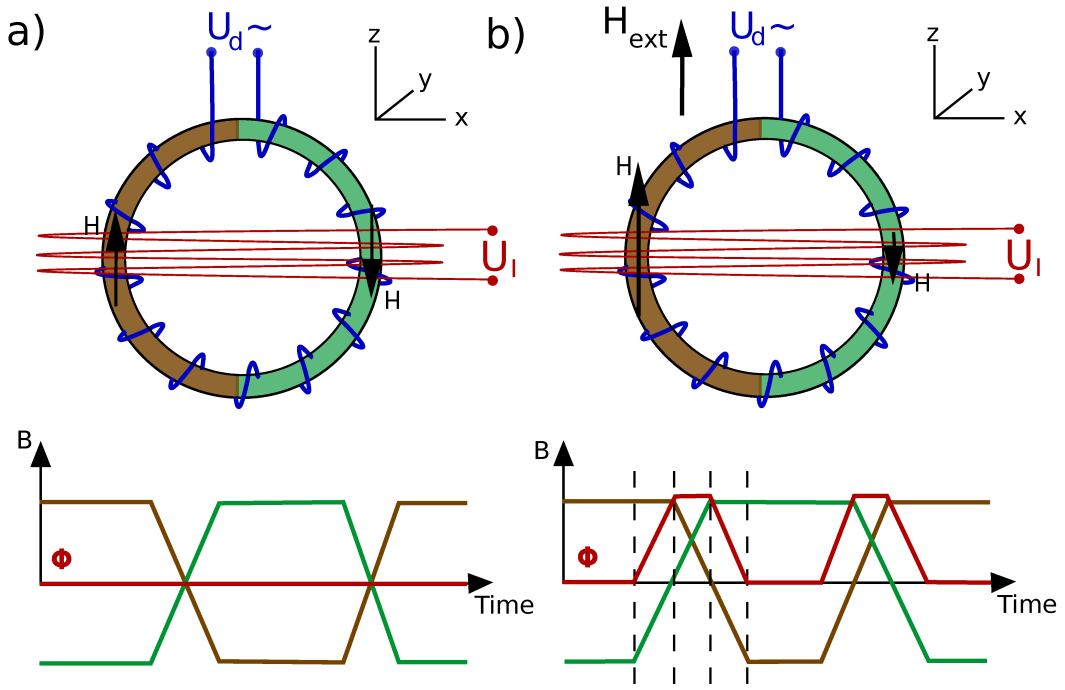

Figure 3.3. Schematic illustration of the working principle of a ring-core FGM as used on MGS. The top row shows the configuration of the magnetometer with the ring-shaped core (brown and green), the driving coil (blue), and the sensing coil (red). The bottom row illustrates the magnetic flux through the sensing coil for the green and brown areas. (a) No external field is applied, and the overall magnetic flux through the sensing coil is zero. Thus, the induced voltage U_I of the sensing coil is zero. (b) An external magnetic field is applied in the z-direction and a periodic voltage is induced in the sensing coil.

(dark red) is then wrapped around the whole configuration and aligned parallel to the xy-plane. Now, the amplitude of the driving voltage U_d is chosen such that the core will saturate. Therefore, any further increase of U_d will only marginally increase the total field $\mathbf{B}_d$. For illustration, the magnetic field in the brown and green areas of the sensing coil are shown in the lower part of Fig. 3.3a with their respective colors. These fields are always opposite in sign, but of equal absolute values. Hence, they cancel over the area of the sensing coil, and the magnetic flux $\Phi = \int_S \mathbf{B}_d \cdot d\boldsymbol{A}_{xy}$ through the sensing coil will be zero (red line). Here, S is the surface area of the sensing coil, and the direction and length of the vector $\boldsymbol{A}_{xy}$ describe the orientation and the cross-section of an infinitesimally small area in the xy-plane, respectively. In contrast, an external magnetic field $\mathbf{H}_{ext} \neq 0$ will break this symmetry (c.f. Fig. 3.3b). In particular, the ambient field $\mathbf{H} = \mathbf{H}_d + \mathbf{H}_{ext}$ in the brown area of the sensing coil will increase, whereas it will decrease in the green area. Therefore, the brown part of the core will desaturate later as compared to the green part of the core. The resulting net flux (red line in Fig. 3.3b) is then time-dependent with a frequency of $2f_0$. As a result, a

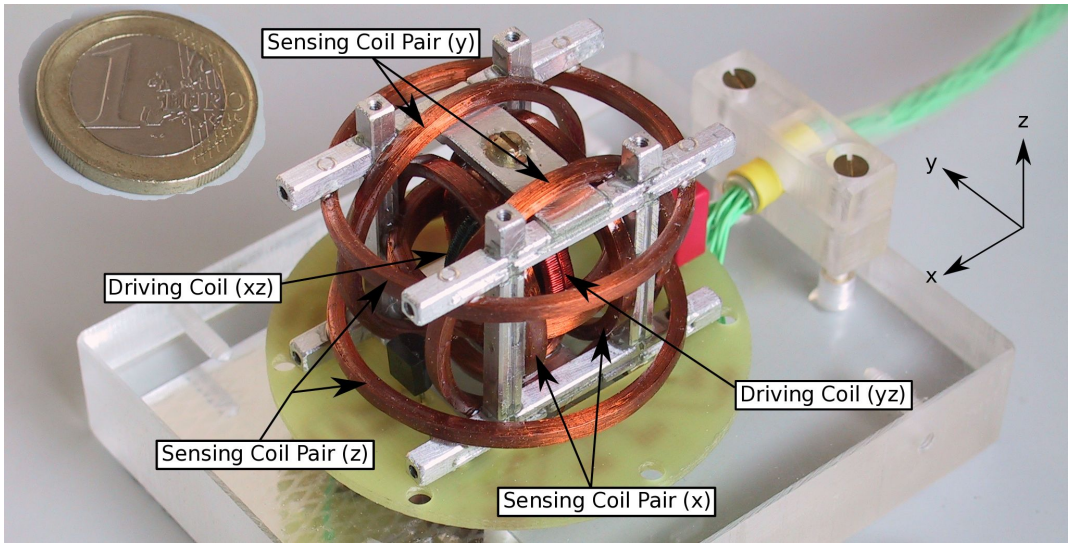

Figure 3.4. Image of the Bepi-Colombo FGM, showing the configuration with three Helmholtz sensing coils and two driving coils. ©IGEP[3]

voltage $U_I = -\dot{\Phi}(t) \neq 0$ is induced in the sensing coil which is proportional to the external field $\mathbf{H}_{ext}$.

The orientation of the sensing coil in the xy-plane guarantees that only the z-component of the external field will be measured. In order to measure the x-component of the external field, the sensing coil has to be rotated to the yz-plane. Overall, a three-axis magnetometer can be realized with two ring-shaped cores and three sensing coils. In practice, some modifications are made to the setup of Fig. 3.3. For example, U_I will be pre-amplified and isolated with a phase-sensitive detector. Further, the sensing coil may also act as a feedback coil by generating a field $\mathbf{H}_f$ to compensate the external field $\mathbf{H}_{ext}$. Then, the output of the sensing coil will be zero and the compensation current is used to measure $\mathbf{H}_{ext}$. In addition, the sensing coils may be realized as a pair of Helmholtz-coils in order to achieve a homogeneous compensation field. As an example, the Bepi-Colombo[4] FGM is shown in Fig. 3.4.

3.4 DATA PRE-PROCESSING AND CALIBRATION

Although S/C generated fields have been minimized [Acuña et al., 2001] for MGS, such fields are still generated by the power supply electronics (PSE) and by the permanent magnets of the traveling wave tube amplifiers (TWTA) (Fig. 3.5, Fig. 1 of Acuña et al. [2001]). In consequence, a model of these S/C fields is needed in order to remove them from the data. Within such a model, Acuña et al. [2001] described the measured magnetic field B_m (in

3 Institut für Geophysik und Extraterrestrische Physik / TU Braunschweig
4 BepiColombo is a mission to Mercury which is scheduled for launch in early 2017.

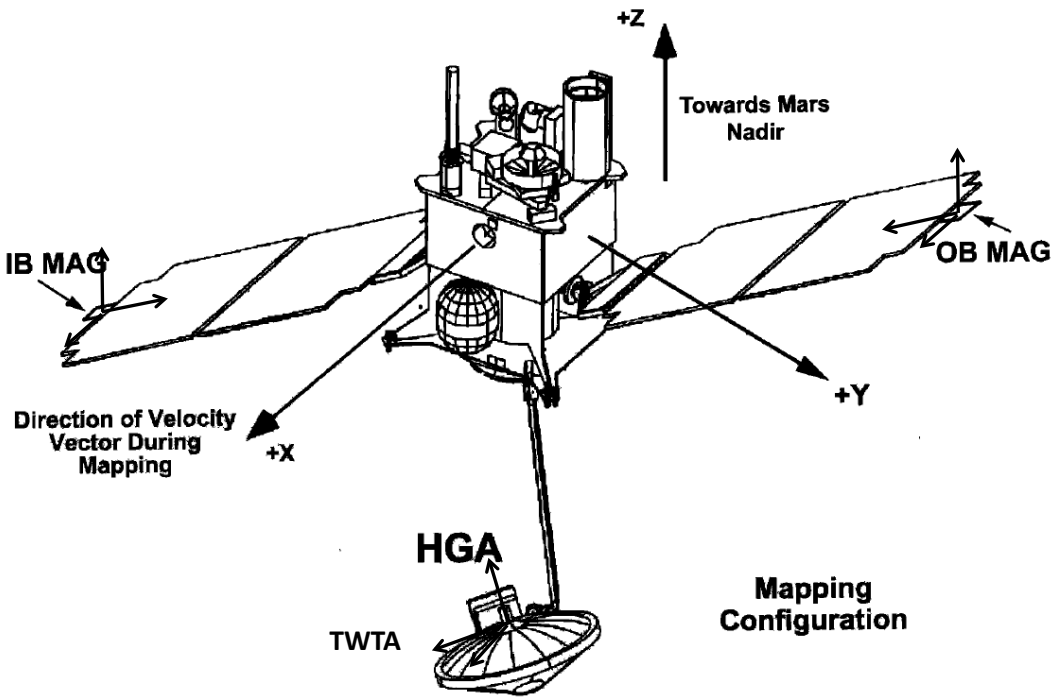

Figure 3.5. Schematic setup of the Mars Global Surveyor (MGS) S/C (Fig. 1 of Acuña et al. [2001], Copyright 2001 by the American Geophysical Union, reprinted with kind permission from publisher John Wiley & Sons Ltd.)

sensor coordinates) as a combination of static and dynamic fields, i.e. by

$$\mathbf{B}_m = \mathbf{B}_0 + \mathbf{T}\mathbf{B}_{S/C} + \mathbf{H}\mathbf{B}_{TWTA} + \mathbf{B}_a + \mathbf{B}_{SP} + \mathbf{T}\mathbf{B}_{PSE}. \tag{3.1}$$

Here, static fields include a constant sensor zero offset $\mathbf{B}_0$, a general static field $\mathbf{B}_{S/C}$ (in S/C body coordinates), and the field $\mathbf{B}_{TWTA}$ related to the TWTA (in high-gain antenna (HGA) coordinates). In addition, the respective coordinate transformations to the MAG system of coordinates are given by $\mathbf{T}$ and $\mathbf{H}$. Hence, $\mathbf{B}_{S/C}$ and $\mathbf{B}_{TWTA}$ may appear dynamic at the location of the MAG sensors in case the solar panels or the HGA are moving. In addition, dynamic fields include $\mathbf{B}_{SP}$ generated by the solar panels and $\mathbf{B}_{PSE}$ generated by the PSE. These fields are assumed to depend linearly on the solar panel and power supply currents, respectively. Finally, the ambient Martian field $\mathbf{B}_a$ is assumed to be equal at the locations of each of the two magnetometers. Then, the difference of the fields as measured by the two FGMs can be inverted for the model parameters, i.e. the different field contributions. For a better determination of these model parameters, the HGA was moved through its various positions on some of the nightside passes in January/February 2000 [Acuña et al., 2001]. In addition, a number of in-flight calibration tests were performed [Acuña et al., 2001].

4

DATA SELECTION & DATA WEIGHTS

In this chapter, the data selection and the estimation of a priori data weights will be described (Sec. 5 and Sec. 6). The fluxgate magnetometers on MGS (MAG) data were downloaded from the Planetary Plasma Interactions Node of the Planetary Data System (PDS)[1] where these data are available in a Cartesian, planetocentric coordinate system and a Cartesian, sun-related coordinate system. For further processing, these data were transformed into a spherical planetocentric coordinate system. In the latter system of coordinates, the magnetic field is expressed in terms of the horizontally north (X), east (Y), and vertically down (Z) field components.

4.1 MAG MPO DATA

The mapping phase orbit (MPO) data set provides dense global coverage with ~176.2 million vector data points. These data were obtained at altitudes of 422.1 km near the north- down to 348.6 km near the south pole, as measured above the mean planetary radius of 3393.5 km. For statistical purposes, we calculate the global data coverage and density on a grid with bins of latitudinal size of $\Delta\theta = 0.5^\circ$. This grid was designed to obtain bins of similar area by setting the longitudinal bin size to

$$\Delta\phi = \frac{\Delta\theta}{\sin(\theta_c)} \tag{4.1}$$

where θ_c is the colatitude at the center of the respective bin. When projected on a radius of 3393.5 km, extreme bin sizes of $306 - 918\,\mathrm{km}^2$ occur only at the poles, and the remaining bins range from $877\,\mathrm{km}^2$ to $883\,\mathrm{km}^2$ in size. As well, empty bins remain only at the poles due to the Mars Global Surveyor (MGS) orbit inclination, and 99.8 % of the bins are filled with 342 data points on average. This corresponds to an average data density of $0.390\,\mathrm{km}^{-2}$ when projected on a radius of 3393.5 km.

The influence of solar wind induced ionospheric currents was reduced by rejecting all MPO dayside data. Dayside data were identified by using the sun-related coordinate system and the solar panel currents, which are both available from the PDS. The remaining ~56.3 million vector measurements at the nightside result in a polar data gap of 4.42° at the north pole and 2.86° at the south pole. Here, the asymmetry of the polar gaps is due to different orbit altitudes at the poles. In addition, one data point was

1 http://ppi.pds.nasa.gov/

selected every 80 km along the surface footprint of the satellite track in order to reduce the required computational cost. For this selection, a random offset at the beginning of each track was introduced to obtain a spatially uniform data sampling. Overall, ~2.58 million data points were retained with an unchanged global coverage of 99.8 % and an average data density of 0.0179 km^{-2} when projected on a radius of 3393.5 km.

Under the assumption of normally distributed noise in the data[2], the standard deviations (STDs) of this noise should be used as data weights when inverting for a field model (c.f. Sec. 5.2). However, these STDs are difficult to assess a priori as possible sources of such noise are not fully understood. Still, the stable altitude of MGS and the dense global coverage of the MPO data allow to statistically estimate these STDs. For this purpose, the data were binned in an almost equal-area grid with $\Delta\theta = 0.5^\circ$ (c.f. Eq. 4.1) and the STD of each bin was calculated. With this choice, the grid size is smaller than typical spatial variations of the crustal magnetic field at orbit altitude. At the same time, the bins contain as many data points as possible in order to obtain robust STDs. Moreover, the data were divided into four epochs of one Martian year each in order to account for seasonal changes of the STDs. For these epochs, an average of $77 - 91$ data points is obtained per bin and the global data coverage remains unchanged. The resulting STDs show a general global trend, but vary considerably between neighboring bins. As the statistics of the noise is expected to vary continuously in space, it is assumed that these strong bin-to-bin variations are due to an insufficient number of data points per bin. Therefore, the obtained values were weighted with the number of data points in each bin and fit to a set of global spherical harmonic (SH) functions up to degree and order eight. The resulting smoothed STDs for the horizontally north (X), east (Y), and vertically down (Z) components for each of the four epochs were used to weight the MPO data ($\mathbf{W}_\mathrm{d}$ in Eqs. 6.23, 6.25, and Eqs. 6.30 - 6.32), and these STDs are shown in Fig. 4.1.

From this figure, the vertically down (Z) field component shows lower STDs than the horizontally north (X) and east (Y) field components. In agreement, the vertically down (Z) component has previously been identified to be less affected by external fields [Luhmann and Brace, 1991; Acuña et al., 1999; Arkani-Hamed, 2004a]. Also, an anticorrelation between the STDs of the horizontally north (X) and east (Y) components and the crustal field strength is observed. Indeed, current sheet crossings which disturb the measurements of the crustal magnetic field occur down to the MPO altitude mainly at regions of low field intensity [Halekas et al., 2006]. Moreover, the obtained STDs continuously increase from the first to the third epoch before a strong decrease is observed for the fourth epoch. Accordingly, the international sunspot number as indicated by the dashed line in Fig. 4.2 reaches a maximum during the first two epochs. However, solar activity was continuously decreasing during the third epoch, for which the largest

2 For a discussion of data noise, see footnote on p. 53.

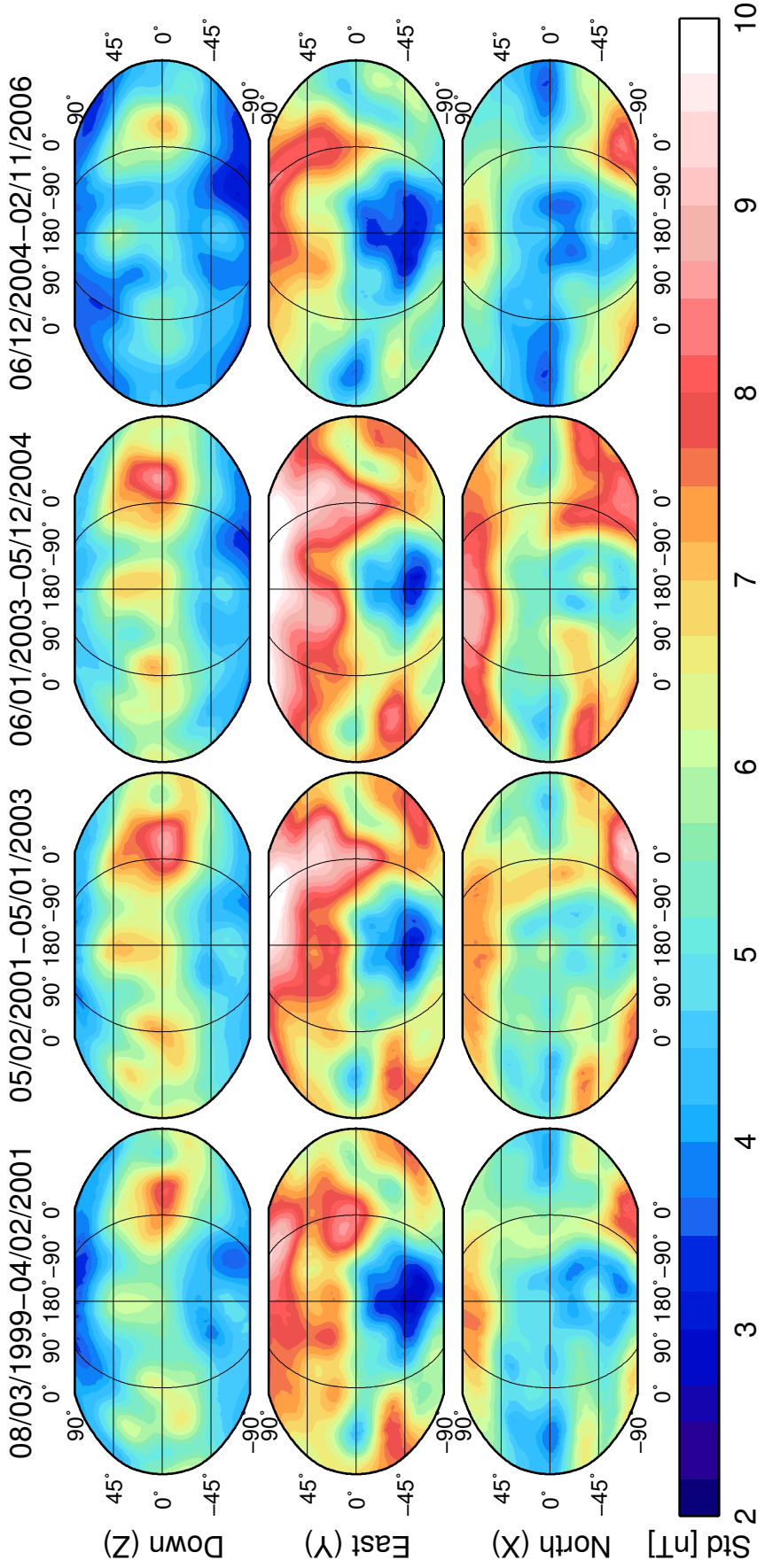

Figure 4.1. This figure shows the data weights which were estimated from the MAG data as obtained during the MPO at different epochs (columns) and for all magnetic field vector components (rows). These data weights were obtained by calculating the STD of the data for each bin on a spatial grid with 0.5° resolution in latitude (Eq. 4.1), and by subsequently fitting SH functions up to degree and order eight in order to obtain a smooth representation. The shown data weights can be considered as a measure of temporally variable non-crustal field contributions to the data (Fig. 2 of Morschhauser et al. [2014], Copyright 2014 by the American Geophysical Union, reprinted with kind permission from publisher John Wiley & Sons Ltd.).

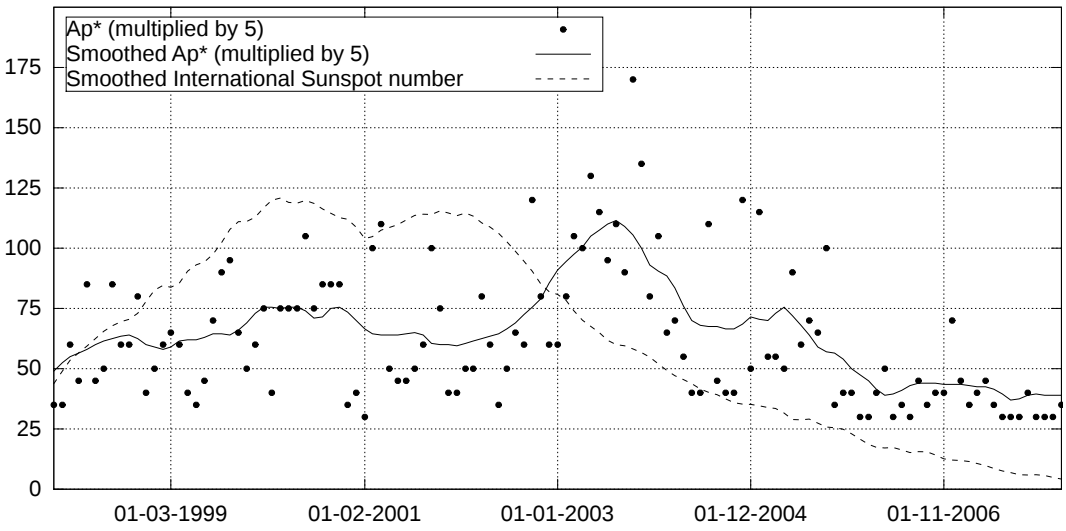

Figure 4.2. The solar activity for the duration of the MGS mission is shown. The smoothed international sunspot number as obtained from the Space Weather Prediction Center (http://www.swpc.noaa.gov/) is indicated by the dashed line. As well, the Ap* index for geomagnetic storm activity is multiplied by five and shown by the dots and the smoothed solid line. This index is available from the National Centers for Environmental Information (www.ngdc.noaa.gov).

STDs are obtained. This discrepancy may be explained by the observation of increased geomagnetic storm activity at the beginning of the declining phase of the solar cycle [Echer et al., 2008, 2013], as indicated by the solid line in Fig. 4.2. In this case, geomagnetic storms may be an indicator for magnetic activity at Mars.

4.2 MAG AB/SPO DATA

During the aerobraking phase (AB)/science phase orbit (SPO) mission phases, ~3.04 million vector measurements have been recorded. In contrast to the MPO data, these data are characterized by strongly varying altitudes. Particularly, the apoapsis reached down to 80 km above the mean surface altitude of 3393.5 km, which allows for a better resolution than the MPO data set[3]. On the other hand, only ~0.49 million data points were obtained at altitudes below the minimum MPO orbit altitude of 348 km. Moreover, 99.39 % of these data were obtained at the dayside, which significantly increases the influence of the solar wind [Cain et al., 2003]. In particular, Brain [2003] argued that the dayside magnetic field is dominated by non-crustal contributions down to altitudes of 200 km. Hence, all dayside AB/SPO data above this altitude were rejected. Again, the solar panel currents and sun-related coordinate system were used to determine if a datum is on the

3 Generally, small scale contributions to the crustal magnetic field are significantly attenuated with increasing altitude.

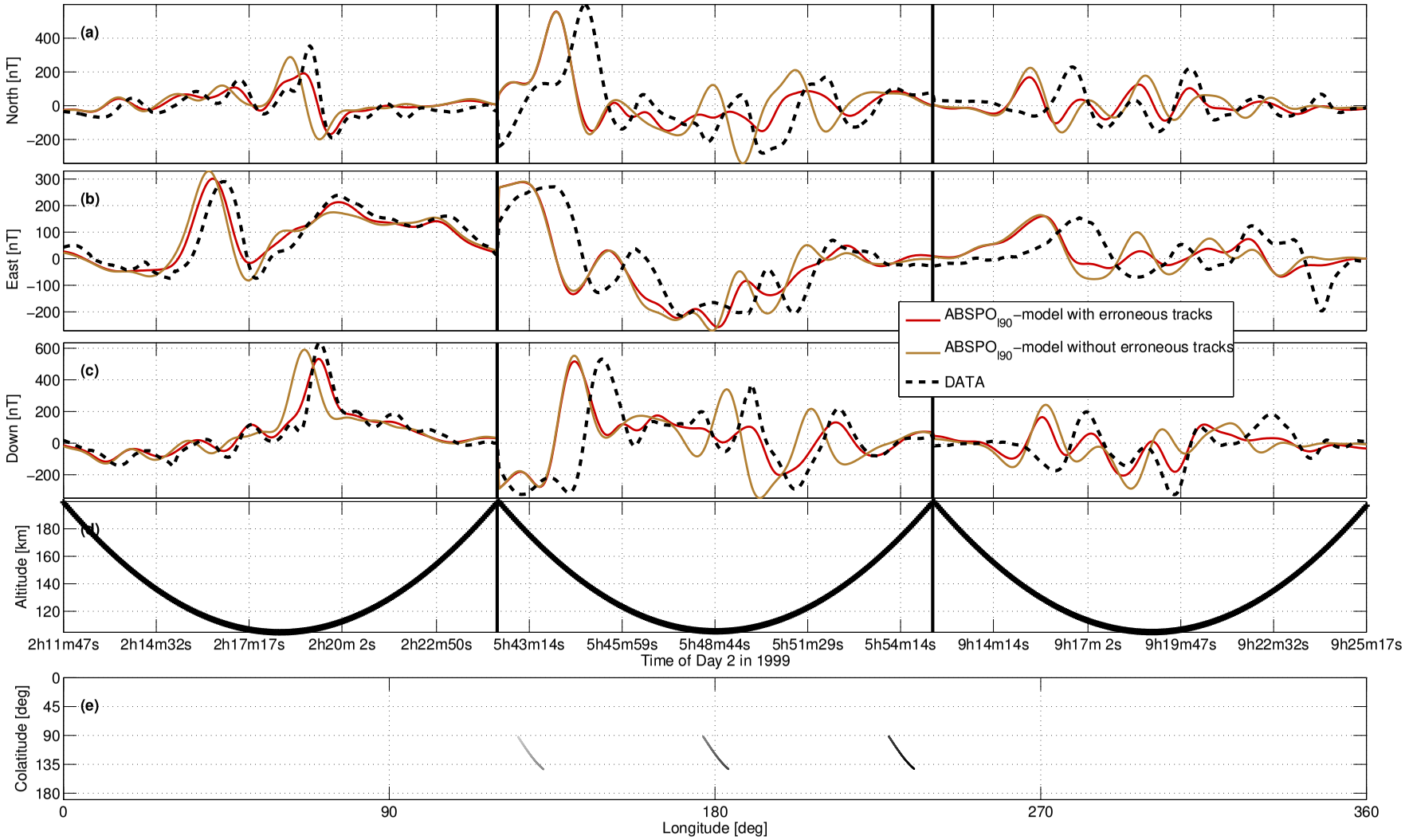

Figure 4.3. From top to bottom, the horizontally north (X), east (Y), and vertically down (Z) components of the measured magnetic field are shown in the upper three panels for an AB track which probably suffers from timestamp errors (dashed line). Two models which were fit to a data set with and without this track are shown by the red and brown lines, respectively. Otherwise, these models are similar to the ABSPO$_{l90}$ model (Fig. 6.1). In the lower two panels, the altitude and the position of the data track are shown. The effect of the erroneous data on the models is particularly evident in the vertically down (Z) component at 2 h 19 m.

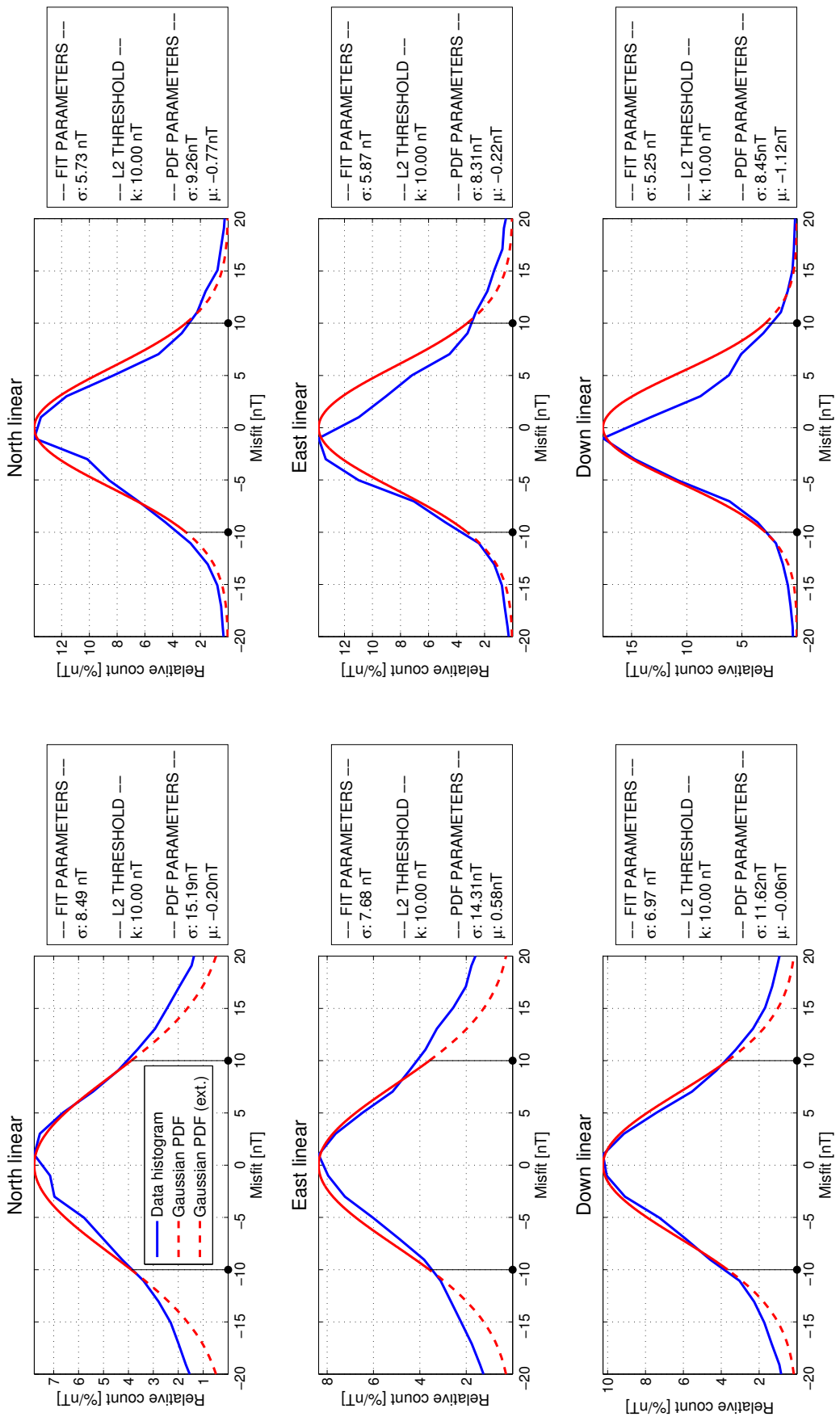

(a) Dayside **(b)** Nightside

Figure 4.4. The histogram of the unweighted residuals between the AB/SPO data and the W model of Fig. 6.1 (blue line) is shown for (a) the dayside and (b) the nightside data. A normal distribution with mean zero ($\mu = 0$) is fit to residuals smaller than or equal to $k = 10\,\mathrm{nT}$ (solid red line). The red dashed line indicates the same normal distribution for larger values of misfit. The resulting STD σ of the normal distribution is shown in the white boxes on the right side of the respective histogram (labeled "Fit parameters"). In addition, the overall STD σ and mean μ of all data points is shown (labeled "PDF parameters").

night- or dayside. Overall, the selected AB/SPO data set contains the nightside data below 348 km and the dayside data below 200 km altitude. With ~0.29 million data points, this data set covers 39.1 % of the planet with an average data density of 0.0051 km^{-2} if projected on a sphere with a radius of 3393.5 km, and if the same grid as for the MPO data is used for binning.

The residuals of the AB/SPO data to a preliminary model ($ABSPO_{l90}$ model in Fig. 6.1) revealed possible timestamp errors in the data for three subsequent periapsis passes (Fig. 4.3). These passes occurred on 2nd of January, 1999, between 02 h 11 m and 09 h 25 m universal time (UT), and the respective data points have been removed from the final data set. As a result, the preliminary model (brown line in Fig. 4.3) better resembles a shifted version of the data (not shown). Apart from that, no other example of such a timestamp error was found. However, such an error may be hard to detect in regions of low field intensity.

Due to the unstable AB/SPO orbit altitude, the STDs of the AB/SPO data cannot be determined in the same way as those of the MPO data. Instead, the respective STDs were calculated from the residuals of the data to a preliminary model (W model in Fig. 6.1). This preliminary model was unregularized and based on the selected MAG data set. Further, the previously determined MPO data weights were used, whereas the AB/SPO data were equally weighted with $\boldsymbol{W}_d = \mathbf{I}$ (c.f. Eqs. 5.12 and 6.31). The resulting histograms of the residuals between the AB/SPO data and this preliminary model are shown by the blue lines in Fig. 4.4. Now, the data weights were determined by fitting these histograms (blue line) to a Gaussian distribution (red line) and ignoring data outliers. As a result, STDs of 8.49 nT, 7.68 nT, and 6.97 nT were obtained for the horizontally north (X), east (Y), and vertically down (Z) components of the dayside data, respectively (Fig. 4.4a). Further, STDs of 5.73 nT, 5.87 nT, and 5.25 nT were obtained for the same components of the nightside data, respectively (Fig. 4.4b). For comparison, Cain et al. [2003] obtained larger values of $6.2 - 7.1$ nT for the nightside and $6.4 - 13.5$ nT for the dayside AB/SPO data. However, Cain et al. [2003] fit the Gaussian envelope to the entire distribution instead of explicitly disregarding the non-Gaussian tails as it was done here.

Part III

INVERSION

First, a general introduction to linear inversion will be given. Then, I will discuss some more specific techniques which are applied to invert the MAG data for a model of the crustal magnetic field.

5

GENERAL LINEAR INVERSION

First, an introduction to the basic principles of linear inversion will be given. Then, the least squares solution will be presented which provides the model parameters of maximum likelihood for normally distributed data noise[1]. Further, it will be discussed how noise in the data can influence the model parameters, and how regularization can stabilize the inversion under the influence of such noise. Finally, alternative measures of data misfit will be mentioned which lead to outlier-robust solutions.

5.1 BASIC PRINCIPLES OF LINEAR INVERSION

We consider a linear physical model which relates a vector $\hat{\mathbf{m}}$ of n known model parameters to a vector $\hat{\mathbf{d}}$ of m predictions for some observables by

$$\mathbf{D}\hat{\mathbf{m}} = \hat{\mathbf{d}} \tag{5.1}$$

where $\mathbf{D}$ is an $m \times n$ matrix describing the model. Usually, the predicted values $\hat{\mathbf{d}}$ will not correspond to the measured data $\mathbf{d}$, as the model is never perfect[1]. Further, the problem of finding the model parameters $\hat{\mathbf{m}}$ from a set of measured data $\mathbf{d}$ is called the inverse problem. The inverse problem has either no solution, one solution, or an infinite number of solutions. If a solution can be obtained[2], it may still be influenced by data noise $\boldsymbol{\epsilon}$ or numerical errors. More quantitatively, the sensitivity of the obtained model parameters $\mathbf{m}$ on noise in the data is described by the condition number κ, defined by

$$\frac{\|\hat{\mathbf{m}} - \mathbf{m}\|}{\|\hat{\mathbf{m}}\|} \leqslant \kappa \frac{\left\|\hat{\mathbf{d}} - \mathbf{d}\right\|}{\left\|\hat{\mathbf{d}}\right\|}. \tag{5.2}$$

1 A perfect and complete model (which is most probably not linear) would perfectly explain the data (neglecting quantum theory, of course). However, all physical models simplify reality as some of the underlying physical processes might be of comparatively weak influence, too complex (nonlinear), not fully understood, or irrelevant to the considered problem. Therefore, some part of the data, which is considered as noise $\boldsymbol{\epsilon} = \mathbf{d} - \hat{\mathbf{d}}$, will remain unexplained by the model. Ideally, such noise should be small compared to the signal and randomly distributed. Else, a revision of the model should be considered.

2 In order to obtain one solution for $\mathbf{d} \neq \mathbf{d}_0$, the matrix $\mathbf{D}$ must be square and non-singular. The latter is the case if the columns of $\mathbf{D}$ are linearly independent, i.e. if no model parameter $\mathbf{m}_i$ can be expressed in terms of any other model parameter $\mathbf{m}_{j\neq i}$. Further, if the observed data are perfectly described by the model, i.e. $\mathbf{d} = \mathbf{d}_0$, one solution will be obtained for any number of data points if $\mathbf{D}$ is non-singular.

Inverse problems with large condition numbers are called ill-conditioned. In the case of an L2 norm[3], the condition number can be calculated from the quotient of the maximum and minimum non-zero singular values of $\mathbf{D}$ [Aster et al., 2013, p. 65ff.].

5.2 THE LEAST-SQUARES SOLUTION

A large number of observations ($m \gg n$) should be used when inverting noisy data[4]. Only then, the underlying distribution of noise in the data can be sufficiently sampled. However, the inverse problem cannot be solved if $m > n$ and if $\mathbf{d} \neq \hat{\mathbf{d}}$ (Eq. 5.1). Instead, we seek the set of model parameters which minimizes the residuals

$$\mathbf{r} = \mathbf{d} - \mathbf{D}\mathbf{m} \tag{5.3}$$

under a specific norm. The best choice for this norm is determined by the corresponding distribution of noise in the data (c.f. Sec. 5.6). For example, an L2 norm will result in the maximum likelihood solution[5] for independent and normally distributed noise with mean $\mu = 0$ and STD $\sigma = 1$ (Aster et al. [2013, p. 27ff.] and Sec. 5.6). This solution minimizes the objective function

$$\Phi_{LS} = \|\mathbf{r}\|_2^2 = \sum_i \mathbf{r}_i^2 = \sum_i (\mathbf{d}_i - (\mathbf{D}\mathbf{m})_i)^2 \tag{5.4}$$

and is therefore known as the least-squares solution. In matrix notation, this equation can be written as

$$\begin{aligned}\Phi_{LS} &= (\mathbf{d} - \mathbf{D}\mathbf{m})^T(\mathbf{d} - \mathbf{D}\mathbf{m}) \\ &= (\mathbf{m}^T\mathbf{D}^T - \mathbf{d}^T)(\mathbf{D}\mathbf{m} - \mathbf{d}) \\ &\overset{6}{=} \mathbf{m}^T\mathbf{D}^T\mathbf{D}\mathbf{m} - 2\mathbf{d}^T\mathbf{D}\mathbf{m} + \mathbf{d}^T\mathbf{d}.\end{aligned} \tag{5.5}$$

Then, the least-squares solution $\mathbf{m}$ is obtained from the minimization of Eq. 5.5 and by solving

$$\frac{\partial \Phi_{LS}}{\partial \mathbf{m}} = \frac{\partial \mathbf{m}^T\mathbf{D}^T\mathbf{D}\mathbf{m}}{\partial \mathbf{m}} - 2\frac{\partial \mathbf{d}^T\mathbf{D}\mathbf{m}}{\partial \mathbf{m}} \overset{!}{=} 0. \tag{5.6}$$

3 The L2 norm for an arbitrary vector $\mathbf{x}$ is defined as $\|\mathbf{x}\|_2 = \sqrt{\sum_i \mathbf{x}_i^2}$.

4 See footnote 1.

5 In a probabilistic sense, the maximum likelihood solution yields the model parameters $\mathbf{m}$ for which the observed data are most probably observed.

6 As $\mathbf{m}^T\mathbf{D}^T\mathbf{d}$ is a scalar and $\mathbf{m}^T\mathbf{D}^T\mathbf{d} = (\mathbf{d}^T\mathbf{D}\mathbf{m})^T$.

In order to solve Eq. 5.6 with respect to $\mathbf{m}$, we consider

$$\begin{aligned}\frac{\partial \mathbf{m}^T\mathbf{D}^T\mathbf{D}\mathbf{m}}{\partial \mathbf{m}_k} =& \frac{\partial(\sum_{i,j,l}\mathbf{D}_{ij}\mathbf{D}_{il}\mathbf{m}_j\mathbf{m}_l)}{\partial \mathbf{m}_k} \\ =& \begin{cases} \sum_{i,l}\mathbf{D}_{ik}\mathbf{D}_{il}\mathbf{m}_l, & \text{if } j = k \\ \sum_{i,j}\mathbf{D}_{ik}\mathbf{D}_{ij}\mathbf{m}_j, & \text{if } l = k \\ 0, & \text{otherwise} \end{cases} \\ =& 2\sum_{i,j}\mathbf{D}_{ik}\mathbf{D}_{ij}\mathbf{m}_j = 2(\mathbf{D}^T\mathbf{D}\mathbf{m})_k \end{aligned} \tag{5.7}$$

and

$$\begin{aligned}\frac{\partial \mathbf{d}^T\mathbf{D}\mathbf{m}}{\partial \mathbf{m}_k} =& \frac{\partial(\sum_i \mathbf{d}_i \sum_j \mathbf{D}_{ij}\mathbf{m}_j)}{\partial \mathbf{m}_k} \\ =& \frac{\partial(\sum_{ij}\mathbf{D}_{ij}\mathbf{d}_i\mathbf{m}_j)}{\partial \mathbf{m}_k} \\ =& \sum_i \mathbf{D}_{ik}\mathbf{d}_i = (\mathbf{D}^T\mathbf{d})_k. \end{aligned} \tag{5.8}$$

Inserting Eqs. 5.7 and 5.8 in Eq. 5.6, and solving for $\mathbf{m}$, we finally obtain

$$\mathbf{m} = (\mathbf{D}^T\mathbf{D})^{-1}\mathbf{D}^T\mathbf{d}. \tag{5.9}$$

Now, we consider the more general case of data noise that is following a multivariate normal distribution with mean $\mu = 0$ and standard deviation (STD) σ_i for the i-th data point. In this case, the maximum-likelihood solution is obtained by minimizing

$$\Phi_{WLS} = \sum_i \frac{(\mathbf{d}_i - (\mathbf{D}\mathbf{m})_i)^2}{\sigma_i^2} \tag{5.10}$$

[Aster et al., 2013, p. 27ff]. By introducing the diagonal weighting matrix $(\mathbf{W})_{ii} = 1/\sigma_i$, where $(.)_{ii}$ is the i-th diagonal element of the respective matrix, we can rewrite Eq. 5.10 as

$$\begin{aligned}\Phi_{WLS} =& (\mathbf{d} - \mathbf{D}\mathbf{m})^T\mathbf{W}^T\mathbf{W}(\mathbf{d} - \mathbf{D}\mathbf{m}) \\ =& (\mathbf{d}_w - \mathbf{D}_w\mathbf{m})^T(\mathbf{d}_w - \mathbf{D}_w\mathbf{m}) \end{aligned} \tag{5.11}$$

where $\mathbf{d}_w = \mathbf{W}\mathbf{d}$ and $\mathbf{D}_w = \mathbf{W}\mathbf{D}$. Then, we find in analogy to Eq. 5.9 that

$$\begin{aligned}\mathbf{m} =& (\mathbf{D}_w^T\mathbf{D}_w)^{-1}\mathbf{D}_w^T\mathbf{d}_w \\ =& (\mathbf{D}^T\mathbf{W}^T\mathbf{W}\mathbf{D})^{-1}\mathbf{D}^T\mathbf{W}^T\mathbf{W}\mathbf{d}. \end{aligned} \tag{5.12}$$

For the sake of completeness, we also consider normally distributed and correlated noise which is described by the data covariance matrix $\mathbf{C}_d = \mathrm{Cov}(\mathbf{d})$. For example, large-scale current systems in the ionosphere may lead to spatial and temporal correlations. More formally, the covariance matrix is defined by $(\mathbf{C}_d)_{ij} = \langle(\mathbf{d}_i - \boldsymbol{\mu}_i)(\mathbf{d}_j - \boldsymbol{\mu}_j)\rangle$ where $\langle\cdot\rangle$ denotes the expectation value. From this definition, the covariance matrix $\mathbf{C}_d$ must be symmetric, and $\mathbf{C}_d$ can be factorized into its eigenvalues. In particular, $\mathbf{C}_d = \mathbf{P}\boldsymbol{\Lambda}\mathbf{P}^T$, where the diagonal matrix $\boldsymbol{\Lambda}$ contains the eigenvalues of $\mathbf{C}_d$, and the columns of $\mathbf{P}$ contain the respective eigenvectors. Now, the maximum likelihood solution with correlated data noise is given by

$$\begin{aligned}\mathbf{m} &= (\mathbf{D}^T\mathbf{C}_d^{-1}\mathbf{D})^{-1}\mathbf{D}^T\mathbf{C}_d^{-1}\mathbf{d} \\ &= (\mathbf{D}^T\mathbf{P}\boldsymbol{\Lambda}^{-1}\mathbf{P}^T\mathbf{D})^{-1}\mathbf{D}^T\mathbf{P}\boldsymbol{\Lambda}^{-1}\mathbf{P}^T\mathbf{d}\end{aligned} \tag{5.13}$$

[Aster et al., 2013, p. 50f.] and can be written in terms of Eq. 5.12 if the diagonal weighting matrix $\boldsymbol{W} = \sqrt{\boldsymbol{\Lambda}^{-1}}\mathbf{P}^T$ is used.

5.3 MODEL PARAMETER CONFIDENCE INTERVALS

In general, the covariance matrix $\mathrm{Cov}(\mathbf{x})$ transforms under a linear transformation $\mathbf{y} = \boldsymbol{A}\mathbf{x}$ as

$$\mathrm{Cov}(\mathbf{y}) = \mathrm{Cov}(\boldsymbol{A}\mathbf{x}) = \boldsymbol{A}\mathrm{Cov}(\mathbf{x})\,\boldsymbol{A}^T \tag{5.14}$$

[Aster et al., 2013, p. 329]. According to Eq. 5.12, the least-squares solution $\mathbf{m}$ is a linear combination of the weighted data $\mathbf{d}_w$ with the transformation matrix $\boldsymbol{A} = (\mathbf{D}_w^T\mathbf{D}_w)^{-1}\mathbf{D}_w^T$. Hence, the covariance matrix $\mathrm{Cov}(\mathbf{m})$ of the model parameters is calculated from the covariance matrix $\mathrm{Cov}(\mathbf{d}_w)$ of the weighted data by

$$\mathrm{Cov}(\mathbf{m}) = (\mathbf{D}_w^T\mathbf{D}_w)^{-1}\mathbf{D}_w^T\mathrm{Cov}(\mathbf{d}_w)\,\mathbf{D}_w\left[(\mathbf{D}_w^T\mathbf{D}_w)^{-1}\right]^T. \tag{5.15}$$

Now, if the data covariance matrix $\mathbf{C}_d$ has been correctly chosen, it follows that $\mathrm{Cov}(\mathbf{d}_w) = \mathbf{I}$, and the model covariance matrix $\mathrm{Cov}(\mathbf{m})$ is given by[7]

$$\mathrm{Cov}(\mathbf{m}) = (\mathbf{D}_w^T\mathbf{D}_w)^{-1}. \tag{5.16}$$

As well, the covariance matrix of the model predictions $\mathbf{d}^* = \mathbf{D}\mathbf{m}$ can be obtained from

$$\mathrm{Cov}(\mathbf{d})^* = \mathbf{D}(\mathbf{D}_w^T\mathbf{D}_w)^{-1}\mathbf{D}^T. \tag{5.17}$$

However, the data covariance matrix $\mathbf{C}_d = \mathrm{Cov}(\mathbf{d})$ is not known a priori. Instead, it is often estimated using rather strong assumptions and simplifi-

7 Note that $(\mathbf{D}_w^T\mathbf{D}_w)^{-1}$ is symmetric.

cations. Therefore, Eqs. 5.16 and 5.17 are only approximations of the true covariance matrices.

In the following, we investigate the confidence intervals of the model parameters $\mathbf{m}$. For this purpose, we consider that the obtained model parameters $\mathbf{m}$ depend on probabilistic data noise. Therefore, they are also the result of a probabilistic process with mean $\boldsymbol{\mu} = \overline{\mathbf{m}}$ and covariance matrix $\mathrm{Cov}(\mathbf{m})$. Further, if the data noise is normally distributed, then the distribution

$$(\overline{\mathbf{m}} - \mathbf{m})^T \mathrm{Cov}(\mathbf{m})^{-1} (\overline{\mathbf{m}} - \mathbf{m}) \tag{5.18}$$

follows a χ^2 distribution[8] with n degrees of freedom [Aster et al., 2013, p. 329]. This distribution can be approximated by a normal distribution ($\mu = n$ / $\sigma = \sqrt{2n}$) for large degrees of freedom, i.e. $n > 100$. Therefore, a p% confidence ellipsoid[9,10] in the model parameter space is defined by

$$(\overline{\mathbf{m}} - \mathbf{m})^T \mathrm{Cov}(\mathbf{m})^{-1} (\overline{\mathbf{m}} - \mathbf{m}) \leqslant \Delta_u^2 \tag{5.19}$$

where Δ_u^2 is calculated from

$$\frac{1}{\sqrt{4n\pi}} \int_0^{\Delta_u^2} e^{\frac{-(x-n)^2}{4n}} dx = \frac{p}{100}. \tag{5.20}$$

As the model covariance matrix $\mathrm{Cov}(\mathbf{m})$ is usually not diagonal, the n-dimensional confidence ellipsoid (Eq. 5.19) is not aligned with the coordinate axes of the model parameter space. Therefore, the confidence intervals of the model parameters are not independent. Still, we may approximate the ellipsoid by an enclosing rectangular box. Then, an upper bound of

$$\delta_u(\mathbf{m}_i) = \pm \Delta_u \sqrt{\mathrm{Cov}(\mathbf{m})_{i,i}} \tag{5.21}$$

is obtained for the confidence intervals of each model parameter (c.f. Gubbins [2004, p. 110f.]). As an example, we consider a multivariate normal distribution with two random variables and the covariance matrix

$$\mathbf{C} = \begin{bmatrix} 2.0 & 0.9 \\ 0.9 & 1.0 \end{bmatrix}. \tag{5.22}$$

8 A χ^2 distribution of degree n is the probability density function (PDF) of the random variable $Z = \sum_{i=1}^{n} X_i^2$, which is a combination of the normally distributed random variables X_i with STDs $\sigma = 1$ and mean $\mu = 0$.

9 With p% probability, the model parameters contained within the p% confidence region will be obtained from an inversion of data with normally distributed data noise.

10 The points $\mathbf{x}$ within an n-dimensional ellipsoid obey $\sum_{i=1}^{n} \frac{x_i^2}{a_i^2} \leqslant 1$ where the a_i are the semimajor axes along the respective coordinate axes.

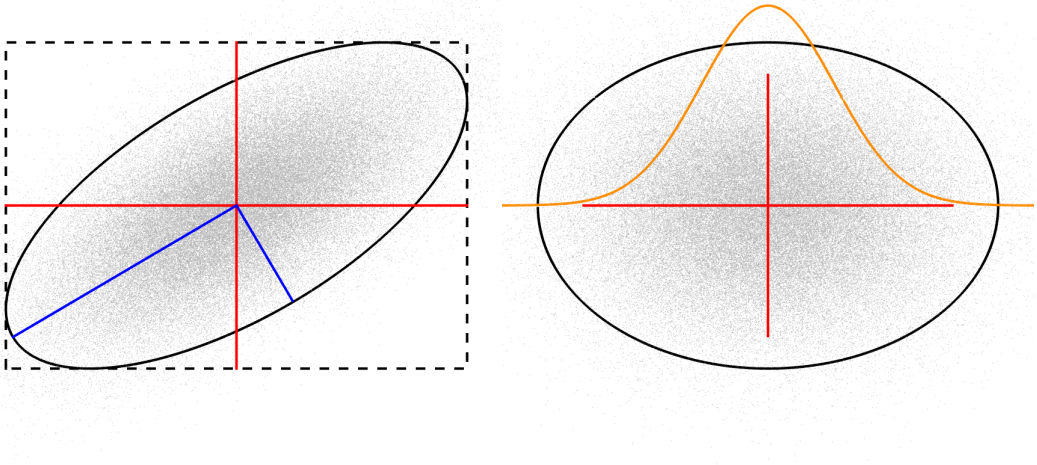

(a) Correlated **(b)** Uncorrelated

Figure 5.1. The distribution of two normally distributed parameters with the covariance matrix of Eq. 5.22 is shown. The boundary of the confidence ellipse that includes a pair of model parameters with a chance of 95% is shown by the black solid line. (a) The full covariance matrix is considered and the upper bounds of the confidence intervals are shown in red (Eq. 5.21). Also, the rectangular box enclosing the error ellipse is shown by the dashed black line, and the principal axes are shown in blue. (b) Lower bound confidence intervals are calculated by neglecting off-diagonal elements in the covariance matrix. In this case, an individual parameter has a 95% chance to be observed in the red confidence intervals (Eq. 5.23).

This distribution is shown in Fig. 5.1a (light gray points) along with the boundary of the 95% confidence ellipse (solid black line) and the corresponding principal axes (blue lines). In addition, the enclosing rectangular box (black dashed line) and the resulting confidence intervals (solid red lines) for each parameter axis are shown. Alternatively, a minimum confidence interval can be obtained if only the diagonal elements of the model covariance matrix are considered, i.e. if the correlations between the model parameters are neglected (Fig. 5.1b). Then, each model parameter $\mathbf{m}_i$ is described by an univariate normal distribution with mean $\mu_i = 0$ and STD $\sigma_i = \sqrt{\mathrm{Cov}\,(\mathbf{m})_{i,i}}$ (orange line). As a result, the p% confidence intervals (red lines) can be obtained from

$$\delta_l(\mathbf{m}_i) = \pm\Delta_l\sqrt{\mathrm{Cov}\,(\mathbf{m})_{i,i}} \tag{5.23}$$

with

$$\frac{2}{\sqrt{2\pi}}\int_0^{\Delta_l} e^{\frac{-x^2}{2}}\,dx = \frac{p}{100} \tag{5.24}$$

[Aster et al., 2013, p. 32]. This result differs from the boundaries of the confidence ellipse (black line), which shows the distribution of observing a certain combination of parameters.

In addition, the smallest and the largest principal axis of the confidence ellipsoid (blue lines in Fig. 5.1) can be interpreted in terms of the best- and poorest-determined model parameter combinations, respectively. In other words, the combined uncertainty of the model parameter combinations which correspond to the semi-minor (major) axis is smallest (largest), respectively. The principal axes of the error ellipsoid have the same directions as the eigenvectors of the respective covariance matrix, and their length can be calculated from $\Delta_u \sqrt{\lambda_i}$, where λ_i are the respective eigenvalues. Therefore, the smallest eigenvalue of Cov $(\mathbf{m})$ determines the confidence interval of the best-determined combination of model parameters.

5.4 MODEL RESOLUTION

In the following, we will investigate how the model parameters $\mathbf{m}$ which resulted from a linear inversion of the data are related to the model parameters $\hat{\mathbf{m}}$ which best describe reality. For this purpose, we assume that the data can be perfectly described by the model, i.e. $\mathbf{d} = \mathbf{D}\hat{\mathbf{m}}$ (Eq. 5.1). Then, the relation between $\hat{\mathbf{m}}$ and $\mathbf{m}$ is described by the resolution matrix $\mathbf{Q}$, i.e.

$$\mathbf{m} = \mathbf{A}\mathbf{d} = \mathbf{A}\mathbf{D}\hat{\mathbf{m}} = \mathbf{Q}\hat{\mathbf{m}}. \tag{5.25}$$

In the special case of the least squares inversion (Eq. 5.9), it then follows that

$$\mathbf{Q} = (\mathbf{D}^T\mathbf{D})^{-1}\mathbf{D}^T\mathbf{D} = \mathbf{I} \tag{5.26}$$

and the model is fully resolved. However, it should be kept in mind that the model is usually insufficient to perfectly describe the data (c.f. Sec. 5.1).

5.5 REGULARIZATION

Depending on the condition number κ (Eq. 5.2) of the inversion matrix[11] $\mathbf{A}$, data noise may significantly influence the obtained model parameters $\mathbf{m}$. As one approach, this influence may be reduced by modifying $\mathbf{A}$ such that its condition number will decrease. For example, the smallest singular values of $\mathbf{A}$ may be set to zero (Sec. 5.1). As an alternative approach, an appropriate additional constraint may be minimized along with the misfit to the data. For the least squares problem, this will result in minimizing

$$\Phi_{DLS} = \Phi_{LS} + \lambda\Phi_R = \|\mathbf{D}\mathbf{m} - \mathbf{d}\|_2^2 + \lambda \|\mathbf{R}\mathbf{m} - \mathbf{b}\|_2^2 \tag{5.27}$$

11 For an unweighted least squares problem, $\mathbf{A} = (\mathbf{D}^T\mathbf{D})^{-1}\mathbf{D}^T$ (Eq. 5.9)

instead of Eq. 5.4. Here, the additional constraint is described by the regularization matrix $\mathbf{R}$ and the regularization vector $\mathbf{b}$. Besides, the regularization parameter λ determines the weight given to the regularization term $\Phi_R = \|\mathbf{Rm} - \mathbf{b}\|_2^2$. In analogy to the ordinary least squares solution (Eq. 5.4), the regularized (or damped) least squares solution can then be obtained by minimizing

$$\begin{aligned}\Phi_{\mathrm{DLS}} &= \left(\begin{bmatrix}\mathbf{D}\\ \sqrt{\lambda}\mathbf{R}\end{bmatrix}\mathbf{m} - \begin{bmatrix}\mathbf{d}\\ \sqrt{\lambda}\mathbf{b}\end{bmatrix}\right)^{\mathsf{T}}\left(\begin{bmatrix}\mathbf{D}\\ \sqrt{\lambda}\mathbf{R}\end{bmatrix}\mathbf{m} - \begin{bmatrix}\mathbf{d}\\ \sqrt{\lambda}\mathbf{b}\end{bmatrix}\right)\\ &=: (\tilde{\mathbf{D}}\mathbf{m} - \tilde{\mathbf{d}})^{\mathsf{T}}(\tilde{\mathbf{D}}\mathbf{m} - \tilde{\mathbf{d}}).\end{aligned} \tag{5.28}$$

Accordingly, the model parameters are obtained from (c.f. Eq. 5.9)

$$\mathbf{m} = (\tilde{\mathbf{D}}^{\mathsf{T}}\tilde{\mathbf{D}})^{-1}\tilde{\mathbf{D}}^{\mathsf{T}}\tilde{\mathbf{d}} \tag{5.29}$$

$$\begin{aligned}&= \left(\begin{bmatrix}\mathbf{D}^{\mathsf{T}} & \sqrt{\lambda}\mathbf{R}^{\mathsf{T}}\end{bmatrix}\begin{bmatrix}\mathbf{D}\\ \sqrt{\lambda}\mathbf{R}\end{bmatrix}\right)^{-1}\begin{bmatrix}\mathbf{D}^{\mathsf{T}} & \sqrt{\lambda}\mathbf{R}^{\mathsf{T}}\end{bmatrix}\begin{bmatrix}\mathbf{d}\\ \sqrt{\lambda}\mathbf{b}\end{bmatrix}\\ &= \left(\mathbf{D}^{\mathsf{T}}\mathbf{D} + \lambda\mathbf{R}^{\mathsf{T}}\mathbf{R}\right)^{-1}(\mathbf{D}^{\mathsf{T}}\mathbf{d} + \lambda\mathbf{R}^{\mathsf{T}}\mathbf{b})\\ &= \left(\mathbf{D}^{\mathsf{T}}\mathbf{D} + \lambda\mathbf{R}^{\mathsf{T}}\mathbf{R}\right)^{-1}\mathbf{D}^{\mathsf{T}}\mathbf{d} + \left(\mathbf{D}^{\mathsf{T}}\mathbf{D} + \lambda\mathbf{R}^{\mathsf{T}}\mathbf{R}\right)^{-1}\lambda\mathbf{R}^{\mathsf{T}}\mathbf{b}.\end{aligned} \tag{5.30}$$

Here, the regularization vector $\mathbf{b}$ introduces a constant summand which is independent of the data vector $\mathbf{d}$, and $\mathbf{b}$ is set to zero in many applications.

In principle, an arbitrary regularization matrix $\mathbf{R}$ can be used. Nevertheless, an appropriate choice for $\mathbf{R}$ should respect the physics of the problem. Further, the choice of the regularization parameter λ is based on a trade-off between model robustness and model resolution. In particular, increasing λ will usually result in a more robust model. At the same time, however, the resolution of the model parameters will decrease as the resolution matrix $\mathbf{Q}$ of the regularized solution is given by

$$\mathbf{Q} \overset{\mathbf{b}=0}{=} (\mathbf{D}^{\mathsf{T}}\mathbf{D} + \lambda\mathbf{R}^{\mathsf{T}}\mathbf{R})^{-1}\mathbf{D}^{\mathsf{T}}\mathbf{D} \neq \mathbf{I}. \tag{5.31}$$

5.6 GENERAL MEASURES OF MISFIT

The unregularized and weighted least-squares solution (Eq. 5.13) results in the model parameters of maximum likelihood only if the data noise is normally distributed [Aster et al., 2013, p27ff.]. However, the data may deviate from a normal distribution due to bad instrument readings or unmodelled events such as disturbances caused by the solar wind [Vennerstrom, 2011]. Then, data outliers will strongly increase the least squares sums of Eqs. 5.4 and 5.10, and the fit to the other data will worsen. In this case, a more robust measure of misfit should be used instead of the L2 norm of the

least-squares inversion.

With a general measure ρ of the residual vector $\mathbf{r}$ (Eq. 5.3), we seek to minimize

$$\phi_G(\mathbf{r}) = \sum_{i=1}^{m} \rho(\mathbf{r}_i) \tag{5.32}$$

[Farquharson and Oldenburg, 1998] by solving

$$\frac{\partial \phi_G(\mathbf{r})}{\partial \mathbf{m}_k} = \sum_{i=1}^{m} \rho'(\mathbf{r}_i) \frac{\partial \mathbf{r}_i}{\partial \mathbf{m}_k} \stackrel{!}{=} 0 \tag{5.33}$$

for the model parameters $\mathbf{m}$. Now, we use

$$\frac{\partial \mathbf{r}_i}{\partial \mathbf{m}_k} = \frac{\partial (\mathbf{d} - \mathbf{D}\mathbf{m})_i}{\partial \mathbf{m}_k} = -\frac{\partial (\sum_{j=1}^{n} \mathbf{D}_{ij}\mathbf{m}_j)}{\partial \mathbf{m}_k} = -\mathbf{D}_{ik} \tag{5.34}$$

and introduce the general misfit matrix $(\mathbf{M})_{ii} = \rho'(\mathbf{r}_i)/\mathbf{r}_i$ [Farquharson and Oldenburg, 1998]. Consequently, we can rewrite Eq. 5.33 as

$$\frac{\partial \phi_G(\mathbf{r})}{\partial \mathbf{m}} = -\mathbf{D}^T\mathbf{M}\mathbf{r} = -\mathbf{D}^T\mathbf{M}(\mathbf{d} - \mathbf{D}\mathbf{m}) \stackrel{!}{=} 0, \tag{5.35}$$

and it follows that

$$\mathbf{m} = (\mathbf{D}^T\mathbf{M}\mathbf{D})^{-1}\mathbf{D}^T\mathbf{M}\mathbf{d}. \tag{5.36}$$

Except for $\rho(\mathbf{r}_i) = \mathbf{r}_i^2$, Eq. 5.36 is a non-linear system of equations as the diagonal weighting matrix $\mathbf{M}$ depends on the residuals $\mathbf{r}$, and hence the model parameters $\mathbf{m}$. Therefore, Eq. 5.36 cannot be solved directly. Instead, the solution may be approximated using the iteratively reweighted least squares (IRLS) algorithm which has been proven to converge [Holland and Welsch, 1977; Farquharson and Oldenburg, 1998]. Within this scheme, a starting model $\mathbf{m}_0$ is obtained from the least-squares solution, i.e. with $\mathbf{M} = \mathbf{I}$ in Eq. 5.36. Then, an approximate solution of the model parameters $\mathbf{m}$ is iteratively calculated from

$$\mathbf{m}_{k+1} = (\mathbf{D}^T\mathbf{M}_k\mathbf{D})^{-1}\mathbf{D}^T\mathbf{M}_k\mathbf{d} \tag{5.37}$$

where

$$(\mathbf{M}_k)_{ii} = \rho'(\mathbf{r}_k)_i/(\mathbf{r}_k)_i \tag{5.38}$$

and $(\mathbf{r}_k)_i = \mathbf{d}_i - (\mathbf{D}\mathbf{m}_k)_i$. As an advantage of the IRLS algorithm, Eq. 5.37 can be solved with the usual least-squares inversion algorithms [Farquharson and Oldenburg, 1998].

The likelihood function $L(\mathbf{m}|\mathbf{d})$ describes the probability density function (PDF) for the model parameters $\mathbf{m}$ under the observation of the data vector $\mathbf{d}$. Now, we seek the weighting function ρ which maximizes $L(\mathbf{m}|\mathbf{d})$ for a given PDF of the data noise. In this derivation, we closely follow Aster et al. [2013, p. 27f.]. The likelihood function is equivalent to the joint PDF $f(\mathbf{d}|\mathbf{m})$ of observing the data $\mathbf{d}$ for a model with the model parameters $\mathbf{m}$. If the data are uncorrelated, the joint PDF $f(\mathbf{d}|\mathbf{m})$ can be written as

$$f(\mathbf{d}|\mathbf{m}) = \prod_{i=1}^{m} \Psi(\mathbf{d}_i, \mathbf{m}) \tag{5.39}$$

where the PDF of each data point is given by $\Psi(\mathbf{r}_i) = \Psi(\mathbf{d}_i - (\mathbf{Dm})_i)$. Instead of maximizing $f(\mathbf{d}|\mathbf{m})$ and $L(\mathbf{m}|\mathbf{d})$, we may equally minimize

$$-\sum_{i=1}^{m} \ln \psi(\mathbf{d}_i, \mathbf{m}) \tag{5.40}$$

as the negative of the natural logarithm ($-\ln(x)$) is a monotonically decreasing function with $\ln(x) \geqslant 0 \; \forall \; \{x|0 < x \leqslant 1\}$. By comparing Eqs. 5.32 and 5.40, we conclude that the maximum likelihood function is obtained when the data noise is distributed according to

$$\Psi(\mathbf{d}, \mathbf{m}) = Ce^{-\rho(\mathbf{d}-\mathbf{Dm})}. \tag{5.41}$$

Here, a constant normalization factor $C > 0$ has been added without changing the model parameters $\mathbf{m}$ which minimize Eq. 5.40.

EXAMPLE As one example, we consider normally distributed data noise with $\sigma_i = 1$, i.e.

$$\Psi(\mathbf{d}_i, \mathbf{m}) = \frac{1}{\sqrt{2\pi}} e^{-\frac{1}{2}(\mathbf{d}_i - (\mathbf{Dm})_i)^2}. \tag{5.42}$$

According to Eq. 5.41, the measure ρ of the misfit is then given by $\rho(\mathbf{r}_i) = 1/2\mathbf{r}_i^2$, and the objective function

$$\Phi_G = \frac{1}{2} \sum_{i=1}^{m} \mathbf{r}_i^2 \tag{5.43}$$

will be minimized. Now, we may ignore the constant factor of $1/2$, and the obtained objective function then corresponds to the objective function of the least squares problem (Eq. 5.4). Hence, the least-squares solution is the maximum likelihood solution under normally distributed data noise [Aster et al., 2013, p27ff.].

6 INVERSION OF MAG DATA

In this work, Mars Global Surveyor (MGS) satellite magnetic field data is inverted for a model of the Martian crustal magnetic field. This model is expressed as an expansion of SH functions which will be described here. Also, various techniques will be presented which we applied in order to obtain a reliable and well-resolved model. These techniques include a joint inversion of internal and external fields, a regularization scheme which allows for sharp field gradients, and a measure of misfit which appropriately treats data outliers.

In Fig. 6.1, the individual steps for deriving the final model of the crustal magnetic field are schematically illustrated. The red part of this figure refers to the used data set and the applied data selection criteria (c.f. Ch. 4). The remaining part of Fig. 6.1 should be read from top to bottom and describes a number of preliminary models (gray trapezoids) which each contain all of the features of their predecessors. These preliminary models have been calculated either to obtain statistical values of the residuals (Eq. 5.3), or to investigate basic model parameters whenever the usage of the final model would have consumed considerably more computational power without significantly changing the results. An example for the former is the determination of the aerobraking phase (AB)/science phase orbit (SPO) data weights (W model, dark blue box), whereas the determination of the damping parameter (L2 model, orange box) and maximum SH degree ($\text{ABSPO}_{\text{Lint}}$ models, light blue box) are examples of the latter.

6.1 MODEL DESCRIPTION: SPHERICAL HARMONICS

In a region Ω without currents and without temporally changing electric fields, it follows from Ampère's law ($\nabla \times \mathbf{B} = 0$) and Stoke's theorem[1] that

$$\oint_S \mathbf{B} \cdot \mathbf{ds} = 0 \tag{6.1}$$

where S is the surface of Ω and $\mathbf{B}$ is the magnetic induction field[2]. As a consequence, the magnetic induction field $\mathbf{B}$ is conservative within the region Ω. Hence, this field can be expressed as the gradient of a scalar potential V by [Blakely, 1995, p. 2ff.]

$$\mathbf{B} = -\nabla V. \tag{6.2}$$

1 For a surface S, a vector field $\mathbf{F}$ and the normal vector $\hat{\mathbf{n}}_S$, Stoke's theorem implies that $\int_S (\boldsymbol{\nabla} \times \mathbf{F}) \cdot \hat{\mathbf{n}}_S \, dS = \oint_S \mathbf{F} \cdot \mathbf{ds}$.

2 The magnetic induction field $\mathbf{B}$ results from microscopic and macroscopic currents $\mathbf{j}$.

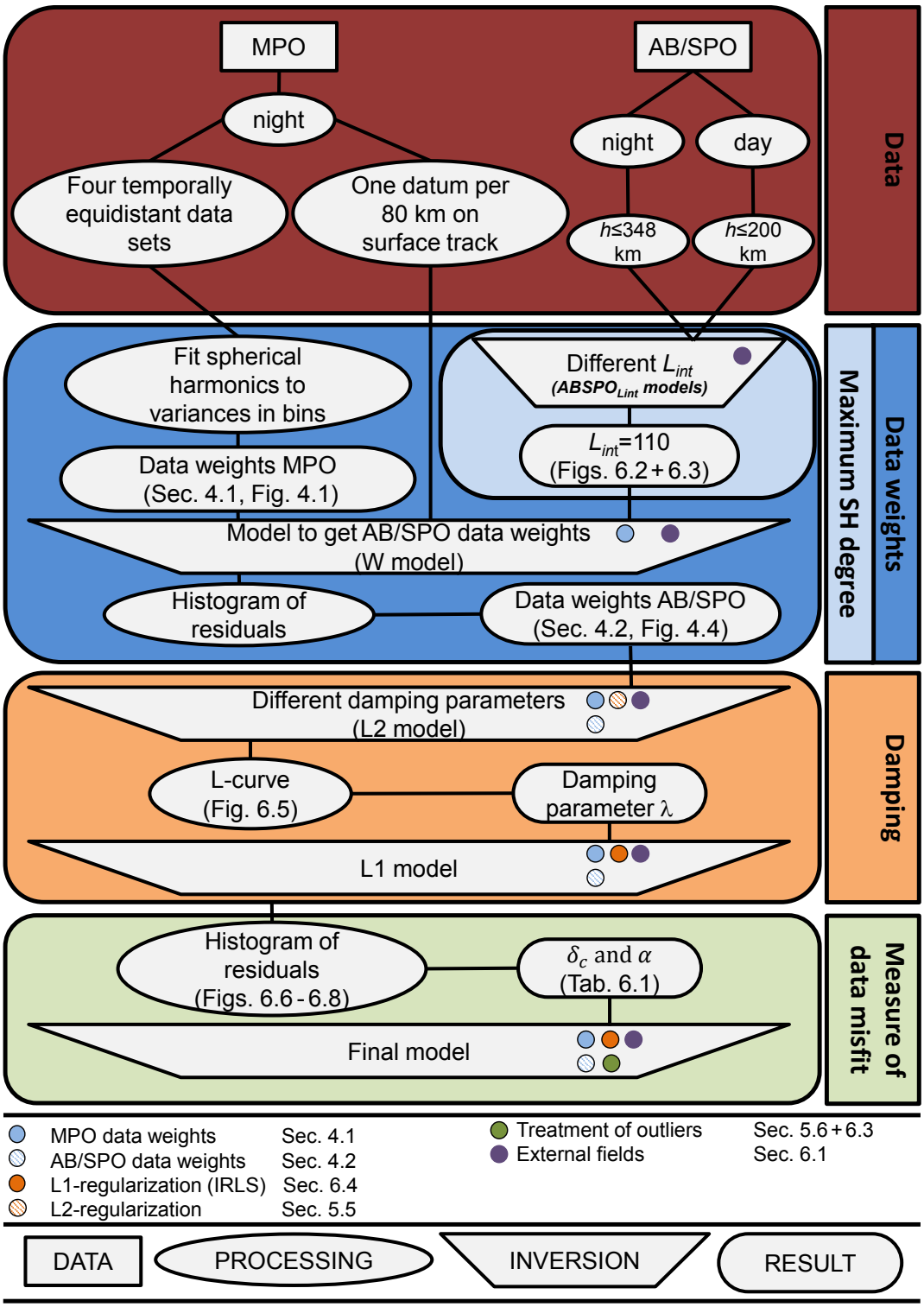

Figure 6.1. A schematic illustration is shown for the steps involved in deriving the presented model of the crustal magnetic field of Mars. A description of the meaning of the symbols is given in the lowest part of the figure. The altitude above the mean radius of Mars is given by h, and L_{int} is the internal maximum degree and order of the SH expansion. The figure should be read from top to bottom and subsequent models (gray trapezoids) contain all of the features of their predecessors. The red area illustrates the initial data selection as described in Ch. 4. The blue area describes the selection of data weights (dark blue) and the maximum SH degree (light blue). The orange area shows how the damping parameter λ is determined, leading to the L2 model ($\mathbf{g}_{0,0}$, Eq. 6.32) and the L1 model ($\mathbf{g}_{0,10}$, Eq. 6.31). Finally, the green area describes the introduction of an appropriate norm for treating data outliers which ultimately leads to the final model ($\mathbf{g}_{2,10}$, Eq. 6.31).

As no magnetic monopoles exist, i.e. $\nabla \cdot \mathbf{B} = 0$, the magnetic scalar potential V obeys Laplace's equation

$$\nabla \cdot \mathbf{B} = \Delta V = 0. \tag{6.3}$$

What is more, the magnetic scalar potential is a harmonic function[3].

Mars is well approximated by a spherical surface, and we express Eq. 6.3 in spherical coordinates (r, θ, ϕ), i.e.

$$\Delta V = \frac{1}{r^2}\left[\frac{\partial}{\partial r}\left(r^2\frac{\partial V}{\partial r}\right) + \frac{1}{\sin\theta}\frac{\partial}{\partial\theta}\left(\sin\theta\frac{\partial V}{\partial\theta}\right) + \frac{1}{\sin^2\theta}\frac{\partial^2 V}{\partial\phi^2}\right] = 0. \tag{6.4}$$

This equation is homogeneous and can be separated into three functions by $V(r, \theta, \phi) = R(r)\Theta(\theta)\Phi(\phi)$. As a result, we obtain

$$r^2\frac{d^2R}{dr^2} + 2r\frac{dR}{dr} - \lambda R = 0, \tag{6.5}$$

$$\frac{1}{\sin\theta}\frac{d}{d\theta}\left(\sin\theta\frac{d\Theta}{d\theta}\right) + \lambda\Theta - \frac{m^2}{\sin^2\theta}\Theta = 0, \tag{6.6}$$

$$\frac{d^2\Phi}{d\phi} = -m^2\Phi. \tag{6.7}$$

Now, these equations can be solved individually: In Eq. 6.5, the n-th power of r is occurring with the n-th derivative of $R(r)$. Therefore, Eq. 6.5 is solved by $R(r) = Ar^l + Br^{-(l+1)}$ with $\lambda = l(l+1)$. Next, we apply the coordinate transformation $\mu = \cos\theta$ to Eq. 6.6. Then, this equation corresponds to the general Legendre equation[4], which is solved by the associated Legendre polynomials[5] P_l^m with $0 \leqslant m \leqslant l$. In consequence, Eq. 6.6 is solved by $\Theta(\theta) = P_l^m(\cos\theta)$. A general real solution to Eq. 6.7 is given by $\Phi(\phi) = C\cos m\phi + D\sin m\phi$. Moreover, as the wavelength of Φ must be given by 2π, it follows that m must be a positive integer number with $m \geqslant 0$. Overall, the solution to the Laplace equation in spherical coordinates (Eq. 6.4) is obtained by combining the separate solutions of Eqs. 6.5 - 6.7 which results

3 A harmonic function is a function that (a) satisfies Laplace's equation (Eq. 6.3), (b) has continuous, single-valued first derivatives, and (c) second derivatives [Blakely, 1995, p. 11].

4 With the coordinate transformation $\mu = \cos\theta$, it follows that $\frac{d}{d\theta} = \sin\theta\frac{d}{d\mu}$, and Eq. 6.6 transforms to the general Legendre equation: $\frac{d}{d\mu}\left((1-\mu^2)\frac{d\Theta}{d\mu}\right) + \lambda\Theta - \frac{m^2}{1-\mu^2}\Theta = (1-\mu^2)\frac{d^2\Theta(\mu)}{d\mu^2} - 2\mu\frac{d\Theta}{d\mu} + \left(l(l+1) - \frac{m^2}{1-\mu^2}\right)\Theta = 0$.

5 The associated Legendre Polynomials can be calculated from $P_l^m(x) = \frac{(-1)^m}{2^l l!}(1-x^2)^{m/2}\frac{d^{l+m}}{dx^{l+m}}(x^2-1)^l$.

in

$$\begin{aligned} V(r,\theta,\phi) = &\sum_{l=1}^{\infty}\sum_{m=0}^{l}\left[A_l r^l \left(C_{A,l,m}\cos m\phi + D_{A,l,m}\sin m\phi\right) P_l^m(\cos\theta)\right] + \\ &+\sum_{l=1}^{\infty}\sum_{m=0}^{l}\left[B_l r^{-l-1}\left(C_{B,l,m}\cos m\phi + D_{B,l,m}\sin m\phi\right) P_l^m(\cos\theta)\right] \\ &=: V_{ext}(r,\theta,\phi) + V_{int}(r,\theta,\phi). \end{aligned} \tag{6.8}$$

with the real coefficients $A_l, B_l, C_{A,l,m}, D_{A,l,m}, C_{B,l,m}, D_{B,l,m}$. What is more, V_{ext} and V_{int} are related to external and internal sources, respectively, as $\lim_{r\to 0} V_{ext}(r) = 0$ and $\lim_{r\to\infty} V_{int}(r) = 0$. Moreover, the term with $l = 0$ has been omitted, as it describes a magnetic monopole.

Usually, the angular contributions to Eq. 6.8 are referred to as real SH functions

$$Y_{lm}(\theta,\phi) = \begin{cases} \sin(|m|\,\phi) P_l^{|m|}(\cos\theta) & \text{, if } m < 0 \\ \cos(m\phi) P_l^m(\cos\theta) & \text{, if } m \geqslant 0 \end{cases} \tag{6.9}$$

where $-l \leqslant m \leqslant l$. In addition, the coefficients $\{C, D\}_{\{A,B\},l,m}$ are usually referred to as the internal and external Gauss coefficients g_l^m and h_l^m with

$$g_l^{m'} = \begin{cases} C_{B,l,m} & \text{, if } m' < 0 \\ D_{B,l,m} & \text{, if } m' \geqslant 0 \end{cases} \tag{6.10}$$

$$h_l^{m'} = \begin{cases} C_{A,l,m} & \text{, if } m' < 0 \\ D_{A,l,m} & \text{, if } m' \geqslant 0. \end{cases} \tag{6.11}$$

Moreover, the SH functions $Y_{lm}(\theta,\phi)$ form an orthogonal basis over the square-integrable functions. In particular, it is

$$\begin{aligned} \frac{1}{4\pi a^2}\int_{\Omega_a} Y_{lm} Y_{l'm'} d\Omega_a &= \begin{cases} 0 & \text{, if } l \neq l' \text{ or } m \neq m' \\ \frac{1}{2l+1} & \text{, if } l = l' \text{ and } m = m' \end{cases} \\ &= \frac{1}{2l+1}\delta_{ll'}\delta_{mm'} \end{aligned} \tag{6.12}$$

if Schmidt semi-normalized SH functions are used. Here, Ω_a is the surface of a sphere with radius a, $d\Omega_a = a^2 \sin\theta d\theta d\phi$ is the infinitesimal surface element of Ω_a in spherical coordinates, and δ is the Kronecker-Delta[6]. With

6 If $l = l'$, $\delta_{ll'} = 1$, else $\delta_{ll'} = 0$.

the help of Eqs. 6.9 - 6.12, we may now rewrite Eq. 6.8 as

$$V(r,\theta,\phi) = \sum_{l=1}^{\infty}\sum_{m=-l}^{l}\left[A_l r^l h_l^m Y_{lm} + B_l r^{-l-1} g_l^m Y_{lm}\right]. \tag{6.13}$$

Then, the Gauss coefficients can be determined from Eqs. 6.12 and 6.13 by

$$\begin{aligned}\int_{\Omega_a}\left\{\begin{array}{c} V_{ext} \\ V_{int}\end{array}\right\} Y_{lm}\,d\Omega_a &= \int_{\Omega_a}\left[\sum_{l'=1}^{\infty}\sum_{m'=-l'}^{l'}\left\{\begin{array}{c} A_{l'} r^{l'} h_{l'}^{m'} \\ B_{l'} r^{-l'-1} g_{l'}^{m'}\end{array}\right\} Y_{l'm'}\right] Y_{lm}\,d\Omega_a = \\ &= \frac{4\pi a^2}{2l+1}\left\{\begin{array}{c} A_l r^l h_l^m \\ B_l r^{-l-1} g_l^m\end{array}\right\} \\ \Rightarrow \left\{\begin{array}{c} h_l^m \\ g_l^m\end{array}\right\} &= \frac{2l+1}{4\pi}\left\{\begin{array}{c} \frac{1}{A_l a^2 r^l} \\ \frac{r^{l+1}}{B_l a^2}\end{array}\right\}\int_{\Omega_a}\left\{\begin{array}{c} V_{ext} \\ V_{int}\end{array}\right\} Y_{lm}\,d\Omega_a. \end{aligned} \tag{6.14}$$

Now, the remaining coefficients A_l, B_l can be chosen freely. In geomagnetism, the convention is to use

$$\begin{aligned} A_l &= 1/(a^{l-1}) \\ B_l &= a^{l+2} \end{aligned} \tag{6.15}$$

such that the Gauss coefficients g_l^m, h_l^m will have units of nT. With this choice, Eq. 6.13 reads as

$$V(r,\theta,\phi) = a\sum_{l=1}^{\infty}\left[\left(\frac{r}{a}\right)^l \sum_{m=-l}^{l} h_l^m Y_{lm} + \left(\frac{a}{r}\right)^{l+1}\sum_{m=-l}^{l} g_l^m Y_{lm}\right]. \tag{6.16}$$

In this study, we use observations of the components of the vector magnetic field **B** pointing horizontally north (X), east (Y), and vertically down (Z). According to Eqs. 6.2 and 6.16, these observables are related to the Gauss coefficients g_l^m, h_l^m (model parameters) by

$$\begin{aligned} X &= \frac{1}{r}\frac{\partial V}{\partial \theta} = \sum_{l=1}^{\infty}\sum_{m=-l}^{l}\left[\left(\frac{a}{r}\right)^{l+2} g_l^m + \left(\frac{r}{a}\right)^{l-1} h_l^m\right]\frac{\partial Y_{lm}}{\partial \theta} \\ Y &= -\frac{1}{r\sin\theta}\frac{\partial V}{\partial \phi} = -\frac{1}{\sin\theta}\sum_{l=1}^{\infty}\sum_{m=-l}^{l}\left[\left(\frac{a}{r}\right)^{l+2} g_l^m + \left(\frac{r}{a}\right)^{l-1} h_l^m\right]\frac{\partial Y_{lm}}{\partial \phi} \\ Z &= \frac{\partial V}{\partial r} = -\sum_{l=1}^{\infty}\sum_{m=-l}^{l}\left[(l+1)\left(\frac{a}{r}\right)^{l+2} g_l^m - l\left(\frac{r}{a}\right)^{l-1} h_l^m\right] Y_{lm}. \end{aligned} \tag{6.17}$$

In this work, we describe the Martian magnetic field at satellite altitude by a series of SH functions (Eq. 6.17). Also, we include the internal (V_{int}) and external (V_{ext}) contributions of the scalar magnetic potential V. These contributions can be separated if a large number of observations is available for all magnetic field vector components at a certain altitude (Gauss [1877], Blakely [1995, p155ff.], Olsen et al. [2010a]). With a reference radius of $a = 3393.5\,\mathrm{km}$, i.e. the average Martian radius, our model is hence described by the scalar potential

$$\begin{aligned} V(r,\theta,\phi,t) =& V_{int}(r,\theta,\phi) + V_{ext}(r,\theta,\phi,t) \\ =& a\sum_{l=1}^{L_{int}} \left(\frac{a}{r}\right)^{(l+1)} \sum_{m=-l}^{l} g_l^m Y_{lm}(\theta,\phi) \\ &+ a \begin{cases} \sum_{l=1}^{L_{ext,n}} \left(\frac{r}{a}\right)^l \sum_{m=-l}^{l} h_{l,n}^m Y_{lm}(\theta,\phi), & t \in t_{night} \\ \sum_{l=1}^{L_{ext,d}} \left(\frac{r}{a}\right)^l \sum_{m=-l}^{l} h_{l,d}^m Y_{lm}(\theta,\phi), & t \in t_{day}. \end{cases} \end{aligned} \tag{6.18}$$

Here, a different external potential is used for the day- and nightside as the characteristics of the respective external fields differ significantly [Olsen et al., 2010a]. Further, L_{int} and $L_{ext,\{d,n\}}$ are the maximum degree and order for the SH expansion of the internal and external day/night potentials, and g_l^m and $h_{l,\{d,n\}}^m$ are the respective internal and external day/night Gauss coefficients. Moreover, we assume a static internal potential V_{int} and ignore seasonal variations of the external potential V_{ext}. As a consequence, the respective Gauss coefficients (g_l^m and $h_{l,\{d,n\}}^m$) will be constant in this model. Furthermore, we use the standard spherical coordinate system for Mars as defined by the International Astronomical Union (IAU)[7]. Also, we denote the radial distance, colatitude and longitude by (r,θ,ϕ), respectively.

The external field as represented by V_{ext} accounts for non-crustal field contributions, i.e. sources outside of the MGS orbit. Such sources exist in all data sets including the mapping phase orbit (MPO) nightside data [Ferguson et al., 2005]. Indeed, the residuals between the MPO nightside data and a preliminary model which consisted of only the internal potential V_{int} were asymmetrically distributed. Therefore, we confirm that non-crustal field contributions must be present in the MPO nightside data. However, the MGS data is not sampling the entire magnetosphere due to the sun-synchronous MPO orbit. Hence, the model of the external magnetic field is not physically meaningful, but is rather absorbing various kinds of noise.

Now, I will turn to the choice of the maximum degree and order L of the different field contributions (Eq. 6.18). Regarding the external field contri-

7 According to IAU, the great circle through the center of the Airy-0 crater defines the zero meridian ($\phi = 0$) on Mars.

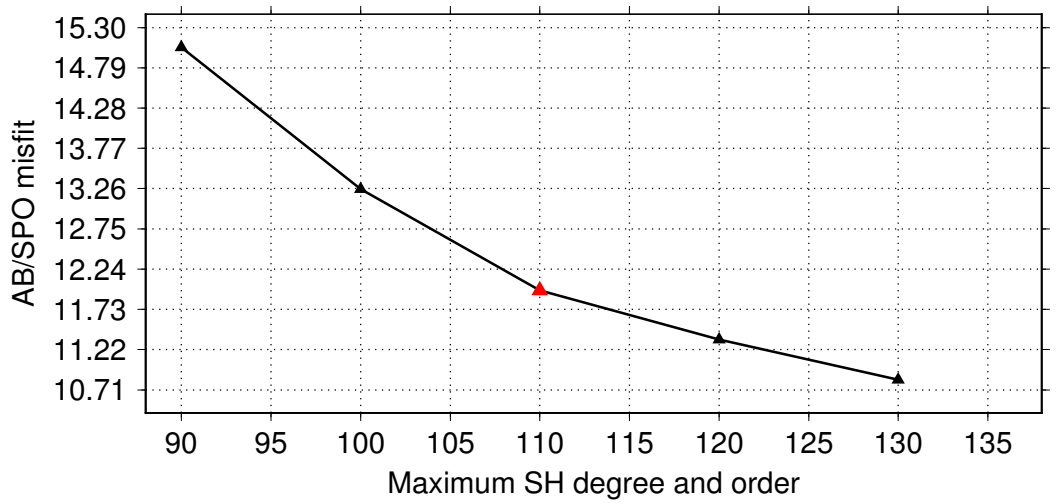

Figure 6.2. Comparison of the residuals to the AB/SPO data for the $\text{ABSPO}_{\text{Lint}}$ models with different maximum SH degree and order L_{int}.

butions, the maximum degree and order $L_{ext,\{d,n\}}$ should be relatively low for the following reasons: First, the static external fields are expected to be global in scale. Second, possible leakage of the crustal field signal into the model of the external field should be avoided. Third, the data coverage of the dayside data, which entirely consists of the AB/SPO data set, is relatively low (Sec. 4.2). For these reasons, $L_{ext,n} = 10$ and $L_{ext,d} = 5$ were chosen for models of the night- and dayside external magnetic field, respectively.
On the other hand, the maximum degree L_{int} of the internal field model should be as high as possible. In particular, the resulting model should reflect the strong field gradients in the AB/SPO data set. Previously, $L_{int} = 90$ was the maximum degree and order of all published models of the crustal magnetic field of Mars (Sec. 1.3). However, Cain et al. [2003] pointed out that $L_{int} = 90$ is not sufficient. Still, higher degree models would have resulted in erroneous fields in some areas due to the limited amount of data available at that time. As well, the signal to noise ratio decreases for contributions of higher SH degree and order. Alike, the computational effort increases with increasing maximum degree and order L. Here, we will will investigate the ability of field models with different L_{int} to fit the AB/SPO data. For this purpose, models with L_{int} ranging from 90 to 130 in increments of 10 were fit to the equally weighted AB/SPO data (c.f. $\text{ABSPO}_{\text{Lint}}$ models in Fig. 6.1). All these models were derived without regularization and without data weights (c.f. Eq. 5.9). Also, they all include an external field model up to degree and order 10, regardless of day- or nightside data. As shown in Fig. 6.2, the resulting standard deviations (STDs) of the residuals between these models and the AB/SPO data decrease more slowly for degrees and orders larger than $L_{int} = 110$ (red triangle in Fig. 6.2). In addition, an exemplary aerobraking track is shown by the black dashed line in

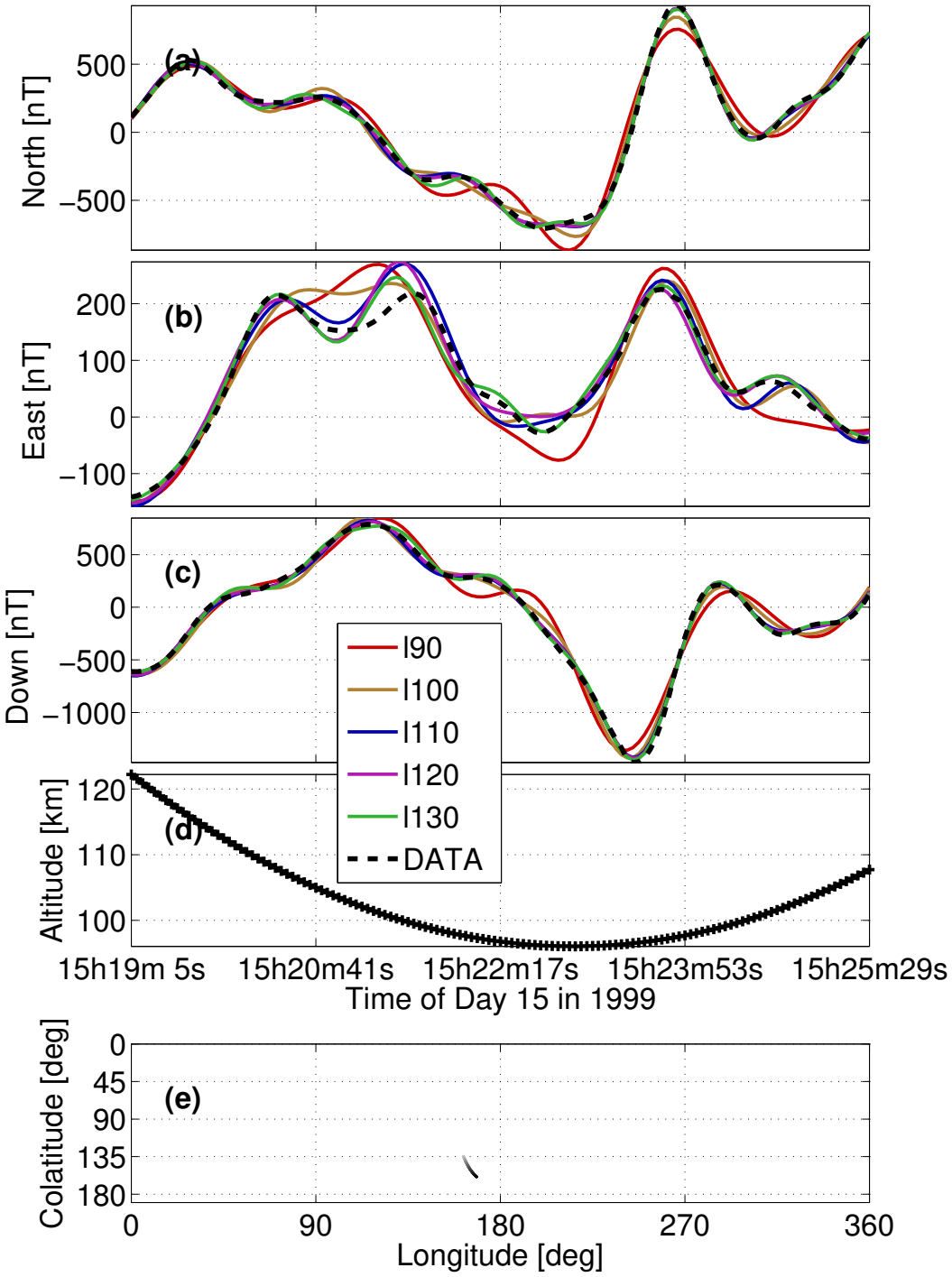

Figure 6.3. (a)-(c) Comparison of different models to the observed vector magnetic field components of a selected AB track. The models were expanded to different maximum SH degrees L_{int}. Further, they include an external field up to degree $L_{ext} = 10$. The models were fit only to the AB/SPO data with equal weighting and without regularization. (d) Altitude and (e) location of the selected AB track. Copyright 2014 by the American Geophysical Union, reprinted from Fig. 3 of Morschhauser et al. [2014] with kind permission from publisher John Wiley & Sons Ltd.

Fig. 6.3 along with the various models (solid lines). Clearly, the model with a maximum SH degree of $L_{int} = 90$ fails to sufficiently represent the data whereas the higher degree models with $L_{int} \geqslant 110$ perform almost equally well. In some cases, however, the fit to the data significantly increases with higher maximum SH degree (e.g., horizontally east (Y) component at around 15 h 20 m 41 s). Overall, we chose a maximum degree and order of $L_{int} = 110$ which corresponds to a spatial resolution of ~195 km at surface altitude. However, it is noted that a higher degree model will provide a better representation of some of the strong anomalies visible in the AB/SPO data.

6.2 DATA INVERSION

Within the limits of noise, we seek the set of Gauss coefficients $\mathbf{g} = [g_l^m, h_l^m]$ that results in the given vector magnetic field observations. According to Eqs. 6.18 and 6.2, the observed magnetic field vector can be expressed as a linear function of the Gauss coefficients. Then, the resulting equations may equally be written in matrix form (Eq. 5.1) as[8]

$$\mathbf{D}\mathbf{g} = \mathbf{d} \tag{6.19}$$

where $\mathbf{d} = (d_1, d_2, ..., d_n)^T$ is the data vector consisting of the $n \approx 2.87$ million data points (Ch. 4), $\mathbf{g}$ is the model vector corresponding to the $m = L_{int}(L_{int}+2) + L_{ext,d}(L_{ext,d}+2) + L_{ext,n}(L_{ext,n}+2) = 12475$ Gauss coefficients, and $\mathbf{D}$ is a $n \times m$ matrix describing the SH model as defined by Eqs. 6.18 and 6.2.

In this work, we will invert for the model parameters $\mathbf{g}$ by minimizing the residuals with a modified Huber norm (Sec. 6.3) in order to reduce the influence of data outliers. Further, we assume that noise in the data is normally distributed except for data outliers, and that data noise is uncorrelated. Therefore, the data covariance matrix $\mathrm{Cov}(\mathbf{d})$ is diagonal and contains the variances of the noise for each data point (Eq. 5.11). This approach may be an oversimplification, and one should in principle take the correlation between data noise into account (Eq. 5.13). However, this would result in a non-diagonal covariance matrix $\mathrm{Cov}(\mathbf{d})$ which cannot be handled easily even with modern computers.

6.3 MEASURE OF DATA MISFIT

Data outliers may negatively influence the result of a least-squares fit. One radical way to avoid their negative influence is to remove them a priori. However, it is difficult to decide which data points can be regarded as data outliers. Alternatively, one may relax the assumption of normally dis-

8 Previously, $\mathbf{m}$ was used for the general set of model parameters. From here on, we will use $\mathbf{g}$ when the Gauss coefficients g_l^m, h_l^m (Eq. 6.17) are used as model parameters.

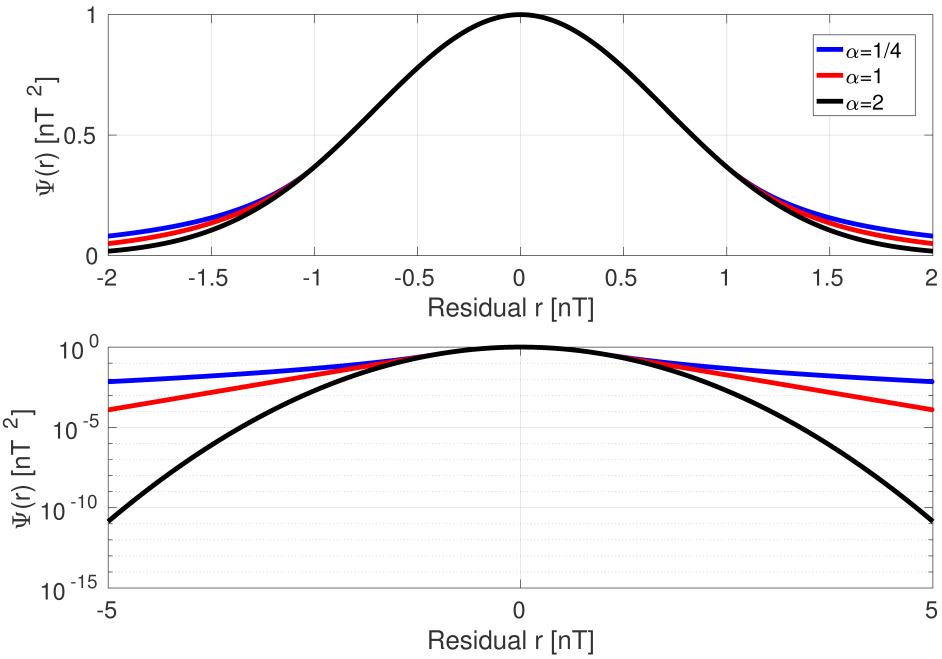

Figure 6.4. (a) PDF $L(x)$ for the expected data noise as specified by Eq. 6.20. Here, the misfit threshold is set to $\delta_c = 1$ and three different values for α were used (c.f. legend). For $\alpha = 2$, an ordinary normal distribution is obtained, for $\alpha = 1$, the distribution as suggested by Huber [1964] is obtained, and for $\alpha = 1/4$, an even wider distribution is obtained. (b) Same as (a), but for $\log \Psi(x)$.

tributed data noise (Sec. 5.6). Here, we introduce a threshold misfit value δ_c to distinguish between a normally distributed part of the data noise and a part which is more compatible with data outliers [Lesur et al., 2015]. Then, the corresponding unnormalized probability density function (PDF) for the expected data noise is given by

$$\Psi(r_i) = \begin{cases} \exp\left(-r_i^2\right) & , |r_i| \leqslant \delta_c \\ \exp\left(\frac{-2|r_i|^\alpha \delta_c^{(2-\alpha)}}{\alpha} + \frac{(2-\alpha)\delta_c^2}{\alpha}\right) & , |r_i| > \delta_c \end{cases} \tag{6.20}$$

where $\mathbf{r}$ is the weighted misfit vector. Further, α determines the shape of the distribution such that lower values of α will allow for a larger tail. In particular, for $\alpha = 2$, $\Psi(r_i)$ represents the normal distribution, and for $\alpha = 1$, $\Psi(r_i)$ represents the PDF as originally suggested by Huber [1964] (Fig. 6.4). Finally, we compare Eq. 6.20 to Eqs. 5.32 and 5.41 and find that

$$\rho_D(r_i) = \begin{cases} r_i^2 & , |r_i| \leqslant \delta_c \\ \left(\frac{2|r_i|^\alpha \delta_c^{(2-\alpha)}}{\alpha} - \frac{(2-\alpha)\delta_c^2}{\alpha}\right) & , |r_i| > \delta_c. \end{cases} \tag{6.21}$$

Further, we weight the data with the weighting matrix $\boldsymbol{W}_d$ (Sec. 5.2) which is diagonal and calculated from

$$(\boldsymbol{W}_d)_{ii} = (\sqrt{\rho_i}\sigma_i)^{-1}. \tag{6.22}$$

Here, $(.)_{ii}$ is the i-th diagonal element of the respective matrix, σ_i are the STDs of the data as described in Sec. 4, and ρ_i are the respective data densities [Schmitz and Cain, 1983][9]. We evaluate the data density on a grid with $\Delta\theta = 0.5^\circ$ and $\Delta\phi = \Delta\theta/\sin(\theta_c)$, where θ_c is the colatitude at the center of the respective bin (Eq. 4.1). Now, we use an iteratively reweighted least squares (IRLS) algorithm to approach the modified Huber norm (Eq. 6.21) and iteratively minimize

$$\Phi_{D,k} = (\mathbf{d} - \mathbf{D}\mathbf{g})^T \boldsymbol{W}_d^T \boldsymbol{M}_{d,k} \boldsymbol{W}_d (\mathbf{d} - \mathbf{D}\mathbf{g}) \tag{6.23}$$

where the misfit matrix $\boldsymbol{M}_{d,k}$ is obtained by comparing Eq. 6.21 to Eq. 5.38,i.e.

$$(\boldsymbol{M}_{d,k})_{ii} = \begin{cases} 1 & , |\mathbf{r}_{i,k}| \leqslant \delta_c \\ (\delta_c/|\mathbf{r}_{i,k}|)^{2-\alpha} & , |\mathbf{r}_{i,k}| > \delta_c. \end{cases} \tag{6.24}$$

Here, $\boldsymbol{M}_{d,k}$ is diagonal and the weighted residuals $\mathbf{r}_i$ are given by $\mathbf{r}_i = (\boldsymbol{W}_d(\mathbf{d} - \mathbf{D}\mathbf{g}_k))_i$. In conclusion, the Gauss coefficients $\mathbf{g}$ will then be obtained by iteratively solving (c.f. Eq. 5.37)

$$\mathbf{g}_{k+1} = \left(\mathbf{D}^T \boldsymbol{W}_d^T \boldsymbol{M}_{d,k} \boldsymbol{W}_d \mathbf{D}\right)^{-1} \mathbf{D}^T \boldsymbol{W}_d^T \boldsymbol{M}_{d,k} \boldsymbol{W}_d \mathbf{d}. \tag{6.25}$$

6.4 L1-REGULARIZATION

Depending on its spatial wavelength, the internal part of the magnetic induction field $\mathbf{B}$ decreases with increasing altitude r. In particular, the intensity of a component of SH degree l is proportional to $r^{-(l+2)}$ (Eq. 6.17). As a result, the intensity of crustal magnetic fields with short spatial wavelengths can fall below the noise level at orbit altitude. In this case, a significant part of the noise might leak into the model of the crustal field, especially for high SH degrees l. Consequently, unrealistically intense global magnetic features of short wavelengths will appear when the model is downward-continued to the planetary surface. Therefore, it has been argued that internal field models should be truncated accordingly [Arkani-Hamed, 2002b, 2004a].

9 Schmitz and Cain [1983] investigated the influence of spatially inhomogeneous data sampling on the resulting model parameter covariance matrix $\mathrm{Cov}(\mathbf{m})$ (Eq. 5.15). In their study, they showed that correlations between model parameters can be minimized by choosing $(\boldsymbol{W}_d)_{ii} = (\sqrt{\rho_i}\sigma_i)^{-1}$.

Still, information on smaller wavelengths can be resolved at least locally if the model is properly regularized. For example, some measure of the resulting model complexity could be minimized along with the data misfit [Parker, 1994; Aster et al., 2013]. The exact choice of this measure is an a priori constraint on the model. In this work, we chose to minimize the roughness of the surface field. Accordingly, an approximation of the surface integral of the absolute horizontal gradient of the vertically down component of the crustal field $|\nabla_H Z_{int}|$ (c.f. Eq. 6.28) is used as a measure for model complexity.

Moreover, an IRLS algorithm has been used to approximate an L1 norm minimization of model complexity (Sec. 5.6 and Farquharson and Oldenburg [1998]). Such a choice implies that $|\nabla_H Z_{int}|$ is expected to follow a Laplacian distribution[10] over the Martian surface (Sec. 5.6). In other words, the L1 norm regularization places a weaker constraint on strong localized gradients when compared to the quadratic measure of an L2 norm. For this reason, strong gradients of the crustal field, as they have been identified in the AB/SPO dataset, will be preserved in the model if the regularization is applied in physical space[11].

Along with an IRLS algorithm, the analytic solution to $|\nabla_H Z_{int}|$ cannot be used. Instead, $\mathbf{Z}_{int} = -\partial V_{int}/\partial r$ is first calculated on a discrete hexagonal grid[12] on the mean planetary surface with a radius of 3393.5 km. Subsequently, the horizontal gradient was calculated by using finite differences in the $\boldsymbol{e}_\phi$ and $\boldsymbol{e}_\theta$ directions and by using Eq. 6.17. The resolution of the discrete grid has been chosen such that there are at least twice as many grid points as model parameters, and 81920 grid points have been used. Formally, the entire operation of calculating $\nabla_H Z_{int}$ can then be described by the linear operator $\mathbf{R}$, such that

$$[\nabla_H Z_{int}]_{\{i\}} = \mathbf{R}\mathbf{g} \tag{6.26}$$

where $[\nabla_H Z_{int}]_{\{i\}}$ is the set of horizontal gradients evaluated at each of the grid points i. Further, $\mathbf{R}$ operates on the internal field coefficients $\mathbf{g}_{int} \subset \mathbf{g}$ only, the diagonal weighting matrix $(\boldsymbol{W}_r)_{ii} = \sqrt{s_i/(4\pi a^2)}$ is introduced to account for the surface areas s_i of each grid point i. Then, the diagonal misfit matrix (c.f. Eq. 5.38)

$$(\boldsymbol{M}_r)_{ii} = \frac{1}{|\mathbf{r}_i|} = \frac{1}{|(\boldsymbol{W}_r \mathbf{R}\mathbf{g})_i|} \tag{6.27}$$

10 The general Laplacian PDF with mean μ and variance $\sigma = 2b^2$ is given by $\Psi(x) = 1/(2b)\exp(-|x-\mu|/b)$.

11 One could also apply the regularization directly on the Gauss coefficients, but this would rather influence the distribution of the resulting Gauss coefficients.

12 Such a grid results in a homogeneous sampling of the crustal field.

is used to regularize the model by approaching an L1 norm with an IRLS algorithm. Overall, the model is regularized by iteratively minimizing

$$\Phi_{R,k} = \mathbf{g}_k^T \mathbf{R}_k^T \mathbf{W}_r^T \mathbf{M}_{r,k} \mathbf{W}_r \mathbf{R}_k \mathbf{g}_k \tag{6.28}$$

in order to approach the minimization of

$$\Phi_R = \frac{1}{4\pi a^2} \int_{\Omega_a} |\nabla_H Z_{int}(a, \theta, \phi)| \, dS_a \approx \sum_i |\nabla_H Z_{int}(a, \theta, \phi)| \, s_i. \tag{6.29}$$

6.5 SUMMARY

In summary, the minimization of Eq. 6.23 (Φ_D) and the minimization of Eq. 6.28 (Φ_R) will be combined such that (c.f. Eq. 5.27)

$$\begin{aligned} \Phi_{k+1,l+1} &= \Phi_{D,k} + \lambda_{k,l} \Phi_{R,l} \\ &= \left[\left(\mathbf{d} - \mathbf{D}\mathbf{g}_{k,l} \right)^T \mathbf{W}_d^T \mathbf{M}_{d,k} \mathbf{W}_d \left(\mathbf{d} - \mathbf{D}\mathbf{g}_{k,l} \right) \right] + \\ &\quad \lambda_{k,l} \left[\mathbf{g}_{k,l}^T \mathbf{R}_l^T \mathbf{W}_r^T \mathbf{M}_{r,l} \mathbf{W}_r \mathbf{R}_l \mathbf{g}_{k,l} \right] \end{aligned} \tag{6.30}$$

where (k, l) refer to the iteration numbers of the IRLS algorithm for the data- and regularization part, respectively (see next page). Then, the Gauss coefficients $\mathbf{g}$ of the final model are obtained by iteratively solving (c.f. Eq. 5.29)

$$\begin{aligned} \mathbf{g}_{k+1,l+1} = &\left(\mathbf{D}^T \mathbf{W}_d^T \mathbf{M}_{d,k} \mathbf{W}_d \mathbf{D} + \lambda_{k,l} \mathbf{R}_l^T \mathbf{W}_r^T \mathbf{M}_{r,l} \mathbf{W}_r \mathbf{R}_l \right)^{-1} \\ &\mathbf{D}^T \mathbf{W}_d^T \mathbf{M}_{d,k} \mathbf{W}_d \mathbf{d} \end{aligned} \tag{6.31}$$

using QR-factorization[13]. Here, the starting model $\mathbf{g}_{0,0}$ was obtained from an unregularized least-squares inversion (L2 model in Fig. 6.1), i.e.

$$\mathbf{g}_{0,0} = \left(\mathbf{D}^T \mathbf{W}_d^T \mathbf{W}_d \mathbf{D} \right)^{-1} \mathbf{D}^T \mathbf{W}_d^T \mathbf{W}_d \mathbf{d}. \tag{6.32}$$

In addition, the damping parameter was adapted with each iteration such that

$$\frac{\Phi_{D,0}}{\Phi_{R,0}} = \frac{\Phi_{D,k}}{\Phi_{R,l}} \Rightarrow \lambda_{k,l} = \lambda_{0,0} \frac{\Phi_{R,0}}{\Phi_{R,l}} \frac{\Phi_{D,k}}{\Phi_{D,0}}. \tag{6.33}$$

(c.f. Eq. 6.30). As it is computationally expensive to use the IRLS algorithm both in the data- and regularization term of Eq. 6.31, these terms were iterated separately (iteration numbers k and l in Eq. 6.31, respectively). As

13 Any invertible matrix $\mathbf{A}$ has a unique factorization $\mathbf{A} = \mathbf{QR}$, where $\mathbf{Q}$ is orthogonal ($\mathbf{Q}^{-1} = \mathbf{Q}^T$), and $\mathbf{R}$ is upper-triangular. The linear system of equations $\mathbf{Ag} = \mathbf{d}$ can then be transformed to $\mathbf{Rg} = \mathbf{Q}^T\mathbf{d}$ which is easily solved as $\mathbf{R}$ is in upper-triangular form.

well, a series of simpler models (c.f. Fig. 6.1) was used to derive the following model parameters: The maximum SH degree and order L_{int} for the internal model (c.f. p. 68 in Sec. 6.1 and $ABSPO_{Lint}$ models in Fig. 6.1), the data weights for the AB/SPO data set (c.f. Sec. 4.2 and W model in Fig. 6.1) and the damping parameter $\lambda_{0,0}$ (see below and L2 model in Fig. 6.1).

The damping parameter $\lambda_{k,l}$ controls the trade-off between model smoothness and fit to the data (Sec. 5.5). A good compromise can be obtained from the so-called L-curve, which is shown in Fig. 6.5. In dependence of the damping parameter $\lambda_{0,0}$ (gray boxes), the L-curve visually compares the measure of model complexity (Eq. 6.29) to the weighted misfit between the data and the model at satellite altitude. In Fig. 6.5, the measure of model complexity is normalized by $4\pi R_p^2$, the weighted misfit to the MPO data is shown by a solid line and triangles, and the weighted misfit to the AB/SPO daytime is shown by a dashed line and circles. Depending on the damping parameter $\lambda_{0,0}$, two regimes can be distinguished in Fig. 6.5: For $\lambda_{0,0} > 1000$, the measure of model complexity remains almost constant while the misfit to the data significantly increases with increasing damping parameter $\lambda_{0,0}$. On the other hand, for $\lambda_{0,0} < 1$, the data misfit remains almost constant while the measure of model complexity increases with decreasing damping parameter. In this regime, field anomalies of the model that are poorly supported by the data will be more and more suppressed with increasing damping parameter. For the MPO data (solid line), the data misfit remains almost constant even for stronger damping up to $\lambda_{0,0} = 100$, as also observed by Whaler and Purucker [2005]. This observation may be explained by the weaker sensitivity of the high-altitude MPO data to small-scale crustal fields. In addition, the MPO data contains less noise than the AB/SPO dayside data. As we seek a model which reasonably fits the data without overfitting noise, a damping parameter in the range $1 \leqslant \lambda \leqslant 1000$ (shown in blue in Fig. 6.5) is considered feasible. Here, we choose $\lambda_{0,0} = 2$, as the IRLS approximation of an absolute measure (L1 norm) of model complexity (Eq. 6.28) will suppress noise more efficiently than the least squares measure (L2 norm), which was used to determine $\lambda_{0,0}$. Still, the exact value of the chosen damping parameter sensitively influences the details of the resulting model (Sec. 9.1).

Starting from $\mathbf{g}_{0,0}$, the models $\{\mathbf{g}_{0,1}, ..., \mathbf{g}_{0,10}\}$ were calculated, i.e. the model was regularized by approximating an L1 norm with ten iterations. In the following, we will refer to the model with the coefficients $\mathbf{g}_{0,10}$ as the L1 model (Fig. 6.1). Further, the model with the coefficients $\mathbf{g}_{0,0}$ will be referred to as the L2 model. Finally, the parameters δ_c and α of the misfit matrix $\mathbf{M}_{d,k}$ (Eq. 6.24) were chosen such that the associated distribution of noise in the data (Eq. 6.20) is a suitable representation of the resulting distribution of the residuals between the data and the L1 model. The corresponding histograms of the weighted residuals to the MPO, the AB/SPO dayside, and the AB/SPO nightside data are indicated by a blue line in Figs. 6.6 - 6.8, respectively. Along with these, the associated Gaussian distributions are

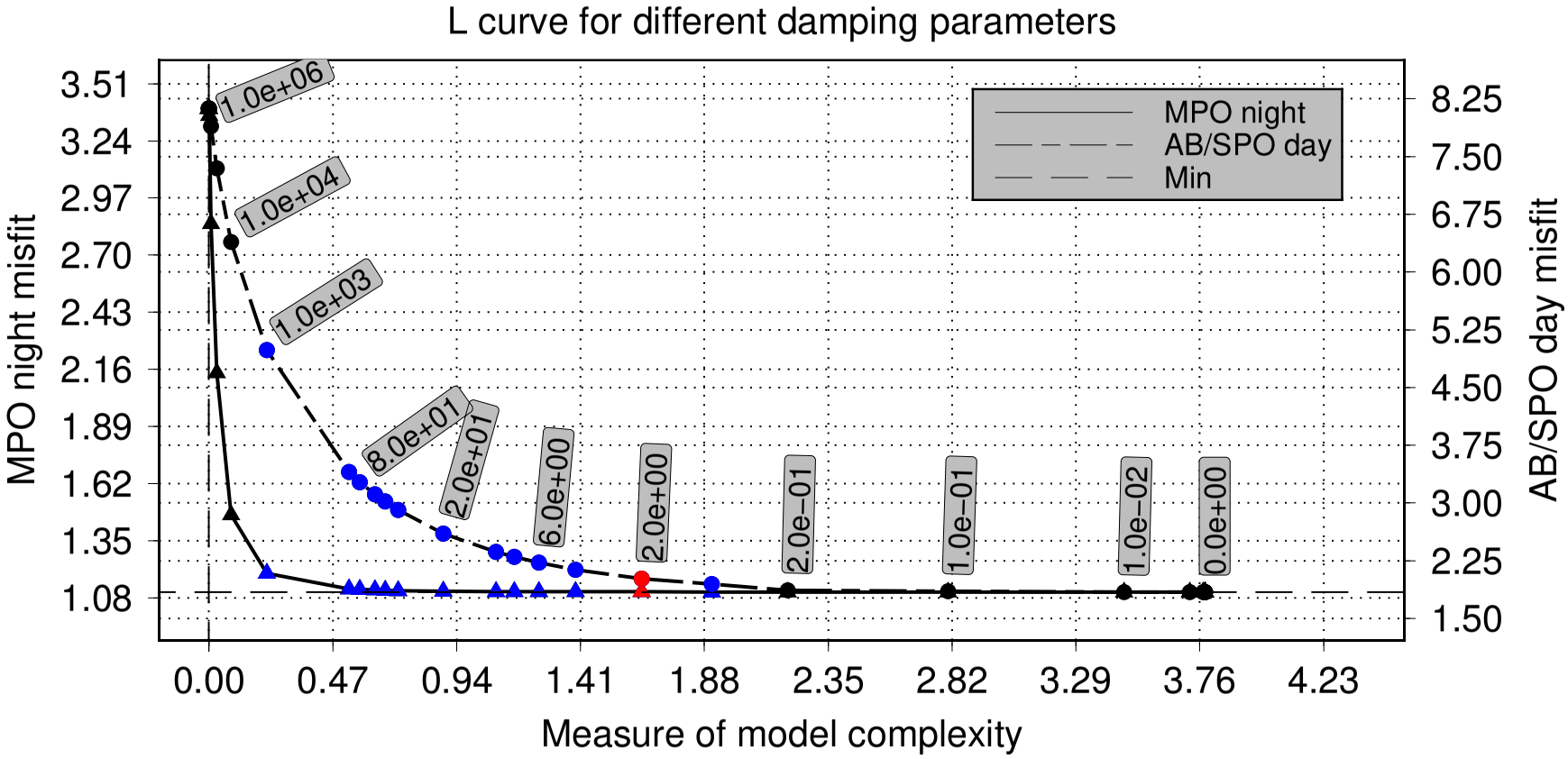

Figure 6.5. The weighted data misfit for MPO data (left ordinate, solid line and triangles) and AB/SPO data (right ordinate, dashed line and circles) is shown in dependency of the chosen measure of model complexity (normalized by $4\pi R_p^2$) for different damping parameters $\lambda_{0,0}$, as indicated by the gray boxes. Very large damping parameters (> 1000) significantly increase the misfit to the data without strongly reducing the model complexity. On the other side, small damping parameters (< 1) increase the model complexity without significantly improving the data misfit. Therefore, admissible damping parameters (shown in blue) are located near the bend of the L-shaped curve. Among these, the selected damping parameter ($\lambda_{0,0} = 2$) is shown in red.

Table 6.1. Adopted values for the parameters δ_c and α for the treatment of data outliers (Eq. 6.20)[a].

DATA SET	COMPONENT	δ_c	α
MPO	X	2.0	0.1
night	Y	2.0	0.1
(Δ_d=80 km)	Z	2.2	0.1
AB/SPO	X	1.0	2.0
day	Y	1.0	2.0
($h \leqslant 200$ km)	Z	1.0	2.0
AB/SPO	X	1.0	2.0
night	Y	1.0	2.0
($h \leqslant 348$ km)	Z	1.0	2.0

[a] The respective values were determined from a fit to the residual histogram of the model $\mathbf{g}_{0,10}$, i.e. the L1 model in Fig. 6.1 (Figs. 6.6 - 6.8). In the column labeled 'Data set', h is altitude and Δ_d is the distance between subsequent data points as measured on the satellite's projected surface track (Ch. 4). Moreover, the horizontally north (X), east (Y), and vertically down (Z) components are denoted with their respective letters.

shown in red, the chosen cut-off values δ_c (Tab. 6.1) by the squares on the ordinates, and the distributions for the treatment of the data outliers (c.f. Eq. 6.20) are shown in black, respectively. In addition, the linear plot on the right-hand side of each of these figures focuses on the normally distributed part of the data (red line), whereas the logarithmic plot on the left-hand side focuses on the tails of the distribution (black line). Clearly, the resulting distribution of the residuals deviates from a Gaussian distribution for large values of misfit. For the MPO data, the chosen values for δ_c and α (Tab. 6.1) result in a PDF which is well supported by the data (Fig. 6.6). For the AB/SPO data, on the other hand, a Gaussian distribution was chosen which is not compatible with the large non-Gaussian tails of the residual distribution (Figs. 6.7 and 6.8). The reason is that a significant part of the larger residuals of the AB/SPO data is due to an insufficient maximum SH degree and order. Hence, the application of a modified Huber norm would result in a worse fit of the strong field gradients which are present in the AB/SPO data.

Finally, two further iterations were made with the adopted values for δ_c and α (Tab. 6.1), and the final model (green box in Fig. 6.1) corresponds to the Gauss coefficients $\mathbf{g}_{2,12}$ of Eq. 6.31.

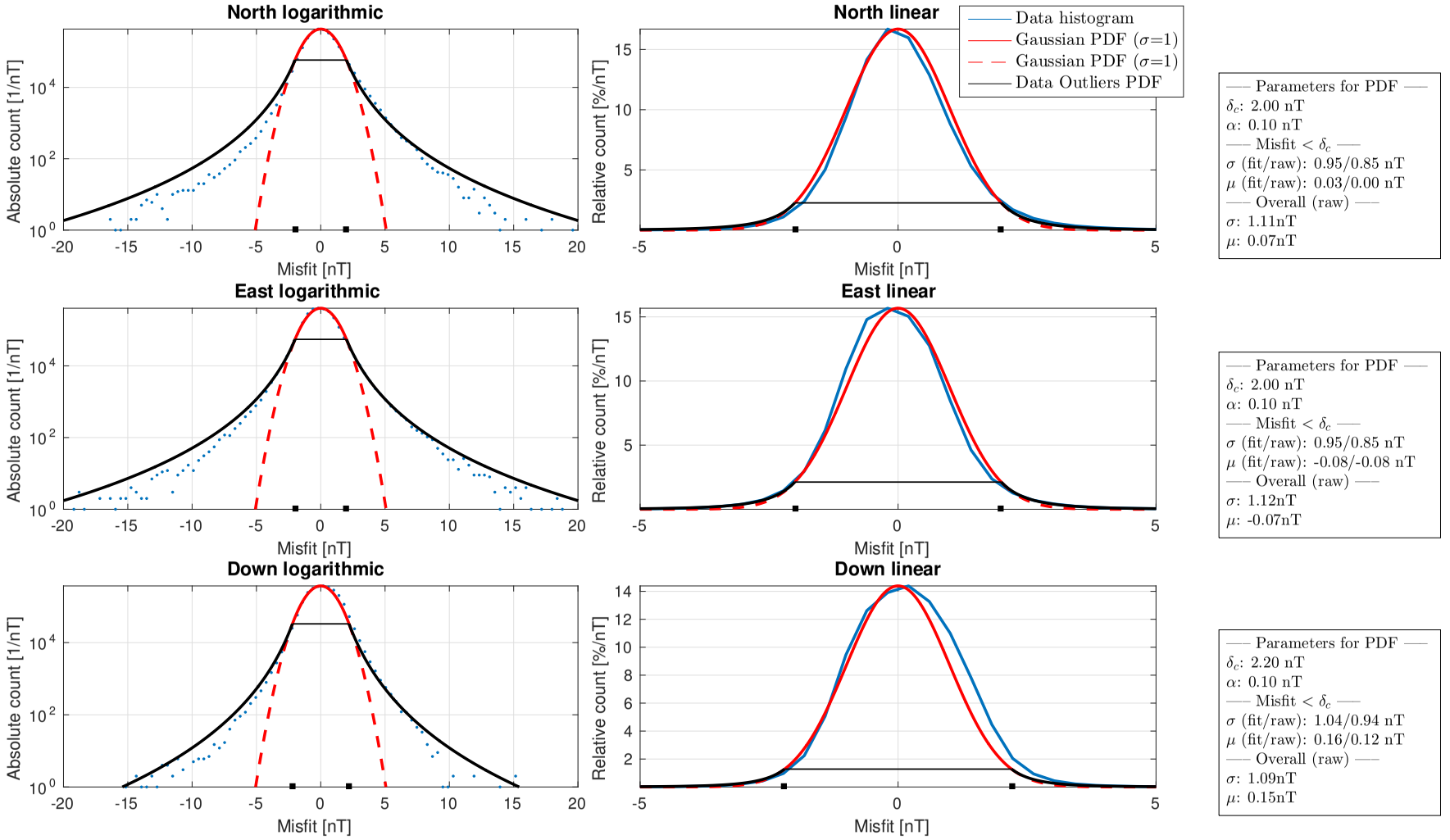

Figure 6.6. The histogram of the weighted residuals (Eq. 6.22) between the MPO nighttime data and the model $\mathbf{g}_{0,10}$ with a damping parameter $\lambda_{0,0} = 2$ (L1 model in Fig. 6.1) is shown. The left panel shows a logarithmic representation of the histogram (blue dots) while the right panel shows a linear representation of the histogram (blue line). Further, the black and red solid lines correspond to the PDF of Eq. 6.20 for misfit values larger and smaller than the threshold δ_c, respectively. For a misfit smaller or equal to δ_c, this PDF corresponds to a normal distribution with standard deviation (STD) $\sigma = 1\,\mathrm{nT}$ and mean $\mu = 0\,\mathrm{nT}$ (red solid and dashed lines). The corresponding threshold value δ_c is indicated by the black squares on the ordinate. In addition, the box on the right-hand side indicates the values for δ_c and α, the STD σ and mean μ of all residuals (Overall), and the STD and mean of the residuals with a misfit smaller than δ_c (Misfit $\leqslant \delta_c$). In the latter case, σ and μ have been calculated from a Gaussian fit to the distribution ('fit') and the misfit values themselves ('raw'). Clearly, the residuals are not well represented by a normal distribution, but the adopted PDF (Eq. 6.20) is a suitable representation.

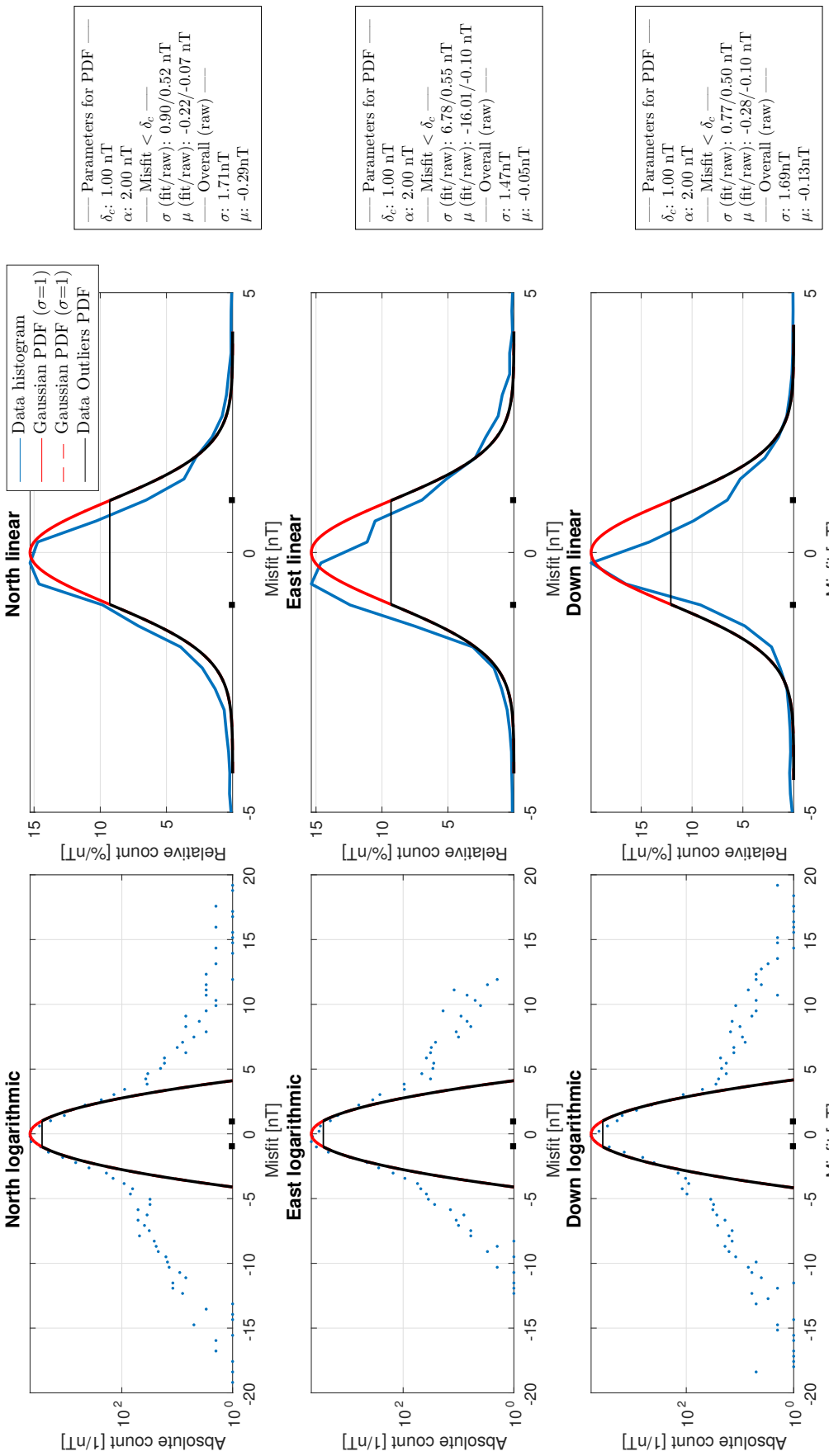

Figure 6.7. The histograms of the weighted AB/SPO dayside data are shown that were used to determine δ_c and α. Else, this figure is similar to Fig. 6.6.

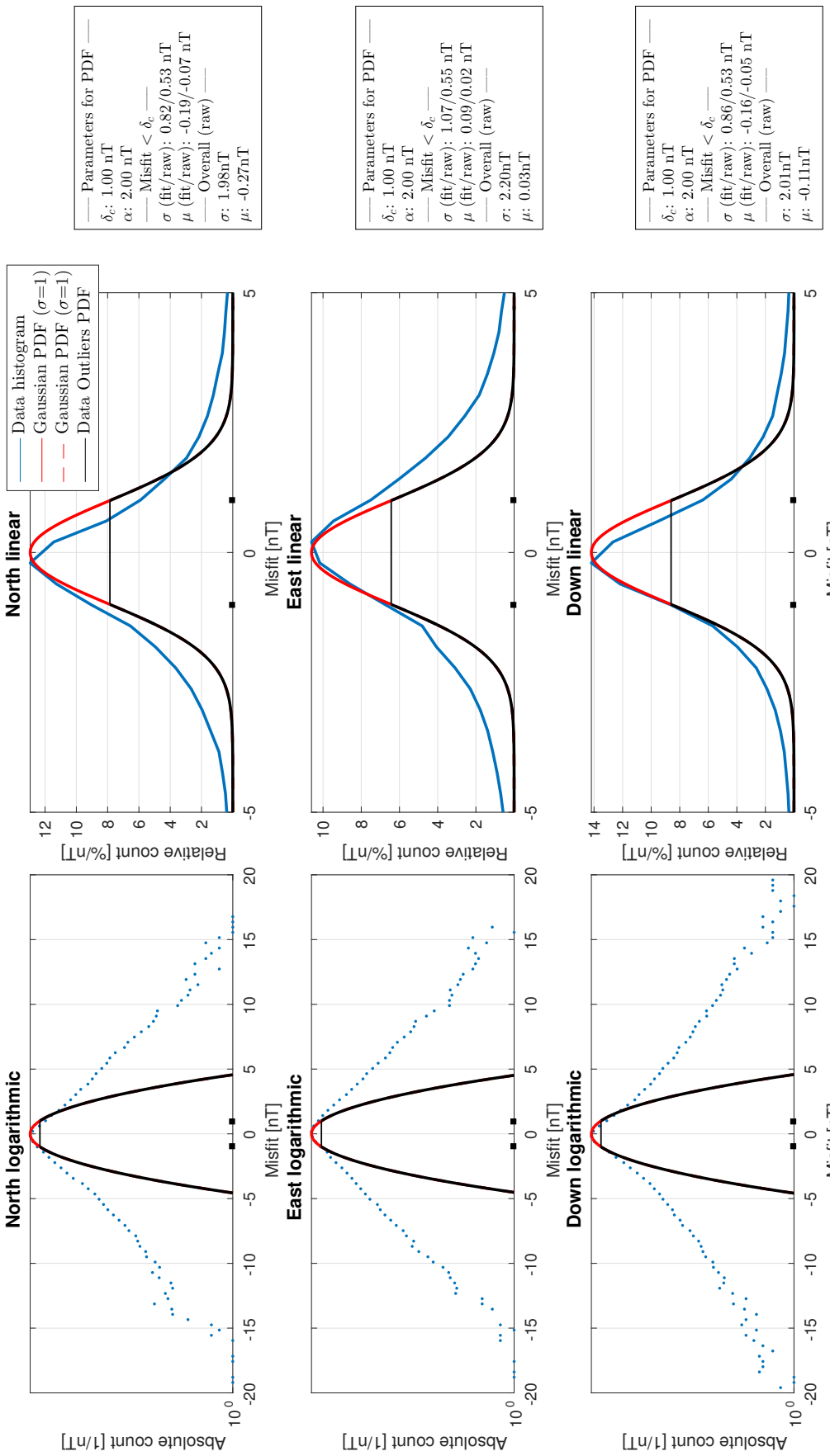

Figure 6.8. The histograms for the weighted AB/SPO nightside data are shown that were used to determine δ_c and α. Else, this figure is similar to Fig. 6.6.

Part IV

RESULTS

First, the derived model of the magnetic field of the Martian crust will be presented by showing and discussing global maps, the power spectrum, and the model covariance matrix. Second, we will investigate the residuals between model predictions and the data, which characterize the quality of the fit. Third, we will conclude this part by comparing the final model to two types of models of the crustal field: on one hand, models that were derived as part of this work and mainly differ from the final model by the used norms and damping parameters. On the other hand, models that were published by other authors using a variety of data inversion and modeling approaches.

7

MODEL OF THE CRUSTAL FIELD

In the following, maps of the crustal magnetic field as predicted by the final model will be presented at different altitudes, including a downward-continuation to the mean planetary radius of 3393.5 km. Also, the characteristics of the obtained Gauss coefficients, the resulting dipole moment, as well as the Mauersberger-Lowes (ML) power spectrum of the model will be displayed and commented on. Further, the model parameter covariance matrix will be discussed which leads to the 95% confidence intervals for the magnetic field predictions at the mean surface altitude. Finally, the model resolution matrix will be presented.

7.1 GLOBAL MAGNETIC FIELD MAPS

In order to reasonably present maps of the crustal magnetic field at different altitudes, an estimate of the global level of noise is necessary. For this purpose, the variances of the predicted field may be used (c.f. Sec. 7.4).

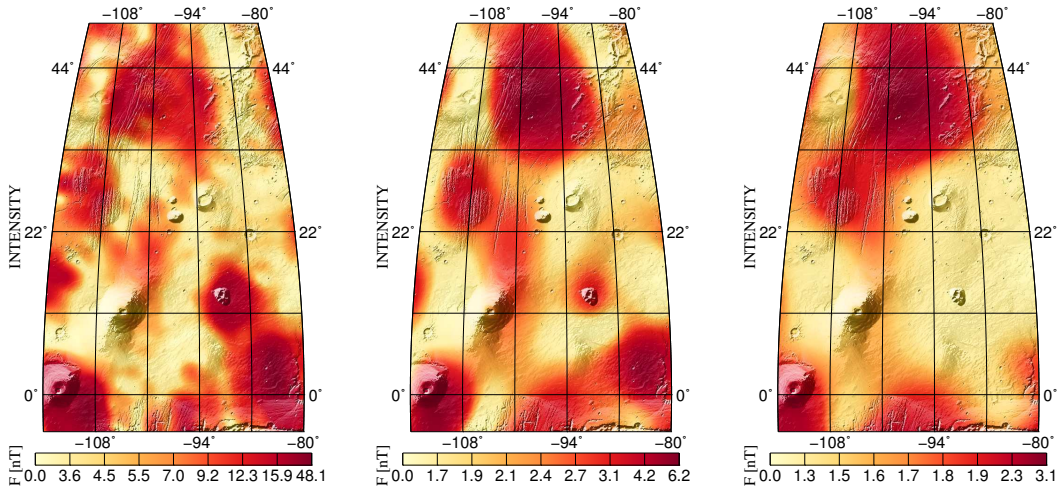

(a) h=0 km **(b)** h=185 km **(c)** h=400 km

Figure 7.1. The crustal magnetic field intensity (F) as predicted by the final model is shown at altitudes of (a) $h = 0$ km, (b) $h = 185$ km, and (c) $h = 400$ km. The map shows a region over Tharsis where the observed field intensity (F) of the ER data ($h = 185$ km) is below the ER detection limit of 3 nT [Lillis et al., 2009]. Consequently, the field intensity (F) predicted by the final model over this region was used to estimate the corresponding noise level at different altitudes. As it is the case for many other figures in this chapter, the location of the region which is visible in this figure is shown on a global MOLA map in Fig. A.1.

However, these variances depend on a priori assumptions, vary largely in dependence of their spatial location, and provide the uncertainty of the predicted field instead of a threshold below which the predicted field can be considered as noise. Therefore, we consider the model field intensity (F) over a region that is most probably devoid of crustal fields as a proxy for the level of noise. With the help of the highly sensitive ER data, such a region was identified over Tharsis[1] [Lillis et al., 2009]. In Fig. 7.1, the crustal field over this area is shown as predicted by the final model at different altitudes. From this figure, conservative estimates of 50, 7, and 4 nT were obtained for the noise level of the global maps at altitudes of $h = 0$ km, $h = 185$ km, and $h = 400$ km, respectively.

Accordingly, global maps of the crustal magnetic field as predicted by the final model are presented in Figs. 7.2 - 7.4. From bottom to top, each of these maps shows the horizontally north (X), east (Y), and vertically down (Z) components and the magnetic field intensity (F) in a global Robinson projection (middle column). Equally, the field is shown in stereographic projections for north- and south polar latitudes (colatitudes $\theta \leqslant 30^\circ$ and $\theta \geqslant 150^\circ$) in the left and right columns, respectively. Along with the field, the major impact basins are indicated by black dashed lines (from left to right: Hellas, Isidis, Utopia, and Argyre). In Fig. 7.2, the model is presented at a radius of $r = 3793.5$ km, corresponding to the Mars Global Surveyor (MGS) mapping phase orbit (MPO) nominal altitude of 400 km. At this altitude, the model is dominated by large-scale anomalies[2]. For example, linear stripes appear in the vertically down (Z) and horizontally north (X) components over Terra Sirenum (TS) and Terra Cimmeria (TC) (Sec. 2.6). What is more, the strongest field intensities (F) of 187 nT are predicted over TS and TC whereas the magnetic field as predicted over the outlined major impact basins and the major volcanic provinces (Tharsis and Elysium) is below the estimated noise level. Also, the northern lowlands are largely devoid of observable magnetic fields, with the exception of a few anomalies near the north pole [Hood and Zakharian, 2001] and the western rim of Arcadia Planitia[3]. The magnetic field map at the ER sampling altitude of 185 km, corresponding to a radius of $r = 3578.5$ km, is shown in Fig. 7.3. At this altitude, many anomalies are resolved into smaller pieces. In particular, the elongated anomalies in the high-field region of the southern highlands appear less prominent. When the model is further downward continued to the mean planetary radius of $r = 3393.5$ km, as shown in Fig. 7.4, even more small scale anomalies become visible. Interesting details of this map include a low field region (45°S/190°E) in TS at the location of an ancient impact crater (Sec. 10.2.2), as well as two isolated

1 Please refer to Fig. A.1 for an overview of regions on Mars.

2 On Earth, a magnetic anomaly is defined as the deviation from the global dipolar field. Here, instead, this term will be used for the crustal field itself.

3 Arcadia Planitia is located northwest of the Tharsis region in the northern lowlands (Fig. A.1).

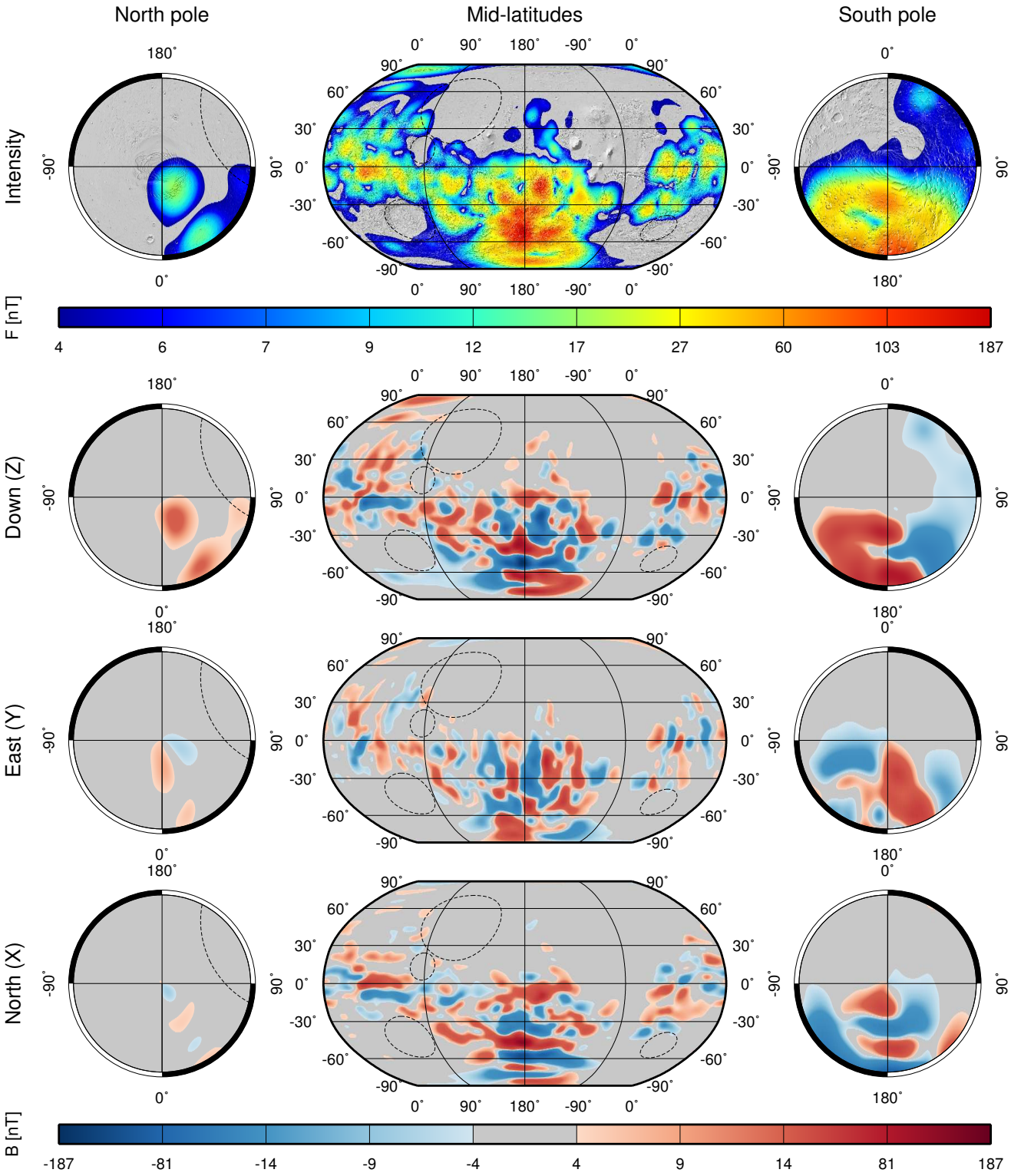

Figure 7.2. Map of the downward-continued crustal magnetic field at an altitude of 400 km, corresponding to the MPO orbit altitude and a radius of 3793.5 km. From bottom to top, the horizontally north (X), east (Y), and vertically down (Z) components as well as the field intensity (F) are shown. From left to right, the North Pole, mid-latitudes and the South Pole are presented. The polar views are in stereographic projection whereas the global maps are shown in Robinson projection. In addition, major impact basins are indicated by dashed lines (from left to right: Hellas, Isidis, Planitia, and Argyre), and the shaded MOLA topography is overlaid on the map of the field intensity (F) (top).

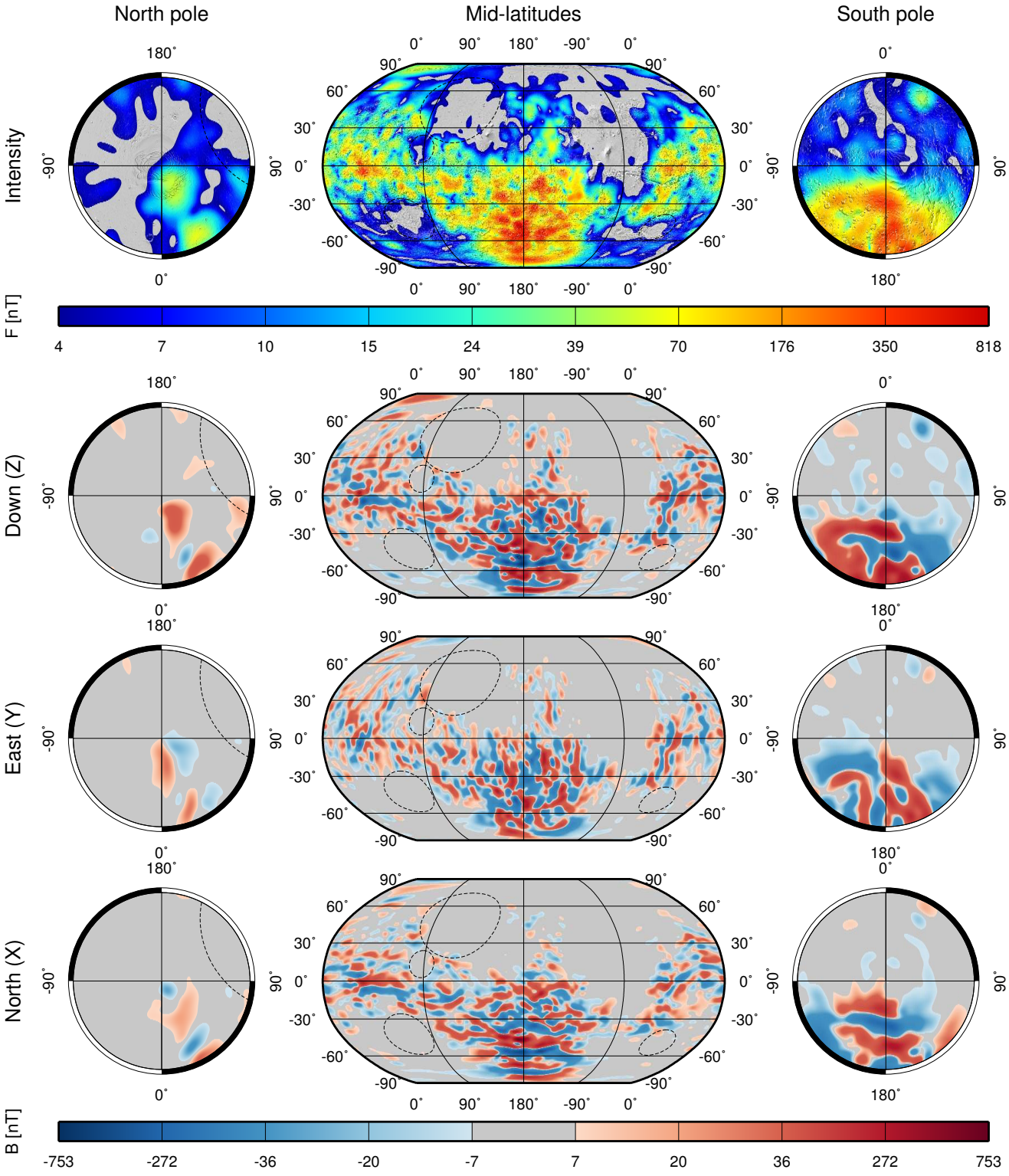

Figure 7.3. Map of the downward-continued crustal magnetic field at an altitude of 185 km, corresponding to the ER sampling altitude and a radius of 3578.5 km. For more information, see caption of Fig. 7.2.

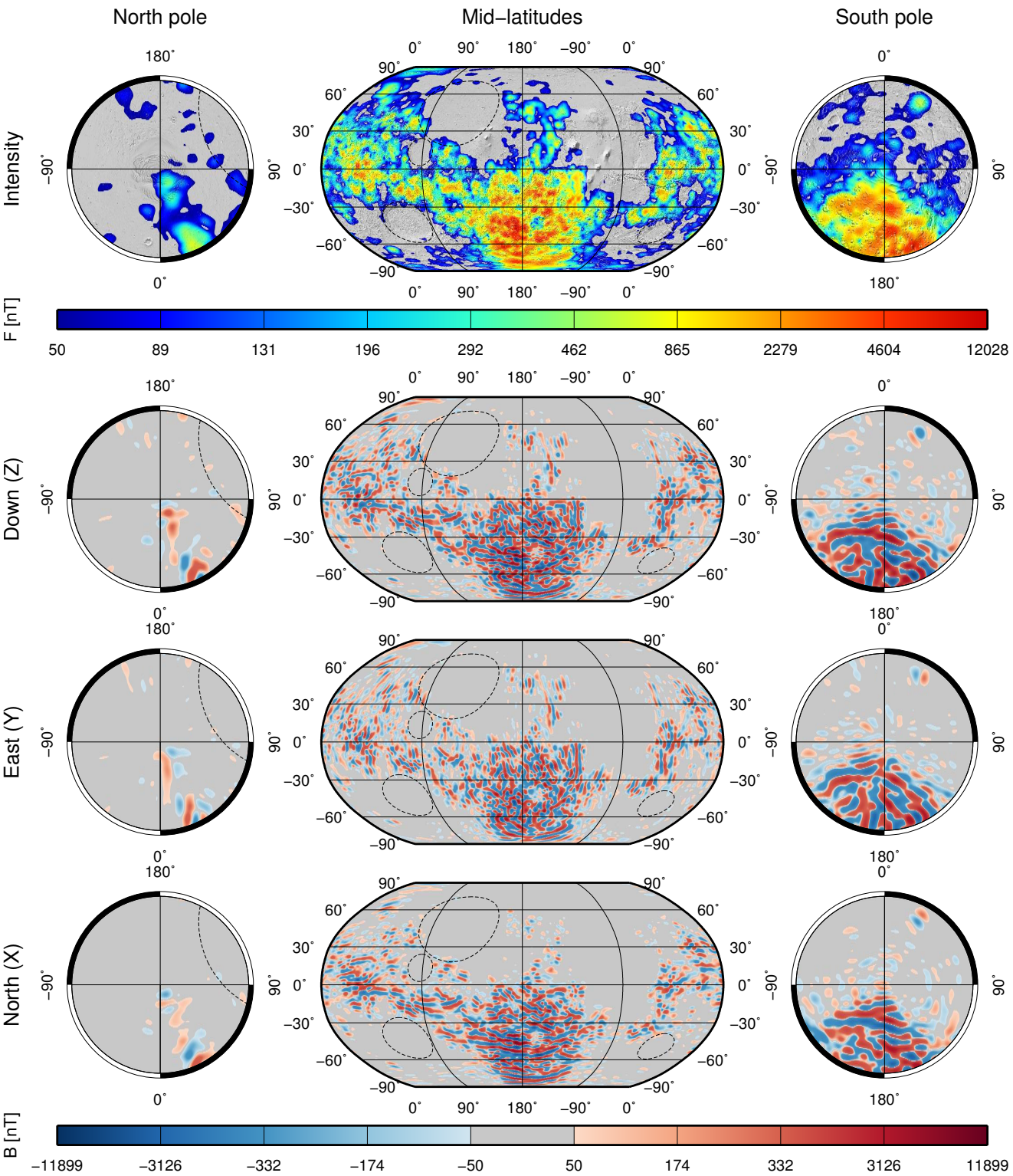

Figure 7.4. Map of the downward-continued crustal magnetic field at the model reference radius of 3393.5 km, corresponding to the mean planetary radius. For more information, see caption of Fig. 7.2.

anomalies (357°E/52°S and 28°E/64°S) in Noachis Terra, between the Hellas and Argyre impact basins. Globally, the minimum and maximum predicted surface fields reach $-11900/+10800\,\mathrm{nT}$ for the vertically down (Z) component, $-6600/+5200\,\mathrm{nT}$ for the horizontally east (Y) component, and $-8500/+9800\,\mathrm{nT}$ for the horizontally north (X) component, respectively. Likewise, the predicted surface peak intensity (F) reaches ~12000 nT, corresponding to twice the lower bound value of ~6000 nT reported by Langlais et al. [2004]. Overall, the presented model reproduces the known features of the Martian crustal field (c.f. Sec. 1.2). Further, the model shows a very low level of noise and is stable even down to surface altitude where many small scale anomalies are resolved.

For completeness, the modeled external day- and nightside fields at the average MPO altitude of 400 km are shown in Figs. 7.5 and 7.6, respectively. As the solar wind is stronger at the dayside than at the nightside, the maximum field intensity (F) of the external field reaches 14.7 nT at the dayside whereas it reaches only 5.9 nT at the nightside. What is more, the external dayside field intensity (F) correlates with the general shape of the crustal field intensity (F) (c.f. Fig. 7.2). As a possible explanation, strong crustal fields may reconnect with the interplanetary magnetic field (IMF) and allow solar wind particles to ionize the neutral atmosphere [Krymskii et al., 2002]. This ionization might then lead to locally stronger external fields. In contrast, the external nightside field is not correlated with the crustal field. Here, the solar wind particles are shielded by the planet and cannot directly penetrate the Martian atmosphere. Instead, the strongest field intensities (F) are obtained near the poles, possibly a result of the draping of the IMF around the planet. As well, this draping of the IMF may be reflected in the strong hemispherical asymmetry of the horizontally north (X) field component [Ferguson et al., 2005; Halekas et al., 2006]. In particular, positive (negative) horizontally north (X) field components are mainly located in the northern (southern) hemisphere. Similarly, Purucker et al. [2000] observed such an asymmetry in their model residuals.

7.2 GAUSS COEFFICIENTS AND DIPOLE MOMENT

In the following, the coefficients $\mathbf{g}$ refer to the Gauss coefficients $\mathbf{g}_{2,12}$ of the final model (Eq. 6.31), and the coefficient g_l^m refers to the Gauss coefficient of the final model with degree l and order m. The Gauss coefficients $\mathbf{g}$ have negative and positive values. However, no particular sign is preferred and no obvious correlation of positive and negative coefficients was found. Therefore, it is sufficient to consider the absolute values of these coefficients. In Fig. 7.7, the absolute Gauss coefficients $\mathbf{g}$ are visualized in dependence of their spherical harmonic (SH) degree l on the ordinate and their SH order m on the abscissa.

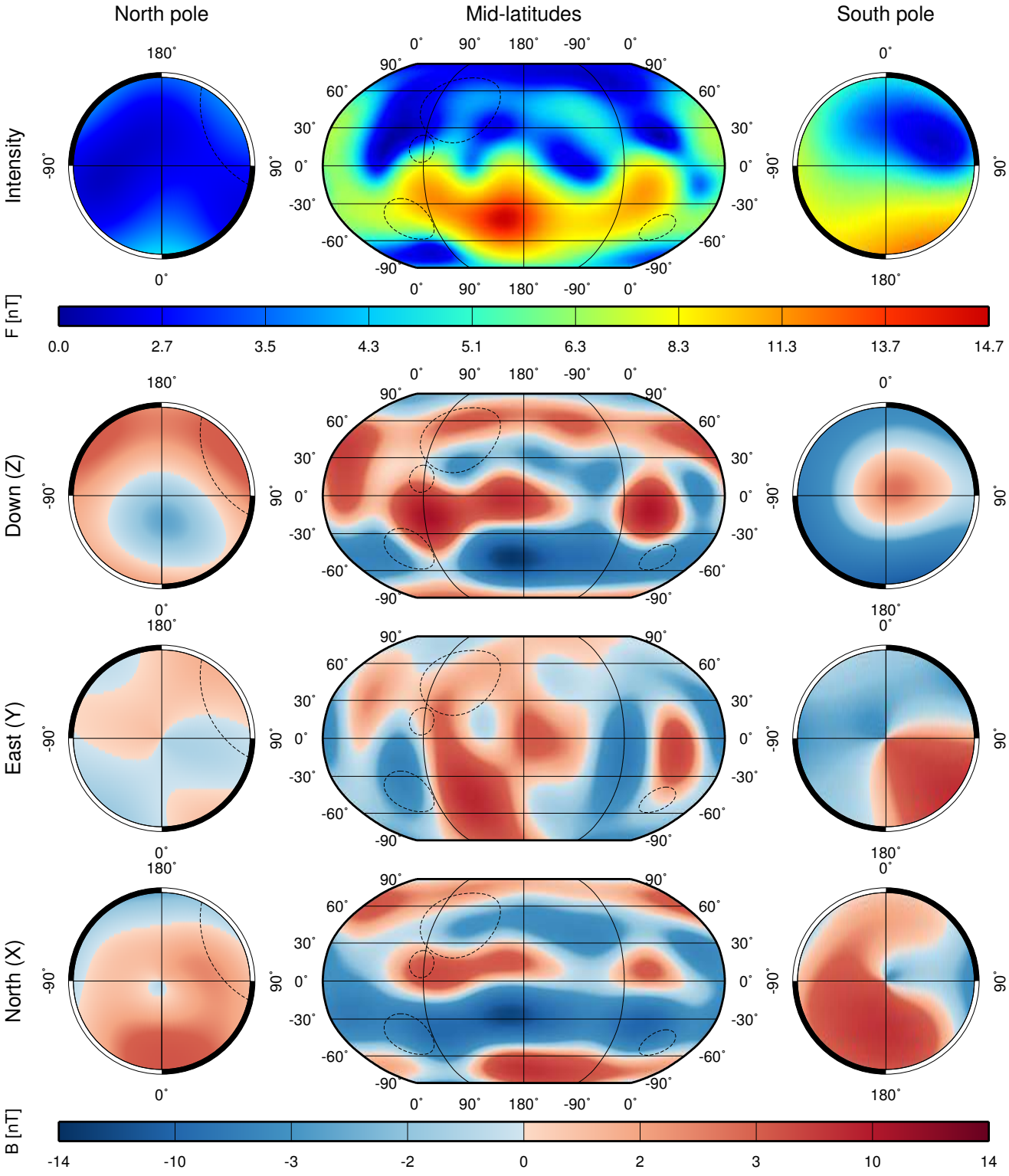

Figure 7.5. The external dayside magnetic field is shown at 400 km altitude, corresponding to the approximate MPO orbit altitude. From bottom to top: The horizontally north (X), east (Y), and vertically down (Z) components and the field intensity (F).

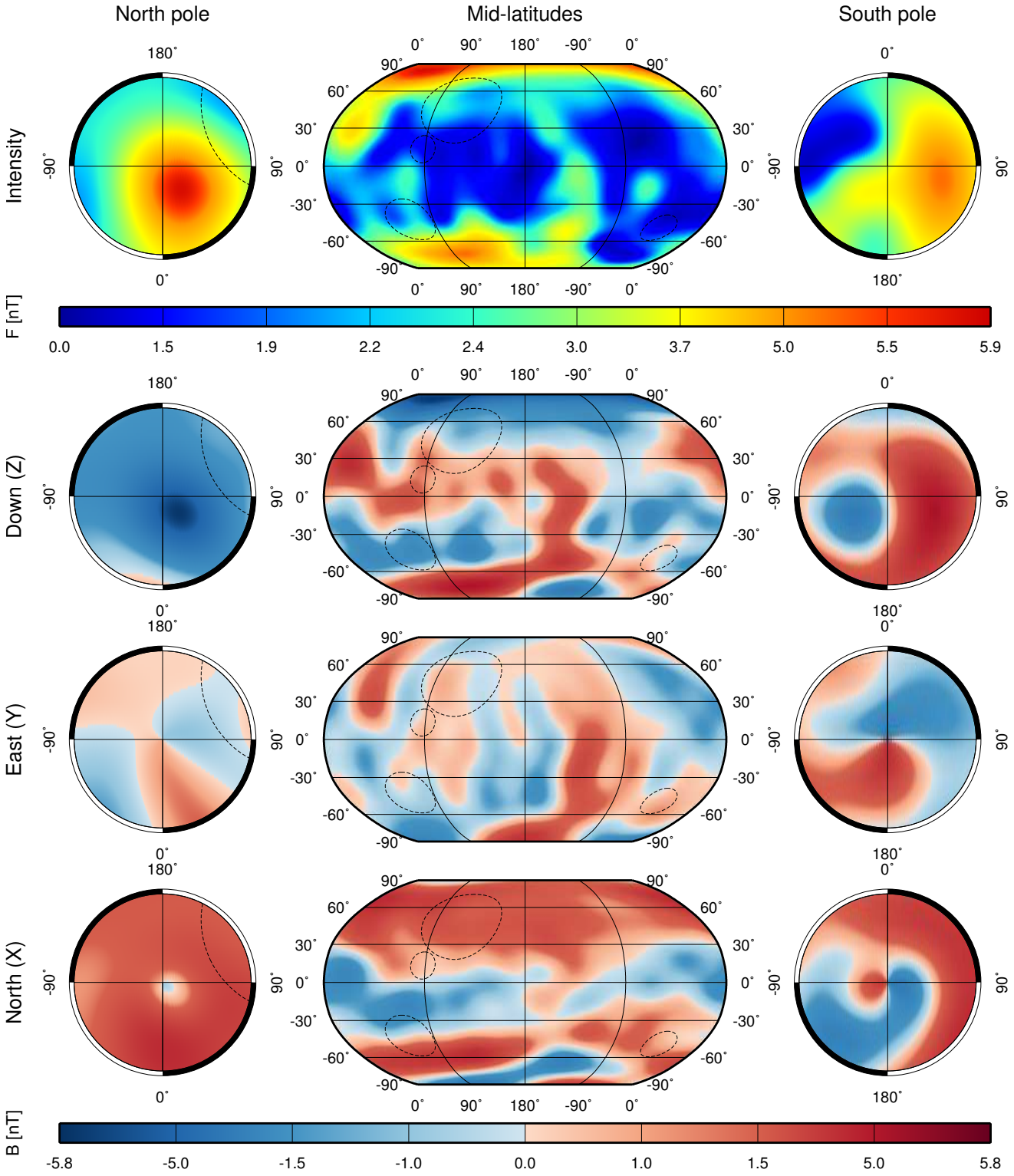

Figure 7.6. Similar to Fig. 7.5, but for the external nightside field.

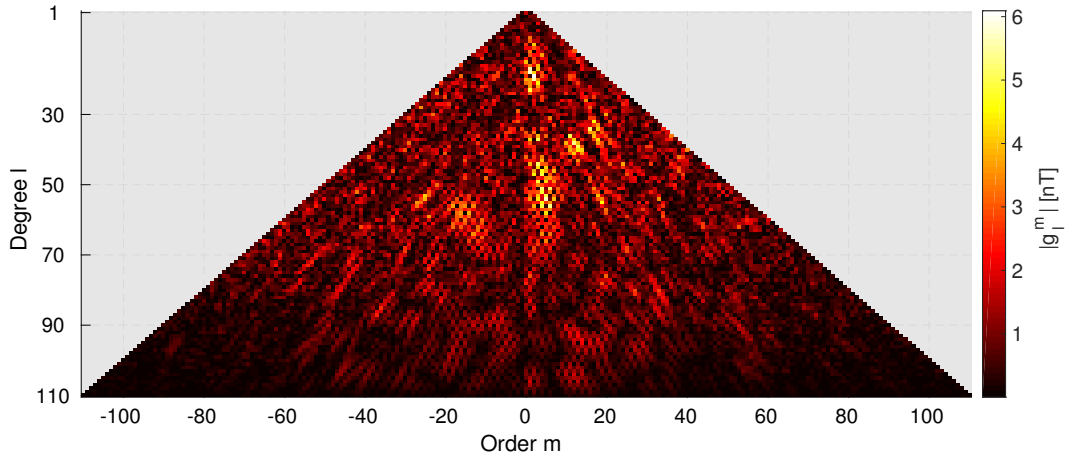

(a) Crustal field

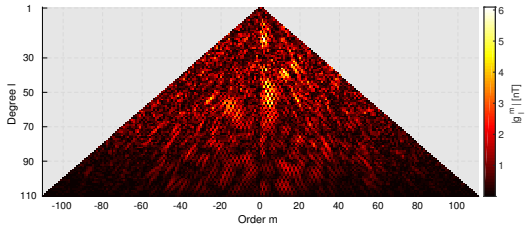

(b) External nighttime field

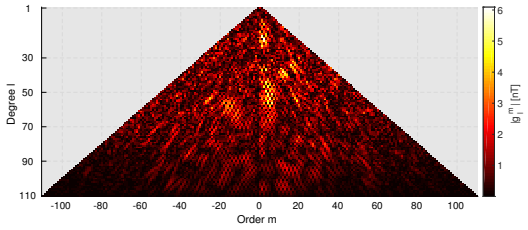

(c) External daytime field

Figure 7.7. The absolute values of the model Gauss coefficients $\mathbf{g}$ in dependence of degree l (ordinate) and order m (abscissa). The Gauss coefficients are color coded and shown for (a) the coefficients of the crustal field, (b) the coefficients of the external nighttime field, and (c) the coefficients of the external daytime field.

With regard to the coefficients $\mathbf{g}$ that correspond to the crustal part of the magnetic field (Fig. 7.7a), the near-zonal[4] coefficients of order $m < 10$ have the largest contributions to the model. Besides, the strongest near-zonal coefficients are mainly of positive orders m. These coefficients correspond to the $(\cos m\phi)$ terms of Eq. 6.9 and reflect the strong fields centered at $\phi = 180°$ longitude. Further, the strongest coefficient is $g_{19}^2 = 6.09\,\mathrm{nT}$, and other strong coefficients $\left(\left|g_l^m\right| \geqslant 3\,\mathrm{nT}\right)$ are found in a relatively few number of clusters. Moreover, no strong Gauss coefficients $\left(\left|g_l^m\right| \geqslant 3\,\mathrm{nT}\right)$ are found for degrees $l > 76$ as a result of the employed regularization scheme.

The Gauss coefficients $\mathbf{g}$ of the external nighttime and daytime fields are shown in Figs. 7.7b and 7.7c, respectively. With regard to the external nighttime field, the strongest Gauss coefficient is relatively weak with $g_3^0 = 0.60\,\mathrm{nT}$, and contributions from coefficients of higher degrees are very small. The external daytime field coefficients, on the other hand, are usually stronger. For these, the axial dipole coefficient shows the largest contribution with $g_1^0 = 2.64\,\mathrm{nT}$.

4 The zonal coefficients g_l^0 of order $m = 0$ are symmetric under rotation along the axis defined by the radial unit vector $\hat{\mathbf{r}}$ with $\theta = 0°$.

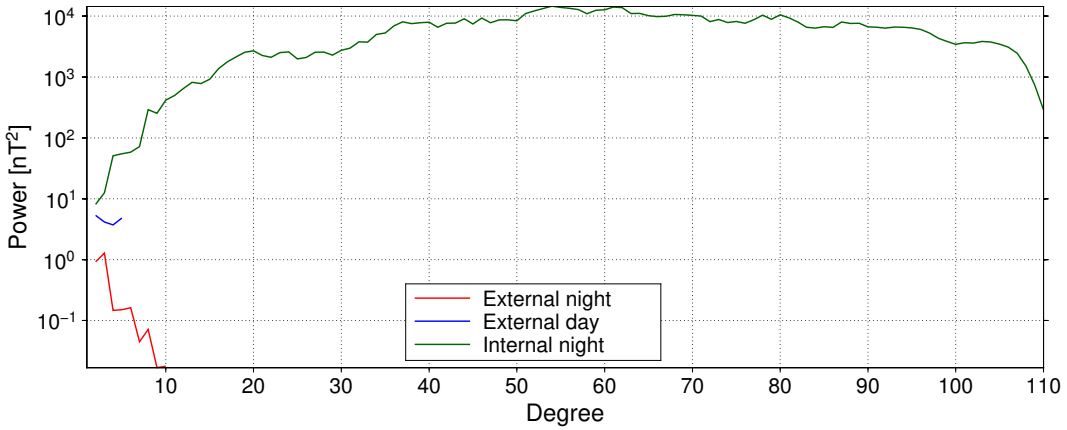

Figure 7.8. For the final model, the ML power spectrum is shown for the internal (green line), the external nighttime (red line), and external daytime (blue line) parts. The power spectrum was calculated at the mean Martian radius of 3393.5 km.

The Martian magnetic field dipole moment $\mathbf{m}$ can be calculated from the Gauss coefficients $\mathbf{g}$ by [Blakely, 1995, p. 167]

$$|\mathbf{m}| = \frac{4\pi}{\mu_0} R_p^3 \sqrt{\sum_{m=-1,0,1} \left(g_{l=0}^m\right)^2} \tag{7.1}$$

and is given by[5]

$$|\mathbf{m}| = \left(7.22 \cdot 10^{17} \pm 1.31 \cdot 10^{17}\right) \text{ Am}^2 \tag{7.2}$$

if the average Martian radius of $R_p = 3393.5\,\text{km}$ is used. This estimate is slightly larger than the estimate of Acuña et al. [2001] ($|\mathbf{m}| < 2 \cdot 10^{17}\,\text{Am}^2$, Sec. 1.2). Also, the Martian dipole moment is five orders of magnitude lower than that of Earth[6] [Finlay et al., 2010].

7.3 POWER SPECTRUM

The ML power spectrum $R(l)$ is a spectral measure of the mean square field in the spherical harmonic domain, i.e.

$$R(l) = \int_\Omega (\mathbf{B} \cdot \mathbf{B})\, d\Omega = (l+1) \left(\frac{a}{r}\right)^{2l+4} \sum_{m=-l}^{l} \left(g_l^m\right)^2 \tag{7.3}$$

5 The given uncertainty is a conservative estimate of the 95% confidence interval for $|\mathbf{m}|$ (c.f. Eq. 5.21). It results from the dipole covariance matrix $\text{Cov}(|\mathbf{m}|)$ which is obtained from the model parameter covariance matrix $\text{Cov}(\mathbf{g})$ (c.f. Eq. 7.4) by $\text{Cov}(|\mathbf{m}|) = \mathbf{J}\text{Cov}(\mathbf{g})\,\mathbf{J}^T$ where $\mathbf{J}_i = \frac{\partial |\mathbf{m}|}{\partial g_0^i} = R_p^6 \left(\frac{4\pi}{\mu_0}\right)^2 \frac{g_0^i}{|\mathbf{m}|}$.

6 The dipole moment of Earth in epoch 2010.0 was about $7.75 \cdot 10^{22}\,\text{Am}^2$ [Finlay et al., 2010].

[Mauersberger, 1956; Lowes, 1966]. The ML power spectrum of the final model, evaluated at the model reference radius of 3393.5 km (i.e., $r = a$), is shown in Fig. 7.8. In this figure, the internal part of the field (the crustal field) is shown in green and the external day- and nightside parts of the field are shown in blue and red, respectively. With regard to the internal field, its spectral power increases with increasing SH degree l and reaches a maximum for degree $l = 54$. When higher degrees $l > 54$ are concerned, the power spectrum is relatively flat, except for a strong drop-off in spectral power for degrees $l > 106$. Concerning the power of the external nightside field, it quickly falls off with increasing SH degree, and is lower than the power of the external dayside field. Even more, the external dayside field almost contributes 50% to the overall power of the dipolar and quadrupolar terms. Besides, its slight increase of power at $l = 5$ may indicate that power of higher degrees is dissipating to lower degrees due to the model truncation at $L_{ext,d} = 5$.

7.4 MODEL PARAMETER COVARIANCE MATRIX

The measured data are the result of a stochastic process if noise in the data is considered to be randomly distributed. In this case, the obtained model parameters also follow a random distribution, and the corresponding model parameter covariance matrix can be determined if the noise in the data is normally distributed and if the forward model is linear (Sec. 5.3). However, the actual distribution of noise in the data is not normal. Also, the model parameters were obtained by applying an iteratively reweighted least squares (IRLS) algorithm (Sec. 6.5) which leads to an iterative system of linearized normal equations (Eq. 6.31). In principle, the parameter covariance matrix may be obtained from these linearized equations. However, these linearized equations depend non-linearly on the model parameters of the previous iteration (c.f. Eqs. 6.30 and 6.31), and therefore non-linearly on the data (Eq. 6.31). Here, we will neglect this non-linear dependency such that the model covariance matrix $\mathrm{Cov}(\mathbf{g})$ can be obtained by comparing Eqs. 5.12, 5.17, 5.29, and Eq. 6.31, resulting in

$$\mathrm{Cov}(\mathbf{g}) = \left(\mathbf{D}^T \mathbf{W}_d^T \mathbf{M}_{d,12} \mathbf{W}_d \mathbf{D} + \lambda_{2,12} \mathbf{R}_2^T \mathbf{W}_r^T \mathbf{M}_{r,2} \mathbf{W}_r \mathbf{R}_2\right)^{-1}. \tag{7.4}$$

Accordingly, the covariance matrix of the model predictions may be calculated from (Eq. 5.17)

$$\begin{aligned} \mathrm{Cov}(\mathbf{d}^*) =& \mathbf{D}^{-1} \mathrm{Cov}(\mathbf{g}) \mathbf{D}^T \\ =& \mathbf{D} \left(\mathbf{D}^T \mathbf{W}_d^T \mathbf{M}_{d,12} \mathbf{W}_d \mathbf{D} + \lambda \mathbf{R}_2^T \mathbf{W}_r^T \mathbf{M}_{r,2} \mathbf{W}_r \mathbf{R}_2\right)^{-1} \mathbf{D}^T. \end{aligned} \tag{7.5}$$

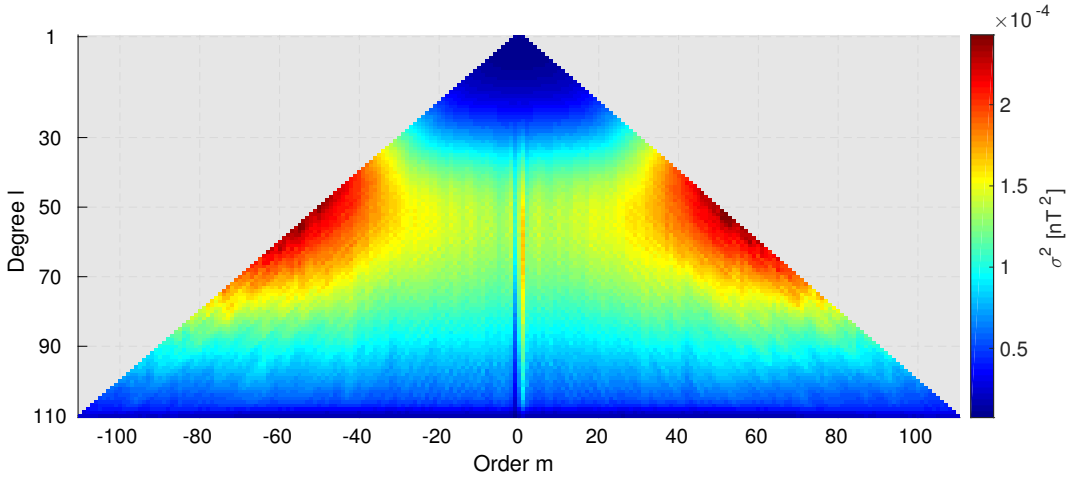

(a) Crustal field

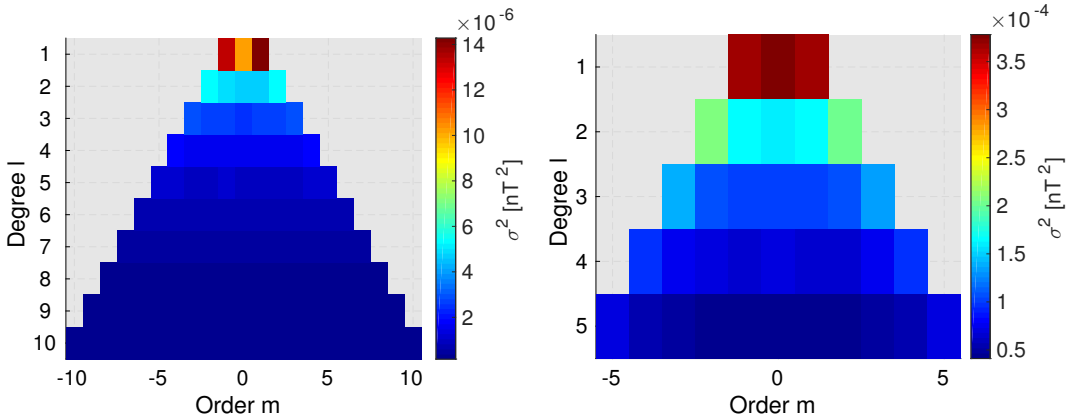

(b) External nighttime field

(c) External daytime field

Figure 7.9. Variances of the final model Gauss coefficients in dependence of degree l (ordinate) and order m (abscissa). The variances are color coded and shown for (a) the coefficients of the crustal field, (b) the coefficients of the external nighttime field, and (c) the coefficients of the external daytime field.

As mentioned in Sec. 5.3, Eq. 5.16 and therefore Eqs. 7.4 and 7.5 are valid only if the weights for the data and regularization[7] have been correctly chosen. However, these weights are usually unknown and have to be estimated a priori (c.f. Ch. 4). For this reason, and because the non-linear dependencies of the model parameters on the observed data have been neglected, the obtained model parameter covariance matrix $\mathrm{Cov}(\mathbf{g})$ as well as the covariance matrix $\mathrm{Cov}(\mathbf{d}^*)$ of the model predictions will at best be feasible approximations.

7 Here, the regularization term was weighted by the damping parameter λ. Therefore, the physical quantity used to regularize the model (Eq. 6.28) was assumed to have a variance of $\sigma_\tau^2 = 1/\lambda$ with mean $\mu = 0$.

MODEL PARAMETER VARIANCES In Fig. 7.9, the variances $\mathrm{Var}(\mathbf{g})_i = \mathrm{Cov}(\mathbf{g})_{ii} = \sigma_i^2$ of the Gauss coefficients of the final model (Eq. 7.4) are shown in dependence of their degree l (ordinate) and order m (abscissa). Similar to the spectral power (Sec. 7.3), the variances of the coefficients that represent the crustal field (Fig. 7.9a) increase with increasing degree l until they start to continuously decrease for degrees $l > 52$. Still, the coefficients of higher degrees are less reliable than coefficients of lower degrees as they are rather constrained by the regularization term[8] than by the data. Further characteristics of the variances include a symmetry in the orders m and an increase with increasing order m for a fixed degree l (Fig. 7.9a). Moreover, the lowest variance for a particular degree l is always reached for $m = -1$, whereas the variance for $m = 1$ is usually large. This is a direct consequence of the satellite orbit inclination ($i = 92.96°$ for the MGS MPO) [Olsen et al., 2010b]. Turning to the variances of the external Gauss coefficients (Figs. 7.9b and 7.9c), the external daytime field coefficients show comparatively large variances (Fig. 7.9c). In contrast, the external nighttime field coefficients show the lowest variances (Fig. 7.9b). Moreover, the variances of the external field coefficients decrease with increasing degree l, whereas the opposite is true for the internal field coefficients (Fig. 7.9a).

MODEL PARAMETER COVARIANCES We neglected any non-diagonal elements of the data covariance matrix $\mathrm{Cov}(\mathbf{d})$ when inverting for the final model (Sec. 6.2). Still, the resulting model parameter covariance matrix $\mathrm{Cov}(\mathbf{g})$ is non-diagonal, i.e. the model parameters are correlated. In Fig. 7.10, these correlations are visualized by showing the normalized[9] decimal logarithms of the absolute covariances with respect to the axial dipole coefficient g_1^0 (Fig. 7.10a), the zonal coefficient g_{70}^0 (Fig. 7.10b), and the sectoral coefficient g_{70}^{70} (Fig. 7.10c) in dependence of degree l (ordinate) and order m (abscissa). For the axial dipole coefficient g_1^0 (Fig. 7.10a), most covariances are two to four orders of magnitudes lower than the variance of g_1^0. The strongest absolute covariances are obtained for coefficients with degrees $l \leqslant 10$, for coefficients with odd degrees l of order $m = 0$, and for coefficients with even degrees $l > 80$ of order $m = 0$. In addition, the external field coefficients (not shown) show significant covariances with the dipolar Gauss coefficient g_1^0. Turning to g_{70}^0 (Fig. 7.10b), the covariances between this coefficient and coefficients of degrees $l < 50$ are usually lower than to coefficients of higher degrees l. This observation has also been made when considering the covariances of other coefficients of degree $l > 50$ (not shown). Similarly, relatively strong covariances are obtained between the sectoral coefficient g_{70}^{70} and coefficients with $l > 50$ (Fig. 7.10c). In this case, the strongest covariances are related to other sectoral coefficients.

8 The regularization term is based on a priori assumptions and does not necessarily represent the true characteristics of the crustal magnetic field.

9 The covariances with respect to the Gauss coefficient g_l^m have been normalized to the variance of g_l^m.

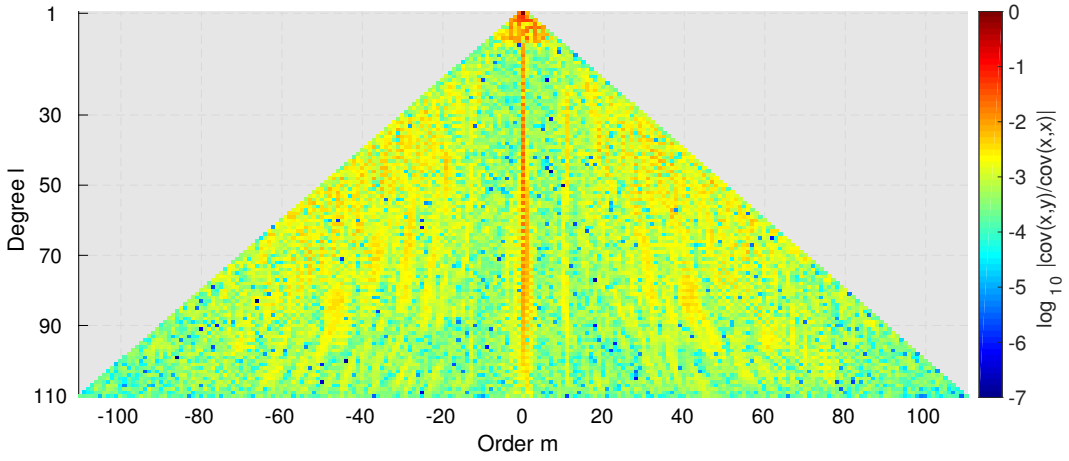

(a) Covariances with respect to g_1^0 ($\mathrm{Cov}\left(\mathbf{g}_1^0, \mathbf{g}_1^0\right) = 8.76 \cdot 10^{-6}\,\mathrm{nT}^2$)

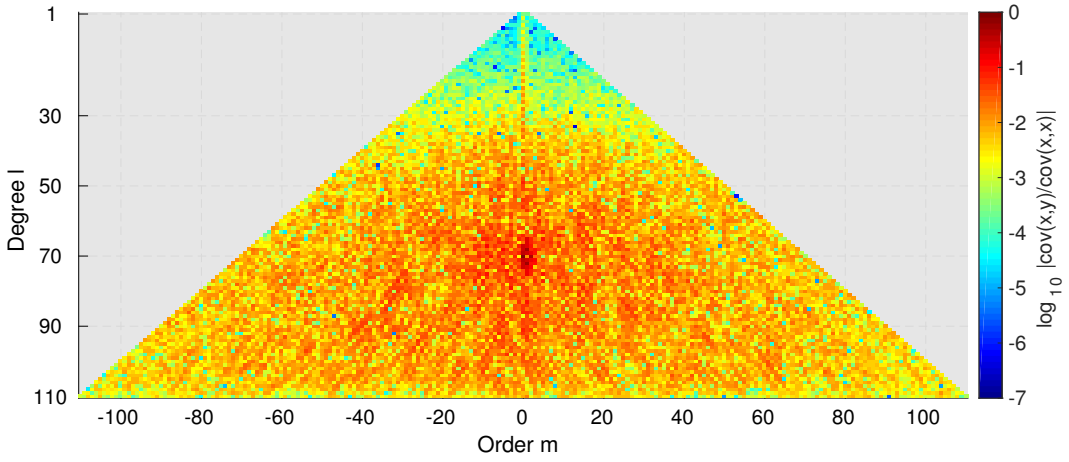

(b) Covariances with respect to g_{70}^0 ($\mathrm{Cov}\left(\mathbf{g}_{70}^0, \mathbf{g}_{70}^0\right) = 1.27 \cdot 10^{-4}\,\mathrm{nT}^2$)

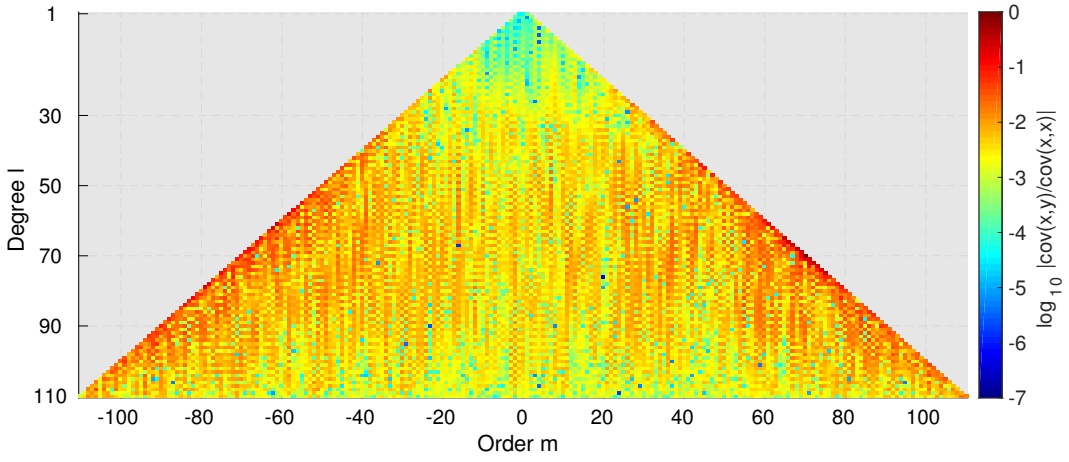

(c) Covariances with respect to g_{70}^{70} ($\mathrm{Cov}\left(\mathbf{g}_{70}^{70}, \mathbf{g}_{70}^{70}\right) = 1.87 \cdot 10^{-4}\,\mathrm{nT}^2$)

Figure 7.10. The color coded decimal logarithm of the normalized absolute values of selected rows of the model parameter covariance matrix $\mathrm{Cov}\,(\mathbf{m})$ is shown in dependence of degree l (ordinate) and order m (abscissa). In addition, the respective variances are given at the bottom of each subfigure.

To summarize, the covariances with respect to the coefficients of degree $l > 50$ are usually stronger than for coefficients of lower degree. For example, the strongest covariances with respect to g_{70}^0 reach 50% of its variance. In contrast, the strongest covariances with respect to g_1^0 reach only 6% of its variance. Overall, the off-diagonal elements of the model covariance matrix cannot be neglected. In other words, the internal Gauss coefficients of the final model are correlated. More quantitatively, the diagonality of the covariance matrix is at most ~7% for g_1^0 and starts to reach $< 2\%$ for SH degrees $l \geqslant 24$.

PRINCIPAL AXES AND EIGENVALUES When the Gauss coefficients are transformed to the coordinate system spanned by the eigenvectors of the covariance matrix, the resulting model parameters will be statistically independent (Sec. 5.3). Moreover, the corresponding eigenvalues can be interpreted as the variances of the new model parameters. Hence, the eigenvector with the smallest (largest) eigenvalue describes the best (worst) determined combination of model parameters.

In Fig. 7.11, the eigenvectors of the best- and worst determined combinations of model parameters are shown for the final model (left column) and an equivalent, but undamped model (right column). The largest contributions to the best-determined parameter combination of the final model (Fig. 7.11a) are made by the coefficients with the highest SH degrees l. Similar to the variances (Fig. 7.9a), however, these coefficients may not be the most reliable ones. Instead, they are rather constrained by the applied regularization. Indeed, the coefficients of highest SH degree l make the largest contributions to the worst-determined combination of model parameters for an undamped model which is otherwise identical to the final model (Fig. 7.11d).

MAGNETIC FIELD COVARIANCE MATRIX With the help of Eqs. 5.21 and 5.23, the covariance matrix $\mathrm{Cov}(\mathbf{d}^*)$ of the model predictions (Eq. 7.5) was used to estimate the corresponding maximum and minimum confidence intervals[10] of the predicted magnetic field (Sec. 5.3), and the resulting 95% confidence intervals at a radius of 3393.5 km (planetary surface) are shown in Fig. 7.12 for (from top to bottom) the horizontally north (X), east (Y), and vertically down (Z) components. In this figure, the upper and lower color bars correspond to the minimum and maximum confidence intervals, respectively, which are related by a constant factor of 57.22 (Eqs. 5.21 and 5.23). Further, these color bars are non-linear as they are based on a histogram of the obtained values. Minimum 95% confidence intervals range from $0.5 - 62.6$ nT and maximum confidence intervals are accordingly

10 The minimum confidence intervals δ_{min} (Eq. 5.23) ignore correlations between the obtained field values whereas the maximum confidence intervals δ_{max} consider the upper bound of such correlations (Eq. 5.21).

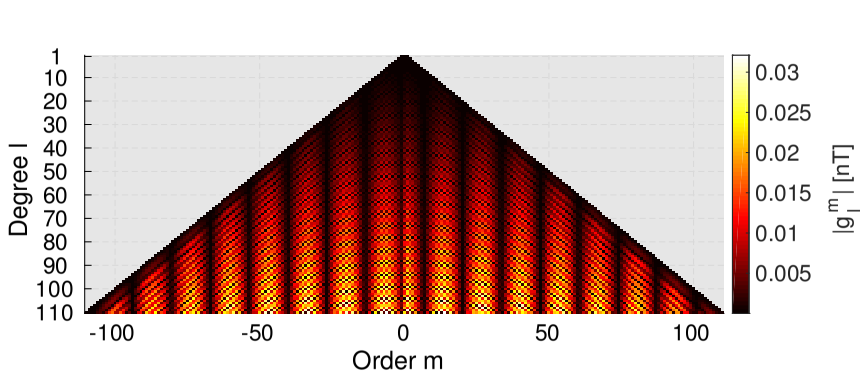

(a) Final model- Best-determined

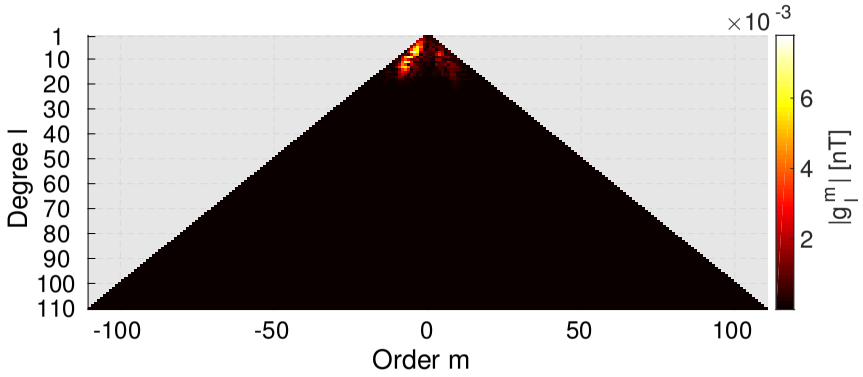

(b) Undamped - Best-determined

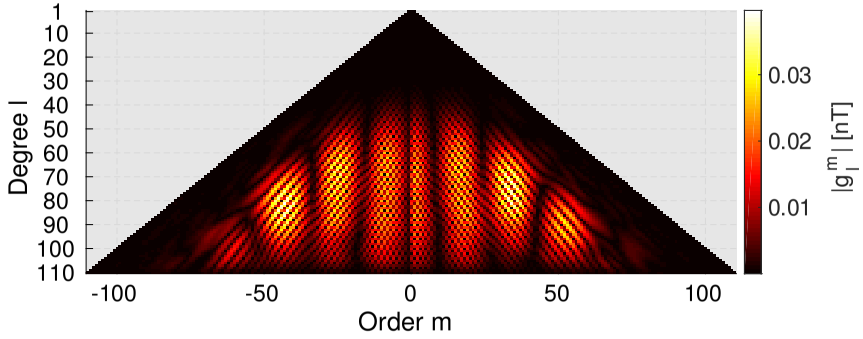

(c) Final model- Worst-determined

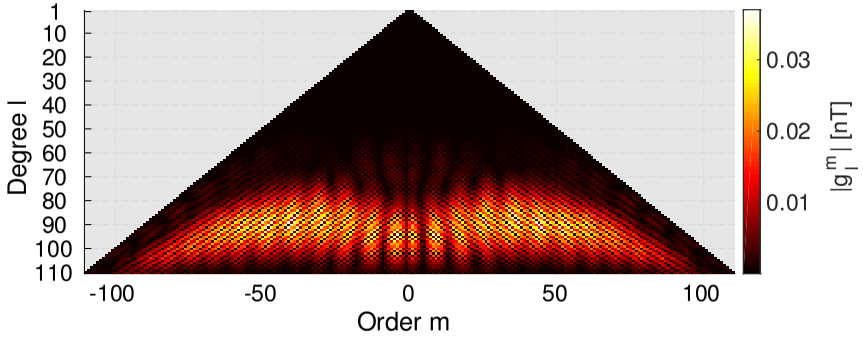

(d) Undamped - Worst-determined

Figure 7.11. The sets of the (top) best- and (bottom) worst-determined model parameters of the (left) final model and an (right) undamped, but otherwise identical model, are shown in dependence of SH degree l (ordinate) and order m (abscissa).

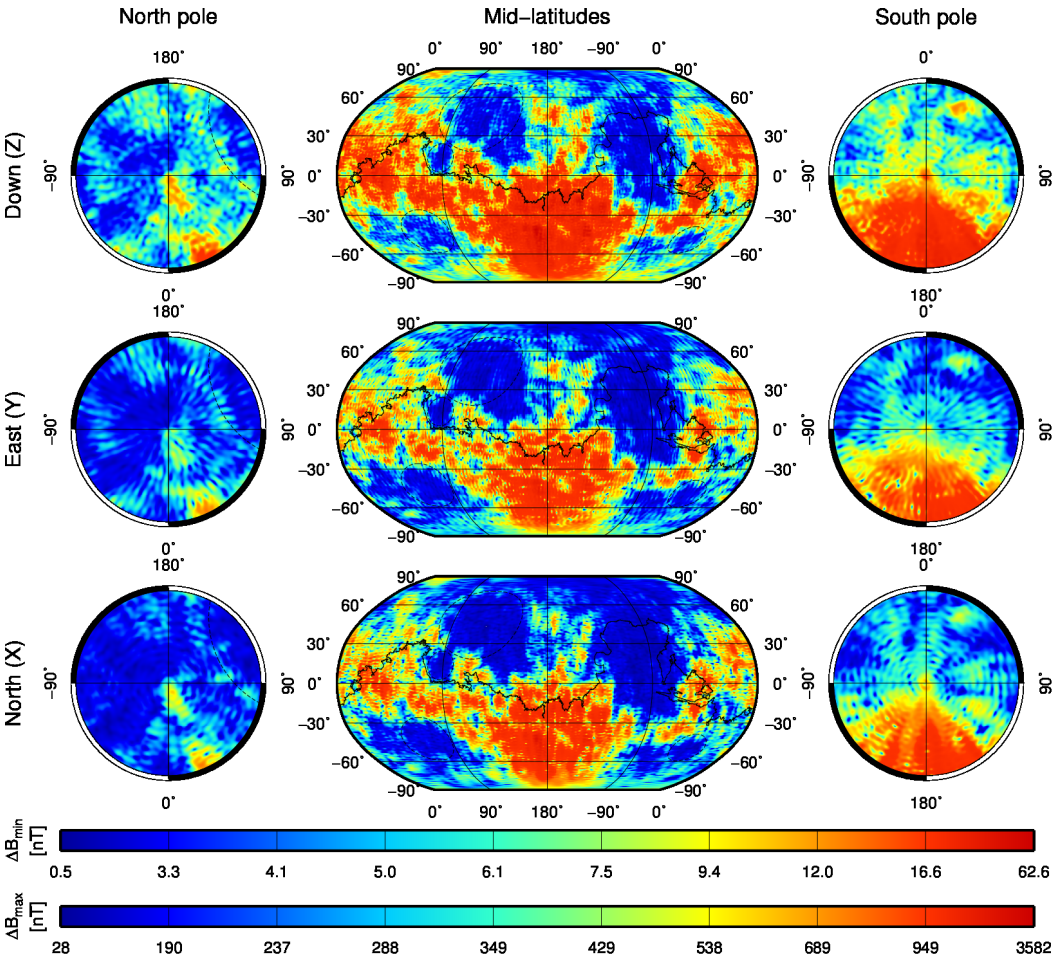

Figure 7.12. A global map of the estimated confidence intervals [nT] of the downward-continued crustal magnetic field at the model reference radius of 3393.5 km (corresponding to the mean planetary radius) is shown here. The upper color bar shows the minimum confidence intervals and the lower color bar shows the maximum confidence intervals. These are related by a constant factor of 57.22 (Eqs. 5.21 and 5.23). For more information, see caption of Fig. 7.2.

larger. As illustrated in Fig. 7.12, the largest confidence intervals were obtained over TC and TS where strong magnetic fields are present (Sec. 1.2). The lowest confidence intervals are associated mainly with weaker fields over the large impact basins, the Tharsis region, and the southern low-field region (Sec. 1.2). Surprisingly, no large uncertainties are associated with polar regions despite of the large estimated noise in the MPO data at the north pole (Fig. 4.1) and despite of the polar data gaps. Presumably, this is a result of regularization, which influences the obtained covariance matrices.

Moreover, the 95% confidence intervals relative to the predicted field are visualized in Fig. 7.13 wherever the respective field is above the estimated noise level of 50 nT (Sec. 7.1). The lowest relative confidence intervals are observed in regions where the strongest magnetic fields are present. In particular, minimum relative confidence intervals (upper color bar) are mostly

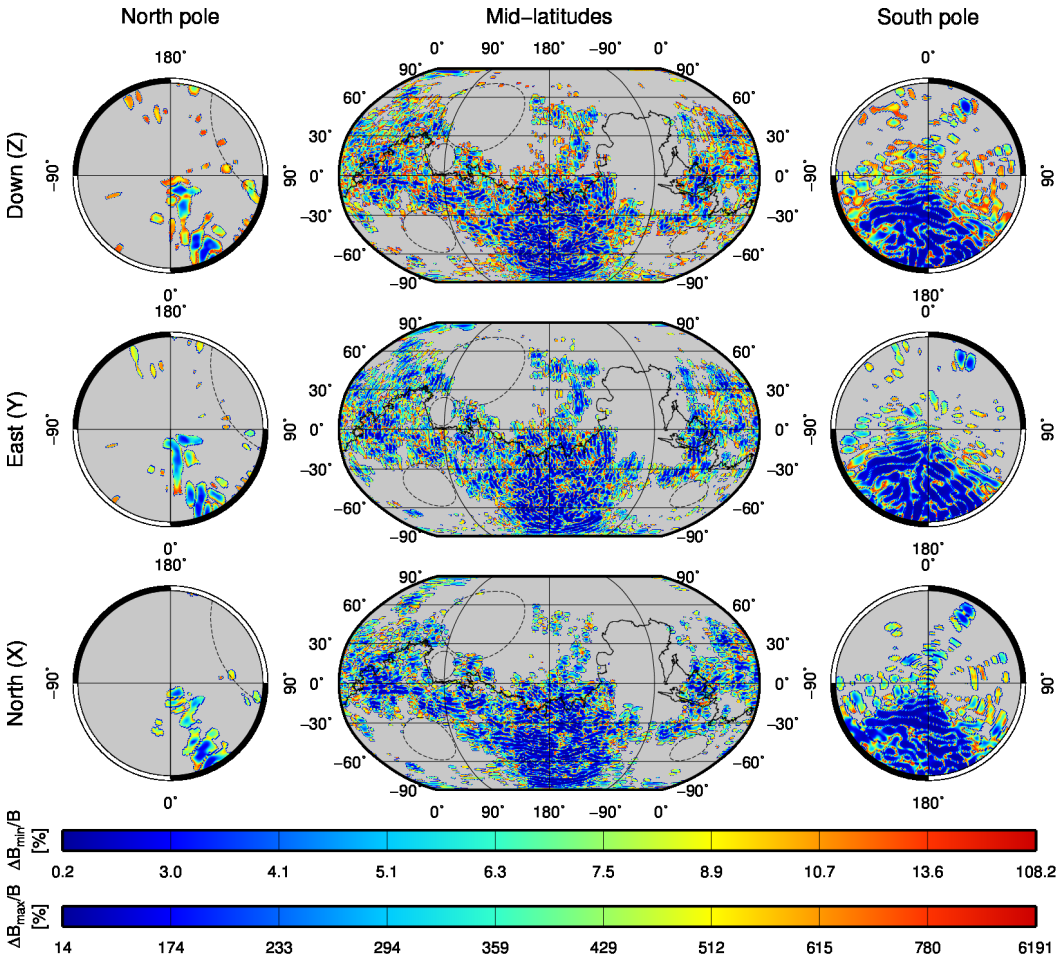

Figure 7.13. A map of the estimated confidence intervals [%] relative to the downward-continued crustal magnetic field at the model reference radius of 3393.5 km (corresponding to the mean planetary radius) is shown here. The upper color bar shows the minimum relative confidence intervals and the lower color bar shows the maximum relative confidence intervals which are related by a constant factor 57.22 (Eqs. 5.21 and 5.23). For more information, see caption of Fig. 7.2.

below 4% in TC and TS, whereas they can reach $>$ 100% in the low-field regions. Maximum relative confidence intervals (lower color bar) are correspondingly larger, and reach already over 100% in TC and TS (Fig. 7.13). Still, maximum confidence intervals should be considered as an extreme upper bound which contains highly improbable model parameter combinations (c.f. Sec. 5.3).

7.5 RESOLUTION MATRIX

The resolution matrix $\mathbf{Q}$ (Sec. 5.4) describes the relation between the obtained model parameters and the unregularized model parameters $\hat{\mathfrak{m}}$ that would perfectly describe noise-free data. For the final model, the resolution

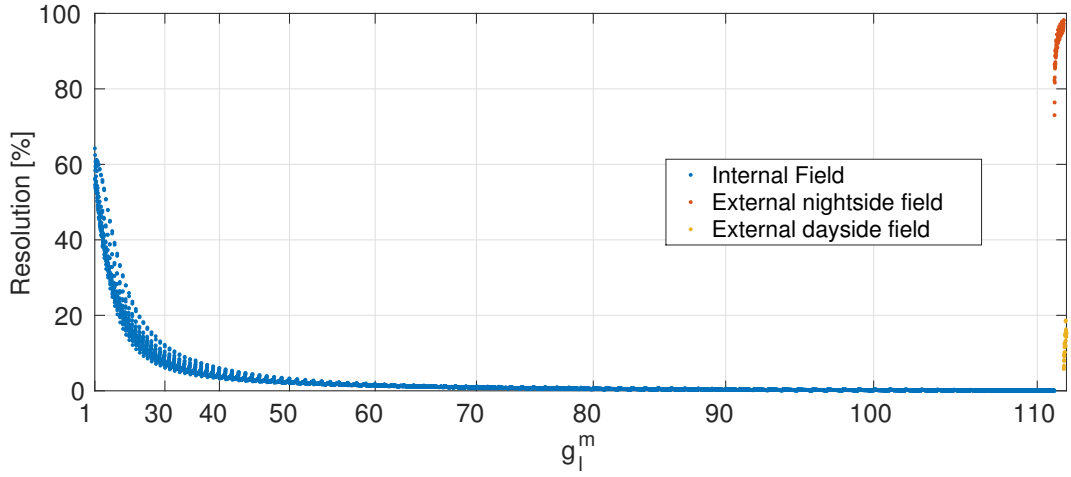

Figure 7.14. The relative resolution of the final model (Eq. 7.7) is shown in this figure for the model parameters of the internal field (blue), the external nightside field (red), and the external dayside field (yellow).

matrix is given by (Eqs. 5.25 and 6.31)

$$\mathbf{Q} = \mathbf{A}^{-1}\mathbf{D} = \left(\mathbf{D}^T\mathbf{W}_d^T\mathbf{M}_d\mathbf{W}_d\mathbf{D} + \lambda\mathbf{R}^T\mathbf{W}_r^T\mathbf{M}_r\mathbf{W}_r\mathbf{R}\right)^{-1} \mathbf{D}^T\mathbf{W}_d^T\mathbf{M}_d\mathbf{W}_d\mathbf{D}. \tag{7.6}$$

The resulting resolution matrix is non-diagonal as the final model has been regularized. In other words, each obtained model parameter $\mathbf{m}$ is a linear combination of the model parameters $\hat{\mathbf{m}}$. Then, the relative resolution of the i-th model parameter $\mathbf{m}_i$ is obtained from

$$\mathbf{R}_i = \frac{\mathbf{Q}_{ii}}{\sum_j |\mathbf{Q}_{ij}|} \cdot 100\%. \tag{7.7}$$

The relative resolution of the crustal field coefficients of the final model is visualized by the blue dots in Fig. 7.14. Among these, the best resolved parameter is g_1^0 with a relative resolution of 64.23 %. However, the relative resolutions quickly decrease to lower than 10 % starting from degrees $l \geqslant 25$. The relative resolutions of the external fields are higher, and shown by the yellow- and red dots for the external day- and nightside fields, respectively. This is not surprising, as the regularization was applied at the surface where external field contributions are low.

8

RESIDUALS

A straightforward measure of the quality of the model fit to the data is given by the residuals, i.e. the differences between model predictions and the respective observations. If the a priori standard deviations (STDs) σ_i of the data (c.f. Sec. 4.1 and 4.2) are considered, then the weighted residuals are given by

$$r_i = \frac{\mathbf{d}_i - \sum_j \mathbf{D}_{ij}\mathbf{m}_j}{\sigma_i}. \tag{8.1}$$

Here, i refers to the i-th datum and j to the j-th model parameter. What is more, this equation transforms to the case of unweighted residuals if $\sigma_i = 1 \; \forall \; i$. In this chapter, the characteristics of the obtained residuals will be investigated by presenting and discussing their statistics and spatial distribution. Moreover, a direct comparison of model predictions to selected data will be shown in order to comment on the ability of the final model to fit the data.

8.1 STATISTICS OF THE RESIDUALS

The statistics of the residuals can be characterized by their mean value μ and their STD σ. The STDs of the weighted residuals will approach one if the a priori STDs σ_i of the data (c.f. Eq. 6.22) have been correctly chosen and if noise in the data is normally distributed. As far as the mean value of the residuals is concerned, a deviation from zero may hint at unmodelled non-random fields resulting from, e.g., ionospheric plasma currents. Further, the correlation coefficient ρ between the model and the data provides information on the quality of the model fit to the data. In particular, a correlation coefficient of one indicates perfect correlation between the model predictions and the data [Purucker et al., 2000; Langlais et al., 2004]. Still, it should be noted that the correlation coefficient does not account for constant offsets.

The mean μ and the STD σ of the weighted (μ^w, σ^w) and unweighted residuals (μ, σ) as obtained from the final model are shown in Tab. 8.1 for different data sets. Along with these, the respective correlation coefficients (ρ) are given. With regard to the unweighted STDs, the vertically down (Z) component shows lower values than the horizontally north (X) and east (Y) components, with the exception of the STDs of the aerobraking phase (AB)/science phase orbit (SPO) nighttime data. This result is in agreement with previous studies [Cain et al., 2003]. As well, it is in agreement with the

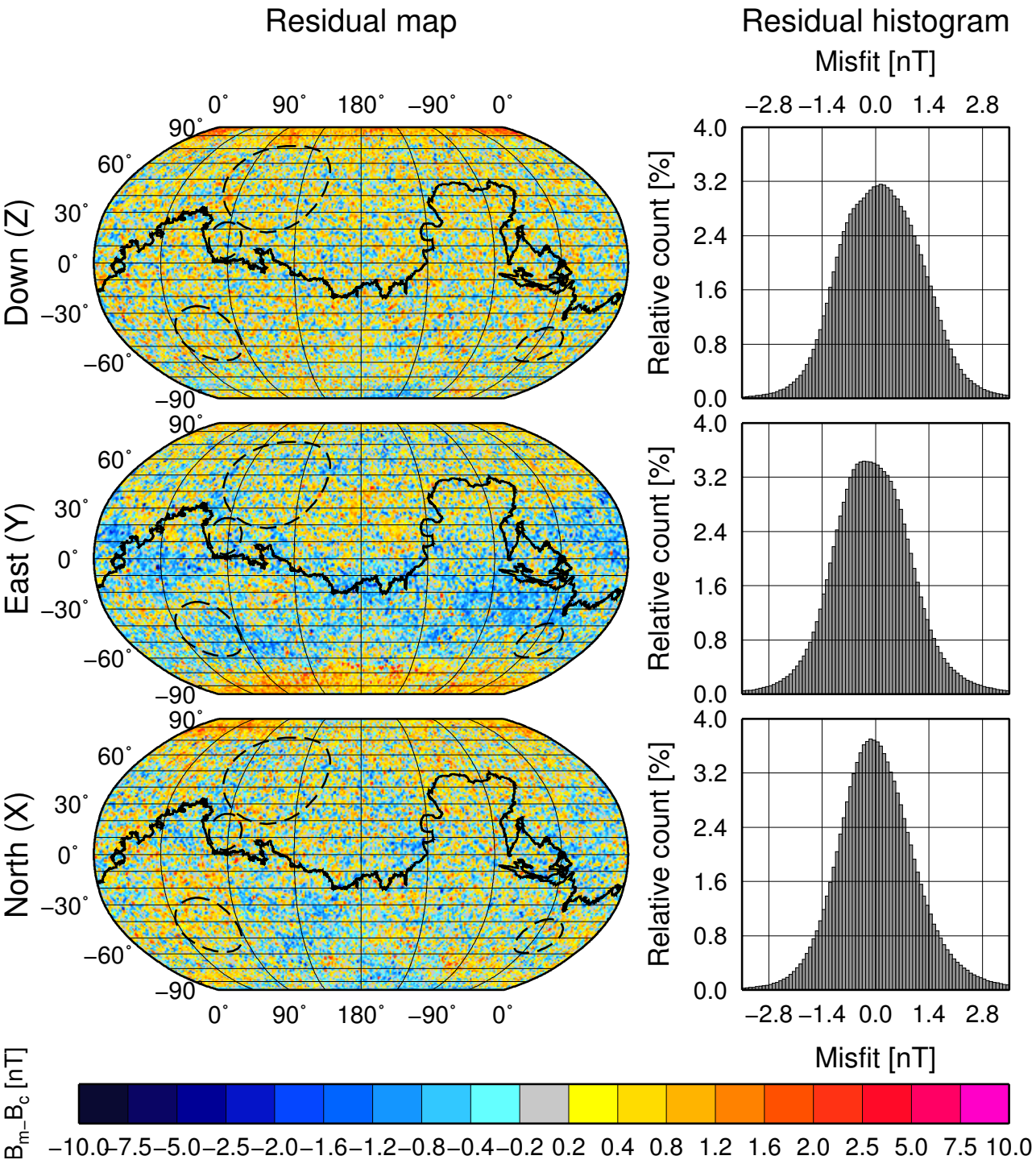

Figure 8.1. The weighted residuals between the final model and the MPO nighttime data for each of the three vector components of the Martian crustal magnetic field are presented in this figure. In the left column, the spatial distribution of the residuals is shown. In the right column, their histograms are shown. The resulting spatial distribution is fairly homogeneous, especially for the least disturbed vertically down (Z) component. Copyright 2014 by the American Geophysical Union, reprinted from Fig. 7 of Morschhauser et al. [2014] with kind permission from publisher John Wiley & Sons Ltd.

Table 8.1. Statistics of the model fit (final model in Fig. 6.1) for different data sets and the horizontally north (X), east (Y), and vertically down (Z) magnetic field components[a].

DATA CLASS		FINAL MODEL				
		σ	σ^w	μ	μ^w	ρ
MPO	X	6.42	1.11	0.43	0.07	0.91
night	Y	7.20	1.12	-0.36	-0.07	0.83
Δ_d=80 km	Z	5.90	1.09	0.81	0.15	0.95
AB/SPO	X	9.78	1.71	-1.65	-0.29	0.99
night	Y	8.62	1.47	-0.32	-0.05	0.98
($h \leqslant 348$ km)	Z	8.86	1.69	-0.69	-0.13	0.99
AB/SPO	X	16.77	1.98	-2.28	-0.27	0.96
day	Y	16.92	2.20	0.24	0.03	0.94
($h \leqslant 200$ km)	Z	14.03	2.01	-0.75	-0.11	0.98

[a] The standard deviation of the residuals is given by σ, the average value of the residuals is given by μ and the correlation coefficient between data and model predictions is given by ρ. The superscript w indicates that the respective values were weighted with their a priori data weights as described in Sec. 4.1 and 4.2.

expectation that external fields are oriented horizontally as they are draping around the planet [Luhmann and Brace, 1991]. In addition, the AB/SPO dayside data show larger unweighted STDs compared to the corresponding nightside data. This is a direct consequence of solar-wind induced fields on the dayside. For the weighted residuals, the lowest STDs of about 1.1 nT were obtained for the mapping phase orbit (MPO) data. Hence, the data-based determination of a priori STDs σ_i for the MPO data was suitable. On the other hand, the residuals of the AB/SPO data show larger STDs, possibly as a result of the non-Gaussian tails in the residual distribution (c.f. Fig. 8.2).

Turning to the mean values of the unweighted residuals, deviations from zero of 2.28 nT and 1.65 nT were obtained for the horizontally north (X) component of the AB/SPO day- and nightside data, respectively. Still, the mean values are always below 1 nT for the other components and the MPO data. For the weighted residuals, the situation is similar, and a maximum mean value of 0.29 was obtained.

8.2 SPATIAL DISTRIBUTION OF THE RESIDUALS

The spatial distribution of the residuals is important in assessing systematic misfits of the model. Ideally, the residuals should be distributed homogeneously over the globe as any visible structure hints at unmodelled fields. Maps of the spatial distribution of the weighted MPO residuals along with

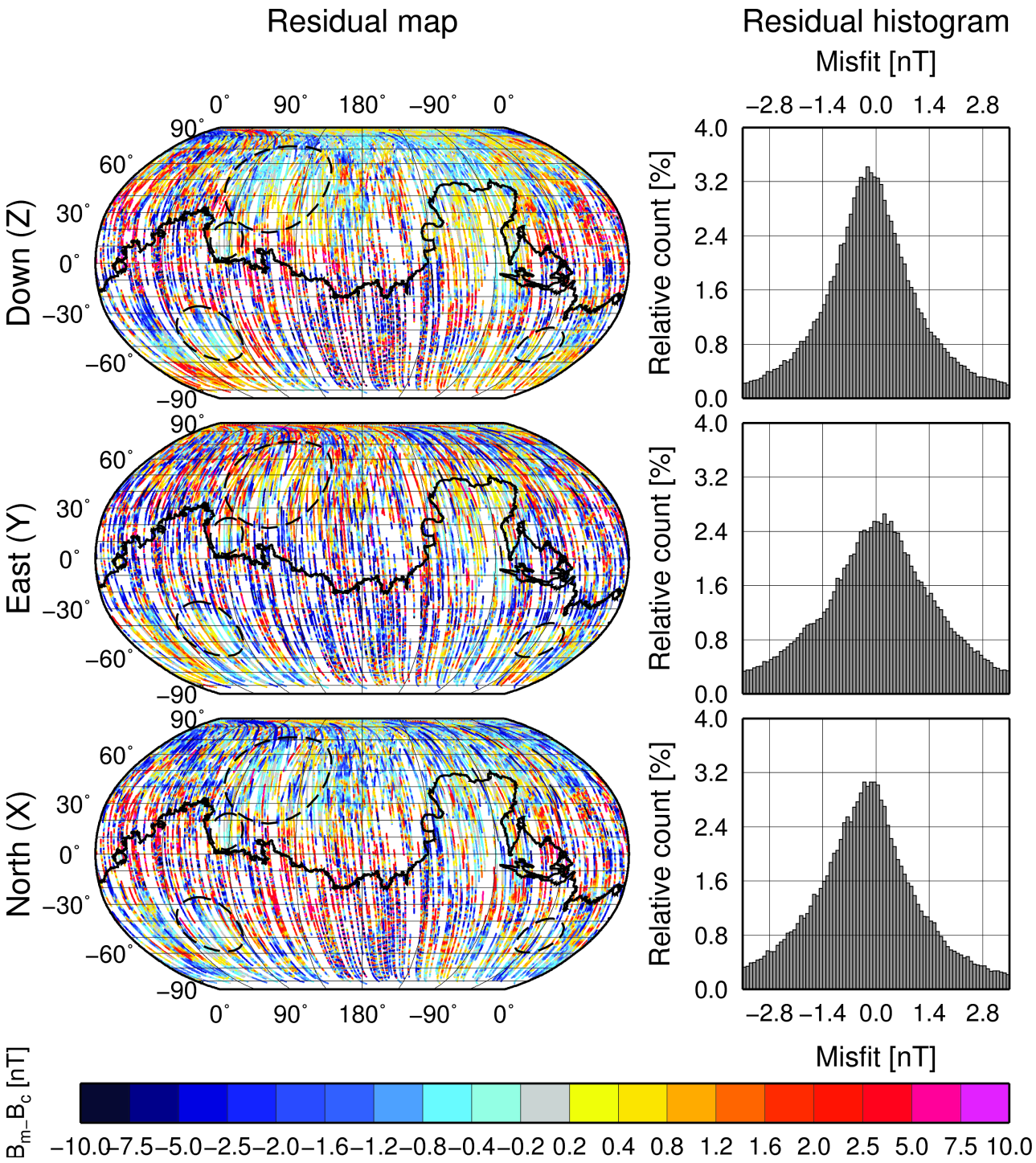

Figure 8.2. The weighted residuals between the final model and the AB/SPO night- and daytime data for each of the three vector components of the Martian crustal magnetic field are presented in this figure. In the left column, the spatial distribution of the residuals is shown. In the right column, their histograms are shown. Small-scale patterns are present in the region of high field intensity over Terra Cimmeria (TC) and Terra Sirenum (TS). This may indicate that a higher SH degree model would be justified to properly represent these data. Copyright 2014 by the American Geophysical Union, reprinted from Fig. 7 of Morschhauser et al. [2014] with kind permission from publisher John Wiley & Sons Ltd.

their histograms are shown in the left and right column of Fig. 8.1, respectively. For the vertically down (Z) component, the residuals are homogeneously distributed, but the horizontally north (X) and east (Y) components show some large-scale spatial correlations. These correlations might result from external fields that are slowly varying with solar activity and that cannot be represented by the static external field model. With regard to the weighted AB/SPO residuals, similar maps are shown in Fig. 8.2. According to this figure, the resulting data histograms have significantly larger tails than for the MPO data. Also, large-scale spatial correlations are visible for all three vector components. Both of these observations may be linked to the increased influence of non-crustal fields on the dayside. What is more, the residuals show small-scale patterns around the 180° meridian in the southern hemisphere where the highest field intensities (F) are present. These small-scale patterns may imply that the chosen maximum spherical harmonic (SH) degree is insufficient to adequately describe the AB/SPO data. Still, the maximum SH degree was chosen as a reasonable compromise between the fit to the data, the stability of the model, and the computational effort (Figs. 6.2 and 6.3).

8.3 DIRECT COMPARISON TO SELECTED DATA

The spatial distribution and statistics of the residuals, as presented above, are the most relevant measures to classify the quality of the fit to the data. In addition, a direct comparison of the model predictions to selected data may be helpful. Such a comparison is shown in Fig. 8.3, where the vertically down (Z) component of selected MPO data is shown in black and the respective predictions of the final model with and without the model nighttime external field are shown in blue and red, respectively. For this figure, the data were selected along a longitudinal profile of $\theta = 145 \pm 1°$ (Fig. 8.3a) and a latitudinal profile of $\phi = 357° \pm 1°$ (Fig. 8.3b). The longitudinal profile covers the strongest fields in Terra Cimmeria (TC) and Terra Sirenum (TS) ($\phi \approx 180°$) as well as the weakest fields over the Hellas ($\phi \approx 70°$) and Argyre ($\phi \approx 320°$) impact basins. From this profile, it is visible that noise in the data is low over the regions of strong fields whereas anomalies may easily be covered by noise in regions of weak fields. As an example, a weak anomaly is visible in the model predictions at $\phi = 340°$(c.f. Sec. 12.1), but hardly in the raw data. The latitudinal profile (Fig. 8.3b) covers a region of medium fields above Terra Arabia ($\theta \approx 60° - 110°$). Otherwise, the fields along this profile are weak. Again, some weak anomalies can hardly be discovered in the raw data due to the low signal to noise ratio. Namely, this is the case for the magnetic field anomaly at $\theta \approx 0° - 60°$ [Hood and Zakharian, 2001] and the above mentioned anomaly near the south pole at $\theta \approx 130° - 150°$. Besides, the contribution of the external field is strongest near the poles and relatively weak at mid-latitudes. For both profiles, some large outliers are present in the data. Such outliers justify the usage of

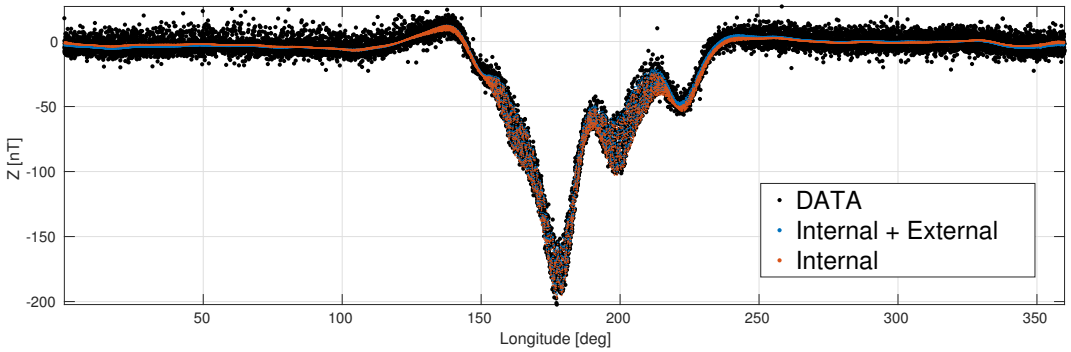

(a) $\theta = 145 \pm 1°$

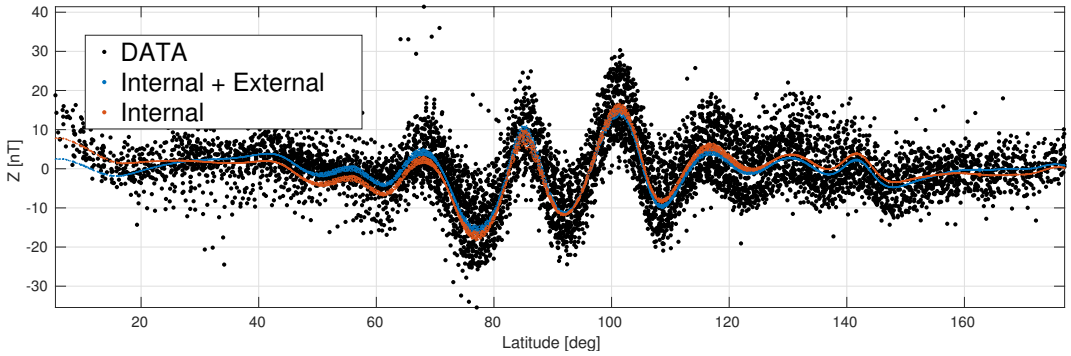

(b) $\phi = 357 \pm 1°$

Figure 8.3. The vertically down (Z) component of the magnetic field as predicted by the final model is shown along with the MPO data for the specified great circles. The data is shown in black, and the model field at the same positions for the final model, including external and internal field contributions, is shown in blue. In addition, the predictions of the crustal part of the final model model are shown in red.

a modified Huber norm, and the presented profiles demonstrate how the final model manages to ignore these. Otherwise, the model predictions approximately correspond to the mean of the data, as it would be expected from a least-squares fit[1,2].

A similar comparison for the AB/SPO is shown in Fig. 8.4 where two selected dayside data tracks are compared with the predictions of the final model[3]. In this figure, along-track data are shown in black, and the corresponding model predictions of the final model with and without external field contributions are shown in blue and red, respectively. Further, the lower panels of the two subfigures depict the location of the chosen satel-

1 The mean value m is the least-squares distance to a set of points x_i. Proof: The minimum of $d = \sum_{i=1}^{N} (m^* - x_i)^2$ with respect to m^* can be found by $\partial d/\partial m^* = -2 \sum_{i=1}^{N} (m^* - x_i) \stackrel{!}{=} 0$. As a result, it follows that $m^* = 1/N \left(\sum_{i=1}^{N} x_i \right) = m$, q.e.d.

2 The applied modified Huber norm is identical to a L2 norm if the data misfit is below a specified threshold (c.f. Sec. 6.3).

3 A profile similar to Fig. 8.3 cannot be shown for the AB/SPO data, as their spatial coverage is sparse.

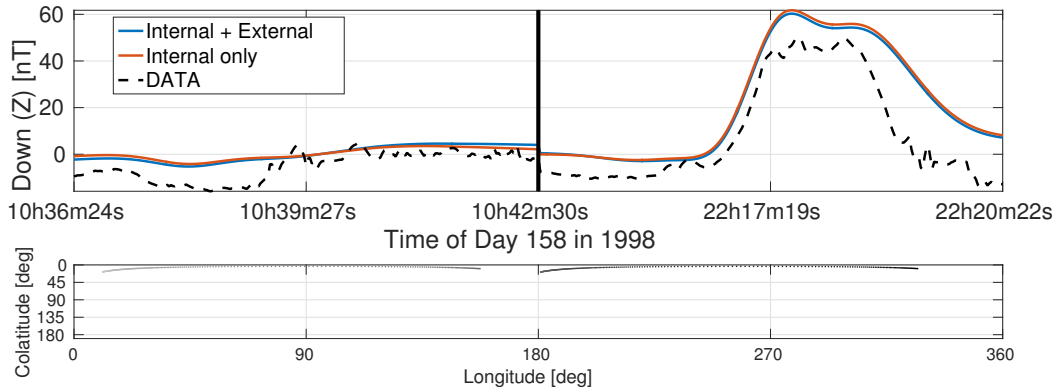

(a) Track near North Pole

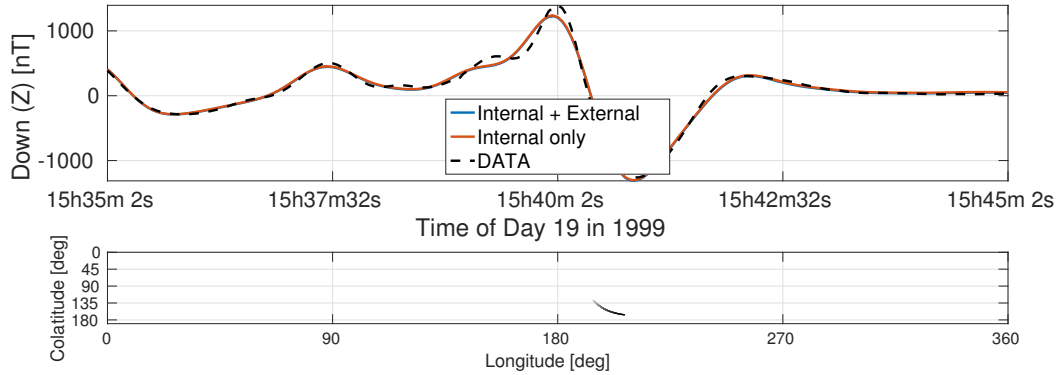

(b) Track in southern Terra Sirenum

Figure 8.4. The vertically down (Z) component of the model field and the corresponding AB/SPO data are shown along two selected MGS tracks. In the upper panels, the data are represented by the black dashed line, and the corresponding field as predicted by the final model, including external and internal field contributions, is represented by the blue solid line. In addition, the internal (crustal) part of the final model is represented by the red solid line. The lower panels show the planetocentric coordinates of the respective tracks.

lite track. In Fig. 8.4a, many small-scale fluctuations are present in the data between 10 h 39 m 27 s and 10 h 42 m 30 s. These fluctuations are most probably caused by external field variations and are not present in the final model. In contrast, the stronger anomaly at around 22 h 17 m 19 s has been fit by the model. This anomaly is consistent with other data tracks and corresponds to the north pole anomaly which has been described by Hood and Zakharian [2001]. In the same way, Fig. 8.4b shows another AB dayside track. This track is located in TS and samples very intense crustal fields. In this case, the model adequately fits the data, with the exception of some relatively small offsets at around 15 h 40 m 2 s. These offsets may result from the truncation of the model at SH degree $l = 110$. If so, a higher maximum degree and order would be required to fit the sharp peak intensities of the data (c.f. Sec. 8.2).

9 COMPARISON

In this chapter, I will discuss the influence and the effectiveness of the techniques which have been used to derive a robust model of the crustal magnetic field of Mars. First, the influence of regularization on the resulting model is addressed by comparing three models with different damping parameters λ. Subsequently, the L2 model[1] and the L1 model are compared in order to illustrate the effectiveness of using an L1 norm for regularization. In the same way, the effect of the applied modified Huber norm is investigated. Finally, I will conclude the chapter by evaluating the obtained final model with respect to previously published models of the crustal magnetic field of Mars.

9.1 REGULARIZATION PARAMETER

The L2 model, the L1 model, as well as the final model were regularized in order to reduce the leakage of noise into the model and in order to obtain a robust model (Sec. 5.5). However, regularization always comes at the cost of introducing a priori assumptions. Hence, it is important to choose a well-balanced trade-off between the influence of these assumptions and the resulting robustness of the model (Fig. 6.5). In the following, I will discuss three models which only differ in the applied damping parameter λ, but are otherwise similar to the L2 model. In particular, damping parameters of

- $\lambda = 0$ (undamped),
- $\lambda = 2$ (damping parameter of the final model, the L1 model, and the L2 model),
- $\lambda = 1000$ (upper limit of the permissible range in Fig. 6.5)

have been chosen in order to better understand the positive and negative influences of the regularization. The lower limit of the permissible range in Fig. 6.5 is $\lambda = 1$, and very close to the value chosen for the final model. Therefore, such a model is not discussed here.

In Fig. 9.1, the variances (Eq. 7.4) of the respective model parameters are presented in dependence of their degree l (ordinate) and order m (abscissa). For the undamped model (Fig. 9.1a), variances increase with increasing spherical harmonic (SH) degree l, reaching a maximum of $6.5 \cdot 10^{-2}\,\mathrm{nT}^2$ for g_{110}^{104}. In contrast, the variances are not only significantly reduced for the

1 For the naming of models, refer to Fig. 6.1 and Sec. 6.5.

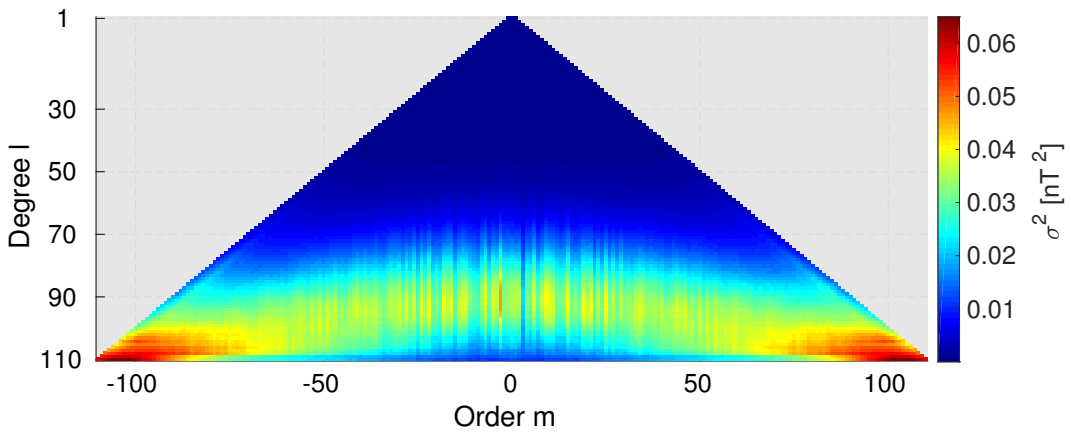

(a) $\lambda = 0$

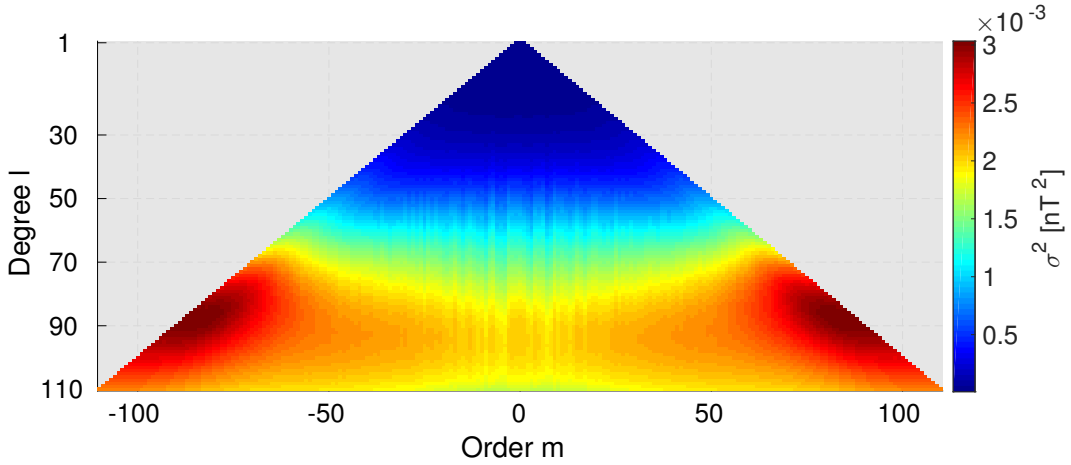

(b) $\lambda = 2$

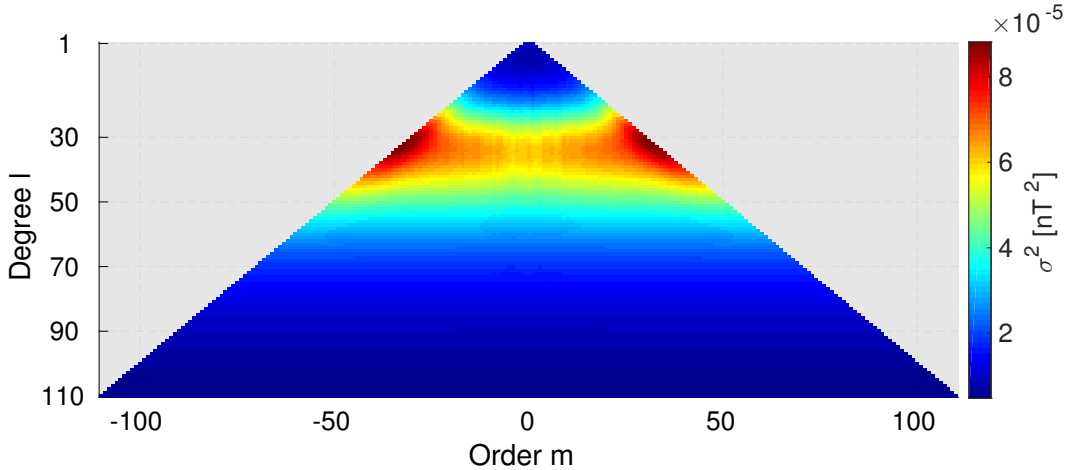

(c) $\lambda = 1000$

Figure 9.1. The variances of three different models are shown in dependence of order m (abscissa) and degree l (ordinate). The models differ only in the used damping parameter λ which is indicated in the respective captions, but are otherwise identical to the L2 model (Sec. 6.1).

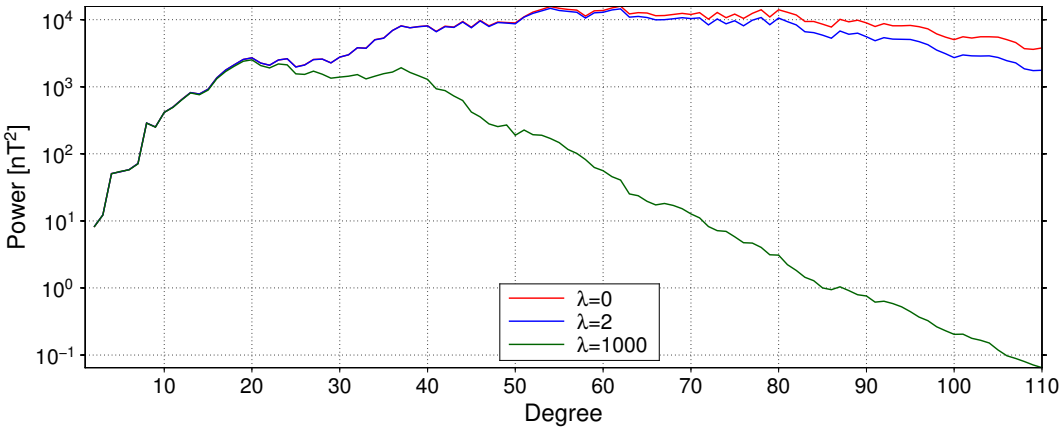

Figure 9.2. The Mauersberger-Lowes (ML) power spectrum at the reference radius of 3393.5 km is shown for models with different damping parameters λ. Otherwise, all the models are identical to the L2 model (Fig. 6.1).

regularized models (Figs. 9.1b and 9.1c), but also start to decrease above a certain SH degree l. In more detail, maximum variances of $3.0 \cdot 10^{-3}\,\mathrm{nT}^2$ (g_{88}^{85}) and $8.8 \cdot 10^{-5}\,\mathrm{nT}^2$ (g_{32}^{-32}) have been obtained for the models with damping coefficients of $\lambda = 2$ and 1000, respectively. Hence, the degree l at which the maximum variance is obtained is lower the stronger the damping coefficient λ. This is a direct consequence of the regularization, which strongly constrains the model at high SH degrees, i.e. at short spatial scales.

The influence of the regularization is also reflected in the Mauersberger-Lowes (ML) power spectrum. In Fig. 9.2, the ML power spectrum at the reference radius of $a = 3393.5\,\mathrm{km}$ is shown for the three different models. For these models, damping parameters of $\lambda = 2$ and $\lambda = 1000$ result in reduced spectral power for SH degrees of $l \geqslant 50$ and $l \geqslant 20$, respectively. Again, these coefficients are rather constrained by the regularization than by the data.

The negative influence of the regularization on the resolution of the model parameters can be quantified by the resolution matrix (Sec. 5.4). In Fig. 9.3, the maximum and the minimum of the relative resolution (Eq. 7.7) over all orders m of each degree l are shown. As expected, the undamped model (red line) is perfectly resolved. For the regularized models, however, the relative resolution decreases with increasing degree l and increasing damping parameter λ. For example, the maximum relative resolution over all degrees l is ~93 % for $\lambda = 2$ (blue line) and ~63 % for $\lambda = 1000$ (green line). As shown in Fig. 9.1, the model parameter variances also decrease with stronger regularization. This trade-off between a low model variance and a good model resolution is fundamental to the technique of regularization.

In Fig. 9.4, the influence of the damping parameter on the resulting model in the spatial domain is illustrated by showing the vertically down (Z) component of the predicted magnetic field at different altitudes (rows) and for

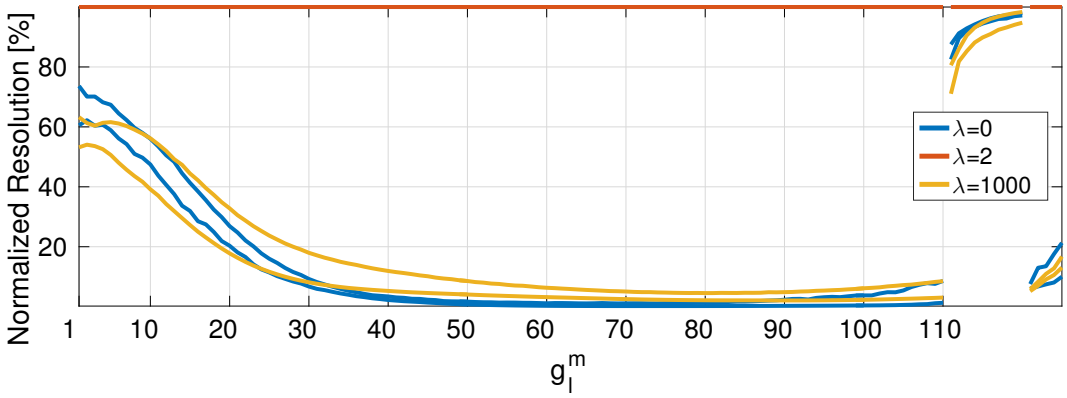

Figure 9.3. For each degree l, the minimum and maximum values of the relative resolution (Eq. 7.6) over all degrees m are shown in red for an undamped model ($\lambda = 0$), and in blue and purple for the models with damping parameters of $\lambda = 2$ and $\lambda = 1000$, respectively. Further, the SH degrees of one to one hundred and ten, as indicated on the abscissa, refer to the model of the crustal field. The coefficients corresponding to the models of the external night- and dayside are shown on the right end of the plot.

different damping parameters (columns) over a selected region. This region is centered at 180°E/0°S and contains strong crustal fields in its southern part and weak fields in its northern part. This choice allows to simultaneously assess the ability of the model to handle noise and to represent strong crustal anomalies. At the approximate mapping phase orbit (MPO) altitude of 400 km (top row of Fig. 9.4), the predicted field is almost independent of the applied damping parameter, at least in the considered range of $0 \leqslant \lambda \leqslant 1000$. In comparison, differences between the models become visible at an altitude of $h = 150$ km (middle row). At this altitude, the undamped model shows more structure on small scales as compared to the other models, especially for the region in the northeast quadrant of the map. However, these small-scale structures probably do not reflect the true nature of the crustal field, as only few AB/SPO data (shown by the color-coded circles) are available in this region. When the model is downward-continued to the mean surface altitude (bottom row), the crustal field predictions of the considered models differ significantly. In particular, many anomalies that are elongated in the north-south direction become visible for the undamped model, mainly in the northern part of the map. Such elongated anomalies are typical for temporally variable noise leaking into the model [Maus et al., 2006; Lesur et al., 2013]. The damped models efficiently suppress these elongated anomalies. At the same time, however, they also suppress strong fields in the southern part of the map, and many small scale anomalies disappear with increasing damping parameter λ. Likewise, peak field intensities (F) are reduced with increasing damping parameter.

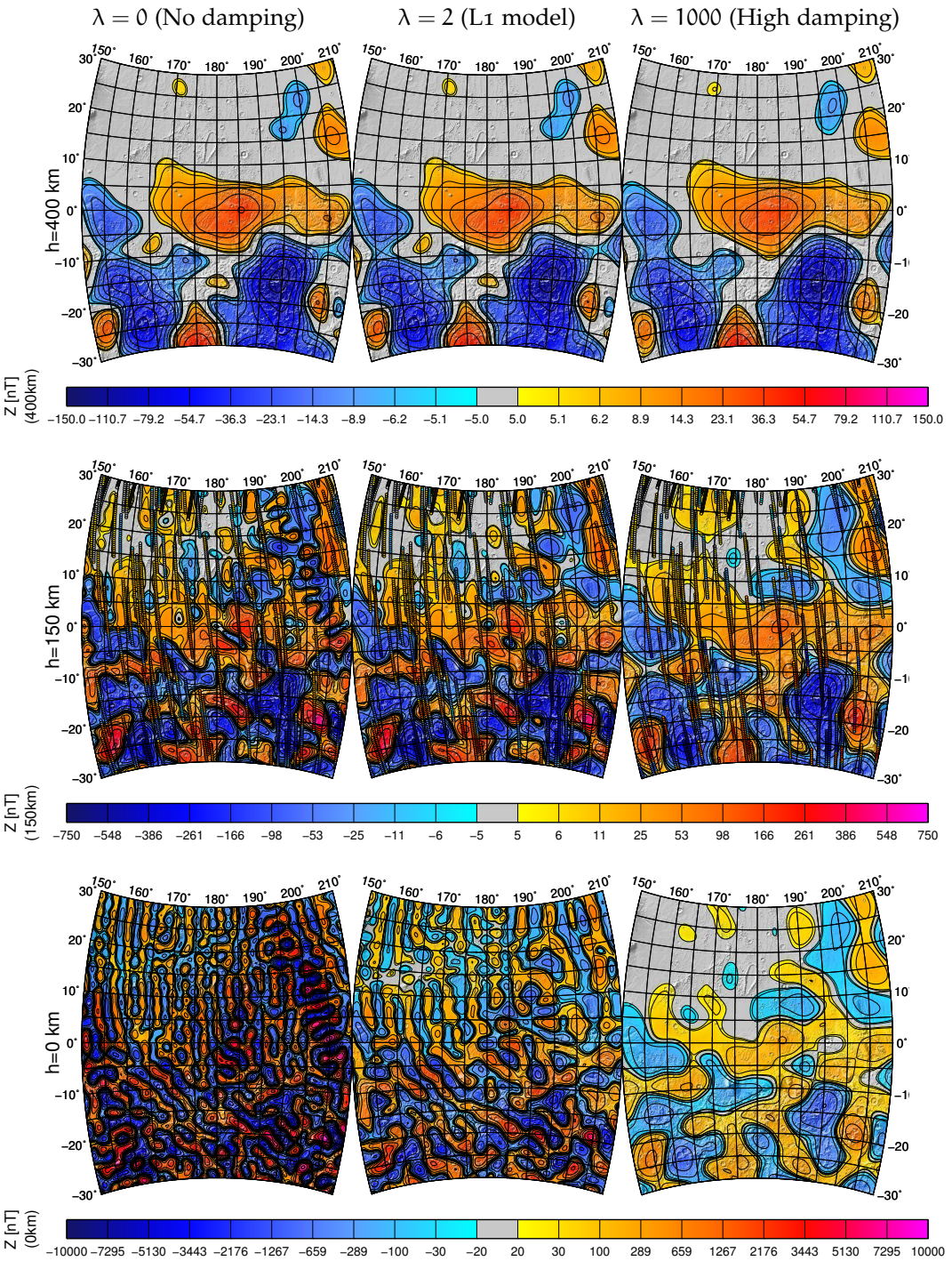

Figure 9.4. The vertically down (Z) component of the crustal field is shown as predicted from models with different damping parameters λ (columns) at altitudes of $h = 400$ km (top row), $h = 150$ km (middle row), and $h = 0$ km (bottom row) above the Martian mean radius of 3393.5 km, respectively. In addition, the shaded MOLA topography is shown. The map is centered at 180°E/0°S, and contains the ancient volcano Apollinaris Patera (Sec. 10.1.1) as well as the dichotomy boundary which separates regions of strong and weak crustal fields over this region. In addition, the AB/SPO data at 150 ± 30 km altitude are plot over the maps of 150 km altitude (middle row). Moreover, the locations of this and the following figures are shown on a global MOLA map in Fig. A.1.

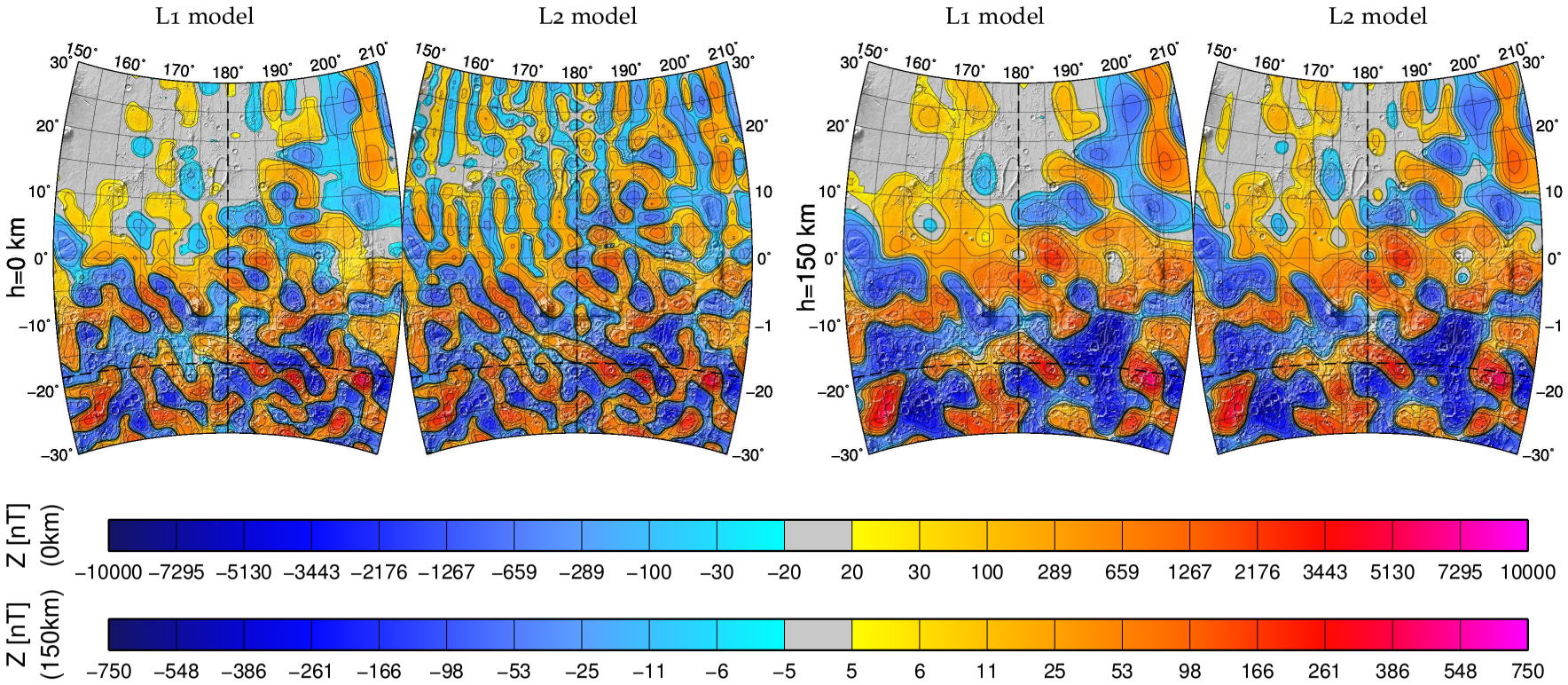

Figure 9.5. The vertically down (Z) component of the crustal field as predicted by the L1 model and the L2 model are compared at the mean surface radius of 3393.5 km ($h = 0$ km) and at $h = 150$ km altitude. The selected region is located at the dichotomy boundary with strong fields above the southern and weak fields above the northern part of the map. The map is centered at 180°E/0°S, close to the ancient volcano Apollinaris Patera, and plotted over shaded MOLA topography.

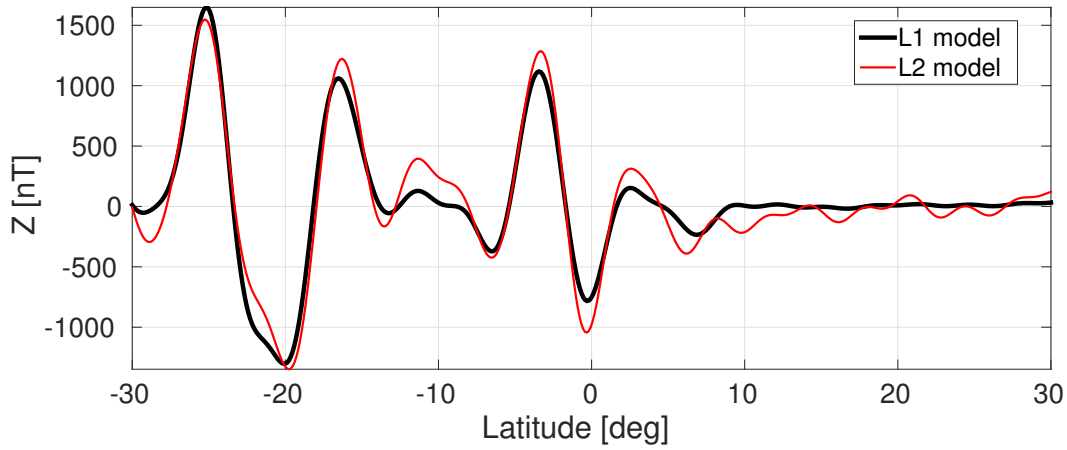

Figure 9.6. Comparison of the vertically down (Z) component of the crustal field as predicted by the L1 model (black line) and the L2 model (red line) along the meridian of $\theta = 180°$E at the mean surface altitude of 3393.5 km (c.f. vertical black dashed line in Fig. 9.5).

In summary, the employed regularization effectively decreases the uncertainty of the model parameters by applying an a priori constraint. For example, this is reflected in the model parameter variances which decrease with increasing damping parameter λ (Fig. 9.1). As well, the employed regularization removes power from weakly constrained coefficients of high SH degree and results in a more stable[2] model (Figs. 9.2 and 9.4). As a drawback, regularization leads to a lower model resolution (Fig. 9.3) and the fit to the crustal part of the signal may suffer (Fig. 6.5). Also, it should be kept in mind that the lower model variances result from an a priori constraint which may not reflect the true characteristics of the crustal field.

9.2 PERFORMANCE OF THE L1-NORM

The final model and the L1 model were regularized by using an iteratively reweighted least squares (IRLS) algorithm in order to approach an L1 norm for model complexity. As an advantage, an L1 norm allows for an efficient regularization which eventually leads to a stable model. With our choice of the measure for model complexity (c.f. Sec. 6.4), it also allows for strong localized gradients which are present in the Mars Global Surveyor (MGS) data (Sec. 1.2). In the same way as it has been done for different damping parameters (Sec. 9.1), the efficiency of the L1 norm will be examined in the following. First, the ML power spectra (Fig. 9.7) of the L1 model (red line) and the L2 model (blue line) are very similar. Differences include $> 1\%$ more power in the L2 model for degrees $39 \leqslant l \leqslant 84$, up to 20% less power in the L2 model for degrees $l > 84$, and a strong drop in power in

2 A stable model can be downward-continued to the surface without poorly constrained coefficients leading to unnaturally strong and correlated predicted fields.

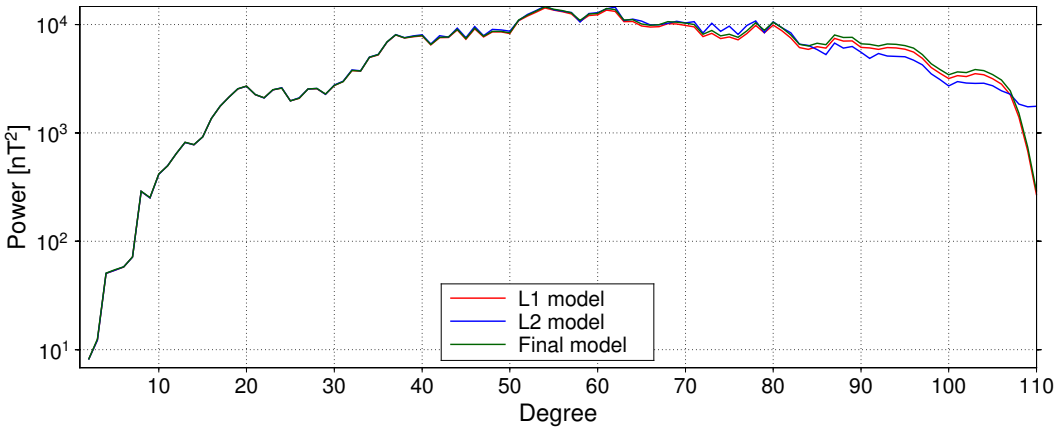

Figure 9.7. ML power spectra of the L1 model (red line), the L2 model (blue line), and the final model (green line), evaluated at the mean Martian radius of 3393.5 km.

the L1 model for degrees $l > 106$. Second, the two models fit the MPO data almost equally well (Tab. 9.1), but the L1 model is more stable when downward-continued. Still, the L1 model provides a slightly weaker fit to the AB/SPO data. Finally, the vertically down (Z) component of the crustal field as predicted by the L1 model is compared in Fig. 9.5 to the respective field predictions of the L2 model (c.f. Fig. 6.1) over the same region as in Fig. 9.4. As shown in Fig. 9.5, the two models differ only slightly at 150 km altitude (right part of the figure). Conversely, they differ significantly when downward-continued to the mean surface altitude (left part of the figure). In particular, the L1 model predicts anomalies that are elongated in the north-south direction and which are present in the northern part of the map. Again, these elongated anomalies are typical for correlated noise leaking into the model [Maus et al., 2006; Lesur et al., 2013], and the L1 model effectively suppresses this noise. In contrast to the L2 model, however, the strong anomalies of the crustal magnetic field in the southern part of the map keep their structure and peak strengths. This is confirmed by Fig. 9.6, where the vertically down (Z) magnetic field component of the L1 model (black line) and the L2 model (red line) are shown at surface altitude along the meridian of $\theta = 180°$E.

9.3 PERFORMANCE OF THE HUBER WEIGHTS

Incompatible data with strong non-crustal contributions have a strong impact on the model when a least-squares measure (L2 norm) of misfit is used. In this work, a modified Huber norm was used to handle such data outliers. This norm downweights data outliers that have a misfit larger than a threshold δ_c, while it preserves a L2 norm for more compatible data (Sec. 6.3). As a consequence, it is expected that the misfit of data outliers increases in the final model as compared to the L1 model. Here, the difference $\boldsymbol{\Delta}$ between

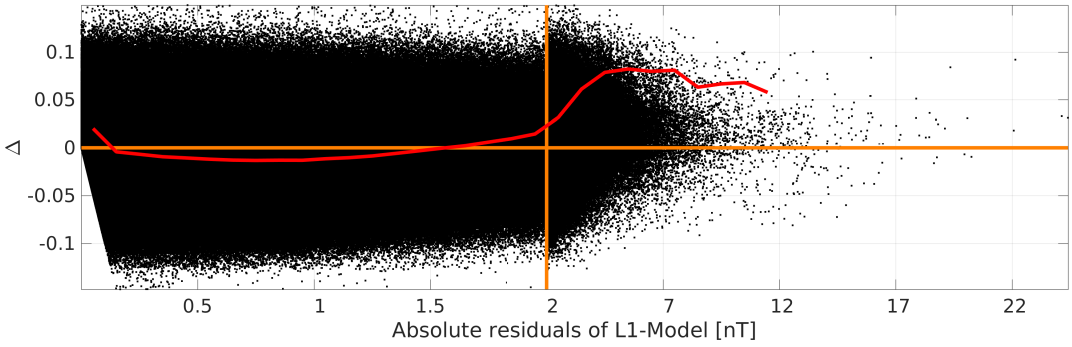

(a) MPO nighttime

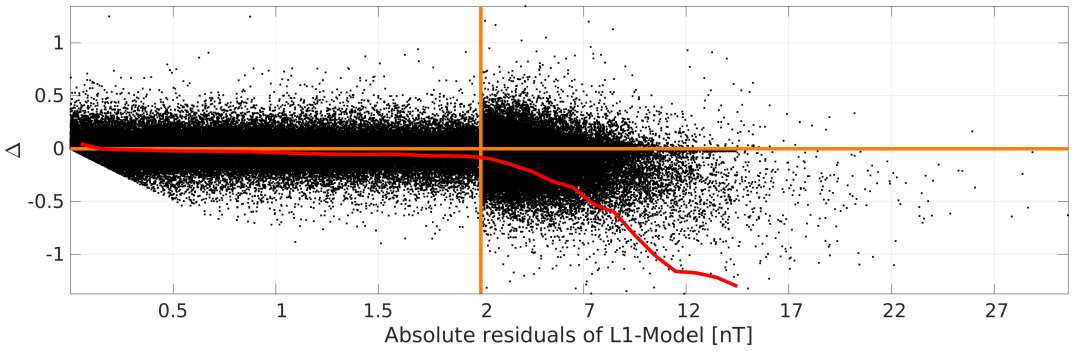

(b) AB/SPO day- and nighttime

Figure 9.8. The difference of the absolute residuals between the final model and the L1 model for different data sets and for the horizontally north (X), east (Y), and vertically down (Z) components (Δ in Eq. 9.1) are shown in dependence of the absolute residuals as calculated from the L1 model. In addition, the red line represents the mean for bins of 0.1 nT for values on the abscissa lower than two and for bins of 1.0 nT otherwise (exaggerated by a factor of five), if more than 100 data points were present in the respective bin. The orange horizontal and vertical lines indicate $\Delta = 0$ and the threshold value $\delta_{c,MPO}$ (Tab. 6.1), respectively. Also, note that the abscissa is stretched for values below one.

the absolute weighted residuals of the final model with Gauss coefficients $\mathbf{g}_{2,12}$ (Eq. 6.31) and those of the L1 model with Gauss coefficients $\mathbf{g}_{0,10}$ will be investigated in order to verify the expected behavior, and Δ is given by

$$\Delta_i = \frac{1}{\sigma_i}\left(\left|\mathbf{d}_i - \sum_j \mathbf{D}_{i,j}(\mathbf{g}_{2,12})_j\right| - \left|\mathbf{d}_i - \sum_j \mathbf{D}_{i,j}(\mathbf{g}_{0,10})_j\right|\right). \tag{9.1}$$

In Fig. 9.8, the Δ_i for all vector components of each datum i are shown as black dots and plotted against the absolute residuals ρ_i of the L1 model, i.e. $\rho_i = \left|\mathbf{r}_i^{L1}\right|$. Further, the Δ_i have been averaged over bins of 1 nT for $\rho_i > 2\,\text{nT}$ and over bins of 0.1 nT for $\rho_i \leqslant 2\,\text{nT}$ and the result is indicated by the red line (exaggerated by a factor of five) if more than 100 data were present in the respective bin. In the following, we will refer to this average

Table 9.1. Statistics of the residuals for the horizontally north (X), east (Y), and vertically down (Z) magnetic field components of the L2 model, the L1 model, and the final model with respect to different data sets[a].

		L2 MODEL			L1 MODEL			FINAL MODEL		
DATA CLASS		σ	σ^w	μ^w	σ	σ^w	μ^w	σ	σ^w	μ^w
MPO	X	6.41	1.11	0.03	6.42	1.11	0.03	6.42	1.11	0.07
night	Y	7.20	1.12	-0.07	7.20	1.12	-0.07	7.20	1.12	-0.07
$\Delta_d = 80\,km$[b]	Z	5.89	1.09	0.15	5.90	1.09	0.15	5.90	1.09	0.15
AB/SPO	X	9.71	1.69	-0.30	9.85	1.72	-0.30	9.78	1.71	-0.29
night	Y	8.51	1.45	-0.06	8.67	1.48	-0.05	8.62	1.47	-0.05
($h \leqslant 348\,km$)	Z	8.67	1.65	-0.14	8.94	1.70	-0.13	8.86	1.69	-0.13
AB/SPO	X	16.61	1.96	-0.29	16.89	1.99	-0.29	16.77	1.98	-0.27
day	Y	16.26	2.12	0.03	17.06	2.22	0.03	16.92	2.20	0.03
($h \leqslant 200\,km$)	Z	13.62	1.95	-0.12	14.24	2.04	-0.12	14.03	2.01	-0.11

[a] The standard deviation of the residuals is given by σ, and the average value of the residuals is given by μ, where the superscript w indicates that the respective values were weighted with their a priori data weights as described in Sec. 4.1 and 4.2.
[b] For the MPO data, the data set has been reduced to save computational resources (Sec. 4.1). In particular, one datum was selected every $\Delta_d = 80\,km$ on the projected surface track of the satellite orbit.

as $\overline{\Delta}$. Moreover, the orange horizontal line indicates unchanged residuals ($\Delta_i = 0$) and the vertical orange line corresponds to the threshold δ_c as used in the final model for the MPO data (Tab. 6.1). With regard to the MPO data (Fig. 9.8a), $\overline{\Delta}$ is above zero if the initial absolute residuals of the L1 model were larger than ~2.0 nT. What is more, $\overline{\Delta}$ significantly increases if the absolute residuals of the L1 model were above the corresponding threshold of $\delta_{c,MPO} = 2.0\,nT$ (Tab. 6.1). Hence, the modified Huber norm indeed leads to a larger misfit for incompatible data. As well, it allows to reduce the misfit to data which are compatible with the model. For the AB/SPO data (Fig. 9.8b), an L2 norm instead of the modified Huber norm has been used, and the misfit to the AB/SPO data is lower for the final model than for the L1 model: Obviously, the application of the modified Huber norm to the MPO data leads to a better fit to the AB/SPO data (c.f. Tab. 9.1), in particular for initial absolute misfits larger than $\delta_{c,MPO} = 2.0\,nT$ (Fig. 9.8b).

9.4 OTHER PUBLISHED MODELS

The final model is compared to the models of the crustal field by Cain et al. [2003], Arkani-Hamed [2004a], and Langlais et al. [2010][3] (c.f. Tab. 1.1).

3 This model is expressed in terms of equivalent source dipoles (ESDs). Here, an equivalent SH model to degree and order 358 as provided by the authors was used to calculate the residuals of this model (c.f. Tab. 9.2). Further, the SH representation was truncated to degree $l = 130$ when the ML power spectrum and the predicted surface fields were examined

Table 9.2. Statistics of the residuals for the horizontally north (X), east (Y), and vertically down (Z) magnetic field components for different published models with respect to different data sets. Note that a larger selection of MPO data has been used as compared to Tabs. 8.1 and 9.1[a].

Data Class		Final model [c]		LA10[d]		CA03[e]		AR04[f]	
		σ	μ	σ	μ	σ	μ	σ	μ
MPO[b]	X	**6.77**	**0.92**	6.81	1.11	6.95	0.94	7.26	0.82
night	Y	**7.74**	-0.10	7.76	-0.10	7.83	-0.10	7.96	-0.11
	Z	**6.21**	**1.07**	6.41	1.08	6.49	1.06	6.33	1.08
AB/SPO	X	**9.78**	-1.65	9.39	**-0.04**	12.33	-0.76	66.78	-3.97
night	Y	**8.62**	-0.32	9.35	**-0.23**	10.24	-0.26	53.30	-2.44
($h \leqslant 348$ km)	Z	**8.86**	-0.69	9.81	-2.32	13.05	**-0.27**	80.28	2.86
AB/SPO	X	16.77	**-2.28**	**16.73**	-3.26	17.95	-2.80	40.68	-3.34
day	Y	**16.92**	0.24	17.62	**0.21**	17.31	0.35	74.74	-0.43
($h \leqslant 200$ km)	Z	**14.03**	-0.75	16.52	-0.89	15.34	**-0.13**	82.69	0.56
ER data ($h = 185$ km)	F	21.45	4.36	**19.68**	2.96	22.41	**2.77**	29.07	-12.28

[a] The standard deviation of the residuals is given by σ, and the average value of the residuals is given by μ. Note that wrong numbers are given in Table 2 of Morschhauser et al. [2014] for the models of Cain et al. [2003] and Langlais et al. [2010]. The numbers given here are correct.
[b] For the MPO data, the full nightside data set of 56.3 million vector measurements has been evaluated.
[c] This work [d] Langlais et al. [2010] [e] Cain et al. [2003] [f] Arkani-Hamed [2004a]

This comparison includes an examination of their misfit to selected data, their robustness when downward continued to the surface, and their power spectra.

As far as the misfit of the selected models to the data is concerned, we examine the standard deviation (STD) σ and the mean μ of the residuals (Sec. 8.1) for four different data sets (Tab. 9.2). These data sets include the MPO nightside data[4], the AB/SPO nightside data below the minimum MPO altitude of $h = 348$ km, the AB/SPO dayside data below $h = 200$ km altitude, and the electron reflectometer (ER) field intensity (F) data as provided by Lillis et al. [2008a]. Overall, it should be kept in mind that this comparison is biased as the pre-processing and selection of data was different for each of the models (c.f. Tab. 1.1). We start by considering the residuals of the final model and the ESD model of Langlais et al. [2010]. In this case, the final model achieves slightly lower STDs σ, except for the horizontally north (X) component of the AB/SPO dayside data and the ER intensity (F) data. However, the mean μ of the model of Langlais et al. [2010] is closer to zero

(Figs. 9.10 and 9.11).

4 This MPO dataset slightly differs from the MPO dataset which was used to derive the final model, where one data point every 80 km was selected.

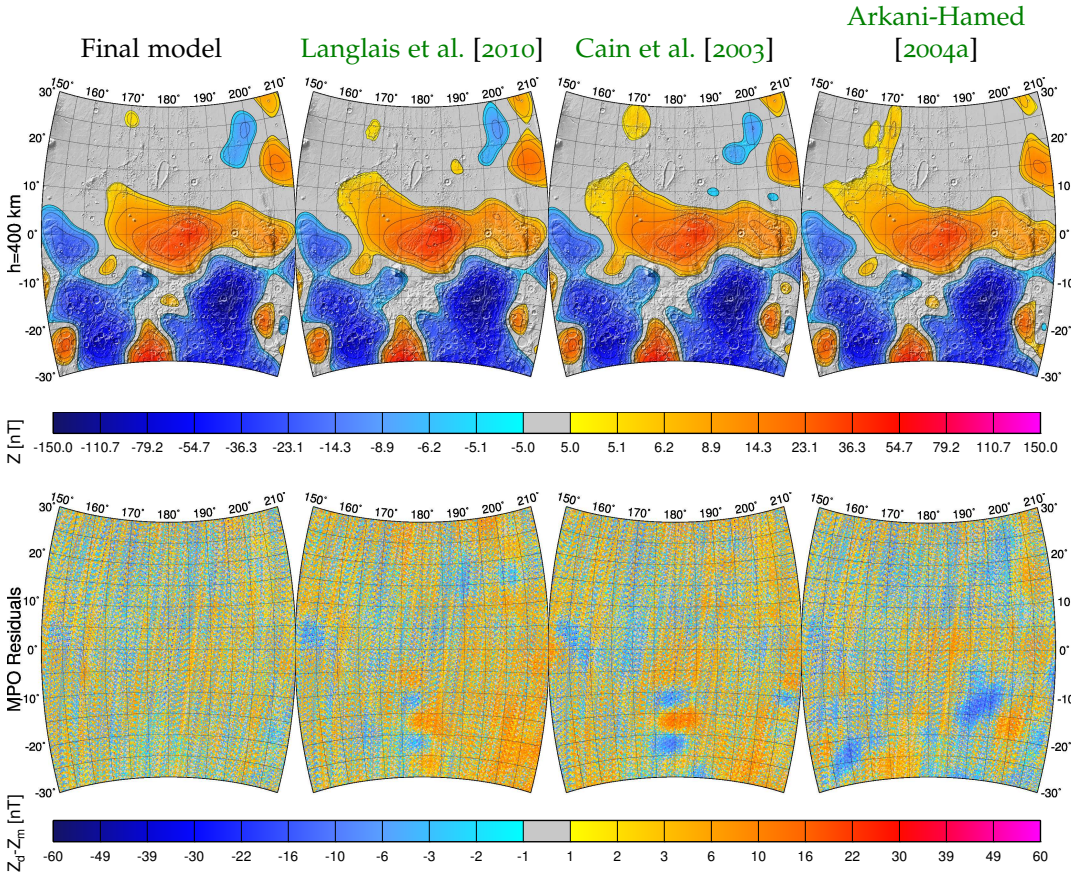

Figure 9.9. The vertically down (Z) field component as predicted by different published models and the final model is presented in this figure. In the top row, the predicted magnetic field at the MPO altitude of $h = 400$ km is shown over a region with strong and weak crustal fields, located at the Martian dichotomy boundary (Fig. 9.4). The map is centered at 180°E/0°S, close to the ancient volcano Apollinaris Patera, and plotted over shaded MOLA topography. In the second row, the residuals to the nighttime MPO data are shown above the same region.

for some AB/SPO data sets. The model of Langlais et al. [2010] is the only model which was also fit to the ER data set, and provides the overall best fit to these data. Still, the ER residuals are relatively large as compared to the AB/SPO residuals. Consequently, we conclude that the ER data are not entirely compatible with the fluxgate magnetometers on MGS (MAG) data. Next, we examine the SH model of Cain et al. [2003]. For this model, a poorer fit to the data is obtained as compared to the final model and to the model of Langlais et al. [2010]. The model of Cain et al. [2003] was expanded up to SH degree $l = 90$ only, which may have resulted in the lower fit to the low altitude AB/SPO nightside data. Finally, the model of Arkani-Hamed [2004a] offers the poorest fit to the AB/SPO data. Again, the reason for the poor fit to the AB/SPO data may be the truncation at degree and order $l = 62$, which is not sufficient to represent the low altitude data. Also,

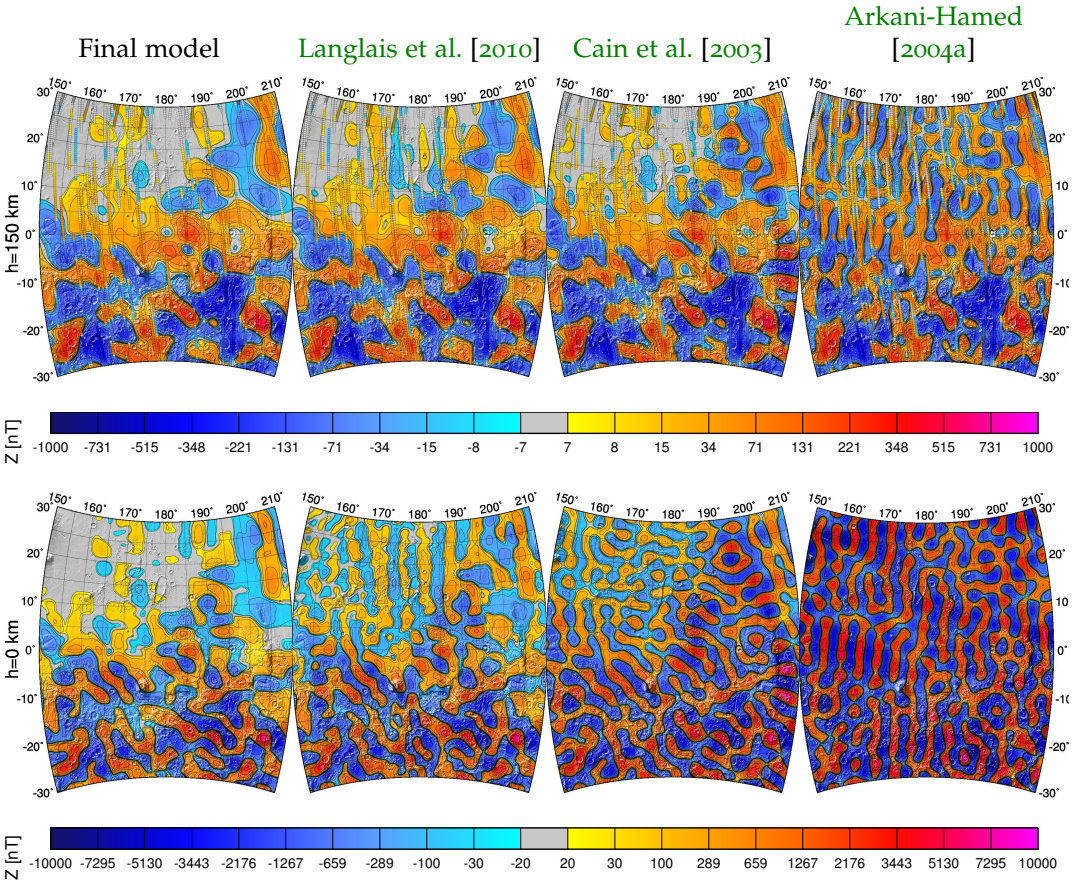

Figure 9.10. The vertically down (Z) field component as predicted by different published models and the final model is shown at different altitudes above the same region as in Fig. 9.9. In the top row, the predicted magnetic field at an altitude of $h = 150\,\text{km}$ is shown along with the AB/SPO data within an altitude of $h = 150 \pm 30\,\text{km}$. In the second row, the field was downward-continued to the mean surface radius of $r = 3393.5\,\text{km}$ ($h = 0\,\text{km}$).

this model is based only on the vertically down (Z) component of the MPO data. The reasoning behind this selection was the reduced contamination of the vertically down (Z) component by external fields. However, this comes at the cost of a poor fit to the remaining MPO data. Overall, the residuals reflect the particular way in which each model was derived. With respect to the STDs σ, the final model provides the best fit to all data sets (shown in bold script in Tab. 9.2) except for the horizontally north (X) component of the AB/SPO dayside data. However, the situation is less clear for the mean values μ. Still, the model of Langlais et al. [2010] is doing the best job in this case.

Next, we compare the different model predictions of the vertically down (Z) component of the magnetic field at the MPO altitude ($h = 400\,\text{km}$) over the same region as in Fig. 9.4. In the top row of Fig. 9.9, the predicted field at this altitude is shown, and the considered models agree well over most

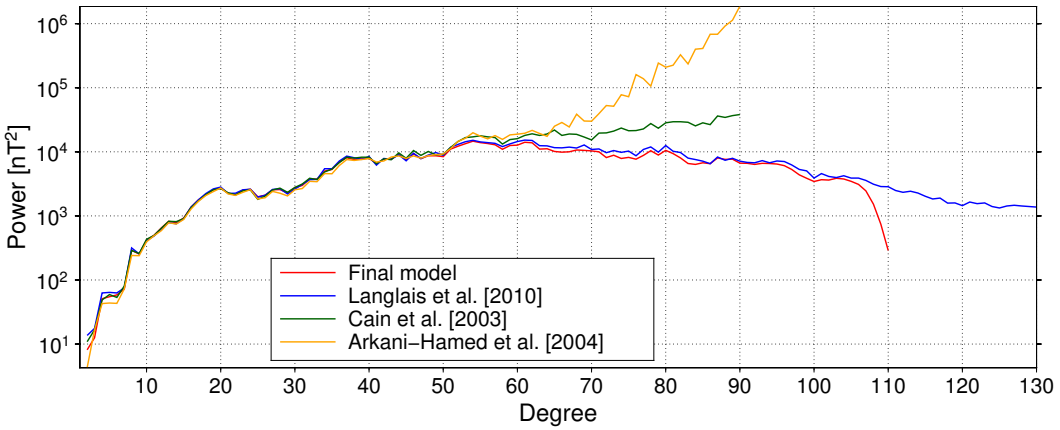

Figure 9.11. The ML power spectrum is shown for different models of the crustal field as evaluated at the mean Martian radius of 3393.5 km. The power spectrum of the final model is shown by a red line. For comparison, the models of Langlais et al. [2010] (green line), Cain et al. [2003] (blue line), and Arkani-Hamed [2004a] (orange line) are also shown.

of the region. Still, local differences exist, for example at 180°E/15°S where a small positive field signature is present in the field predictions of the final model and the model of Arkani-Hamed [2004a] only. Indeed, when the respective residuals are considered (bottom row of Fig. 9.9), it turns out that these models better resemble the data at this location. Even more, the final model offers the best fit to the MPO data in the complete displayed region. Turning to the predicted field at lower altitudes, we consider the vertically down (Z) component at an altitude of $h = 150$ km (top row of Fig. 9.10) for the same region as above. At this altitude, the final model as well as the models of Langlais et al. [2010] and Cain et al. [2003] are still similar. The model of Arkani-Hamed [2004a], however, suffers from noise in the form of latitudinally elongated anomalies (c.f. Sec. 9.2). At the surface altitude (bottom row of Fig. 9.10), such anomalies appear in most of the published models. The unregularized model of Arkani-Hamed [2004a] should not be used at this altitude, and the unregularized model of Cain et al. [2003] shows significant noise in the northern part of the map, especially where AB/SPO data are missing. The model of Langlais et al. [2010], on the other hand, shows a relatively low level of noise. Still, the final model shows the overall lowest level of noise, but slightly less detail in the southern part of the region. In any case, it is difficult to asses which part of the predicted field is real and which part is influenced by noise. Generally, the downward-continued field should be interpreted with utmost care. As well, the limited model resolution and the a priori assumptions should be kept in mind when interpreting the magnetic field map.

To conclude, the ML power spectra of the different models are shown in Fig. 9.11. On the whole, their shapes are similar, i.e. the respective peaks and troughs occur at around the same SH degree in most cases. Likewise,

the power spectrum of the final model falls within $1000\,\mathrm{nT}^2$ of the other considered models for SH degrees $l < 46$. For higher degrees, however, the power spectra start to diverge as the signal to noise ratio of the data decreases.

Overall, the final model shows the least amount of noise over regions of low field intensity (Fig. 9.10). At the same time, the final model model provides a good fit to the data and preserves the sharp localized anomalies in the high-field regions. Amongst other techniques, this has been mainly achieved by applying an L1 norm for regularization (Fig. 9.5).

Part V

APPLICATION TO OPEN QUESTIONS

The final model will be used to address some of the open questions discussed in Ch. 2. First, I will address the lifetime of the Martian dynamo by investigating the magnetic signature of ancient volcanoes and impact craters. Next, a model of the magnetization is derived which can be used to constrain magnetic minerals. Finally, I will present some examples of isolated magnetic field anomalies which contain information on paleopole directions. Throughout this chapter, however, the respective discussions will neither be exhaustive nor quantitative. Rather, I intend to outline how the final model can be used to decipher the mysteries of Mars.

10 TIMING OF THE CORE DYNAMO

It is widely accepted that the Martian crust was magnetized by a global magnetic field of internal origin, i.e. a field originating from a core dynamo [Acuña et al., 1998]. However, it is disputed when and how long this internal field was active (Sec. 2.1): On one hand, the lack of an observable field over the largest impact basins suggests a cessation time of around $4.0-4.1$ Gyr ago (early Noachian, Michael [2013]) [Acuña et al., 1999; Mohit and Arkani-Hamed, 2004; Lillis et al., 2008; Lillis et al., 2013a]. On the other hand, the magnetic signatures of most volcanoes indicate a dynamo shutdown at around $3.6-3.7$ Gyr ago (early Hesperian, Michael [2013]) [Lillis et al., 2006; Langlais and Purucker, 2007; Hood et al., 2010; Milbury et al., 2012]. In comparison to these studies, the robustness of the final model and its high resolution will allow to study the magnetic field signature of impact craters and volcanoes at surface altitude. In consequence, the coalescence effect[1] will be reduced and anomalies of smaller spatial scale can be analyzed.

10.1 MAGNETIC SIGNATURE OF VOLCANOES

Lithospheric temperatures in active volcanic regions can exceed the Curie temperature. Then, the respective magnetic minerals will acquire thermoremanent magnetization if an ambient field is present. Similarly, previously magnetized crust will thermally be demagnetized if an ambient field is absent [Johnson and Phillips, 2005; Lillis et al., 2006] (Sec. 2.3). Hence, the magnetic signature of volcanic regions can be used to constrain the lifetime of the Martian core dynamo (e.g., Langlais and Purucker [2007]; Hood et al. [2010]; Lillis et al. [2006]). As a caveat, however, Lillis et al. [2013a] mentioned that this approach works under two restrictions only: first, a large volume of crust must be (de)magnetized at approximately the same time, requiring large magma chambers, sills and dikes. Second, the surface age of the volcanic feature does not necessarily correspond to the age of the (de)magnetization event. In particular, intrusions might be important and earlier events could be covered by later activity. With this in mind, the magnetic signatures of the highland volcanoes Apollinaris Patera, Tyrrhena Patera, Hadriaca Patera, and Syrtis Major will be discussed[2]. In addition, I will present the magnetic signature associated with a recently discovered volcanic region in Arabia Terra. Finally, a short comment on the magnetic

1 The coalescence effect describes the blurring of magnetic field anomalies of small wavelengths with increasing altitude.

2 Please refer to Fig. A.1 for an overview of regions on Mars.

signature of highland volcanoes in Malea Planum will conclude this chapter. However, the most prominent volcanic regions, namely Tharsis and Elysium, will not be discussed. These volcanic regions have been active throughout the history of Mars, may have been largely demagnetized, and have been investigated elsewhere [Johnson and Phillips, 2005; Lillis et al., 2009].

10.1.1 *Apollinaris Patera*

Apollinaris Patera, an ancient Martian volcano, is located near the dichotomy boundary (Fig. 10.1a). It is marked by a black-white circle in Fig. 10.1 and is surrounded by Elysium Planitia to its northwest, Gusev crater[3] to its south, and part of the Medusae Fossae formation in Lucus Planum to its east [Werner, 2009; Hood et al., 2010]. The volcanic edifice is elevated by 5 km relative to its surroundings and it extends to 189 x 278 km in size [Plescia, 2004] (Fig. 10.1a). Turning to the age of Apollinaris Mons, crater counting statistics indicate that the main volcanic edifice was emplaced at around 3.81 Gyr ago [Werner, 2009; Robbins et al., 2011] (Noachian volcanic edifice unit (Nve) in Fig. 10.1f). Its latest activity is preserved in the caldera as well as a southward extending lava fan (Hesperian volcanic edifice unit (Hve) in Fig. 10.1f) which are dated to $3.52 - 3.71$ Gyr [Werner, 2009; Robbins et al., 2011]. Further, a high-density magma chamber is indicated by a positive gravity anomaly of about 400 mGal (Fig. 10.1e) [Langlais and Purucker, 2007].

As indicated by the dark gray points in Fig. 10.1b, ER data are missing over Apollinaris Patera[4], and the only low-altitude data over Apollinaris Patera were obtained from two AB dayside data tracks (labeled A and B

3 Gusev crater is the landing site of the Mars Exploration Rover "Opportunity".

4 The ER cannot sample the Martian magnetic field in regions of closed field lines (Sec. 3.2).

Figure 10.1. (Next page.) In this figure, different aspects of the region surrounding the volcano Apollinaris Patera are shown: (a) MOLA topography with the location of Apollinaris Patera (black-white solid circle) (b) The magnetic field intensity (F) as measured by ER at 185 km altitude. Dark gray points indicate areas where data are missing, and light gray points indicate field intensities (F) that are below the detection limit. (c) Magnetic field intensity (F) and horizontal field directions at the surface altitude as predicted by the final model. (d) Field intensity (F) as predicted by the final model at 185 km altitude. The colored circles represent the AB/SPO field intensity (F) and larger circles represent data which is closer to the mapped altitude. (e) Free-air gravity model JPL MRO0110B2, truncated at SH degree $l = 95$ [Konopliv et al., 2011] (f) Geologic map of Tanaka et al. [2014]. The reference to colors and geological units can be found in the original publication [Tanaka et al., 2014]. The location of this and the following figures is shown on a global MOLA map in Fig. A.1.

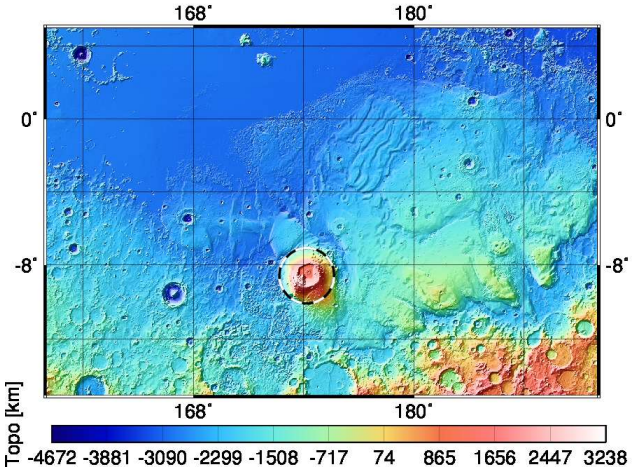

(a) MOLA Topography

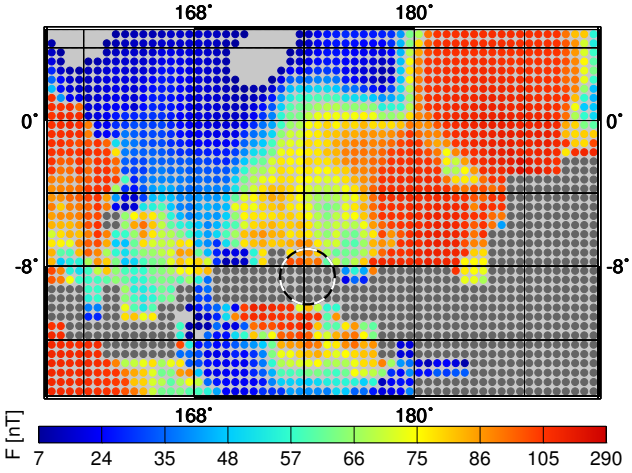

(b) ER data at 185 km altitude [Lillis et al., 2008a]

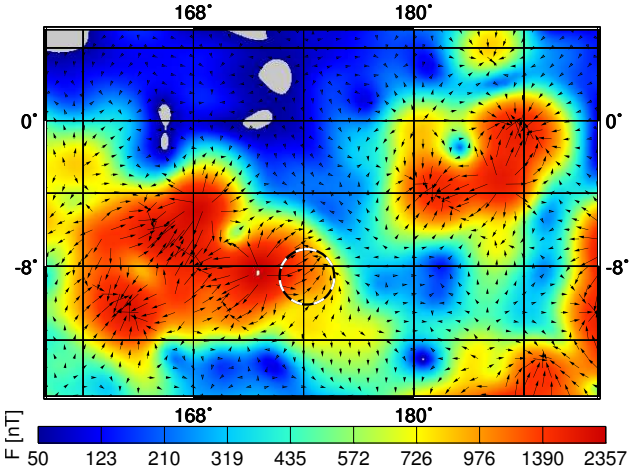

(c) Crustal field at surface altitude

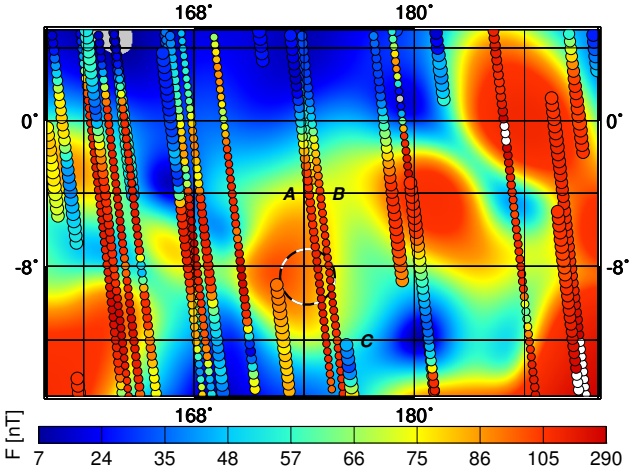

(d) Crustal field at 185 km altitude

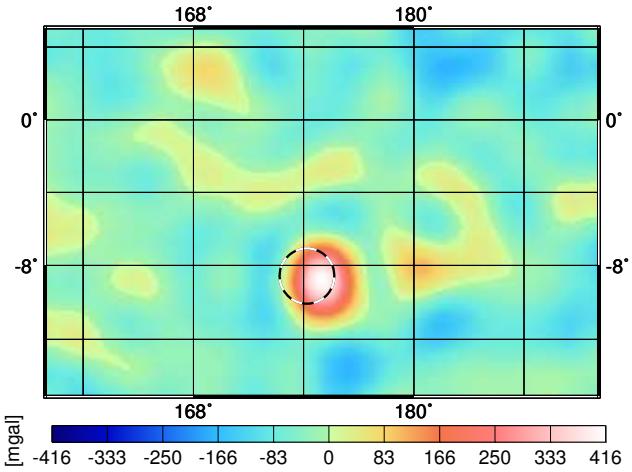

(e) Free-Air gravity [Konopliv et al., 2011]

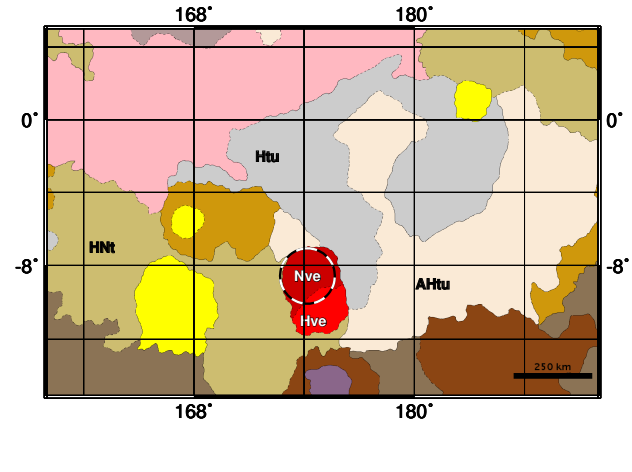

(f) Geologic Map [Tanaka et al., 2014]

Figure 10.1. Caption on previous page.

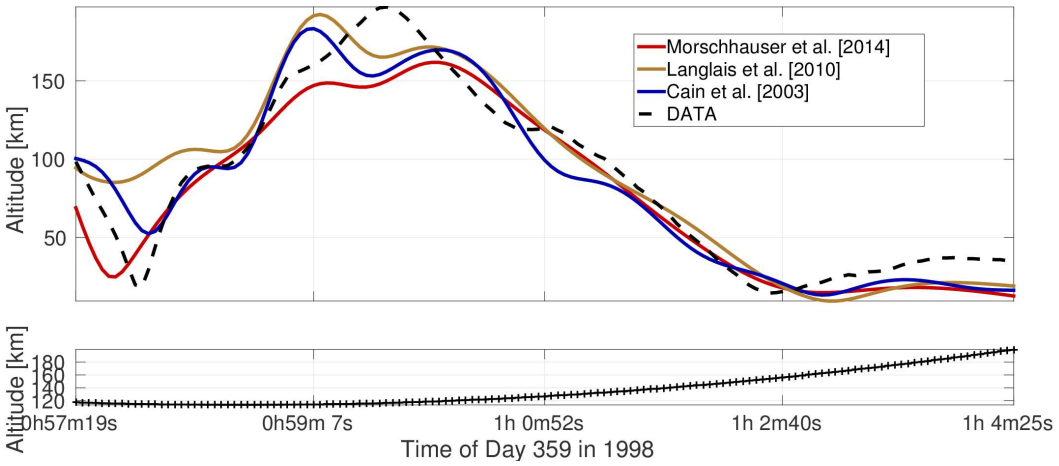

(a) Profile A of Fig. 10.1d

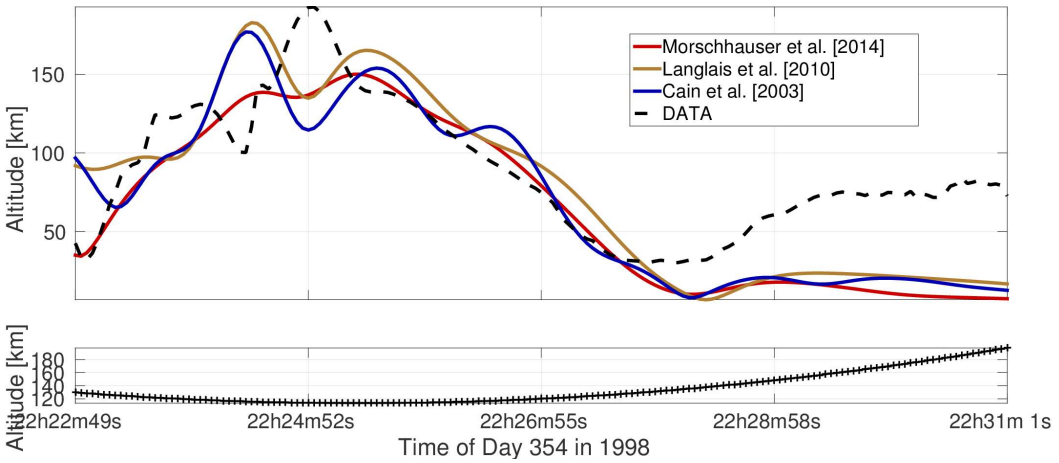

(b) Profile B of Fig. 10.1d

Figure 10.2. Two AB/SPO data tracks over Apollinaris Patera are shown along with several published models of the crustal magnetic field. As well, the altitude over the mean surface and the timestamps of the data are shown. The profiles correspond to (a) the profile A and (b) the profile B of Fig. 10.1d.

in Fig. 10.1d[5]). Hood et al. [2010] interpreted these data[6] as evidence for a positive magnetic anomaly associated with Apollinaris Patera, and this interpetation is in accordance with two models of the crustal field [Whaler and Purucker, 2005; Langlais and Purucker, 2007]. As well, the final model predicts a magnetic field anomaly at Apollinaris Mons with a maximum field intensity (F) of about 85 nT at 185 km altitude (Fig. 10.1d). However, this anomaly is weaker than for the two AB data tracks. In detail, the modeled and observed field intensities (F) are shown by a solid red and dotted black line in Fig. 10.2, respectively. For comparison, the model predictions of Cain et al. [2003] (solid blue line) and Langlais et al. [2010] (solid brown

5 The AB tracks are indicated by color-coded circles, and the largest circles are closest to the altitude of 185 km.

6 These tracks are labeled B and C in Fig. 3 of Hood et al. [2010].

line) are also shown in this figure. The two data tracks are poorly fit by the models, which indicates either an insufficient model resolution or an external field disturbance. Indeed, large transient fields are present in track B [Hood et al., 2010] at ~22 h23 m and after ~22 h28 m (Fig. 10.2b). Although these transient fields have disappeared for track A, it was recorded only four days later, when a disturbed magnetosphere might not have fully returned to quiet conditions. In addition, the neighboring track labeled C in Fig. 10.1d shows a significantly weaker field as compared to tracks A and B.

Fig. 10.1c displays the surface field intensity (F) and the horizontal field directions as predicted by the final model at surface altitude. At this altitude, a strong anomaly is observed over the Hesperian-Noachian transition units (HNt in Fig. 10.1f) to the west of Apollinaris Patera. In contrast to this strong anomaly, the predicted field is weak to the east of the volcano where Amazonian and Hesperian transition units (AHtu) or Hesperian transition undivided units (Htu) are located. Similarly, the predicted field is weak over the Hesperian volcanic edifice unit (Hve) to the south of Apollinaris Patera. For this reason, it is suggested that the core dynamo may have been extinct when Apollinaris Patera formed. In particular, the strong fields to the west of the volcano may be a relic of a previously magnetized unit which was partially demagnetized by later volcanic activity. Still, it cannot be completely ruled out that the same volcanic activity thermally magnetized the crust [Langlais and Purucker, 2007; Hood et al., 2010]. The latter interpretation would imply an active core dynamo in the the early Hesperian (< 3.8 Gyr ago) whereas the former interpretation implies a dynamo shutdown in the Noachian (> 3.8 Gyr ago).

10.1.2 *Tyrrhena Patera*

The low-relief volcano Tyrrhena Patera (black-white circle labeled T in Fig. 10.3) is located ~1500 km northeast to the rim of the Hellas impact basin, extends ~600 km in diameter, and surmounts the surrounding region of Hesperia Planum by $1.0 - 3.0$ km [Plescia, 2004; Werner, 2009; Robbins et al., 2011] (Fig. 10.3a). The main part of Tyrrhena Patera is classified as a Noachian volcanic edifice unit (Nve in Fig. 10.3f) and was in place at $3.7 - 4.0$ Gyr ago [Williams et al., 2008; Werner, 2009]. At about the same time, Hesperia Planum was formed, an early Hesperian volcanic unit (eHv) [Tanaka et al., 2014; Werner, 2009] which may have resulted from magmatic activity at Tyrrhena Patera [Williams et al., 2008]. Later activity at Tyrrhena Patera occurred until ~1.7 Gyr ago [Werner, 2009], was effusive [Plescia, 2004], and resulted in the late Hesperian volcanic unit (lHv in Fig. 10.3f). As well, a resurfacing event occurred in Hesperia Planum at around 3.12 Gyr ago [Werner, 2009]. Apart from that, a gravity anomaly is present near the caldera (Fig. 10.3e), which may indicate a magma chamber at the location of the black dashed circle in Fig. 10.3 [Kiefer, 2003b]. However, Grott and

Wieczorek [2012] argue that a filled magma chamber is not necessary to explain this gravity anomaly.

Milbury et al. [2012] analyzed the fluxgate magnetometers on MGS (MAG) data and found paleopoles of high latitudes in Hesperia Planum, which they interpreted in favor of a dynamo shutdown in the early Hesperian. In contrast, the ER data (Fig. 10.3b) show a weaker field intensity (F) in Hesperia Planum as compared to its surroundings [Mitchell et al., 2007; Lillis et al., 2008a]. Consequently, Lillis et al. [2008a] concluded that volcanic activity may have partially demagnetized this region, and that the Martian dynamo was inactive when Tyrrhena Patera and Hesperia Planum formed. As well, the field intensity (F) as predicted by the final model at surface altitude (Fig. 10.3c) is low over the caldera, over most of Hesperia Planum, and over the suggested magma chamber [Kiefer, 2003b]. Conversely, the strongest fields are predicted mostly over early Noachian highland units (eNh in Sec. 10.3f).

In conclusion, the predictions of the final model suggest that volcanic activity in Hesperia Planum and at Tyrrhena Patera demagnetized Noachian-aged crust, in agreement with the findings of Lillis et al. [2008a]. However, a large volume of intrusions might be necessary to demagnetize the large area of Hesperia Planum. Also, the lowest predicted field intensities (F) are located ~400 km to the west of the volcanic edifice. Therefore, the low-field region over Hesperia Planum cannot unambiguously be related to thermal demagnetization by Tyrrhena Patera.

10.1.3 *Hadriaca Patera*

Hadriaca Patera (black-white circle labeled H in Fig. 10.3) is located at the northeastern rim of the Hellas impact basin (Fig. 10.3a). Similar to Tyrrhena Patera, it is a highland volcano with a flat relief of 1.2 km [Plescia, 2004; Robbins et al., 2011] and an extension of about 330 x 550 km [Plescia, 2004]. The main edifice of Hadriaca Patera was emplaced at around $3.7 - 3.9$ Gyr ago, and volcanic activity at its flanks occurred up to $3.3 - 3.5$ Gyr ago (Hesperian volcanic edifice unit (Hve) in Fig. 10.3f). Younger resurfacing events date to $1.1 - 1.6$ Gyr ago [Williams et al., 2008; Werner, 2009], but may not be related to volcanic activity [Werner, 2009; Robbins et al., 2011].

With the help of the ER magnetic field intensity (F) data (Fig. 10.3b), Lillis et al. [2006] discovered a magnetic field anomaly above Hadriaca Patera. In consequence, they argued that either Hadriaca Patera formed before the Hellas impact basin or that the core dynamo was active after the Hellas impact basin formed. In the former case, the Hellas impact may have destroyed the pre-Hellas volcanic edifice, and only deep-seated thermoremanent magnetization (TRM) could have survived. In comparison to the ER data, the final model predicts a less distinctive magnetic signature at an altitude of 185 km (Fig. 10.3d) above Hadriaca Patera (black-white circle labeled H in Fig. 10.3a). In addition, no corresponding anomaly is predicted

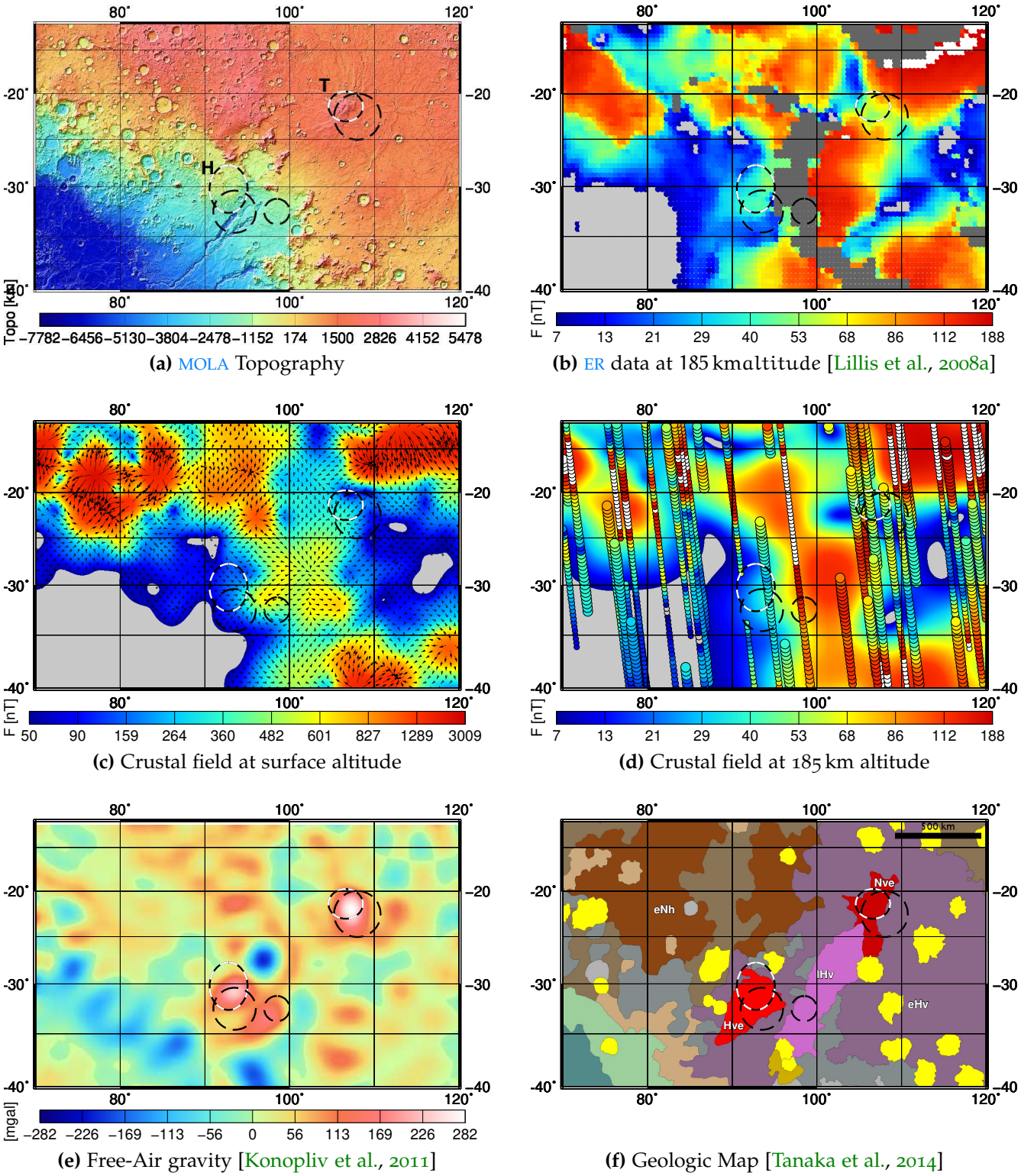

(a) MOLA Topography

(b) ER data at 185 km altitude [Lillis et al., 2008a]

(c) Crustal field at surface altitude

(d) Crustal field at 185 km altitude

(e) Free-Air gravity [Konopliv et al., 2011]

(f) Geologic Map [Tanaka et al., 2014]

Figure 10.3. In this figure, different aspects of the region surrounding the volcanoes Tyrrhena Patera (labeled T in (a)) and Hadriaca Patera (labeled H in (a)) are shown. The locations of Hadriaca Patera and Tyrrhena Patera are indicated by black-white solid circles. Further, the locations of possible magma chambers [Kiefer, 2003a] are indicated by dashed black circles. For more details of the figure, please refer to the caption of Fig. 10.1.

by the final model at surface altitude (Fig. 10.3c). Even more, weaker field intensities (F) at surface altitude approximately correlate with two subsurface magma chambers (black dashed circles), which would explain the associated gravity anomalies (Fig. 10.3e) [Kiefer, 2003a]. Therefore, post-Hellas volcanic activity at Hadriaca Patera may have thermally demagnetized a previously magnetized region, which is still visible to the east of Hadriaca Patera. In this scenario, the Martian core dynamo was inactive when the Hellas impact basin and Hadriaca Patera formed.

10.1.4 *Syrtis Major*

Syrtis Major Planum is located west of the Isidis impact basin (Fig. 10.4a) and extends to over 1100 km in diameter [Schaber, 1982; Hiesinger and Head, 2004]. It is covered by Hesperian-aged lava sheets [Hiesinger and Head, 2004; Tanaka et al., 2014] with an age of $3.56 - 3.71$ Gyr [Michael, 2013] and a thickness of $0.5 - 1.0$ km [Hiesinger and Head, 2004] (early Hesperian volcanic unit (eHv) in Fig. 10.4f). Furthermore, a large central depression is present in Syrtis Major Planum (Fig. 10.4a), which may have formed by the collapse of an excavated magma chamber [Werner, 2009]. Similarly, two volcanic calderas within this depression (black-white circles in Fig. 10.4), namely Meroe Patera to the north and Nili Patera to the south, may have formed [Robbins et al., 2011] at ~3.75 Gyr [Werner, 2009; Robbins et al., 2011] and at ~2.25 Gyr ago [Robbins et al., 2011], respectively. In addition, a positive free-air gravity anomaly (Fig. 10.4e) is present at the location of the central depression, which may indicate the presence of dense residual cumulates in the collapsed magma chamber [Kiefer, 2004]. Kiefer [2004] modeled these residual cumulates as two cylinders with a vertical thickness of 10 km and obtained best-fit locations as marked by the solid white circles in Fig. 10.4[7].

Turning to the magnetic field at Syrtis Major Planum, Lillis et al. [2008a] and Lillis et al. [2015] observed an hourglass-shaped region of weak field intensities (F) in the ER data over the central depression of Syrtis Major Planum (Fig. 10.4b). Accordingly, they provided a detailed model of thermal demagnetization by sills and dikes in this region. Likewise, Milbury et al. [2012] argued on the basis of MAG data that the volcanic events related to Nili and Meroe Paterae thermally demagnetized the crust. As well, the magnetic field intensities (F) as predicted by the final model at an altitude of 185 km (Fig. 10.4d) and at the mean surface altitude (Fig. 10.4c) show a region of low fields at the location of the two calderas (black-white circles) and at the location of the modeled magma chambers (solid white circles). Hence, the magnetic signature of Syrtis Major Planum implies that the Martian dynamo was inactive since $3.56 - 3.75$ Gyr ago.

7 The exact shape, extent, and location of the buried load cannot be uniquely constrained from gravity data alone, and the obtained solution is non-unique [Kiefer, 2004].

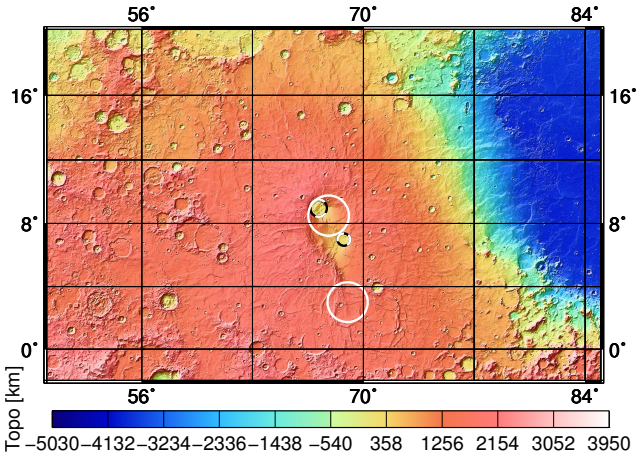

(a) MOLA Topography

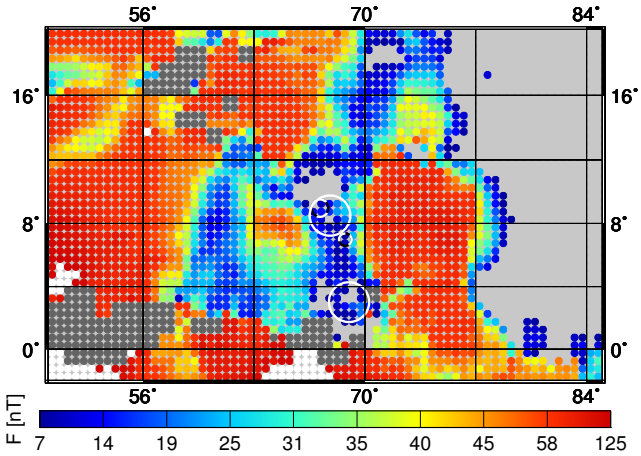

(b) ER data at 185 km altitude [Lillis et al., 2008a]

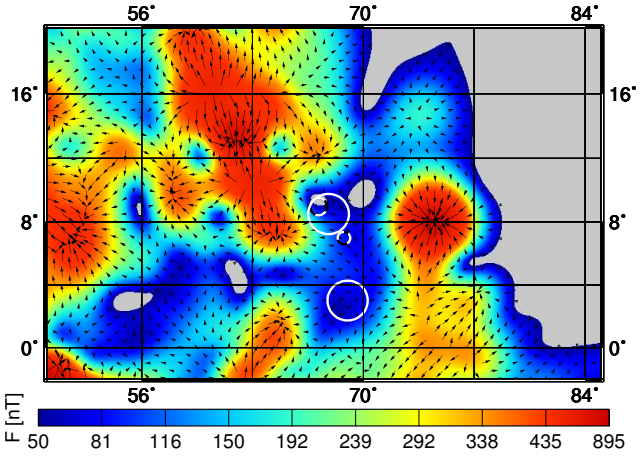

(c) Crustal field at surface altitude

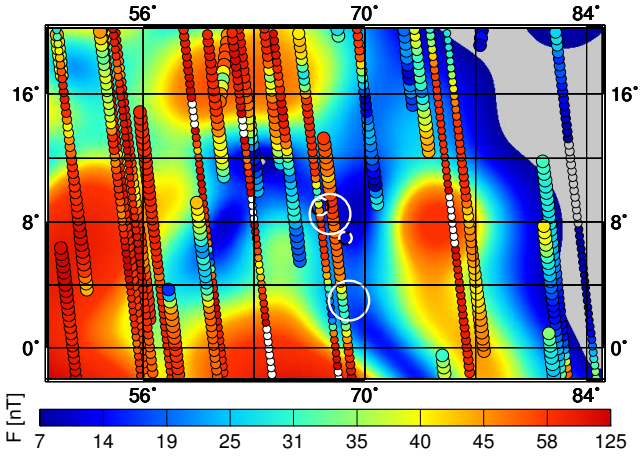

(d) Crustal field at 185 km altitude

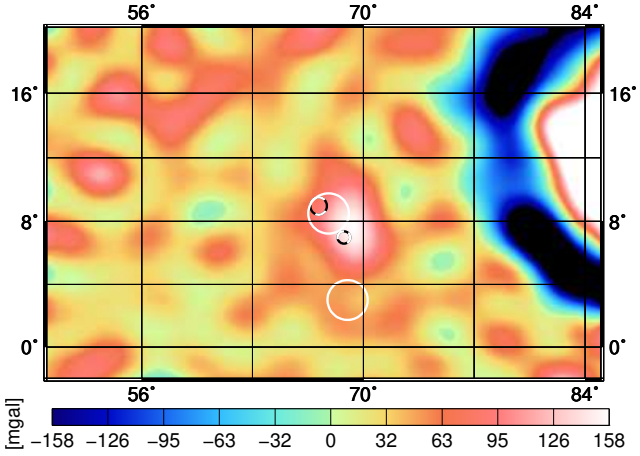

(e) Free-Air gravity [Konopliv et al., 2011]

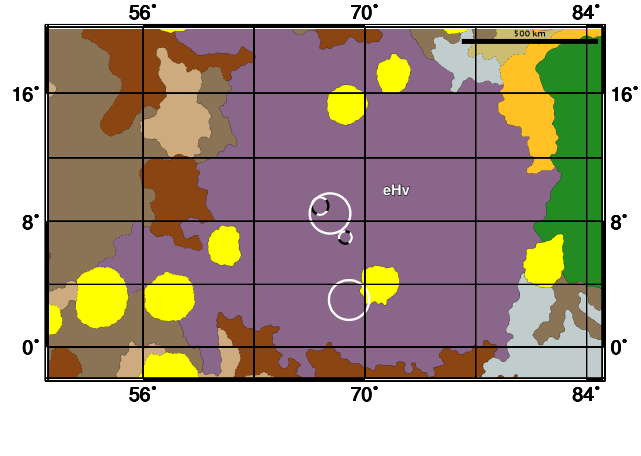

(f) Geologic Map [Tanaka et al., 2014]

Figure 10.4. Different aspects of Syrtis Major Planum are shown. The eastern border of the map also shows the western part of the Isidis impact basin. In addition, the locations of Nili Patera (south) and Meroe Patera (north) are indicated by black-white solid circles, and the location of possible magma chambers [Kiefer, 2004], as obtained from gravity data, are shown by solid white circles. For more details of the figure, please refer to the caption of Fig. 10.1.

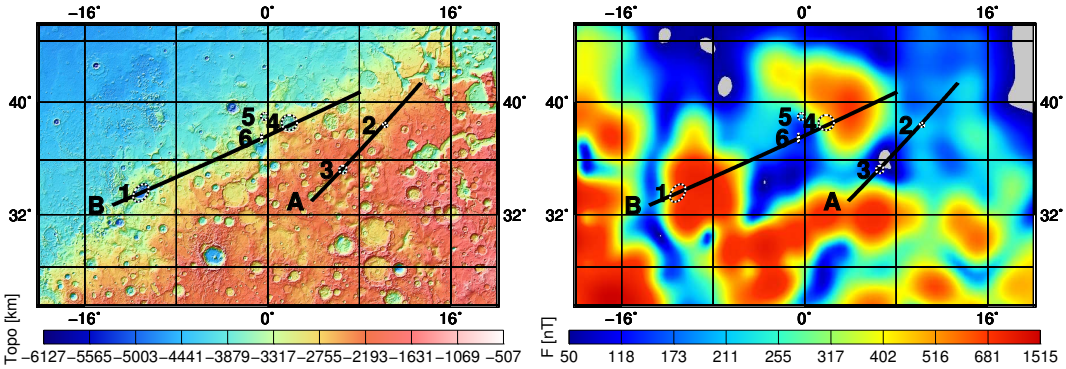

(a) MOLA Topography **(b)** Lithospheric field at surface altitude

Figure 10.5. (a) The MOLA topography and (b) the magnetic field intensity (F) as predicted by the final model at surface altitude are shown over Arabia Terra. The numbered black-white ellipses refer to the volcanic calderas suggested by Michalski and Bleacher [2013], namely Eden Patera (1), Euphrates Patera (2), Siloe Patera (3), Ismenia Patera (4), Oxus Patera (5), and Oxus Cavus (6). The lettered lines correspond to the profiles shown in Fig. 10.6.

10.1.5 *Arabia Terra*

Recently, Michalski and Bleacher [2013] identified a volcanic province close to the dichotomic boundary in Arabia Terra (Figs. 10.5 and A.1). In more detail, this volcanic province consists of several volcanic calderas that are morphologically similar to degraded impact craters [Michalski and Bleacher, 2013]. In Fig. 10.5, these calderas are marked by numbered black-white ellipses and shown along with the MOLA topography (Fig. 10.5a) and the magnetic field intensity (F) as predicted by the final model at surface altitude (Fig. 10.5b). In addition, Fig. 10.6 shows the surface magnetic field intensity (F) along the profiles corresponding to the black lines in Fig. 10.5. These profiles are labeled by letters, which also mark the point where the corresponding distance is 0 km in Fig. 10.6. As well, the individual calderas are marked by vertical solid red lines in Fig. 10.6.

For Eden Patera (labeled 1) and Euphrates Patera (labeled 2), which show the most unambiguous signs of volcanic activity [Michalski and Bleacher, 2013], no distinct magnetic signature is observed (Fig. 10.5b and Fig. 10.6). As well, this is the case for Ismenia Patera (labeled 4) , although it is located at the rim of a larger positive anomaly (c.f. profile B). Hence, the corresponding main magma chambers of these calderas either are spatially offset from the respective caldera, or cannot be resolved by the final model, or may have only weakly (de)magnetized the crust. In contrast, Oxus Cavus (labeled 6) and Siloe Patera (labeled 3) can be related to a local magnetic field minimum. Consequently, these calderas may have partially demagnetized the crust and the Martian core dynamo may have been extinct at the time of their formation. However, the size of these calderas is at the reso-

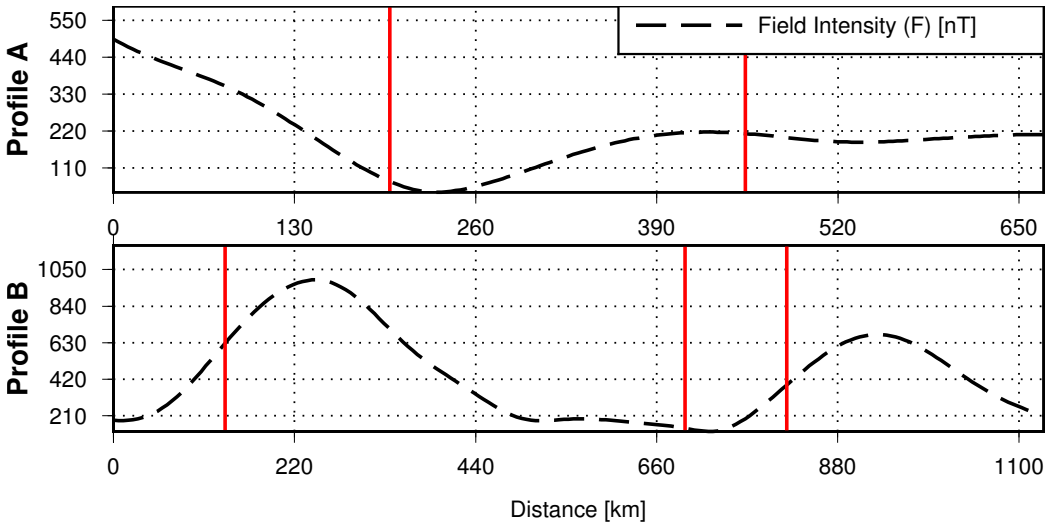

Figure 10.6. The magnetic field intensity (F) along the two profiles of Fig. 10.5 is shown as predicted by the final model at surface altitude. The distance is measured along the respective track from west to east. In addition, the vertical red lines correspond to the locations of the volcanic calderas that have been discovered by Michalski and Bleacher [2013] and which are also indicated by black-white ellipses in Fig. 10.5.

lution limit of the final model, and other areas of weak fields in the shown region cannot be linked to any visible geological structures.

In any case, the ages of the described calderas in Arabia Terra are unknown. Still, it is estimated that they formed in the late Noachian to early Hesperian period [Michalski and Bleacher, 2013], and accurate age determinations of these features would provide further constraints on the magnetic history of Mars.

10.1.6 *Malea Planum*

The highland volcanoes Pityusa Patera, Malea Patera, Peneus Patera, and Amphitrites Patera are shown in Fig. 10.7. These volcanoes are located within Malea Planum, a late Noachian volcanic unit [Tanaka et al., 2014] at the southwestern rim of the Hellas impact basin [Williams et al., 2009]. Out of these, Amphitrites Patera is the only caldera associated with a positive gravity anomaly [Williams et al., 2009], and was emplaced at about $3.6-3.8$ Gyr ago [Williams et al., 2009; Werner, 2009]. Likewise, the remaining volcanic sites in Malea Planum formed at around 3.8 Gyr ago [Williams et al., 2009].

With the exception of an isolated anomaly west of Pityusa Patera (labeled 4), Malea Planum lacks any detectable magnetic fields (Fig. 10.7b). Likewise, the volcanic structures in this region are not related to any crustal magnetic fields. This observation may be explained by either of the following three

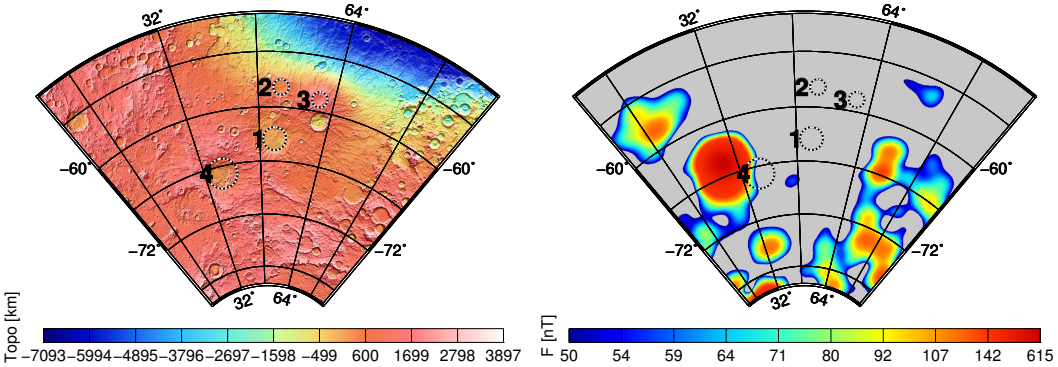

(a) MOLA Topography **(b)** Crustal field at surface altitude

Figure 10.7. (a) The MOLA topography and (b) the magnetic field intensity (F) as predicted by the final model at surface altitude are shown for a region over Malea Planum. The numbered black-white ellipses refer to the highland volcanoes Malea Patera (1), Peneus Patera (2), Amphitrites Patera (3), and Pityusa Patera (4).

scenarios: the core dynamo had ceased operating when these volcanoes were active, the TRM associated with these volcanoes is below the detection limit of the final model, or the same (unknown) process responsible for the surrounding low-field region is responsible for the lack of any magnetic signatures above these calderas.

10.2 MAGNETIC SIGNATURES OF IMPACT CRATERS

Impacts on a planetary crust may alter the crustal magnetization through shock and thermal de/magnetization (e.g., Hood et al. [2003]; Mohit and Arkani-Hamed [2004]; Shahnas and Arkani-Hamed [2007]; Louzada et al. [2011]; Lillis et al. [2013b]). In particular, impacts simultaneously reset the surface age and the magnetization within a large volume of crust, which is usually not the case for volcanoes [Lillis et al., 2013a]. Hence, magnetic signatures of impact craters can be used to constrain the lifespan of the Martian core dynamo. Nevertheless, an impact crater with no observable magnetic field may still have formed when the core dynamo was active [Solomon et al., 2005; Lillis et al., 2010b; Hood et al., 2010][8].

It is widely accepted that the magnetic signatures of impact craters are consistent with a shutdown of the core dynamo at around 4.1 Gyr ago (e.g., Acuña et al. [1999]; Lillis et al. [2008]; Lillis et al. [2013a]; Robbins et al. [2013]). However, previous studies were limited to large craters, as the magnetic signatures of small craters cannot be resolved at the Mars Global

8 Several scenarios have been suggested when this might happen: (1) if coherence wavelengths are either too small or too large [Lillis et al., 2010b; Carporzen et al., 2005], (2) if single domain (SD) minerals cannot form due to slow cooling rates in thick impact melt sheets [Hood et al., 2010], or (3) if the magnetic signature of impact craters was erased by, e.g., aqueous alteration [Solomon et al., 2005].

Surveyor (MGS) sampling altitudes. Here, we will use the final model to predict the magnetic field at surface altitude, to reinvestigate the magnetic signature of the large impact basins, and to analyze the magnetic field signature of selected impact craters down to ~150 km in diameter.

10.2.1 *Large basins*

The magnetic signature of impact craters with diameters larger than ~1000 km and ~500 km may be resolved from satellite data at the mapping phase orbit (MPO) and AB/SPO/ER altitudes, respectively [Lillis et al., 2008; Lillis et al., 2010b]. For any smaller craters, one cannot distinguish between demagnetized and magnetized craters, as neighboring fields may contribute to the field observed over the respective crater at orbit altitude.

The largest apparent impact basins on Mars, namely Hellas, Argyre, and Isidis, lack any observable magnetic fields in the MAG data [Acuña et al., 1999; Arkani-Hamed, 2001b] and to a great part in the ER data as well [Lillis et al., 2008; Lillis et al., 2010b]. Based on their ages of $3.97 - 4.08$ Gyr (Hellas), $3.95 - 3.96$ Gyr (Argyre), and $3.83 - 4.04$ Gyr (Isidis) [Nimmo and Tanaka, 2005; Frey, 2008; Werner, 2008; Fassett and Head, 2011; Robbins et al., 2013], it was concluded that the Martian core dynamo was extinct at $\sim 4.0 - 4.1$ Gyr ago (e.g., Acuña et al. [1999]; Lillis et al. [2008]; Lillis et al. [2013a]).

In addition to the large apparent impact basins mentioned above, several buried basins have been discovered from an analysis of crustal thickness and MOLA topography data [Frey et al., 1999, 2002; Frey, 2008]. In Fig. 10.8, all dated impact basins with diameters $D \geqslant 924$ km [Frey et al., 2002; Robbins et al., 2013] are shown by purple ellipses along with the magnetic field intensity (F) as predicted by the final model at surface altitude. Not surprisingly, the magnetic field intensities (F) at the Hellas, Argyre, and Isidis impact basins are below the detection limit of the final model. As well, the Utopia (4.11 Gyr), the North Polar (4.12 Gyr), the North Tharsis (4.13 Gyr), and the In Amazonis (4.15 Gyr, all ages by Frey [2008] and Lillis et al. [2013a]) impact basins lack any observable fields. Still, two younger craters are present within In Amazonis [Robbins et al., 2013] which may obscure its previous magnetic signature [Lillis et al., 2013a]. Similarly, North Polar and North Tharsis may have been demagnetized by the same process as the surrounding low-field regions (possibly volcanic activity of Tharsis [Lillis et al., 2013a]). Further, the Utopia impact basin is characterized by weak magnetic anomalies occurring along most of its crater rim, except for its southeastern quadrangle, where Elysium might have thermally demagnetized the crust. Therefore, Mitchell et al. [2007] suggested that the core dynamo might have been active when Utopia formed. Other impact basins with weaker field intensities (F) at their centers as compared to their surroundings include Prometheus ($4.03 - 4.06$ Gyr, [Robbins et al., 2013]), Acidalia (4.11 Gyr), Chryse (4.14 Gyr), and Amenthes (4.22 Gyr, all ages by

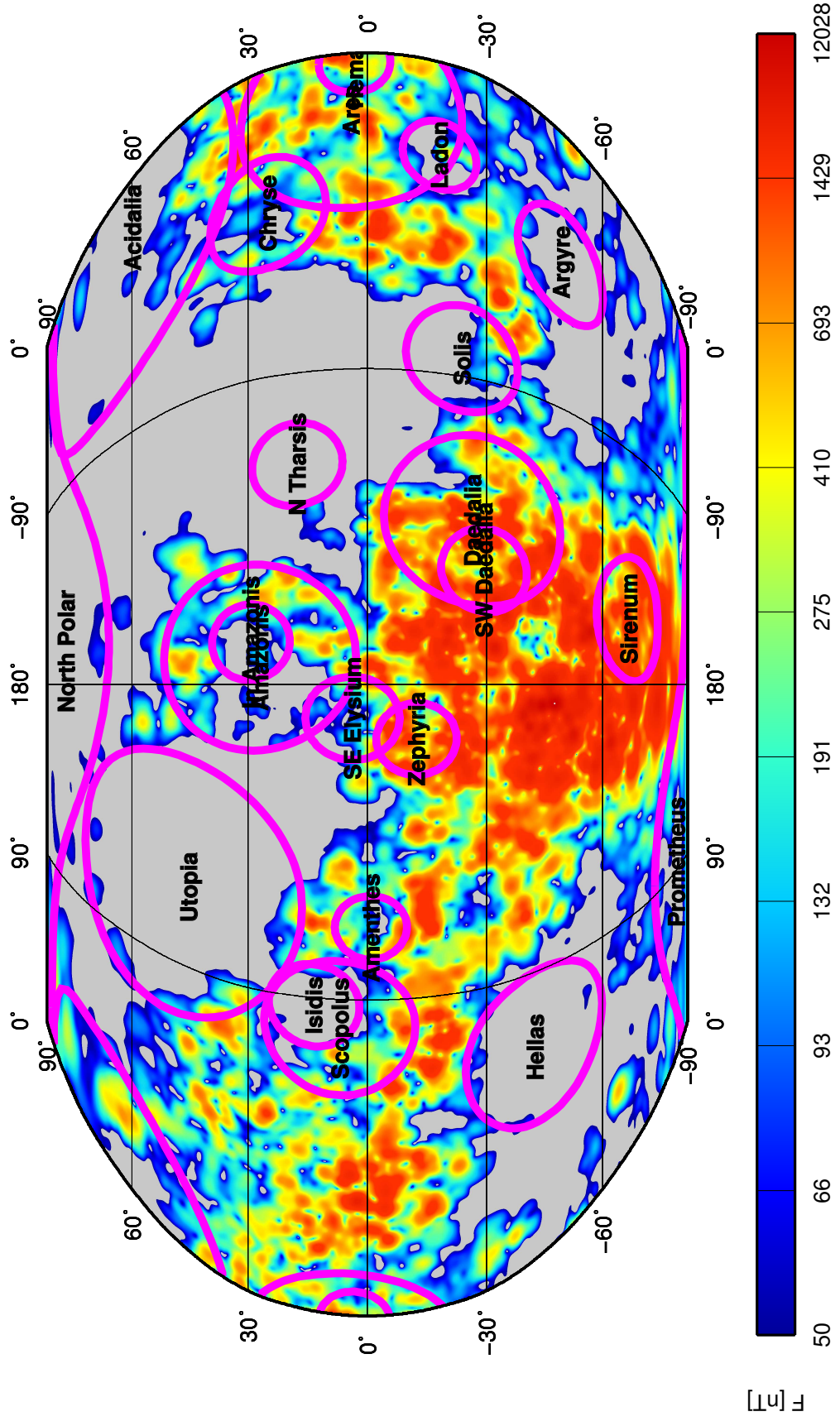

Figure 10.8. A global map of the magnetic field intensity (F) is shown as predicted by the final model at surface altitude. Further, all dated impact basins $\geqslant$ 924 km in diameter D [Frey, 2008; Robbins et al., 2013] are indicated by thick purple circles and labeled with their names.

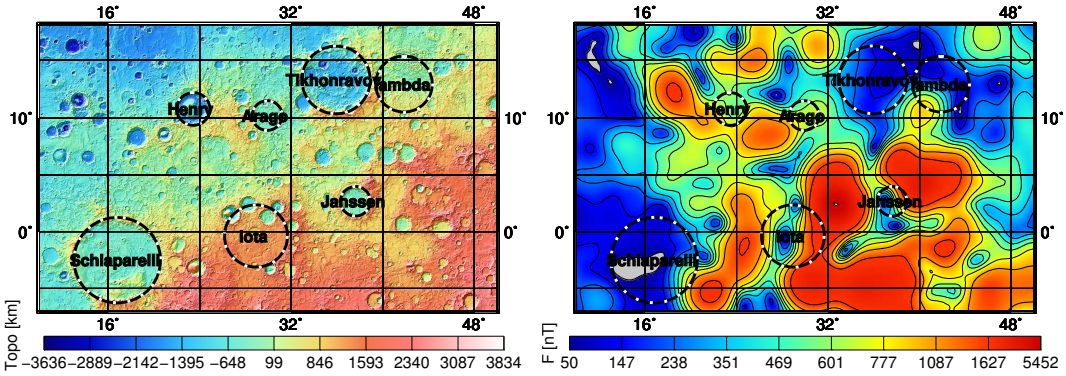

(a) MOLA Topography **(b)** Crustal field at surface altitude

Figure 10.9. (a) MOLA topography and (b) surface magnetic field intensity (F) as predicted by the final model at surface altitude for a region in western Terra Sabaea. In addition, all craters with diameters 150 km $\leqslant$ D $\leqslant$ 500 km are highlighted by black-white circles with their names written at their centers. For unnamed craters, the same Greek letters as in Robbins et al. [2013] are used.

Frey [2008] and Lillis et al. [2013a]). The remaining basins have ages of 4.13 – 4.20 Gyr [Frey, 2008; Robbins et al., 2013; Lillis et al., 2013a], and are associated with comparable or stronger magnetic fields than their surroundings. For example, Amazonis (4.15 Gyr) hosts stronger field intensities (F) as its surroundings, Ladon (4.17 – 4.18 Gyr) features a strong field intensity (F) within its center, and Solis may have been thermally demagnetized in its northern half by Tharsis volcanism. Hence, these impact basins may have formed when the core dynamo was active.

To sum up, no detectable fields were observed in impact basins of $<$ 4.15 Gyr in age. On the other hand, positive magnetic signatures were observed for basins with ages of $>$ 4.13 Gyr. The only exception is Amenthes with an age of ~4.22 Gyr, but its low-field signature is not as distinct as for most of the younger basins. Therefore, a core dynamo may have been active until 4.13 – 4.15 Gyr ago, which is in agreement with previous studies (e.g., Lillis et al. [2008]).

10.2.2 *Smaller craters*

Magnetic field observations at the MGS sampling altitudes cannot directly be used to investigate the magnetic field signature of craters smaller than ~500 km in diameter (Sec. 10.2.1). The main reason is that smaller wavelengths are attenuated more strongly with increasing altitude (Eq. 6.17). In addition, a magnetic field might be observed over a demagnetized region if the ratio of the demagnetized area and the observation altitude is below a certain threshold (c.f. Sec. 1.4). As a workaround, Lillis et al. [2010b] and

Lillis et al. [2013a] used a statistical approach[9] which is suitable for craters down to 300 km in diameter. As an alternative, the final model can be used to investigate the surface magnetic field signature of impact craters with diameters down to 195 km[10].

TERRA SABAEA Exemplarily, we investigate the surface magnetic field signatures of impact craters with diameters of 150 km $\leqslant$ D $\leqslant$ 500 km that are located in the western part of Terra Sabaea (Fig. 10.9). Among these craters, a central field minimum is observed for Janssen (154 km in diameter, 3.83 – 3.93 Gyr) in age[11]), Schiaparelli (446 km, 3.91 – 3.93 Gyr [Werner, 2008; Robbins et al., 2013]), iota (326 km, 4.10 – 4.17 Gyr), Henry (168 km, 3.93 – 4.00 Gyr), and Tikhonravov (344 km, 4.12 – 4.19 Gyr [Robbins et al., 2013] and 4.10 Gyr [Werner, 2008]). Conversely, no central field minimum can be related to Arago (152 km, 3.73 – 4.03 Gyr) and lambda (285 km, not dated).

For the five craters with a central field minimum, the normalized circumferential average of the magnetic field intensity (F) as a function of the radial distance to the center of the respective crater is shown in Fig. 10.10 for the MPO altitude of 400 km (blue line), the ER sampling altitude of 185 km (black line), and the mean surface altitude of 3393.5 km (red line). For Schiaparelli (crater 1, 446 km in diameter), the field profiles at altitudes of 400 km and 185 km are compatible with a magnetized or partially demagnetized crater, which is in accordance with the ER data [Shahnas and Arkani-Hamed, 2007; Lillis et al., 2013b]. In contrast, the surface field intensity (F) drops to almost zero in the center of the crater (Fig. 10.9b), and a strong field contrast is observed between the surface field intensities (F) inside and outside the crater rim (Fig. 10.10), which rather suggests that Schiaparelli is demagnetized. The crater iota (crater 2, 324 km in diameter) shows no significant difference in its magnetic field signature at altitudes of 185 km and at surface altitude, which may be explained by large coherence wavelengths. Further, Jannsen (crater 3, 154 km in diameter) and Henry (crater 4, 168 km in diameter) are at the resolution limit of the final model. Interestingly, the field contrast of Henry is largest at an altitude of 185 km. Clearly, this example not only demonstrates how the characteristics of the magnetic signature can change with altitude, mainly depending on the coherence wavelength of the magnetized crust, but also that the final model may not be used to investigate

9 Lillis et al. [2010b] and Lillis et al. [2013a] simulate the crustal magnetization by randomly oriented sources with a given coherence wavelength. Subsequently, the resulting magnetization distribution is partially demagnetized within a cylindrical area. Then, the resulting magnetic field ratio of field intensities (F) inside and outside the crater rim is calculated. In a Monte Carlo approach, this procedure is repeated for several random magnetization distributions and for different observation altitudes. In this way, the probability to observe the measured ratio of field intensities (F) can be calculated in dependence of the degree of demagnetization.

10 With a maximum SH degree of L = 110, as used for the final model, the spatial wavelength is about $2\pi R/L \approx 195$ km.

11 Ages and diameters as given by Robbins et al. [2013], if not otherwise specified.

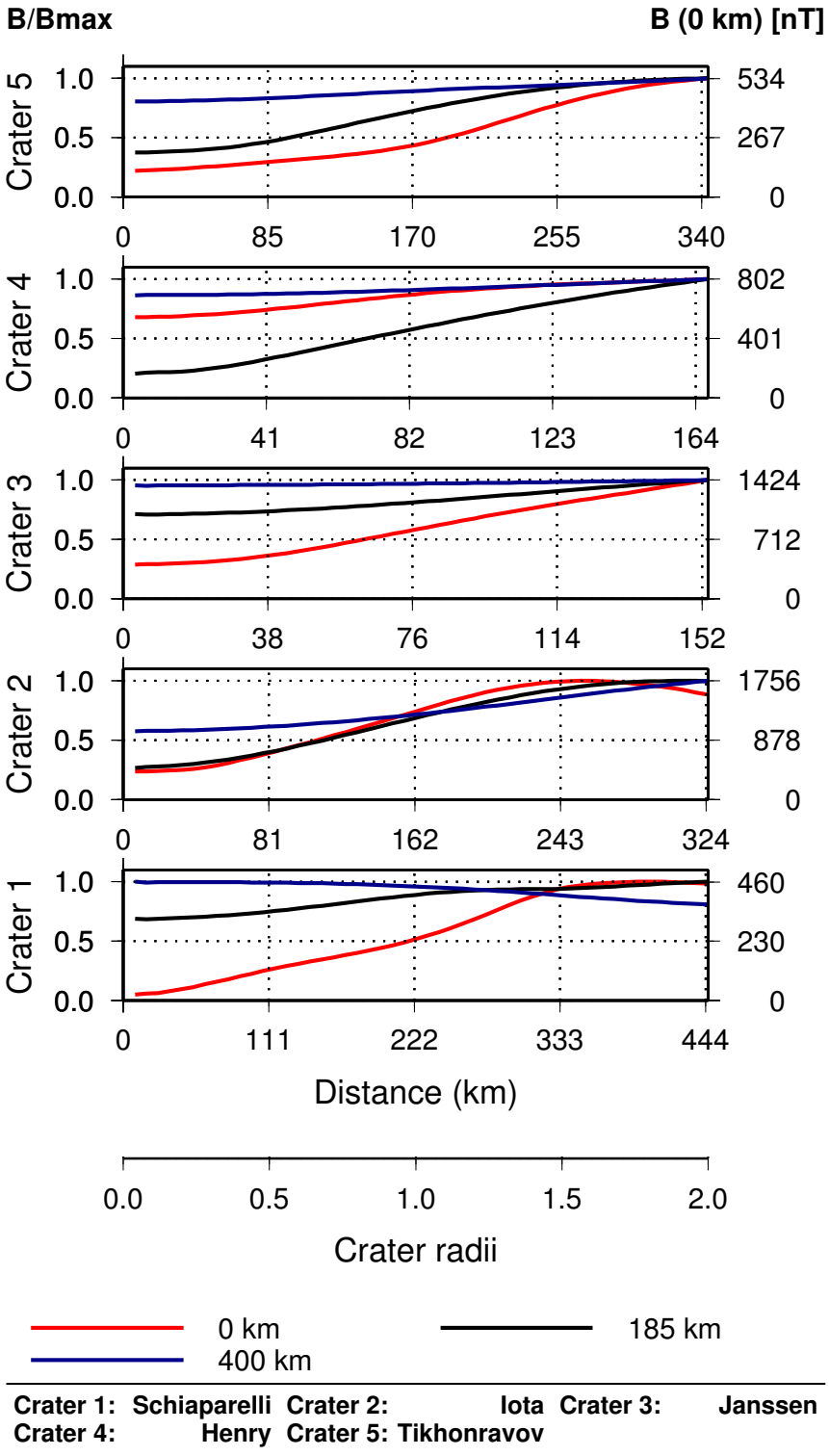

Figure 10.10. The circumferentially averaged magnetic field intensity (F) of selected craters as predicted by the final model at the MPO altitude of 400 km (blue), the ER sampling altitude of 185 km (black) and the mean surface altitude of 0 km (red) are shown. The craters have been selected based on the presence of a central field minimum in Fig. 10.9. On the left ordinate, the relative field intensity (F) is given, whereas the absolute field intensity (F) at surface altitude is given on the right ordinate. Copyright 2014 by the American Geophysical Union, reprinted from Fig. 13 of Morschhauser et al. [2014] with kind permission from publisher John Wiley & Sons Ltd.

craters below the resolution limit of ~195 km. Finally, the magnetic field profile of Tikhonravov (crater 5, 344 km in diameter) is compatible with a demagnetized crater. This conclusion is in accordance with the results of Langlais et al. [2004], but in contrast to the results of Lillis et al. [2013a], who found that Tikhonravov is at least partially magnetized.

To sum up, Jannsen and Schiaparelli, both < 4.0 Gyr in age, feature a distinct low-field region in their centers. In contrast, the equally young craters Henry and Arago show a weak magnetic field contrast at surface altitude and cannot be associated with a low-field region. However, these two craters are at the resolution limit of the final model and their magnetic signature may not sufficiently be resolved. The older craters Tikhonravov and iota, with ages of $4.10 - 4.19$ Gyr, may as well be demagnetized. However, Tikhonravov is located within a larger region of low fields, which may have formed by a process that is unrelated to the impact. In conclusion, the ages and associated field signatures of the investigated craters are mostly consistent with a dynamo shutdown earlier than $4.10 - 4.19$ Gyr ago. Nevertheless, the magnetic signature of small craters such as Henry and Arago may not be fully resolved. Moreover, many circular low-field regions are present that cannot be related to any particular impact crater. In some cases, the low-field region at the center of small craters may therefore be unrelated to these impacts. Hence, the magnetic signatures of small craters should be interpreted with care.

TRACES OF AN IMPACT IN TERRA SIRENUM The global map of the magnetic field intensity (F) at surface altitude (Fig. 7.4 on p. 89) features a remarkable low-field region which is shown in detail in Fig. 10.11. This region is located within the strongly cratered terrain of Terra Sirenum (TS) (Fig. 10.11a), very close to the strongest crustal fields on Mars (Figs. 10.11b and 10.11c). Interestingly, the location and extension of a previously identified multiring basin (T. Sirenum) with ring diameters of 500 and 1000 km (black circles in Fig. 10.11) [Schultz et al., 1982] match the location and extension of this low-field region. Within this impact basin, the predicted surface field decreases from about 3500 nT at the outer crater rim to less than 70 nT at the crater center. In consequence, impact demagnetization is a viable explanation for this low-field region. As the age of T. Sirenum is currently unknown, we examine the ages of overprinted craters [Robbins et al., 2013] which are indicated by the white circles in Fig. 10.11. From this analysis, we obtain a lower age limit of $3.67 - 4.09$ Gyr for T. Sirenum, which is compatible with a dynamo shutdown at ~4.10 Gyr ago [Lillis et al., 2013a].

Previously, Nimmo and Gilmore [2001] concluded on the basis of AB/SPO data that the crater T. Sirenum is magnetized. These data are shown by colored circles in Fig. 10.11c along with the field intensity (F) as predicted by the final model at 185 km altitude. Indeed, the magnetic field contrast of the low-field anomaly with respect to its surroundings is lower at this

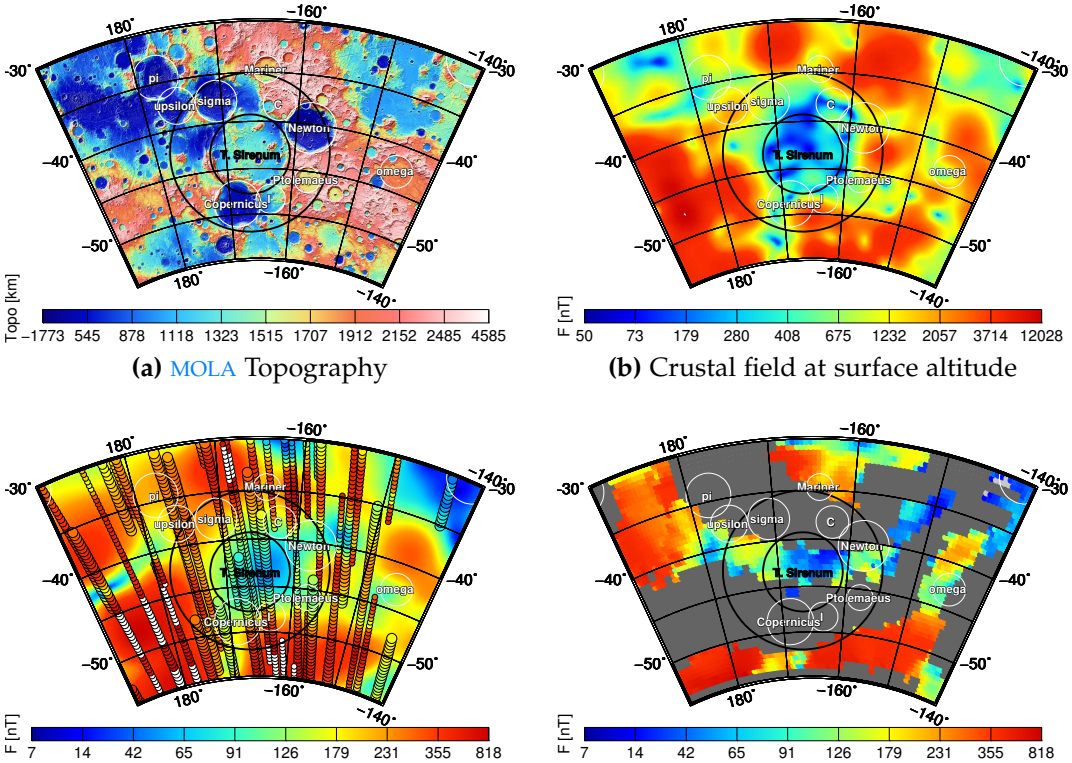

(a) MOLA Topography

(b) Crustal field at surface altitude

(c) Crustal field at 185 km altitude

(d) ER data at 185 km altitude [Lillis et al., 2008a]

Figure 10.11. (a) The MOLA topography, (b) the magnetic field intensity (F) as predicted by the final model at the mean surface altitude, (c) the magnetic field intensity (F) as predicted by the final model at the ER sampling altitude, and (d) the magnetic field intensity (F) as measured by the ER are shown over an area in TS that includes a remarkable low-field region. A previously identified multiring basin [Schultz et al., 1982] is outlined by black circles, and other craters with diameters 150 km $\leqslant$ D $\leqslant$ 500 km in this area are marked by white circles. In addition, the AB/SPO data over this area are shown by colored circles along with the predicted field at 185 km altitude (c). These circles vary in size, and larger circles are closer to the map altitude of 185 km. Further, gray areas in the ER data (d) indicate regions where no ER data is available due to closed crustal magnetic field lines.

altitude than at surface altitude. However, the low-field region is still visible at 185 km altitude, particularly in the ER data (Fig. 10.11d).

10.3 SUMMARY

We have reanalyzed the magnetic signatures of most volcanoes and of selected impact craters on Mars with respect to the timing of the Martian core dynamo. For this purpose, the crustal magnetic field as predicted by the final model was evaluated at the mean surface altitude of 3393.5 km. In contrast to previous interpretations, we have demonstrated that no volcanic

province or individual volcano on Mars shows convincing signs of TRM. Therefore, we conclude that the Martian core dynamo was already inactive at the time of the oldest visible traces of major volcanic activity, at around 4.0 Gyr ago. In agreement with this result, the magnetic field signatures of large impact basins with diameters $D > 924$ km suggest that the Martian core dynamo ceased at around $4.13 - 4.15$ Gyr ago. Further, we have identified a region of very low crustal magnetic fields which is most probably related to the multiring basin T. Sirenum. With an estimated age of at least $3.67 - 4.09$ Gyr, a lack of strong magnetic fields over this crater is also in accordance with our findings above. The magnetic field signatures of smaller craters are more difficult to assess, as these signatures are efficiently attenuated with observation altitude. Therefore, previous studies based on ER and MAG data were restricted to craters of diameters $D < 300$ km. Here, we exemplarily the magnetic field signatures of craters with diameters of $D = 152 - 446$ km in Terra Sabaea. As a result, we found that these smaller craters are consistent with a dynamo shutdown at $4.10 - 4.19$ Gyr ago. In particular, the crater Schiaparelli ($D = 446$ km, $3.91 - 3.93$ Gyr) appears to be demagnetized in contrast to previous findings.

Overall, the magnetic signatures of volcanic structures and impact craters are in agreement with a dynamo shutdown in the Noachian at around 4.1 Gyr ago. This conclusion is in agreement with previous studies based on impact basins (e.g., Acuña et al. [1999]; Mohit and Arkani-Hamed [2004]; Lillis et al. [2008]; Lillis et al. [2013a]), but not with some of the earlier studies based on volcanoes [Lillis et al., 2006; Langlais and Purucker, 2007; Hood et al., 2010; Milbury et al., 2012].

11 MAGNETIZATION AND MAGNETIC MINERALS

This chapter describes the work of a collaboration with Foteini Vervelidou[1] who significantly contributed to the results.

The inversion of magnetic field data for the underlying distribution of magnetization is not unique as an infinite number of magnetization distributions results in the same magnetic field. In other words, the null space of this problem is infinite. However, if the magnetization is confined to a spherical shell, Gubbins et al. [2011] showed that the null space can be separated by an expansion in complex vector spherical harmonic (SH) functions. These functions are orthogonal over the sphere, denoted by $\mathbf{Y}^m_{l,l+1}$, $\mathbf{Y}^m_{l,l-1}$, and $\mathbf{Y}^m_{l,l}$, and represent the parts $\mathcal{E}$, $\mathcal{I}$, and $\mathcal{T}$ of the magnetization which result in a magnetic field observable only external to the magnetized shell ($\mathbf{Y}^m_{l,l+1}$), only inside the magnetized shell ($\mathbf{Y}^m_{l,l-1}$), and only internal to the magnetized shell ($\mathbf{Y}^m_{l,l}$) [Gubbins et al., 2011]. Hence, the magnetization can be expanded as

$$\mathbf{M}(r,\theta,\phi) = \sum_{l,m} \left(E^m_l \mathbf{Y}^m_{l,l+1} + I^m_l \mathbf{Y}^m_{l,l-1} + T^m_l \mathbf{Y}^m_{l,l} \right) = \mathcal{E} + \mathcal{I} + \mathcal{T} \tag{11.1}$$

where E^m_l, I^m_l, and T^m_l refer to the respective expansion coefficients.

Now, $\mathcal{E} + \mathcal{T}$ span the null space and $\mathcal{I}$ is uniquely related to the observed crustal field [Gubbins et al., 2011]. Hence, the coefficients I^m_l of the magnetization can be obtained from the Gauss coefficients g^m_l, h^m_l of a model of the crustal magnetic field. For instance, Gubbins et al. [2011] obtained[2]

$$\begin{Bmatrix} \mathrm{Re}\left(I^m_l\right) \\ \mathrm{Im}\left(I^m_l\right) \end{Bmatrix} = \frac{10^7}{\mu_0} \frac{a}{\sqrt{l \epsilon_m}} \begin{Bmatrix} +g^{m,c}_l \\ -g^{m,s}_l \end{Bmatrix} \tag{11.2}$$

for an infinitely thin magnetized layer located at the reference radius a of the model. Here, $\epsilon_m = 2 - \delta_{m0}$ where δ_{m0} is the usual Kronecker delta[3], and $g^{m,c}_l$ and $g^{m,s}_l$ refer to the internal Gauss coefficients associated with the cosine and sine terms of the real SH functions (Eq. 6.9). The part $\mathcal{I}$ of the magnetization is necessary and sufficient to describe the observed field

1 Geoforschungszentrum Potsdam, foteini.vervelidou(at)gfz-potsdam.de.

2 Here, Système Internationale (SI) units are used, the Gauss coefficients g^m_l, h^m_l are given in nT, and the reference radius a is given in km. Further, the resulting coefficients $I^m_{g/h,l}$ have units of ampere (A).

3 If $x = y$, then $\delta_{xy} = 1$, else $\delta_{xy} = 0$.

outside of the magnetized shell. In other words, no part of the magnetization $\mathcal{I}$ can be removed without changing the resulting magnetic field, but an infinite number of magnetization distributions as described by the null space spanned by $\mathcal{E} + \mathcal{T}$ (Eq. 11.1) may be added. As a result, the total magnetization may locally be lower than the necessary magnetization $\mathcal{I}$.

We applied this framework to the final model and made two improvements to the work of Gubbins et al. [2011]. First, we found that complex SH as used by Gubbins et al. [2011] lead to spurious longitudinal magnetizations[4]. Therefore, we use real vector SH with

$$\mathbf{Y}_{lm,l-1} = \frac{1}{r^{l-1}\sqrt{l}} \nabla \left[r^l Y_{lm}(\theta, \phi) \right] \tag{11.3}$$

for the part describing $\mathcal{I}$ and analogous expressions for the other two parts. Then, the real expansion coefficients with units of ampere (A) can be obtained from

$$I_{lm} = \frac{10^7}{\mu_0} \frac{a}{\sqrt{l}} g_l^m \tag{11.4}$$

where m is now taking values from $-l$ to l (c.f. Eq. 6.9). Second, we modified Eq. 11.2 to allow for a magnetic shell thickness of d [km], with its top located at the reference radius a. In this case,

$$I_{lm} = \frac{10^4}{\mu_0} \frac{a^{l+2}}{\sqrt{l}} \frac{1}{d} \left[\int_{a-d}^{a} r^{l+1} \mathbf{M}(r, \theta, \phi) dr \right]^{-1} g_l^m, \tag{11.5}$$

where the coefficients I_{lm} have units of A/m. Now, if a radially independent magnetization $\mathbf{M}(\theta, \phi)$ is considered, the integral in Eq. 11.5 is given by

$$\int_{a-d}^{a} r^{l+1} \mathbf{M}(\theta, \phi) dr = \frac{a^{l+2} - (a-d)^{l+2}}{l+2} \mathbf{M}(\theta, \phi) \tag{11.6}$$

and the coefficients I_{lm} can be calculated from

$$I_{lm} = \frac{10^4}{\mu_0} \frac{l+2}{\sqrt{l}} \frac{1}{d} \left[1 - \left(1 - \frac{d}{a} \right)^{l+2} \right]^{-1} g_l^m. \tag{11.7}$$

With regard to the final model, we use a magnetized layer thickness of $d = 40\,\text{km}$ (Sec. 2.2) and present the resulting necessary magnetization $\mathcal{I}$ in Fig. 11.1. The overall pattern of this magnetization is similar to that of the magnetic field at surface altitude (Fig. 7.4), but differences exist in detail (Fig. 11.2). Turning to the extreme values, we observe a maximum

4 This problem may be related to Eq. 11.2, where the orders m take only positive values on the right-hand side, while both positive and negative values are necessary on the left-hand side in order for Eq. 11.1 to hold.

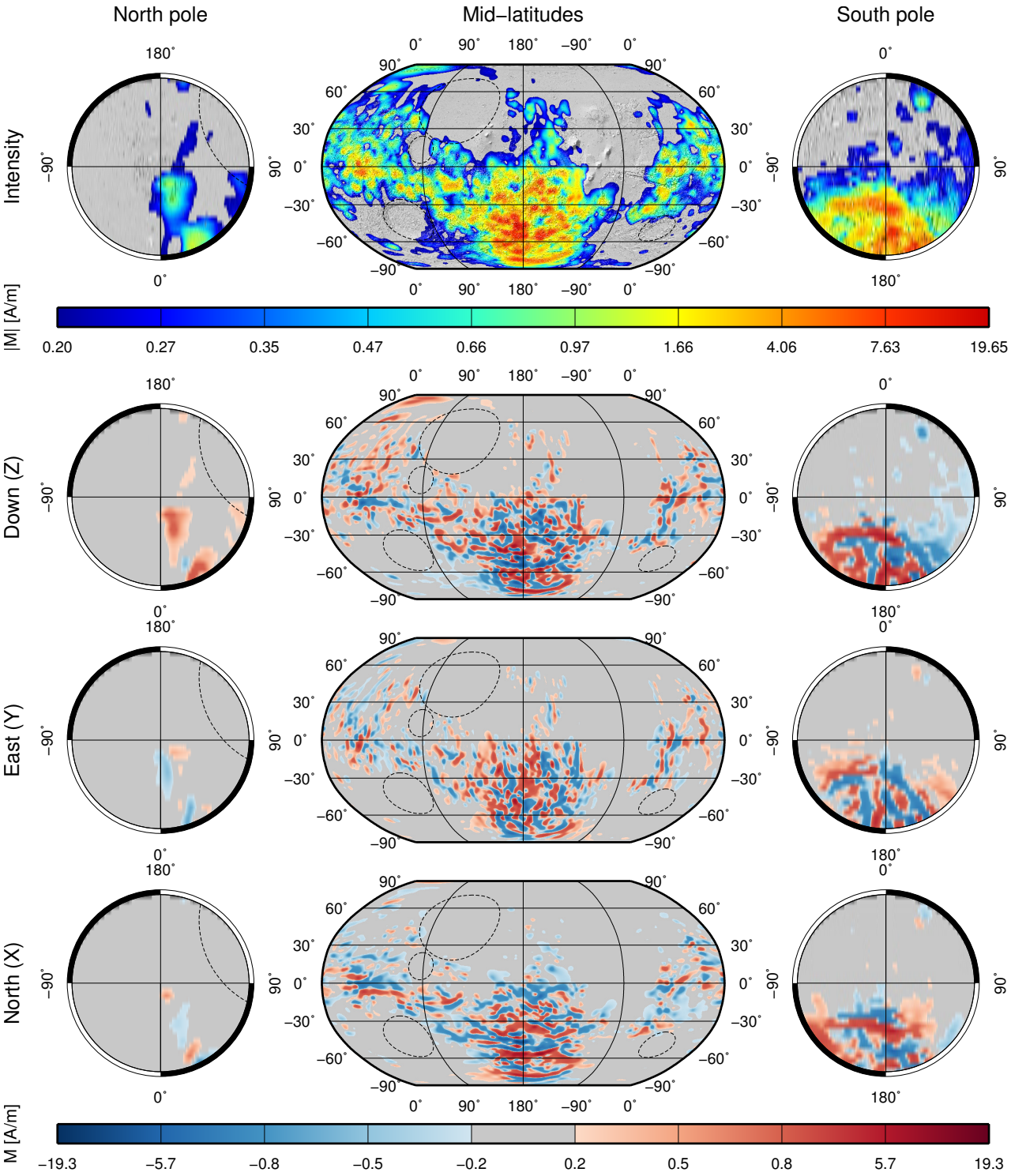

Figure 11.1. The magnetization is shown which is necessary to explain the magnetic field as predicted by the final model. The magnetization extends over a 40 km thick layer with radially uniform magnetization. From bottom to top, the horizontally north (X), east (Y), and vertically down (Z) components, and the magnetization intensity (F) are shown.

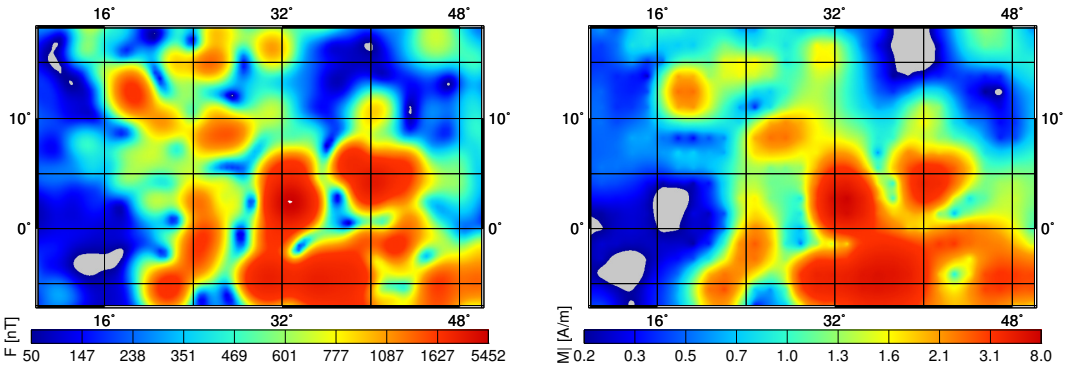

(a) Crustal field at surface altitude **(b)** Magnetization of a 40 km thick layer

Figure 11.2. (a) The magnetic field intensity (F) as predicted by the final model at surface altitude and the (b) magnetization intensity (F) that is necessary to explain this field are presented for the same region as shown in Fig. 10.9. The magnetization has been obtained for a 40 km thick layer of radially uniform magnetization.

magnetization of ~20 A/m for the intensity (F), and minimum and maximum magnetizations of −16/13 A/m, −7/9 A/m, and −19/12 A/m for the horizontally north (X), east (Y), and vertically down (Z) components, respectively. In good agreement, Purucker et al. [2000] obtained −22/17 A/m for the vertically down (Z) component and Langlais et al. [2004] obtained ±12A/m for all components (Tab. 2.1) whereas larger values of 44 A/m for the intensity (F) and of 25 A/m for all components were obtained by Arkani-Hamed [2002c][5] and Whaler and Purucker [2005][5], respectively. Still, tese results are in accordance with our magnetization model which describes the necessary magnetization, and the actual magnetization may be larger.

Now, we will address the question which magnetic minerals could support the necessary magnetization of 20 A/m. For this purpose, we calculated the required volume concentrations for some candidate minerals (c.f. Tab. 2.1). It turns out that single domain (SD)- and multi domain (MD) hematites require $\geqslant$ 2 % and 0.8 − 17 % volume mineral content, respectively. However, these minerals have not been discovered in Shergottite, Nakhlite, and Chassignite meteorites (SNCs) (Sec. 2.3). Further, SD pyrrhotite requires 0.2 − 2 % volume mineral content, and slightly larger values of 2 − 4 wt.% were obtained by Dunlop and Arkani-Hamed [2005]. However, pyrrhotite has a low Curie temperature and is easily demagnetized by impacts. Finally, SD magnetite requires a volume concentration of 0.08 − 1.00 % and has been discovered in SNCs, making it the most promising candidate (Sec. 2.3). Still, SD magnetite is hard to form in intrusive sills and dikes, and the relatively young SNCs may not be representative for the highly magnetized Noachian crust (Sec. 2.3).

5 For comparison, their magnetizations were linearly scaled to a 40 km thick magnetized layer.

12 ISOLATED MAGNETIC ANOMALIES - PALEOPOLES

With regard to the open questions in Ch. 2, the analysis of isolated anomalies and paleopoles can contribute to study the early tectonic regime of Mars (Sec. 2.6), true polar wander related to the emplacement of the Tharsis bulge (Sec. 2.5), or crustal magnetization (Sec. 2.2). Usually, paleopole positions are estimated by fitting one or more homogeneously magnetized sources of a given shape and depth to a lithospheric field anomaly. Ideally, an isolated anomaly should be chosen that corresponds to a geological feature or to a gravitational anomaly (Sec. 2.5). In the following, we will give examples of isolated anomalies which the final model allows to resolve properly. As a next step, these isolated anomalies may be used to estimate paleopole positions and to analyze their uncertainty with the model covariance (Sec. 7.4) and resolution matrices (Sec. 7.5).

12.1 SOUTH POLAR

As shown in Fig. 12.1, two isolated anomalies are located between the Hellas and Argyre impact basins. More accurately, anomaly A (Fig. 12.1a) is located at 357°E/52°S in Noachis Terra, and anomaly B (Fig. 12.1a) is located at 28°E/64°S at the western edge of Malea Planum, a region of the late Noachian volcanic plains (Sec. 10.1.6).

The presence of these anomalies is confirmed by the ER (Fig. 12.1e) and the AB/SPO data (filled circles in Fig. 12.1f). Further, both the surface field intensity (F) along with the horizontal field components (Fig. 12.1b) and the vertically down (Z) component (Fig. 12.1d) at surface altitude as predicted by the final model indicate that these anomalies may originate from two almost vertically oriented dipoles, each opposite in sign. If their true magnetization pattern is indeed resolved, and if the Martian core field was dipolar, it follows that these anomalies must have acquired their magnetization at high magnetic latitudes. Also, at least one pole reversal of the Martian core dynamo must have occurred in this case [Arkani-Hamed, 2001a; Frawley and Taylor, 2004].

Acuña et al. [2001] already discovered anomaly B in the mapping phase orbit (MPO) data, but no paleomagnetic pole positions have been calculated for this anomaly. Anomaly A, on the other hand, was discovered only with the final model [Morschhauser et al., 2014]. Previously, its discovery may have been hampered for two reasons which are related to its weak field signature: First, it can easily be masked by non-lithospheric noise, and second, anomaly A is hardly visible at the MPO altitude where many lithospheric field models have been evaluated.

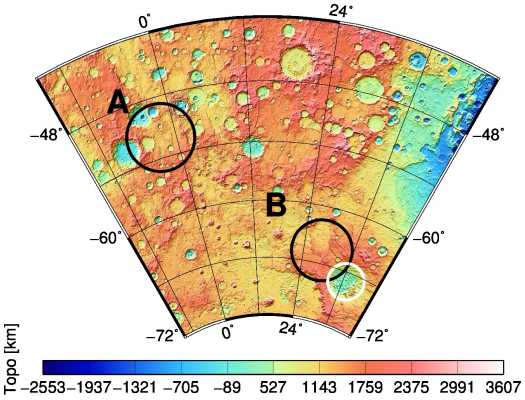

(a) MOLA Topography

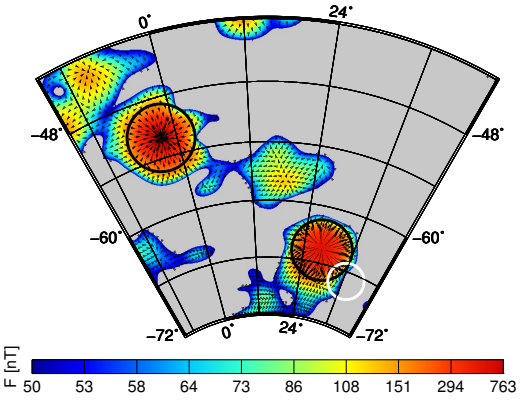

(b) Field intensity (F) and horizontal field at surface altitude

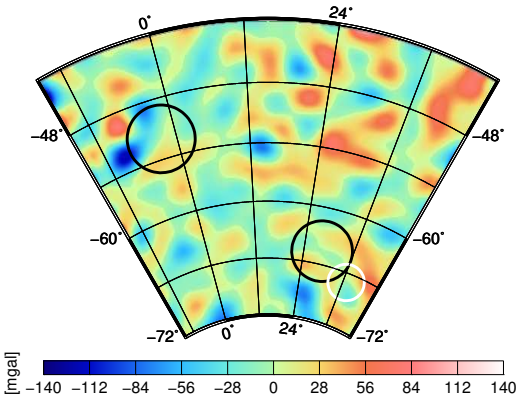

(c) Free-Air gravity [Konopliv et al., 2011]

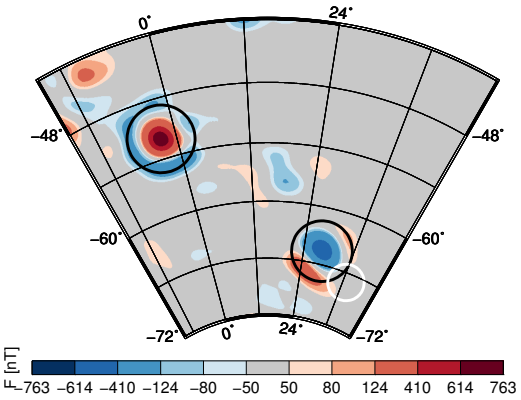

(d) Vertically down (Z) component at surface altitude

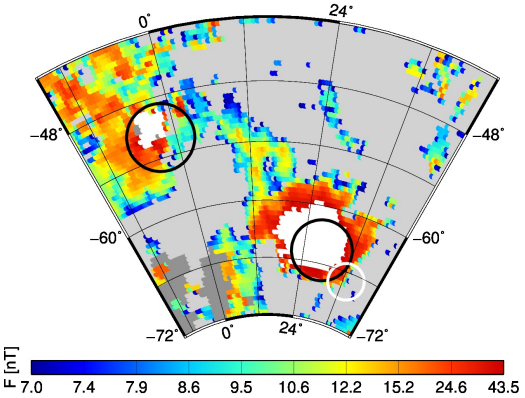

(e) ER data at 185 km altitude [Lillis et al., 2008a]

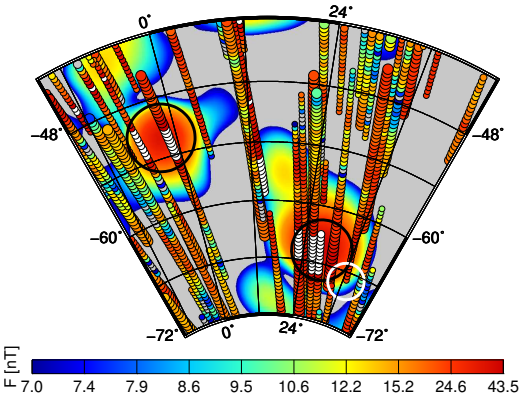

(f) Lithospheric field at 185 km altitude

Figure 12.1. Two isolated magnetic anomalies (black circles) are shown which are located in Noachis Terra. As well, the Noachian volcanic unit Pityusa Patera is shown (white circle). In detail, the subfigures display (a) the MOLA topography, (b) the magnetic field intensity (F) (colors) and the horizontal components (black arrows) as predicted by the final model at the mean surface altitude, (c) the free-air gravity [Konopliv et al., 2011], (d) the vertically down (Z) component of the magnetic field as predicted by the final model at the mean surface altitude, (e) the magnetic field intensity (F) as measured by the ER at ~185 km altitude, and (f) the magnetic field intensity (F) as predicted by the final model at 185 km altitude along with the measured AB/SPO data (filled circles which are larger when closer to 185 km).

The source of these anomalies is unknown, and no obvious geologic (not shown), topographic (Fig. 12.1a), or gravimetric (Fig. 12.1c) feature is associated with them. Anomaly B, however, is located above a late Noachian volcanic unit [Tanaka et al., 2014] in Malea Planum, about 250 km from the center of Pityusa Patera (white solid circle in Fig. 12.1). However, if Pityusa Patera is related to anomaly B, it remains questionable why the other volcanoes in Malea Planum, all of similar age and morphology [Williams et al., 2009], are not associated with a magnetic signature (Sec. 10.1.6).

12.2 ARCADIA PLANITIA

Another two isolated anomalies, spaced ~450 km apart, are presented in Fig. 12.2 (black-white ellipses). These anomalies are located near the western rim of Arcadia Planitia in the northern lowlands, and centered at 167°E/57°N (anomaly A) and 168°E/49°N (anomaly B).

The magnetic field intensity (F) along with the horizontal field vectors and the vertically down (Z) component of the magnetic field as predicted by the final model are displayed at two altitudes in Fig. 12.2: the fields at surface altitude are shown in Figs. 12.2b and 12.2f, respectively, and the fields at an altitude of 185 km are shown in Figs. 12.2c and 12.2g, respectively. From a qualitative assessment, anomaly A may represent a vertically oriented dipole, while anomaly B may either represent a horizontally oriented dipole with a declination of ~60° or a dipole with an inclination of ~30° and a declination of ~90°. The two anomalies cannot be related to any topographic (Fig. 12.2a) or geologic (not shown) surface feature. Concerning the gravity data (Fig. 12.2e), we observe a larger region with negative free-air anomalies in the vicinity of the magnetic anomalies. Yet, these gravity anomalies do not uniquely correspond to the magnetic field anomalies.The ER data (Fig. 12.2h) confirm a local field maximum at the locations of these two anomalies. However, the field signature of anomaly A is offset by ~150 km, which is possibly too large to be explained by the spatial uncertainty of 50 – 150 km in the ER data [Lillis et al., 2008a]. In any case, this offset cannot be confirmed by the AB/SPO data (Fig. 12.2d). Further, the AB/SPO data show a stronger field signature over anomaly B as compared to the predictions of the final model. Otherwise, many of the AB/SPO data are noisy with some neighboring tracks showing very different field intensities (F).

At surface altitude, the two magnetic anomalies are more distinct and better separated (Figs. 12.2b and 12.2f) than at an altitude of 185 km (Figs. 12.2c and 12.2g). Especially, the field signature of anomaly B may be masked at altitudes of $\geqslant$ 185 km by stronger fields located towards its southeast. Hence, the downward continued field contains valuable information on isolated anomalies which can be revealed with a robust model of the crustal field only.

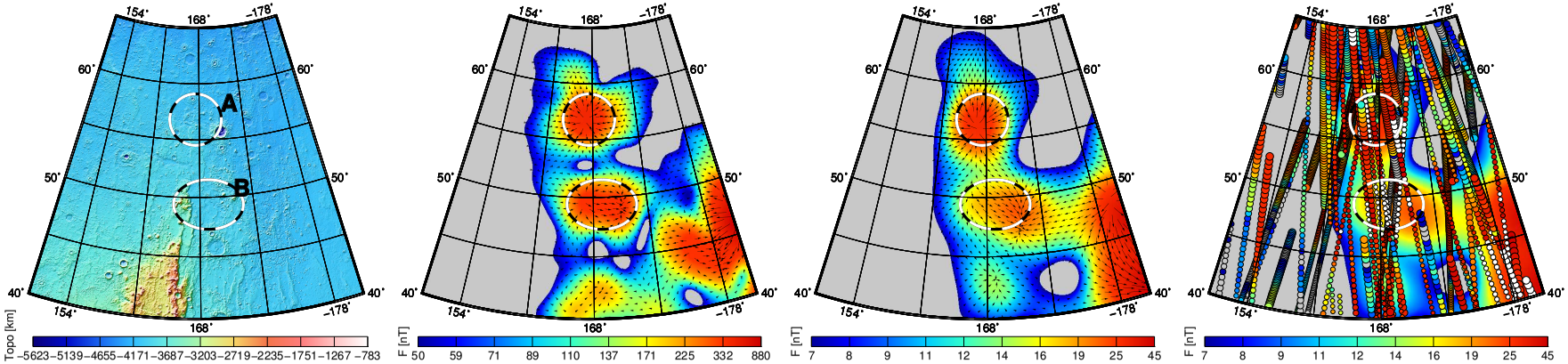

(a) MOLA Topography

(b) Field intensity (F) and horizontal field at surface altitude

(c) Field intensity (F) and horizontal field at 185 km altitude

(d) AB/SPO data along with field intensity (F)

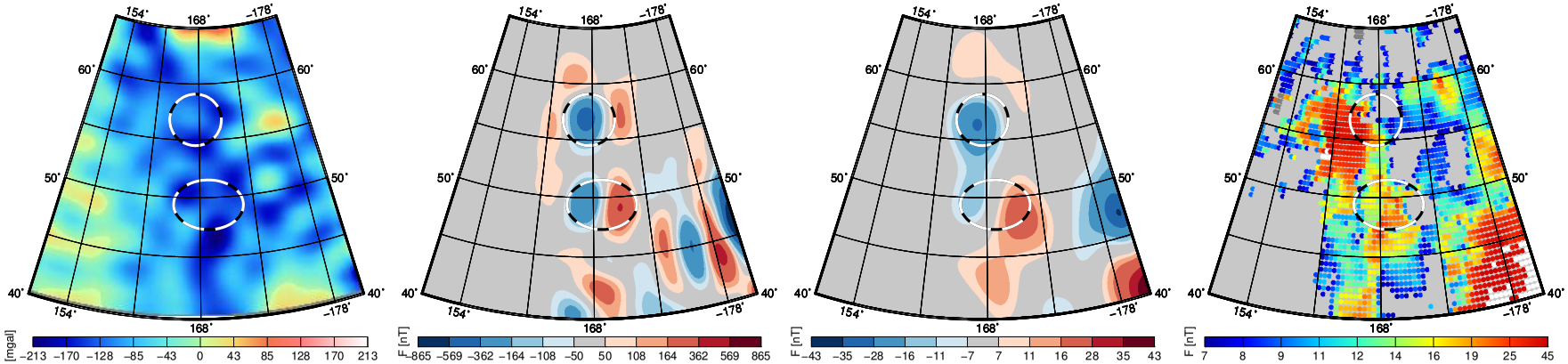

(e) Free-Air gravity [Konopliv et al., 2011]

(f) Vertically down (Z) component at surface altitude

(g) Vertically down (Z) component at 185 km altitude

(h) ER data at 185 km altitude [Lillis et al., 2008a]

Figure 12.2. Different aspects are shown for a region in Arcadia Planitia where two isolated magnetic field anomalies are located (black-white ellipses). These aspects include (a) the MOLA topography, (b) the magnetic field intensity (F) (colors) and the horizontal components (black arrows) as predicted by the final model at the mean surface altitude, (c) the magnetic field intensity (colors) and the horizontal components (black arrows) as predicted by the final model at 185 km altitude, (d) the AB/SPO data (larger circles are closer to an altitude of 185 km) along with field intensity (background colors), (e) the free-air gravity [Konopliv et al., 2011], (f) the vertically down (Z) component of the magnetic field as predicted by the final model at the mean surface altitude, (g) the vertically down (Z) component of the magnetic field intensity (F) as predicted by the final model at 185 km altitude, and (h) the ER data showing the magnetic field intensity (F) at 185 km altitude.

Part VI

SUMMARY & OUTLOOK

SUMMARY & OUTLOOK

In previous studies based on data of the Mars Global Surveyor (MGS) mission (Ch. 3), it was unambiguously shown that the main contribution to the Martian magnetic field is of crustal origin (Sec. 1.1). This crustal magnetic field is intimately connected with the thermal evolution, mineralogy, chemistry, and tectonics of Mars, making magnetic field data very valuable in order to understand the history of Mars. The MGS data allowed to study the Martian magnetic field in unprecedented detail (Sec. 1.2 and 1.3) and many new questions were raised along with these data (Ch. 2). For example, the crustal magnetic field was most probably magnetized in a core dynamo field, but it is disputed when and how long this core dynamo was active (Sec. 2.1). Also, little is known about the dynamics of the Martian core dynamo. In particular, it is unknown how often pole reversals have occurred and how magnetic paleopole positions can be interpreted (Sec. 2.5). Furthermore, the Martian crustal field is about one order of magnitude stronger than that of Earth, but it is unknown which minerals contribute to this strong remanent magnetization (Sec. 2.3), and how thick the magnetized layer is (Sec. 2.2).

Models of the crustal magnetic field are a powerful tool in order to answer these questions. Such models consist of a physically consistent description of the crustal field. Hence, they allow extracting the crustal part of the satellite magnetic field data in a controlled mathematical way. Also, they allow projecting the data on a constant altitude, ideally down to the planetary surface (Sec. 1.4). In this way, magnetic anomalies of smaller scale may be resolved which can then be interpreted in the context of the regional geology, gravity, mineralogy, and topography.

Several models of the crustal magnetic field of Mars have been published which are based on MGS magnetic field data. In comparison to these, the model derived in this work improves upon two properties: The spatial and spectral resolution of the model, and the robustness of the model (Sec. 1.4). For this purpose, several techniques have been applied (Ch. 6): First, a meaningful selection of all available data from the fluxgate magnetometers on MGS (MAG) was used (Ch. 4). Then, the resolution of the model was increased as compared to previous models. In detail, the model was expanded in terms of spherical harmonic (SH) functions up to degree and order 110 which corresponds to a spatial resolution of ~195 km (Sec. 6.1), and a simple parametrization of the external day- and nightside fields was included (Sec. 6.1). In addition, the mapping phase orbit (MPO) data were weighted with a priori data weights. These weights are based on the statistics of the data instead of a preliminary model (Sec. 4.1 and 6.3). Further, we did not reject data a priori except for one aerobraking phase (AB) data track

(Sec. 4.2). Instead, data outliers were handled by approximating a modified Huber norm (Sec. 6.3). Finally, the model was regularized by approximating an L1 norm in order to suppress noise in the model (Sec. 6.4).

The resulting model is a good representation of all known characteristics of the Martian magnetic field (Sec. 7.1 - 7.3), it provides a good fit to the data (Ch. 8), and it is stable when downward-continued to the surface (Ch. 9). As compared to an L2 norm, it was shown that the applied approximation of an L1 norm for regularization significantly improved the robustness of the model while allowing for strong local field gradients in the model (Sec. 9.2). Further, it was demonstrated that the usage of a modified Huber norm to fit the data successfully reduced the influence of data outliers (Sec. 9.3). In the following, we will summarize how we used our model to address the open questions mentioned above. For this purpose, the crustal magnetic field as predicted by the model at the mean surface altitude of 3393.5 km was analyzed together with the topography, geology, and gravity data.

The timing of the Martian core dynamo was investigated by analyzing a variety of volcanoes (Sec. 10.1). Most interestingly, the magnetic signatures of the volcanoes Apollinaris Patera and Hadriaca Patera have previously been interpreted in favor of a late dynamo shutdown at around $3.6-3.7$ Gyr ago (e.g., Hood et al. [2010]). In contrast, we found that the surface magnetic signature of Apollinaris Patera rather suggests that the volcano has demagnetized a previously emplaced larger magnetized region (Sec. 10.1.1). This interpretation implies a dynamo shutdown earlier than $\sim$3.8 Gyr ago. Moreover, we interpret the surface magnetic signature of Hadriaca Patera in favor of an early dynamo shutdown prior to $\sim$3.9 Gyr (Sec. 10.1.3), as opposed to earlier findings [Lillis et al., 2006]. As well, other volcanic regions on Mars were found to support a dynamo shutdown earlier than about 3.8 Gyr ago (Sec. 10.1.4, Sec. 10.1.6, and Sec. 10.1.2), in agreement with previous studies [Lillis et al., 2008a, 2015]. Overall, we reinterpret the magnetic signature of the Martian volcanoes to be compatible with a shutdown of the core dynamo in the Noachian, prior to $\sim$3.9 Gyr ago. In contrary to previous findings, no known volcano was found to possess a magnetic field signature indicating strong thermoremanent magnetization (TRM).

In addition, the timing of the Martian core dynamo was investigated by analyzing the magnetic field signatures of impact craters (Sec. 10.2): Large basins with diameters of $D > 924$ km were found to possess a stronger (weaker) magnetic field than their surroundings if the basin was > 4.13 Gyr (< 4.15 Gyr) in age (Sec. 10.2.1). The only weak exception is Amenthes with an age of $\sim$4.22 Gyr. The magnetic signature of smaller craters is more difficult to assess as the observation altitude acts as a low-pass filter for the magnetic field. Therefore, we downward continued our model to the surface altitude in order to analyze the magnetic signature above such craters. In Terra Sirenum (TS), a previously unknown low-field region was found above the ancient multiring basin T. Sirenum ($500-1000$ km) for which we estimated a lower age limit of $\sim 3.67-4.09$ Gyr (Sec. 10.2.2). Further,

we analyzed seven craters down to a diameter of D = 150 km in Terra Sabaea (Sec. 10.2.2). Out of these, five craters (3.83 – 4.19 Gyr) show a central field minimum, in contrast to the previous interpretation that one of these craters, Schiaparelli (3.91 – 3.93 Gyr), is partially magnetized [Shahnas and Arkani-Hamed, 2007; Lillis et al., 2013b]. Taken together, current evidence suggests that the Martian core dynamo most probably ceased at around 4.1 Gyr ago, in agreement with the work of Lillis et al. [2008].

Observations of the crustal magnetic field do not uniquely constrain the magnetization of the Martian crust. Still, the magnetization can be estimated if further assumptions on the sources of the magnetic field are made (Sec. 2.2). Here, we assume that a 40 km thick layer of the crust is magnetized with a radially uniform magnetization (Sec. 2.2), that the crustal field is well described by our model, and that the magnetization only contains spectral wavelengths below SH degree and order 110 (Ch. 11). In this case, the part of the magnetization that is necessary to explain the observed crustal field can directly be calculated from the Gauss coefficients of the final model (Sec. 11). As a result, we find that the Martian crust must be magnetized with at least 20 A/m in order to explain the strongest observed fields. In turn, this magnetization is consistent with TRM of single domain (SD) magnetite with a volume concentration of about 1 % in a 40 km thick magnetized layer if it was magnetized in a field of 50 μT (Ch. 11). SD magnetite has been discovered in Shergottite, Nakhlite, and Chassignite meteorites (SNCs) and is characterized by a strong and stable TRM. However, it requires fast cooling, and is not easily formed in intrusive sills and dikes (Sec. 2.3). Alternatively, hematite-ilmenite lamellae or multi domain (MD) hematite may also explain the required magnetization, but these minerals have not been detected in SNCs.

The magnetic field generated by the Earth's core dynamo is changing on secular timescales. Even more, pole reversals are known to occur every ten thousand to million of years (e.g., Cande and Kent [1995]). On Mars, the dynamics of the extinct core dynamo can only be investigated by studying the crustal field. For this purpose, many authors have estimated paleopole positions by modeling the magnetization of crustal field anomalies (Sec. 2.5). With this method, the most reliable results are usually obtained if the modeled field anomaly is isolated. The presented model of the crustal magnetic field helps to improve estimates of paleopole positions by its ability to resolve isolated anomalies (Ch. 12). In particular, we have discovered isolated anomalies near the south pole (Sec. 12.1) and Arcadia Planitia (Sec. 12.2) which support the hypothesis of magnetic pole reversals on Mars (Sec. 2.5). In future studies, these anomalies can be used in combination with the resolution matrix of the presented model (Sec. 7.5) to improve the estimates of paleopole positions. In addition, the respective covariance matrix (Sec. 7.4) can be used to estimate the robustness of the derived paleopole positions. Such estimates are necessary to investigate polar wander and the dynamics of the core dynamo field, but are largely missing in the literature.

In the future, the presented model of the crustal magnetic field may be improved by adding data of the Mars Atmosphere and Volatile Evolution (MAVEN) mission. This satellite was inserted into Martian orbit at the end of 2014 and is equipped with two fluxgate magnetometers (FGMs) at the tips of its solar panels. It provides magnetic field data down to an altitude of 125 km [Jakosky et al., 2015]. Further, the model could be improved if correlations between data points are taken into account. However, a good understanding of the external fields is required for this purpose. Also, a higher resolution of the model could be anticipated in order to fit the small-scale variations in the low-altitude data.

In conclusion, we have derived a robust model of the crustal magnetic field of Mars in terms of SH functions. Using this model, we studied the surface magnetic field signature associated with volcanoes and impact craters. As a result, we found that the Martian core dynamo most probably ceased to operate in the Noachian, at around $4.0 - 4.1$ Gyr ago. In addition, we have presented a model of the magnetization. From this model, we concluded that the magnetization must locally reach up to 20 A/m in a 40 km thick crust. Finally, we have shown that the presented model can contribute to better constrain magnetic paleopoles by resolving isolated magnetic field anomalies.

Part VII

APPENDIX

A

NOMENCLATURE ON MARS

Figure A.1. The color-coded Mars Orbiter Laser Altimeter (MOLA) topography is shown along with the boundaries and names of regions on Mars according to the International Astronomical Union (IAU). As well, the regions which have been studied in this work are shown with the references to the respective figures. In all maps, planetocentric latitudes with east longitudes are shown in black and planetographic latitudes with west longitudes are shown in red. Further, mid-latitudes are shown in a mercator projection and polar latitudes are shown in a stereographic projection. The maps are publicly available from the U.S. Geological Survey (USGS), National Aeronautics and Space Administration (NASA) and IAU at *http:planetarynames.wr.usgs.govimagesmola_regional_boundaries.pdf* (downloaded October, 10th, 2015).

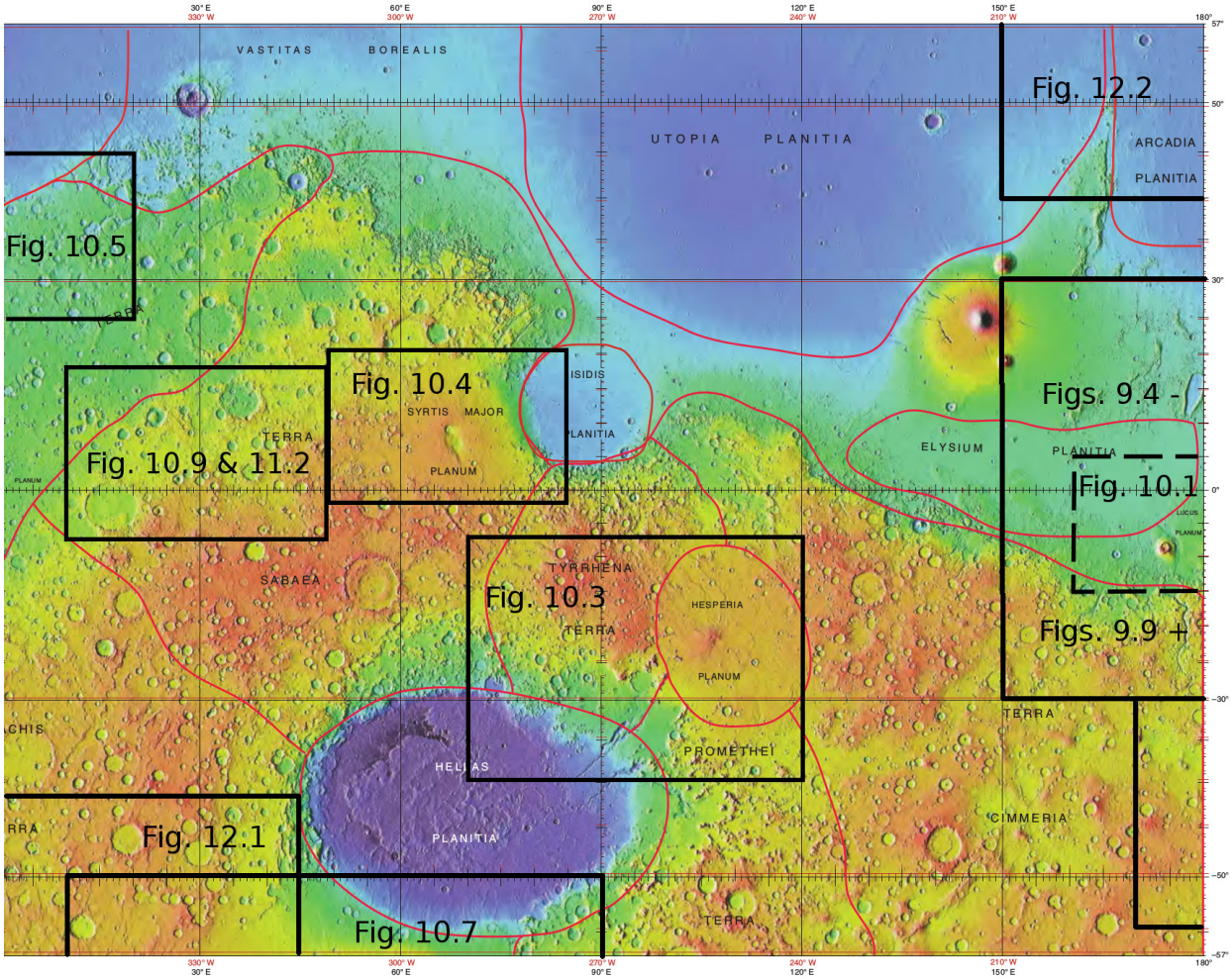

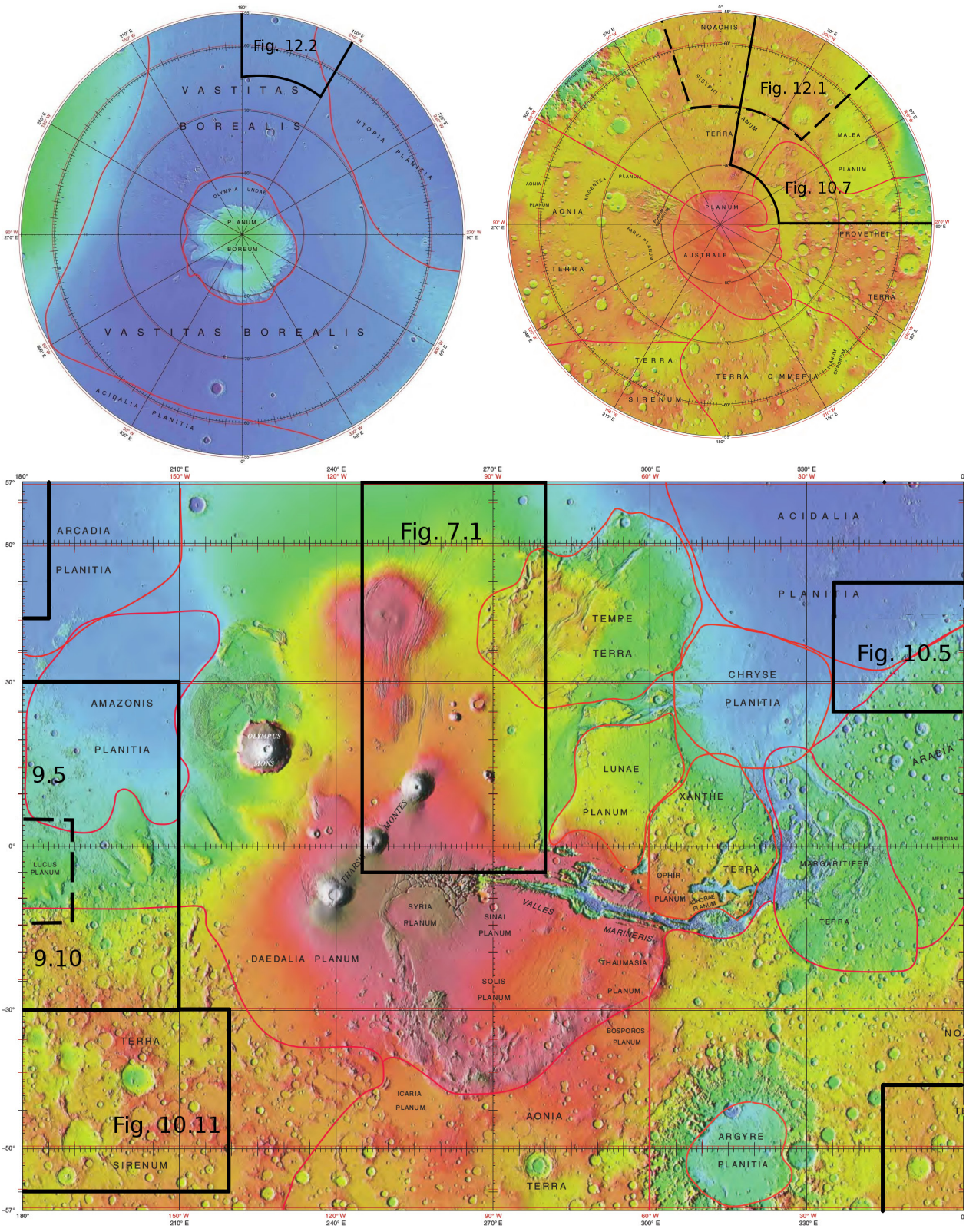
Fig. 12.2
VASTITAS BOREALIS
PLANUM BOREUM
OLYMPIA UNDAE
UTOPIA PLANITIA
ACIDALIA PLANITIA
Fig. 12.1
Fig. 10.7
NOACHIS
TERRA
MALEA PLANUM
AONIA PLANUM
ARGENTEA PLANUM
PARVA PLANUM
AUSTRALE
PROMETHEI
CIMMERIA
SIRENUM
Fig. 7.1
ARCADIA PLANITIA
AMAZONIS PLANITIA
ACIDALIA PLANITIA
TEMPE TERRA
CHRYSE PLANITIA
Fig. 10.5
OLYMPUS MONS
THARSIS MONTES
LUNAE PLANUM
XANTHE TERRA
ARABIA TERRA
9.5
9.10
LUCUS PLANUM
SYRIA PLANUM
SINAI PLANUM
VALLES MARINERIS
OPHIR PLANUM
MARGARITIFER TERRA
DAEDALIA PLANUM
THAUMASIA PLANUM
SOLIS PLANUM
BOSPOROS PLANUM
ICARIA PLANUM
AONIA TERRA
ARGYRE PLANITIA
Fig. 10.11
SIRENUM TERRA

Part VIII

BIBLIOGRAPHY

M. H. Acuña, J. E. P. Connerney, P. Wasilewski, R. P. Lin, K. A. Anderson, C. W. Carlson, J. McFadden, D. W. Curtis, H. Reme, and A. Cros. Mars Observer magnetic fields investigation. *J. Geophys. Res.*, 97:7799–7814, May 1992. doi: 10.1029/92JE00344.

M. H. Acuña, J. E. P. Connerney, P. Wasilewski, R. P. Lin, K. A. Anderson, C. W. Carlson, J. McFadden, D. W. Curtis, D. Mitchell, H. Reme, C. Mazelle, J. A. Sauvaud, C. D'Uston, A. Cros, J. L. Medale, S. J. Bauer, P. Cloutier, M. Mayhew, D. Winterhalter, and N. F. Ness. Magnetic Field and Plasma Observations at Mars: Initial Results of the Mars Global Surveyor mission. *Science*, 279(5357):1676–1680, March 1998. doi: 10.1126/science.279.5357.1676.

M. H. Acuña, J. E. P. Connerney, N. F. Ness, R. P. Lin, D. Mitchell, C. W. Carlson, J. McFadden, K. A. Anderson, H. Reme, C. Mazelle, D. Vignes, P. Wasilewski, and P. Cloutier. Global Distribution of Crustal Magnetization Discovered by the Mars Global Surveyor MAG/ER Experiment. *Science*, 284(5415):790–793, April 1999. doi: 10.1126/science.284.5415.790.

M. H. Acuña, J. E. P. Connerney, P. Wasilewski, R. P. Lin, D. Mitchell, K. A. Anderson, C. W. Carlson, J. McFadden, H. Rème, C. Mazelle, D. Vignes, S. J. Bauer, P. Cloutier, and N. F. Ness. Magnetic field of Mars: Summary of results from the aerobraking and mapping orbits. *J. Geophys. Res.*, 106:23403–23418, October 2001. doi: 10.1029/2000JE001404.

A. L. Albee. Mars 2000. *Annu. Rev. Earth Planet. Sci.*, 28:281–304, May 2000. doi: 10.1146/annurev.earth.28.1.281.

A. L. Albee, R. E. Arvidson, F. Palluconi, and T. Thorpe. Overview of the Mars Global Surveyor mission. *J. Geophys. Res.*, 106:23291–23316, October 2001. doi: 10.1029/2000JE001306.

H. Amit, U. R. Christensen, and B. Langlais. The influence of degree-1 mantle heterogeneity on the past dynamo of Mars. *Phys. Earth Planet. Int.*, 189:63–79, November 2011. doi: 10.1016/j.pepi.2011.07.008.

J. C. Andrews-Hanna, M. T. Zuber, and W. B. Banerdt. The borealis basin and the origin of the martian crustal dichotomy. *Nature*, 453(7199):1212–1215, June 2008. doi: 10.1038/nature07011.

M. Antretter, M. Fuller, E. Scott, M. Jackson, B. Moskowitz, and P. Solheid. Paleomagnetic record of Martian meteorite ALH84001. *J. Geophys. Res.*, 108(E6):5049, June 2003. doi: 10.1029/2002JE001979.

J. Arkani-Hamed. Paleomagnetic pole positions and pole reversals of Mars. *Geophys. Res. Lett.*, 28(17):3409–3412, September 2001a. doi: 10.1029/2001GL012928.

J. Arkani-Hamed. A 50-degree spherical harmonic model of the magnetic field of Mars. *J. Geophys. Res.*, 106(E10):23197–23208, October 2001b. doi: 10.1029/2000JE001365.

J. Arkani-Hamed. Correction to "A 50-degree spherical harmonic model of the magnetic field of Mars" by Jafar Arkani-Hamed. *J. Geophys. Res.*, 107:5012, March 2002a. doi: 10.1029/2002JE001853.

J. Arkani-Hamed. An improved 50-degree spherical harmonic model of the magnetic field of mars derived from both high-altitude and low-altitude data. *J. Geopys. Res.*, 107(E10): 5083, 2002b. doi: 10.1029/2001JE001835.

J. Arkani-Hamed. Magnetization of the Martian crust. *J. Geophys. Res.*, 107(E5):5032, May 2002c. doi: 10.1029/2001JE001496.

J. Arkani-Hamed. Thermoremanent magnetization of the martian lithosphere. *J Geophys Res-space*, 108(E10), 2003. doi: 10.1029/2003JE002049.

J. Arkani-Hamed. A coherent model of the crustal magnetic field of Mars. *J. Geopys. Res.*, 109:E09005, 2004a. doi: 10.1029/2004JE002265.

J. Arkani-Hamed. Timing of the Martian core dynamo. *J. Geopys. Res.*, 109:E03006, March 2004b. doi: 10.1029/2003JE002195.

J. Arkani-Hamed. On the possibility of single-domain/pseudo-single-domain magnetic particles existing in the lower crust of mars: Source of the strong magnetic anomalies. *J. Geophys. Res.*, 110(E12):E12009, 2005a. doi: 10.1029/2005JE002535.

J. Arkani-Hamed. Giant impact basins trace the ancient equator of Mars. *J. Geophys. Res.*, 110:E04012, April 2005b. doi: 10.1029/2004JE002343.

J. Arkani-Hamed. Did tidal deformation power the core dynamo of Mars? *Icarus*, 201(1): 31–43, May 2009. doi: 10.1016/j.icarus.2009.01.005.

J. Arkani-Hamed. Possible crippling of the core dynamo of Mars by Borealis impact. *J. Geophys. Res.*, 115:12021, December 2010. doi: 10.1029/2010JE003602.

J. Arkani-Hamed. Life of the Martian dynamo. *Phys. Earth Planet. In.*, 196:83–96, April 2012. doi: 10.1016/j.pepi.2012.02.008.

J. Arkani-Hamed and D. Boutin. Paleomagnetic poles of mars: Revisited. *J. Geopys. Res.*, 109(E3):E03011, March 2004. doi: 10.1029/2003JE002229.

J. Arkani-Hamed and D. Boutin. Is the primordial crust of Mars magnetized? *Icarus*, 221: 192–207, September 2012a. doi: 10.1016/j.icarus.2012.07.030.

J. Arkani-Hamed and D. Boutin. Low-magnetic crust underlying south province of mars. *Icarus*, 217(1):209–230, January 2012b. doi: 10.1016/j.icarus.2011.10.023.

J. Arkani-Hamed and P. Olson. Giant impact stratification of the Martian core. *Geophys. Res. Lett.*, 37:L02201, January 2010. doi: 10.1029/2009GL041417.

J. Arkani-Hamed, R. A. Langel, and M. Purucker. Scalar magnetic anomaly maps of Earth derived from POGO and Magsat data. *J. Geophys. Res.*, 99(B12):24075–24090, December 1994. doi: 10.1029/94JB00930.

J. Arkani-Hamed, B. Seyed-Mahmoud, K. D. Aldridge, and R. E. Baker. Tidal excitation of elliptical instability in the Martian core: Possible mechanism for generating the core dynamo. *J. Geophys. Res.*, 113:E06003, June 2008. doi: 10.1029/2007JE002982.

R. C. Aster, B. Borchers, and C. H. Thurber. *Parameter Estimation and Inverse Problems*. Elsevier - Academic Press, 2nd edition, 2013. ISBN 978-0-12-385048-5.

J. L. Bandfield. A Global View of Martian Surface Compositions from MGS-TES. *Science*, 287(5458):1626–1630, March 2000. doi: 10.1126/science.287.5458.1626.

R. J. Blakely. *Potential Theory in Gravity & Magnetic Applications*. Cambridge University Press, 1995. ISBN 0-521-57547-8.

D. Boutin and J. Arkani-Hamed. Pole wandering of Mars: Evidence from paleomagnetic poles. *Icarus*, 181(1):13–25, March 2006. doi: 10.1016/j.icarus.2005.10.025.

A. Bouvier, J. Blichert-Toft, and F. Albarède. Martian meteorite chronology and the evolution of the interior of Mars. *Earth Planet. Sci. Lett.*, 280:285–295, April 2009. doi: 10.1016/j.epsl.2009.01.042.

D. A. Brain. Martian magnetic morphology: Contributions from the solar wind and crust. *J. Geopys. Res.*, 108(A12):1424, 2003. doi: 10.1029/2002JA009482.

D. Breuer and T. Spohn. Early plate tectonics versus single-plate tectonics on Mars: Evidence from magnetic field history and crust evolution. *J. Geophys. Res.*, 108(E7):5072, July 2003. doi: 10.1029/2002JE001999.

D. Breuer and T. Spohn. Viscosity of the Martian mantle and its initial temperature: Constraints from crust formation history and the evolution of the magnetic field. *Planet. Space Sci.*, 54:153–169, February 2006. doi: 10.1016/j.pss.2005.08.008.

D. Breuer, S. Labrosse, and T. Spohn. Thermal Evolution and Magnetic Field Generation in Terrestrial Planets and Satellites. *Space Sci. Rev.*, 152:449–500, May 2010. doi: 10.1007/s11214-009-9587-5.

R. F. Butler. *Paleomagnetism: magnetic domains to geologic terranes*. Blackwell Scientific Publications, 1992. ISBN 978-0865420700.

J. C. Cain, B. B. Ferguson, and D. Mozzoni. An n = 90 internal potential function of the Martian crustal magnetic field. *J. Geopys. Res.*, 108(E2):5008, 2003. doi: 10.1029/2000JE001487.

S. C. Cande and D. V. Kent. Revised calibration of the geomagnetic polarity timescale for the Late Cretaceous and Cenozoic. *J. Geophys. Res.*, 100:6093–6095, April 1995. doi: 10.1029/94JB03098.

L. Carporzen, S. A. Gilder, and R. J. Hart. Palaeomagnetism of the Vredefort meteorite crater and implications for craters on Mars. *Nature*, 435:198–201, May 2005. doi: 10.1038/nature03560.

E. Chassefière, B. Langlais, Y. Quesnel, and F. Leblanc. The fate of early Mars' lost water: The role of serpentinization. *J. Geophys. Res.*, 118:1123–1134, May 2013. doi: 10.1002/jgre.20089.

L.-Y. Chiao, J.-R. Lin, and Y.-C. Gung. Crustal magnetization equivalent source model of mars constructed from a hierarchical multiresolution inversion of the mars global surveyor data. *J. Geopys. Res.*, 111(E12):E12010, December 2006. doi: 10.1029/2006JE002725.

P. R. Christensen and S. W. Ruff. Formation of the hematite-bearing unit in Meridiani Planum: Evidence for deposition in standing water. *J. Geophys. Res.*, 109:E08003, August 2004. doi: 10.1029/2003JE002233.

P. R. Christensen, J. L. Bandfield, R. N. Clark, K. S. Edgett, V. E. Hamilton, T. Hoefen, H. H. Kieffer, R. O. Kuzmin, M. D. Lane, M. C. Malin, R. V. Morris, J. C. Pearl, R. Pearson, T. L. Roush, S. W. Ruff, and M. D. Smith. Detection of crystalline hematite mineralization on Mars by the Thermal Emission Spectrometer: Evidence for near-surface water. *J. Geophys. Res.*, 105:9623–9642, April 2000. doi: 10.1029/1999JE001093.

P. R. Christensen, M. B. Wyatt, T. D. Glotch, A. D. Rogers, S. Anwar, R. E. Arvidson, J. L. Bandfield, D. L. Blaney, C. Budney, W. M. Calvin, A. Fallacaro, R. L. Fergason, N. Gorelick, T. G. Graff, V. E. Hamilton, A. G. Hayes, J. R. Johnson, A. T. Knudson, H. Y. McSween, G. L. Mehall, L. K. Mehall, J. E. Moersch, R. V. Morris, M. D. Smith, S. W. Squyres, S. W. Ruff, and M. J. Wolff. Mineralogy at Meridiani Planum from the Mini-TES Experiment on the Opportunity Rover. *Science*, 306:1733–1739, December 2004. doi: 10.1126/science.1104909.

S. M. Cisowski. Magnetic studies on Shergotty and other SNC meteorites. *Geochim. Cosmochim. Acta*, 50:1043–1048, June 1986. doi: 10.1016/0016-7037(86)90386-8.

R. I. Citron and S. Zhong. Constraints on the formation of the Martian crustal dichotomy from remnant crustal magnetism. *Phys Earth Planet In*, 212:55–63, December 2012. doi: 10.1016/j.pepi.2012.09.008.

D. A. Clark. Magnetic petrophysics and magnetic petrology: aids to geological interpretation of magnetic surveys. *J. Aust. Geol. Geophys.*, 17(2):83–103, 1997.

J. E. P. Connerney, M. H. Acuna, P. J. Wasilewski, N. F. Ness, H. Reme, C. Mazelle, D. Vignes, R. P. Lin, D. L. Mitchell, and P. A. Cloutier. Magnetic Lineations in the Ancient Crust of Mars. *Science*, 284:794–798, April 1999. doi: 10.1126/science.284.5415.794.

J. E. P. Connerney, M. H. Acuña, P. J. Wasilewski, G. Kletetschka, N. F. Ness, H. Rème, R. P. Lin, and D. L. Mitchell. The global magnetic field of Mars and implications for crustal evolution. *Geophys. Res. Lett.*, 28:4015–4018, November 2001. doi: 10.1029/2001GL013619.

J. E. P. Connerney, M. H. Acuña, N. F. Ness, T. Spohn, and G. Schubert. Mars Crustal Magnetism. *Space Sci. Rev.*, 111(1):1–32, March 2004. doi: 10.1023/B:SPAC.0000032719.40094.1d.

J. E. P. Connerney, M. H. Acuña, N. F. Ness, G. Kletetschka, D. L. Mitchell, R. P. Lin, and H. Reme. Tectonic implications of Mars crustal magnetism. *Proc. Nat. Acad. Sci.*, 102:14970–14975, October 2005. doi: 10.1073/pnas.0507469102.

S. A. Curtis and N. F. Ness. Remanent magnetism at Mars. *Geophys. Res. Lett.*, 15:737–739, August 1988. doi: 10.1029/GL015i008p00737.

W. Dietrich and J. Wicht. A hemispherical dynamo model: Implications for the Martian crustal magnetization. *Phys Earth Planet In*, 217:10–21, April 2013. doi: 10.1016/j.pepi.2013.01.001.

S. S. Dolginov. On the magnetic field of Mars - Mars 5 evidence. *Geophys. Res. Lett.*, 5:93–95, January 1978. doi: 10.1029/GL005i001p00093.

S. S. Dolginov and L. N. Zhuzgov. The magnetic field and the magnetosphere of the planet Mars. *Planet. Space Sci.*, 39:1493–1510, November 1991. doi: 10.1016/0032-0633(91)90077-N.

S. S. Dolginov, Y. G. Yeroshenko, and L. N. Zhuzgov. Magnetic field in the very close neighborhood of Mars according to data from the Mars 2 and Mars 3 spacecraft. *J. Geophys. Res.*, 78(22):4779–4786, August 1973. doi: 10.1029/JA078i022p04779.

S. S. Dolginov, E. G. Eroshenko, and L. N. Zhuzgov. The magnetic field of Mars according to the data from the Mars 3 and Mars 5. *J. Geophys. Res.*, 81(19):3353–3362, July 1976. doi: 10.1029/JA081i019p03353.

M. Dryer and G. R. Heckman. Application of the Hypersonic analog to the Standing Shock of Mars. *Sol. Phys.*, 2:112–124, July 1967. doi: 10.1007/BF00155897.

D. J. Dunlop and J. Arkani-Hamed. Magnetic minerals in the Martian crust. *J. Geophys. Res.*, 110(E12):E12S04, 2005. doi: 10.1029/2005JE002404.

D. J. Dunlop and G. Kletetschka. Multidomain hematite: A source of planetary magnetic anomalies? *Geophys. Res. Lett.*, 28:3345–3348, 2001. doi: 10.1029/2001GL013125.

D. J. Dunlop and Ö. Özdemir. *Rock Magnetism: Fundamentals and Frontiers*. Cambridge University Press, 1997. ISBN 9780521000987.

M. D. Dyar, S. A. McEnroe, E. Murad, L. L. Brown, and H. Schiellerup. The relationship between exsolution and magnetic properties in hemo-ilmenite: Insights from Mössbauer spectroscopy with implications for planetary magnetic anomalies. *Geophys. Res. Lett.*, 31: L04608, February 2004. doi: 10.1029/2003GL019076.

E. Echer, W. D. Gonzalez, B. T. Tsurutani, and A. L. C. Gonzalez. Interplanetary conditions causing intense geomagnetic storms (Dst <= -100 nT) during solar cycle 23 (1996-2006). *J. Geophys. Res.*, 113:A05221, May 2008. doi: 10.1029/2007JA012744.

E. Echer, B. T. Tsurutani, and W. D. Gonzalez. Interplanetary origins of moderate (-100 nT < Dst < -50 nT) geomagnetic storms during solar cycle 23 (1996-2008). *J. Geophys. Res.*, 118:385–392, January 2013. doi: 10.1029/2012JA018086.

A. Fairén, J. Ruiz, and F. Anguita. An origin for the linear magnetic anomalies on mars through accretion of terranes: Implications for dynamo timing. *Icarus*, 160(1):220–223, November 2002. doi: 10.1006/icar.2002.6942.

C. G. Farquharson and D. W. Oldenburg. Non-linear inversion using general measures of data misfit and model structure. *Geophys. J. Int.*, 134:213–227, July 1998. doi: 10.1046/j.1365-246X.1998.00555.x.

C. I. Fassett and J. W. Head. Sequence and timing of conditions on early mars. *Icarus*, 211 (2):1204–1214, February 2011. doi: 10.1016/j.icarus.2010.11.014.

J. Feinberg, H. Wenk, P. Renne, and G. Scott. Epitaxial relationships of clinopyroxene-hosted magnetite determined using electron backscatter diffraction (EBSD) technique. *Am. Mineral.*, 89(2-3):462–466, February 2004. doi: 10.2138/am-2004-2-328.

B. B. Ferguson, J. C. Cain, D. H. Crider, D. A. Brain, and E. M. Harnett. External fields on the nightside of Mars at Mars Global Surveyor mapping altitudes. *Geophys. Res. Lett.*, 32:L16105, August 2005. doi: 10.1029/2004GL021964.

E. C. Ferré, S. A. Friedman, F. Martín-Hernández, J. M. Feinberg, J. L. Till, D. A. Ionov, and J. A. Conder. Eight good reasons why the uppermost mantle could be magnetic. *Tectonophysics*, 624:3–14, June 2014. doi: 10.1016/j.tecto.2014.01.004.

C. C. Finlay, S. Maus, C. D. Beggan, T. N. Bondar, A. Chambodut, T. A. Chernova, A. Chulliat, V. P. Golovkov, B. Hamilton, M. Hamoudi, R. Holme, G. Hulot, W. Kuang, B. Langlais, V. Lesur, F. J. Lowes, H. Lühr, S. MacMillan, M. Mandea, S. McLean, C. Manoj, M. Menvielle, I. Michaelis, N. Olsen, J. Rauberg, M. Rother, T. J. Sabaka, A. Tangborn, L. Tøffner-Clausen, E. Thébault, A. W. P. Thomson, I. Wardinski, Z. Wei, and T. I. Zvereva. International Geomagnetic Reference Field: the eleventh generation. *Geophys. J. Int.*, 183:1216–1230, December 2010. doi: 10.1111/j.1365-246X.2010.04804.x.

J. J. Frawley and P. T. Taylor. Paleo-pole positions from martian magnetic anomaly data. *Icarus*, 172(2):316–327, December 2004. doi: 10.1016/j.icarus.2004.07.025.

H. Frey. Ages of very large impact basins on Mars: Implications for the late heavy bombardment in the inner solar system. *Geophys. Res. Lett.*, 35:L13203, July 2008. doi: 10.1029/2008GL033515.

H. Frey and R. A. Schultz. Large impact basins and the mega-impact origin for the crustal dichotomy on Mars. *Geophys. Res. Lett.*, 15:229–232, March 1988. doi: 10.1029/GL015i003p00229.

H. Frey, S. E. H. Sakimoto, and J. H. Roark. Discovery of a 450 km diameter, multi-ring basin on Mars through analysis of MOLA topographic data. *Geophys. Res. Lett.*, 26(12): 1657–1660, Jun 1999. doi: 10.1029/1999gl900357.

H. V. Frey, J. H. Roark, K. M. Shockey, E. L. Frey, and S. E. H. Sakimoto. Ancient lowlands on Mars. *Geophys. Res. Lett.*, 29(10):1384, May 2002. doi: 10.1029/2001gl013832.

M. Funaki, V. Hoffmann, and N. Imae. Estimate of the magnetic field of Mars based on the magnetic characteristics of the Yamato 000593 nakhlite. *Met. Planet. Sci.*, 44:1179–1191, August 2009. doi: 10.1111/j.1945-5100.2009.tb01216.x.

J. Gattacceca, R. H. Hewins, J.-P. Lorand, P. Rochette, F. Lagroix, C. Cournède, M. Uehara, S. Pont, V. Sautter, R. B. Scorzelli, C. Hombourger, P. Munayco, B. Zanda, H. Chennaoui, and L. FerrièRe. Opaque minerals, magnetic properties, and paleomagnetism of the Tissint Martian meteorite. *Met. Planet. Sci.*, 48:1919–1936, October 2013. doi: 10.1111/maps.12172.

J. Gattacceca, P. Rochette, R. B. Scorzelli, P. Munayco, C. Agee, Y. Quesnel, C. Cournède, and J. Geissman. Martian meteorites and Martian magnetic anomalies: A new perspective from NWA 7034. *Geophys. Res. Lett.*, 41:4859–4864, July 2014. doi: 10.1002/2014GL060464.

C. F. Gauss. Allgemeine Theorie des Erdmagnetismus. In *Werke*, volume 5, pages 119–193. Springer Berlin Heidelberg, 1877. ISBN 978-3-642-49319-5. doi: 10.1007/978-3-642-49319-5_5.

L. L. Griffith and E. L. Shock. A geochemical model for the formation of hydrothermal carbonates on Mars. *Nature*, 377:406–408, October 1995. doi: 10.1038/377406a0.

M. Grott and M. A. Wieczorek. Density and lithospheric structure at Tyrrhena Patera, Mars, from gravity and topography data. *Icarus*, 221:43–52, September 2012. doi: 10.1016/j.icarus.2012.07.008.

D. Gubbins. *Time Series Analysis and Inverse Theory for Geophysicists*. Cambridge University Press, March 2004. ISBN 978-0-52-152569-5.

D. Gubbins, D. Ivers, S. M. Masterton, and D. E. Winch. Analysis of lithospheric magnetization in vector spherical harmonics. *Geophys. J. Int.*, 187:99–117, October 2011. doi: 10.1111/j.1365-246X.2011.05153.x.

H. P. Gunnlaugsson, Ö. Helgason, L. Kristjánsson, P. Nørnberg, H. Rasmussen, S. Steinþórsson, and G. Weyer. Magnetic properties of olivine basalt: Application to Mars. *Phys. Earth Planet. Int.*, 154:276–289, March 2006. doi: 10.1016/j.pepi.2005.09.012.

J. S. Halekas, D. A. Brain, R. J. Lillis, M. O. Fillingim, D. L. Mitchell, and R. P. Lin. Current sheets at low altitudes in the Martian magnetotail. *Geophys. Res. Lett.*, 33:L13101, July 2006. doi: 10.1029/2006GL026229.

C. G. A. Harrison. Questions About Magnetic Lineations in the Ancient Crust of Mars. *Science*, 287(5453):547, 2000. doi: 10.1126/science.287.5453.547a.

K. P. Harrison and R. E. Grimm. Controls on Martian hydrothermal systems: Application to valley network and magnetic anomaly formation. *J. Geophys. Res.*, 107:5025, May 2002. doi: 10.1029/2001JE001616.

W. K. Hartmann and G. Neukum. Cratering Chronology and the Evolution of Mars. *Space Sci. Rev.*, 96(1):165–194, 2001. doi: 10.1023/a:1011945222010.

S. A. Hauck and R. J. Phillips. Thermal and crustal evolution of Mars. *J. Geophys. Res.*, 107 (E7):5052, July 2002. doi: 10.1029/2001JE001801.

H. Hiesinger and J. W. Head. The Syrtis Major volcanic province, Mars: Synthesis from Mars Global Surveyor data. *J. Geophys. Res.*, 109:E01004, January 2004. doi: 10.1029/2003JE002143.

P. W. Holland and R. E. Welsch. Robust regression using iteratively reweighted least-squares. *Commun. Stat. A-Theor.*, 6(9):813–827, January 1977. doi: 10.1080/03610927708827533.

L. L. Hood and L. L. H. Zakharian. Mapping and modeling of magnetic anomalies in the northern polar region of Mars. *J. Geopys. Res.*, 106(E7):14601–14619, 2001. doi: 10.1029/2000JE001304.

L. L. Hood, N. C. Richmond, E. Pierazzo, and P. Rochette. Distribution of crustal magnetic fields on Mars: Shock effects of basin-forming impacts. *Geophys. Res. Lett.*, 30(6):1281, March 2003. doi: 10.1029/2002GL016657.

L. L. Hood, C. N. Young, N. C. Richmond, and K. P. Harrison. Modeling of major martian magnetic anomalies: Further evidence for polar reorientations during the Noachian. *Icarus*, 177(1):144–173, September 2005. doi: 10.1016/j.icarus.2005.02.008.

L. L. Hood, N. Richmond, K. Harrison, and R. Lillis. East-west trending magnetic anomalies in the Southern Hemisphere of Mars: Modeling analysis and interpretation. *Icarus*, 191(1):113–131, November 2007. doi: 10.1016/j.icarus.2007.04.025.

L. L. Hood, K. P. Harrison, B. Langlais, R. J. Lillis, F. Poulet, and D. A. Williams. Magnetic anomalies near Apollinaris Patera and the Medusae Fossae Formation in Lucus Planum, Mars. *Icarus*, 208:118–131, July 2010. doi: 10.1016/j.icarus.2010.01.009.

P. J. Huber. Robust estimation of a location parameter. *Ann. Math. Stat.*, 35(1):73–101, 1964.

M. Humayun, A. Nemchin, B. Zanda, R. H. Hewins, M. Grange, A. Kennedy, J.-P. Lorand, C. Göpel, C. Fieni, S. Pont, and D. Deldicque. Origin and age of the earliest Martian crust from meteorite NWA 7533. *Nature*, 503:513–516, November 2013. doi: 10.1038/nature12764.

B. M. Hynek, R. E. Arvidson, and R. J. Phillips. Geologic setting and origin of Terra Meridiani hematite deposit on Mars. *J. Geophys. Res.*, 107(E10):5088, October 2002. doi: 10.1029/2002JE001891.

B. M. Jakosky and R. J. Phillips. Mars' Volatile and climate history. *Nature*, 412:237–244, July 2001.

B. M. Jakosky, R. P. Lin, J. M. Grebowsky, J. G. Luhmann, D. F. Mitchell, G. Beutelschies, T. Priser, M. Acuna, L. Andersson, D. Baird, D. Baker, R. Bartlett, M. Benna, S. Bougher, D. Brain, D. Carson, S. Cauffman, P. Chamberlin, J.-Y. Chaufray, O. Cheatom, J. Clarke, J. Connerney, T. Cravens, D. Curtis, G. Delory, S. Demcak, A. DeWolfe, F. Eparvier, R. Ergun, A. Eriksson, J. Espley, X. Fang, D. Folta, J. Fox, C. Gomez-Rosa, S. Habenicht,

J. Halekas, G. Holsclaw, M. Houghton, R. Howard, M. Jarosz, N. Jedrich, M. Johnson, W. Kasprzak, M. Kelley, T. King, M. Lankton, D. Larson, F. Leblanc, F. Lefevre, R. Lillis, P. Mahaffy, C. Mazelle, W. McClintock, J. McFadden, D. L. Mitchell, F. Montmessin, J. Morrissey, W. Peterson, W. Possel, J.-A. Sauvaud, N. Schneider, W. Sidney, S. Sparacino, A. I. F. Stewart, R. Tolson, D. Toublanc, C. Waters, T. Woods, R. Yelle, and R. Zurek. The Mars Atmosphere and Volatile Evolution (MAVEN) Mission. *Space Sci. Rev.*, 195: 3–48, December 2015. doi: 10.1007/s11214-015-0139-x.

C. L. Johnson and R. J. Phillips. Evolution of the Tharsis region of Mars: insights from magnetic field observations. *Earth Planet. Sci. Lett.*, 230(3-4):241–254, February 2005. doi: 10.1016/j.epsl.2004.10.038.

D. M. Jurdy and M. Stefanick. Mars magnetic field: Sources and models for a quarter of the southern hemisphere. *Icarus*, 203:38–46, September 2009. doi: 10.1016/j.icarus.2009.04.027.

T. Keller and P. J. Tackley. Towards self-consistent modeling of the martian dichotomy: The influence of one-ridge convection on crustal thickness distribution. *Icarus*, 202:429–443, August 2009. doi: 10.1016/j.icarus.2009.03.029.

W. S. Kiefer. Gravity Evidence for Extinct Magma Chamber System on Mars. Number 3252 in International Conference on Mars, Pasadena, California, March 2003a.

W. S. Kiefer. Gravity Evidence for Extinct Magma Chambers on Mars: Tyrrhena Patera and Hadriaca Patera. Number 1234 in Lunar and Planetary Science Conference, League City, TExas, March 2003b.

W. S. Kiefer. Gravity evidence for an extinct magma chamber beneath Syrtis Major, Mars: a look at the magmatic plumbing system. *Earth Planet. Sci. Lett.*, 222:349–361, May 2004. doi: 10.1016/j.epsl.2004.03.009.

H. H. Kieffer. Mars Consortium global maps. In *Third International Colloquium on Mars*, volume 3, pages 133–135, 1981.

G. Kletetschka, P. J. Wasilewski, and P. T. Taylor. Unique thermoremanent magnetization of multidomain sized hematite: Implications for magnetic anomalies. *Earth Planet. Sci. Lett.*, 176:469–479, March 2000a. doi: 10.1016/S0012-821X(00)00016-9.

G. Kletetschka, P. J. Wasilewski, and P. T. Taylor. Mineralogy of the sources for magnetic anomalies on Mars. *Met. Planet. Sci.*, 35:895–899, September 2000b. doi: 10.1111/j.1945-5100.2000.tb01478.x.

G. Kletetschka, P. J. Wasilewski, and P. T. Taylor. Hematite vs. magnetite as the signature for planetary magnetic anomalies? *Phys. Earth Planet. Int.*, 119:259–267, May 2000c. doi: 10.1016/S0031-9201(00)00141-2.

G. Kletetschka, P. J. Wasilewski, and P. T. Taylor. The role of hematite ilmenite solid solution in the production of magnetic anomalies in ground- and satellite-based data. *Tectonophysics*, 347:167–177, March 2002. doi: 10.1016/S0040-1951(01)00243-8.

G. Klingelhöfer, R. V. Morris, B. Bernhardt, C. Schröder, D. S. Rodionov, P. A. de Souza, A. Yen, R. Gellert, E. N. Evlanov, B. Zubkov, J. Foh, U. Bonnes, E. Kankeleit, P. Gütlich, D. W. Ming, F. Renz, T. Wdowiak, S. W. Squyres, and R. E. Arvidson. Jarosite and Hematite at Meridiani Planum from Opportunity's Mössbauer Spectrometer. *Science*, 306:1740–1745, December 2004. doi: 10.1126/science.1104653.

D. Kobayashi and K. F. Sprenke. Lithospheric drift on early Mars: Evidence in the magnetic field. *Icarus*, 210(1):37–42, November 2010. doi: 10.1016/j.icarus.2010.06.015.

A. S. Konopliv, S. W. Asmar, W. M. Folkner, Ö. Karatekin, D. C. Nunes, S. E. Smrekar, C. F. Yoder, and M. T. Zuber. Mars high resolution gravity fields from MRO, Mars seasonal gravity, and other dynamical parameters. *Icarus*, 211:401–428, January 2011. doi: 10.1016/j.icarus.2010.10.004.

A. M. Krymskii, T. K. Breus, N. F. Ness, M. H. AcuñA, J. E. P. Connerney, D. H. Crider, D. L. Mitchell, and S. J. Bauer. Structure of the magnetic field fluxes connected with crustal magnetization and topside ionosphere at Mars. *J. Geophys. Res.*, 107(A9):1245, September 2002. doi: 10.1029/2001JA000239.

R. A. Langel, C. C. Schnetzler, J. D. Phillips, and R. J. Horner. Initial vector magnetic anomaly map from Magsat. *Geophys. Res. Lett.*, 9:273–276, April 1982. doi: 10.1029/GL009i004p00273.

B. Langlais and M. Purucker. A polar magnetic paleopole associated with Apollinaris Patera, Mars. *Planet. Space Sci.*, 55:270–279, February 2007. doi: 10.1016/j.pss.2006.03.008.

B. Langlais, M. E. Purucker, and M. Mandea. Crustal magnetic field of Mars. *J. Geopys. Res.*, 109(E2):E02008, February 2004. doi: 10.1029/2003JE002048.

B. Langlais, R. Lillis, and M. Purucker. An improved model of the magnetic lithospheric field of Mars using both MGS-MAG and MGS-ER measurements. Number EPSC2010-393 in European Planetary Science Congress, Rome, Italy, September 2010.

V. Lesur. Introducing localized constraints in global geomagnetic field modelling. *Earth Plan. Space*, 58(4):477–483, April 2006. doi: 10.1186/BF03351943.

V. Lesur and A. Jackson. Exact solutions for internally induced magnetization in a shell. *Geophysical Journal International*, 140:453–459, February 2000. doi: 10.1046/j.1365-246X.2000.00046.x.

V. Lesur, M. Rother, F. Vervelidou, M. Hamoudi, and E. Thébault. Post-processing scheme for modelling the lithospheric magnetic field. *Solid Earth*, 4:105–118, March 2013. doi: 10.5194/se-4-105-2013.

V. Lesur, M. Rother, I. Wardinski, R. Schachtschneider, M. Hamoudi, and A. Chambodut. Parent magnetic field models for the IGRF-12 GFZ-candidates. *Earth Planets Space*, 67:87, December 2015. doi: 10.1186/s40623-015-0239-6.

M. Leweling and T. Spohn. Mars: a magnetic field due to thermoremanence? *Planet. Space Sci.*, 45:1389–1400, November 1997. doi: 10.1016/S0032-0633(97)00186-4.

K. W. Lewis and F. J. Simons. Local spectral variability and the origin of the Martian crustal magnetic field. *Geophys. Res. Lett.*, 39:L18201, September 2012. doi: 10.1029/2012GL052708.

R. J. Lillis. Mapping crustal magnetic fields at Mars using electron reflectometry. *Geophys. Res. Lett.*, 31(15):L15702, 2004. doi: 10.1029/2004GL020189.

R. J. Lillis, M. Manga, D. L. Mitchell, R. P. Lin, and M. H. Acuna. Unusual magnetic signature of the Hadriaca Patera Volcano: Implications for early Mars. *Geophys. Res. Lett.*, 33:L03202, February 2006. doi: 10.1029/2005GL024905.

R. J. Lillis, H. V. Frey, and M. Manga. Rapid decrease in Martian crustal magnetization in the Noachian era: Implications for the dynamo and climate of early Mars. *Geophys. Res. Lett.*, 35(14):L14203, July 2008. doi: 10.1029/2008GL034338.

R. J. Lillis, H. V. Frey, M. Manga, D. L. Mitchell, R. P. Lin, M. H. Acuña, and S. W. Bougher. An improved crustal magnetic field map of Mars from electron reflectometry: Highland volcano magmatic history and the end of the martian dynamo. *Icarus*, 194(2):575–596, April 2008a. doi: 10.1016/j.icarus.2007.09.032.

R. J. Lillis, D. L. Mitchell, R. P. Lin, and M. H. Acuña. Electron reflectometry in the martian atmosphere. *Icarus*, 194:544–561, April 2008b. doi: 10.1016/j.icarus.2007.09.030.

R. J. Lillis, J. Dufek, J. E. Bleacher, and M. Manga. Demagnetization of crust by magmatic intrusion near the Arsia Mons volcano: Magnetic and thermal implications for the development of the Tharsis province, Mars. *J. Volcanol. Geoth. Res.*, 185(1-2):123–138, August 2009. doi: 10.1016/j.jvolgeores.2008.12.007.

R. J. Lillis, S. W. Bougher, F. González-Galindo, F. Forget, M. D. Smith, and P. C. Chamberlin. Four Martian years of nightside upper thermospheric mass densities derived from electron reflectometry: Method extension and comparison with GCM simulations. *J. Geophys. Res.*, 115:E07014, July 2010a. doi: 10.1029/2009JE003529.

R. J. Lillis, M. E. Purucker, J. S. Halekas, K. L. Louzada, S. T. Stewart-Mukhopadhyay, M. Manga, and H. V. Frey. Study of impact demagnetization at Mars using Monte Carlo modeling and multiple altitude data. *J. Geopys. Res.*, 115:E07007, July 2010b. doi: 10.1029/2009JE003556.

R. J. Lillis, S. Robbins, M. Manga, J. S. Halekas, and H. V. Frey. Time history of the Martian dynamo from crater magnetic field analysis. *J. Geophys. Res.*, 118:1488–1511, July 2013a. doi: 10.1002/jgre.20105.

R. J. Lillis, S. T. Stewart, and M. Manga. Demagnetization by basin-forming impacts on early Mars: Contributions from shock, heat, and excavation. *J. Geophys. Res.*, 118:1045–1062, May 2013b. doi: 10.1002/jgre.20085.

R. J. Lillis, J. Dufek, W. S. Kiefer, B. A. Black, M. Manga, J. A. Richardson, and J. E. Bleacher. The Syrtis Major volcano, Mars: A multidisciplinary approach to interpreting its magmatic evolution and structural development. *J. Geophys. Res.*, page n/a–n/a, 2015. doi: 10.1002/2014je004774.

K. L. Louzada, S. T. Stewart, B. P. Weiss, J. Gattacceca, R. J. Lillis, and J. S. Halekas. Impact demagnetization of the Martian crust: Current knowledge and future directions. *Earth Planet. Sci. Lett.*, 305:257–269, May 2011. doi: 10.1016/j.epsl.2011.03.013.

F. J. Lowes. Mean-square values on sphere of spherical harmonic vector fields. *J. Geophys. Res.*, 71:2179–2179, April 1966. doi: 10.1029/JZ071i008p02179.

J. G. Luhmann and L. H. Brace. Near-Mars space. *Rev. Geophys.*, 29:121–140, May 1991. doi: 10.1029/2007JA012744.

M. M. Marinova, O. Ahoronson, and E. Asphaug. Mega-impact formation of theMars hemispheric dichotomy. *Science*, 453:1216–1219, 2008. doi: 10.1038/nature07070.

P. Mauersberger. Das Mittel der Energiedichte des geomagnetischen Hauptfeldes an der Erdoberfläche und seine säkulare Änderung. *Gerlands Beitr. Geophys.*, 65:207–215, 1956.

S. Maus, M. Rother, K. Hemant, C. Stolle, H. Lühr, A. Kuvshinov, and N. Olsen. Earth's lithospheric magnetic field determined to spherical harmonic degree 90 from CHAMP satellite measurements. *Geophys. J. Int.*, 164:319–330, February 2006. doi: 10.1111/j.1365-246X.2005.02833.x.

M. A. Mayhew. Inversion of satellite magnetic anomaly data. *J Geophys. - Z. Geophys.*, 45 (2):119–128, 1979.

C. A. McCammon, S. A. McEnroe, P. Robinson, K. Fabian, and B. P. Burton. High efficiency of natural lamellar remanent magnetisation in single grains of ilmeno-hematite calculated using Mössbauer spectroscopy. *Earth Planet. Sci. Lett.*, 288:268–278, October 2009. doi: 10.1016/j.epsl.2009.09.030.

S. A. McEnroe and L. L. Brown. A closer look at remanence-dominated aeromagnetic anomalies: Rock magnetic properties and magnetic mineralogy of the Russell Belt microcline-sillimanite gneiss, northwest Adirondack Mountains, New York. *J. Geophys. Res.*, 105:16437–16456, July 2000. doi: 10.1029/2000JB900051.

S. A. McEnroe, M. Polve, and G. Juve. Chemical and petrographic characterization of ilmenite and magnetite in oxide-rich cumulates of the Sokndal Region, Rogaland, Norway. *Norweg. Geol. Surv. Bull.*, 436:49–56, 2000.

S. A. McEnroe, R. J. Harrison, P. Robinson, U. Golla, and M. J. Jercinovic. Effect of fine-scale microstructures in titanohematite on the acquisition and stability of natural remanent magnetization in granulite facies metamorphic rocks, southwest Sweden: Implications for crustal magnetism. *J. Geophys. Res.*, 106(B12):30523–30546, January 2001a. doi: 10.1029/2001JB000180.

S. A. McEnroe, P. Robinson, and P. Panish. Aeromagnetic anomalies, magnetic petrology, and rock magnetism of hemo-ilmenite- and magnetite-rich cumulate rocks from the Sokndal Region, South Rogaland, Norway. *Am. Mineral.*, 86(11-12):1447–1468, November 2001b. doi: 10.2138/am-2001-11-1213.

S. A. McEnroe, R. J. Harrison, P. Robinson, and F. Langenhorst. Nanoscale haematite-ilmenite lamellae in massive ilmenite rock: an example of 'lamellar magnetism' with implications for planetary magnetic anomalies. *Geophys. J. Int.*, 151:890–912, December 2002. doi: 10.1046/j.1365-246X.2002.01813.x.

G. E. McGill and S. W. Squyres. Origin of the Martian crustal dichotomy - Evaluating hypotheses. *Icarus*, 93:386–393, October 1991. doi: 10.1016/0019-1035(91)90221-E.

D. McKenzie. Planetary science: Plate tectonics on Mars? *Nature*, 399:307–308, May 1999. doi: 10.1038/20554.

H. J. Melosh. Tectonic patterns on a reoriented planet - Mars. *Icarus*, 44:745–751, December 1980. doi: 10.1016/0019-1035(80)90141-4.

G. G. Michael. Planetary surface dating from crater size-frequency distribution measurements: Multiple resurfacing episodes and differential isochron fitting. *Icarus*, 226:885–890, September 2013. doi: 10.1016/j.icarus.2013.07.004.

J. R. Michalski and J. E. Bleacher. Supervolcanoes within an ancient volcanic province in Arabia Terra, Mars. *Nature*, 502:47–52, October 2013. doi: 10.1038/nature12482.

C. Milbury and G. Schubert. Search for the global signature of the Martian dynamo. *J. Geophys. Res.*, 115:E10010, October 2010. doi: 10.1029/2010JE003617.

C. Milbury, G. Schubert, C. A. Raymond, S. E. Smrekar, and B. Langlais. The history of Mars' dynamo as revealed by modeling magnetic anomalies near Tyrrhenus Mons and Syrtis Major. *J. Geophys. Res.*, 117:E10007, October 2012. doi: 10.1029/2012JE004099.

D. L. Mitchell, R. P. Lin, C. Mazelle, H. Rème, P. A. Cloutier, J. E. P. Connerney, M. H. Acuña, and N. F. Ness. Probing Mars' crustal magnetic field and ionosphere with the MGS Electron Reflectometer. *J. Geopys. Res.*, 106:23419–23428, October 2001. doi: 10.1029/2000JE001435.

D. L. Mitchell, R. J. Lillis, R. P. Lin, J. E. P. Connerney, and M. H. Acuna, M. H.a. A global map of Mars' crustal magnetic field based on electron reflectometry. *J. Geopys. Res.*, 112 (E1), January 2007. doi: 10.1029/2005JE002564.

D. Moehlmann, W. Riedler, J. Rustenbach, K. Schwingenschuh, J. Kurths, U. Motschmann, T. Roatsch, K. Sauer, and H. T. M. Lichtenegger. The question of an internal Martian magnetic field. *Planet. Space Sci.*, 39:83–88, February 1991. doi: 10.1016/0032-0633(91)90130-3.

P. S. Mohit and J. Arkani-Hamed. Impact demagnetization of the martian crust. *Icarus*, 168:305–317, April 2004. doi: 10.1016/j.icarus.2003.12.005.

J. M. Moore. Mars Blueberry fields for ever. *Nature*, 428:711–712, April 2004. doi: 10.1038/428711a.

A. Morschhauser, M. Grott, and D. Breuer. Crustal recycling, mantle dehydration, and the thermal evolution of mars. *Icarus*, 212(2):541–558, April 2011. doi: 10.1016/j.icarus.2010.12.028.

A. Morschhauser, V. Lesur, and M. Grott. A spherical harmonic model of the lithospheric magnetic field of Mars. *J. Geophys. Res.*, 119:1162–1188, June 2014. doi: 10.1002/2013JE004555.

T. Nagata. *Rock Magnetism*. Maruzen Ltd., 1961.

N. F. Ness, M. H. Acuña, J. Connerney, P. Wasilewski, C. Mazelle, J. Sauvaud, D. Vignes, C. D'Uston, H. Reme, R. Lin, D. L. Mitchell, J. McFadden, D. Curtis, P. Cloutier, and S. J. Bauer. MGS magnetic fields and electron reflectometer investigation: discovery of paleomagnetic fields due to crustal remanence. *Adv. Space Res.*, 23:1879–1886, January 1999. doi: 10.1016/S0273-1177(99)00271-9.

G. A. Neumann, M. T. Zuber, M. A. Wieczorek, P. J. McGovern, F. G. Lemoine, and D. E. Smith. Crustal structure of Mars from gravity and topography. *J. Geophys. Res.*, 109: E08002, August 2004. doi: 10.1029/2004JE002262.

F. Nimmo. Dike intrusion as a possible cause of linear Martian magnetic anomalies. *Geology*, 28:391, May 2000. doi: 10.1130/0091-7613(2000)28<391:DIAAPC>2.0.CO;2.

F. Nimmo and M. S. Gilmore. Constraints on the depth of magnetized crust on Mars from impact craters. *J. Geophys. Res.*, 106(E6):12315–12324, June 2001. doi: 10.1029/2000JE001325.

F. Nimmo and D. J. Stevenson. Influence of early plate tectonics on the thermal evolution and magnetic field of Mars. *J. Geophys. Res.*, 105:11969–11980, May 2000. doi: 10.1029/1999JE001216.

F. Nimmo and K. Tanaka. Early Crustal Evolution of Mars. *Annu. Rev. Earth Planet. Sci.*, 33:133–161, January 2005. doi: 10.1146/annurev.earth.33.092203.122637.

F. Nimmo, S. D. Hart, D. G. Korycansky, and C. B. Agnor. Implications of an impact origin for the martian hemispheric dichotomy. *Nature*, 453(7199):1220–1223, June 2008. doi: 10.1038/nature07025.

L. Nyquist, D. Bogard, C.-Y. Shih, A. Greshake, D. Stoeffler, and O. Eugster. Ages and geologic histories of martian meteorites. *Space Sci. Rev.*, 96(1/4):105–164, 2001. doi: 10.1023/a:1011993105172.

N. Olsen, K.-H. Glassmeier, and X. Jia. Separation of the Magnetic Field into External and Internal Parts. *Space Sci. Rev.*, 152:135–157, May 2010a. doi: 10.1007/s11214-009-9563-0.

N. Olsen, G. Hulot, and T. J. Sabaka. Measuring the Earth's Magnetic Field from Space: Concepts of Past, Present and Future Missions. *Space Sci. Rev.*, 155:65–93, August 2010b. doi: 10.1007/s11214-010-9676-5.

Ö. Özdemir and W. O'Reilly. An experimental study of thermoremanent magnetization acquired by synthetic monodomain titanomaghemites. *J. Geom. Geoel.*, 34:467–478, 1982. doi: 10.5636/jgg.34.467.

R. L. Parker. *Geophysical Inverse Theory*. Princeton University Press, 1994. ISBN 978-069103634-2.

R. L. Parker. Ideal bodies for Mars magnetics. *J. Geopys. Res.*, 108:5006, January 2003. doi: 10.1029/2001JE001760.

R. L. Parker, L. Shure, and J. A. Hildebrand. The Application of Inverse Theory to Seamount Magnetism. *Rev. Geophys.*, 25(1):17–40, February 1987. doi: 10.1029/RG025i001p00017.

V. G. Perminov. The Difficult Road to Mars: A brief History of Mars Exploration in the Soviet Union. In *Monographs in aerospace history*, volume 15. National Aeronautics and Space Administration Headquarters, Washington, D.C., 1999.

R. J. Phillips. Ancient Geodynamics and Global-Scale Hydrology on Mars. *Science*, 291 (5513):2587–2591, March 2001. doi: 10.1126/science.1058701.

J. B. Plescia. Morphometric properties of Martian volcanoes. *J. Geophys. Res.*, 109:E03003, March 2004. doi: 10.1029/2002JE002031.

M. Purucker, D. Ravat, H. Frey, C. Voorhies, T. Sabaka, and M. Acuña. An altitude-normalized magnetic map of Mars and its interpretation. *Geophys. Res. Lett.*, 27:2449–2452, 2000. doi: 10.1029/2000GL000072.

Y. Quesnel, B. Langlais, and C. Sotin. Local inversion of magnetic anomalies: Implication for Mars crustal evolution. *Planet. Space Sci.*, 55:258–269, February 2007. doi: 10.1016/j.pss.2006.02.004.

Y. Quesnel, C. Sotin, B. Langlais, S. Costin, M. Mandea, M. Gottschalk, and J. Dyment. Serpentinization of the martian crust during Noachian. *Earth Planet. Sci. Lett.*, 277:184–193, January 2009. doi: 10.1016/j.epsl.2008.10.012.

D. Ravat. Interpretation of Mars southern highlands high amplitude magnetic field with total gradient and fractal source modeling: New insights into the magnetic mystery of Mars. *Icarus*, 214:400–412, August 2011. doi: 10.1016/j.icarus.2011.05.004.

C. Reese and V. Solomatov. Early martian dynamo generation due to giant impacts. *Icarus*, 207(1):82–97, May 2010. doi: 10.1016/j.icarus.2009.10.016.

W. Riedler, K. Schwingenschuh, D. Moehlmann, V. N. Oraevskii, E. Eroshenko, and J. Slavin. Magnetic fields near Mars - First results. *Nature*, 341:604–607, October 1989. doi: 10.1038/341604a0.

W. Riedler, K. Schwingenschuh, H. Lichtenegger, D. Mohlmann, J. Rustenbach, Y. Yeroshenko, J. Achache, J. Slavin, J. G. Luhmann, and C. T. Russell. Interaction of the solar wind with the planet Mars - PHOBOS 2 magnetic field observations. *Planet. Space Sci.*, 39:75–81, February 1991. doi: 10.1016/0032-0633(91)90129-X.

S. J. Robbins, G. D. Achille, and B. M. Hynek. The volcanic history of Mars: High-resolution crater-based studies of the calderas of 20 volcanoes. *Icarus*, 211:1179–1203, February 2011. doi: 10.1016/j.icarus.2010.11.012.

S. J. Robbins, B. M. Hynek, R. J. Lillis, and W. F. Bottke. Large impact crater histories of Mars: The effect of different model crater age techniques. *Icarus*, 225:173–184, July 2013. doi: 10.1016/j.icarus.2013.03.019.

J. H. Roberts and J. Arkani-Hamed. Impact heating and coupled core cooling and mantle dynamics on Mars. *J. Geophys. Res.*, 119:729–744, April 2014. doi: 10.1002/2013JE004603.

J. H. Roberts and S. Zhong. Degree-1 convection in the Martian mantle and the origin of the hemispheric dichotomy. *J. Geophys. Res.*, 111:6013–6035, 2006. doi: 10.1029/2005JE002668.

J. H. Roberts and S. Zhong. The cause for the north south orientation of the crustal dichotomy and the equatorial location of Tharsis on Mars. *Icarus*, 190:24–31, September 2007. doi: 10.1016/j.icarus.2007.03.002.

J. H. Roberts, R. J. Lillis, and M. Manga. Giant impacts on early Mars and the cessation of the Martian dynamo. *J. Geophys. Res.*, 114:E04009, April 2009. doi: 10.1029/2008JE003287.

P. Robinson, R. J. Harrison, S. A. McEnroe, and R. B. Hargraves. Lamellar magnetism in the haematite-ilmenite series as an explanation for strong remanent magnetization. *Nature*, 418:517–520, August 2002. doi: 10.1038/nature00942.

P. Robinson, R. J. Harrison, S. A. McEnroe, and R. B. Hargraves. Nature and origin of lamellar magnetism in the hematite-ilmenite series. *Am. Mineral.*, 89(5-6):725–747, 2004. doi: 10.1038/nature00942.

P. Rochette. Crustal magnetization of Mars controlled by lithology or cooling rate in a reversing dynamo? *Geophys. Res. Lett.*, 33:L02202, January 2006. doi: 10.1029/2005GL024280.

P. Rochette, J.-P. Lorand, G. Fillion, and V. Sautter. Pyrrhotite and the remanent magnetization of SNC meteorites: a changing perspective on Martian magnetism. *Earth Planet. Sci. Lett.*, 190:1–12, July 2001. doi: 10.1016/S0012-821X(01)00373-9.

P. Rochette, G. Fillion, R. Ballou, F. Brunet, B. Ouladdiaf, and L. Hood. High pressure magnetic transition in pyrrhotite and impact demagnetization on Mars. *Geophys. Res. Lett.*, 30:1683, July 2003. doi: 10.1029/2003GL017359.

P. Rochette, J. Gattacceca, V. Chevrier, V. Hoffmann, J. P. Lorand, M. Funaki, and R. Hochleitner. Matching Martian crustal magnetization and magnetic properties of Martian meteorites. *Met. Planet. Sci.*, 40:529, April 2005. doi: 10.1111/j.1945-5100.2005.tb00961.x.

J. Ruiz. The very early thermal state of Terra Cimmeria: Implications for magnetic carriers in the crust of Mars. *Icarus*, 203:454–459, October 2009. doi: 10.1016/j.icarus.2009.05.021.

J. Ruiz, P. J. McGovern, and R. Tejero. The early thermal and magnetic state of the cratered highlands of Mars. *Earth Planet. Sci. Lett.*, 241:2–10, January 2006. doi: 10.1016/j.epsl.2005.10.016.

S. K. Runcorn. On the interpretation of lunar magnetism. *Phys. Earth Planet. Int.*, 10: 327–335, August 1975. doi: 10.1016/0031-9201(75)90059-X.

C. T. Russell. The magnetic field of Mars - Mars 3 evidence reexamined. *Geophys. Res. Lett.*, 5:81–84, January 1978a. doi: 10.1029/GL005i001p00081.

C. T. Russell. The magnetic field of Mars - Mars 5 evidence re-examined. *Geophys. Res. Lett.*, 5:85–88, January 1978b. doi: 10.1029/GL005i001p00085.

C. T. Russell, J. G. Luhmann, J. R. Spreiter, and S. S. Stahara. The magnetic field of Mars - Implications from gas dynamic modeling. *J. Geophys. Res.*, 89:2997–3003, May 1984. doi: 10.1029/JA089iA05p02997.

G. G. Schaber. Syrtis Major: a low-relief volcanic shield. *J. Geophys. Res.*, 87:9852–9866, November 1982. doi: 10.1029/JB087iB12p09852.

D. R. Schmitz and J. C. Cain. Geomagnetic spherical harmonic analyses: 1. Techniques. *J. Geopys. Res.*, 88:1222–1228, January 1983. doi: 10.1029/JB088iB02p01222.

D. Schroeer and R. C. Nininger. Morin Transition in α-Fe_2O_3 Microcyrstals. *Phys. Rev. Lett.*, 19:632–634, September 1967. doi: 10.1103/PhysRevLett.19.632.

G. Schubert and T. Spohn. Thermal history of Mars and the sulfur content of its core. *J Geophys Res-space*, 95:14095–14104, August 1990. doi: 10.1029/JB095iB09p14095.

G. Schubert, C. T. Russell, and W. B. Moore. Geophysics: Timing of the Martian dynamo. *Nature*, 408:666–667, December 2000. doi: 10.1038/35047163.

P. H. Schultz, R. A. Schultz, and J. Rogers. The structure and evolution of ancient impact basins on Mars. *J. Geophys. Res.*, 87:9803–9820, November 1982. doi: 10.1029/JB087iB12p09803.

E. R. D. Scott and M. Fuller. A possible source for the Martian crustal magnetic field. *Earth Planet. Sci. Lett.*, 220:83–90, March 2004. doi: 10.1016/S0012-821X(04)00032-9.

H. Shahnas and J. Arkani-Hamed. Viscous and impact demagnetization of Martian crust. *J. Geophys. Res.*, 112:E02009, February 2007. doi: 10.1029/2005JE002424.

F. J. Simons, F. A. Dahlen, and M. A. Wieczorek. Spatiospectral Concentration on a Sphere. *SIAM Rev.*, 48:504–536, January 2006. doi: 10.1137/S0036144504445765.

N. H. Sleep. Martian plate tectonics. *J. Geophys. Res.*, 99(E3):5639–5655, March 1994. doi: 10.1029/94JE00216.

D. E. Smith, M. T. Zuber, H. V. Frey, J. B. Garvin, J. W. Head, D. O. Muhleman, G. H. Pettengill, R. J. Phillips, S. C. Solomon, H. J. Zwally, W. B. Banerdt, and T. C. Duxbury. Topography of the Northern Hemisphere of Mars from the Mars Orbiter Laser Altimeter. *Science*, 279:1686–1692, March 1998. doi: 10.1126/science.279.5357.1686.

E. J. Smith, L. Davis Jr., P. J. Coleman Jr., and D. E. Jones. Magnetic Field Measurements near Mars. *Science*, 149(3689):1241–1242, 1965. doi: 10.1126/science.149.3689.1241.

C. W. Snyder and V. I. Moroz. *Spacecraft exploration of Mars*, pages 71–119. The University of Arizona Press, 1992. ISBN 0-8165-1257-4.

S. C. Solomon, O. Aharonson, J. M. Aurnou, W. B. Banerdt, M. H. Carr, A. J. Dombard, H. V. Frey, M. P. Golombek, S. A. Hauck, J. W. Head, B. M. Jakosky, C. L. Johnson, P. J. McGovern, G. A. Neumann, R. J. Phillips, D. E. Smith, and M. T. Zuber. New Perspectives on Ancient Mars. *Science*, 307:1214–1220, February 2005. doi: 10.1126/science.1101812.

G. Spada, R. Sabadini, and E. Boschi. Long-term rotation and mantle dynamics of the Earth, Mars, and Venus. *J. Geophys. Res.*, 101:2253–2266, 1996. doi: 10.1029/95JE03222.

K. F. Sprenke. Martian magnetic paleopoles: A geostatistical approach. *Geophys. Res. Lett.*, 32(9):L09201, 2005. doi: 10.1029/2005GL022840.

K. F. Sprenke and L. L. Baker. Magnetization, Paleomagnetic Poles, and Polar Wander on Mars. *Icarus*, 147:26–34, September 2000. doi: 10.1006/icar.2000.6439.

K. F. Sprenke, L. L. Baker, and A. F. Williams. Polar wander on Mars: Evidence in the geoid. *Icarus*, 174:486–489, April 2005. doi: 10.1016/j.icarus.2004.11.009.

S. Stanley, L. Elkins-Tanton, M. T. Zuber, and E. M. Parmentier. Mars' Paleomagnetic Field as the Result of a Single-Hemisphere Dynamo. *Science*, 321:1822–1825, September 2008. doi: 10.1126/science.1161119.

D. J. Stevenson. Mars' core and magnetism. *Nature*, 412:214–219, July 2001. doi: 10.1038/35084155.

D. J. Stevenson, T. Spohn, and G. Schubert. Magnetism and thermal evolution of the terrestrial planets. *Icarus*, 54:466–489, June 1983. doi: 10.1016/0019-1035(83)90241-5.

A. J. Stewart, M. W. Schmidt, W. van Westrenen, and C. Liebske. Mars: A New Core-Crystallization Regime. *Science*, 316:1323–1325, June 2007. doi: 10.1126/science.1140549.

K. L. Tanaka, J. A. Skinner, J. M. Dohm, R. P. Irwin, E. J. Kolb, C. M. Fortezzo, T. Platz, G. G. Michael, and T. M. Hare. Geologic map of mars. *Scientific Investigations Map*, Jul 2014. ISSN 2329-132X. doi: 10.3133/sim3292.

E. Thébault, J. J. Schott, and M. Mandea. Revised spherical cap harmonic analysis (R-SCHA): Validation and properties. *J. Geophys. Res.*, 111:B01102, January 2006. doi: 10.1029/2005JB003836.

E. Thébault, F. Vervelidou, V. Lesur, and M. Hamoudi. The satellite along-track analysis in planetary magnetism. *Geophys. J. Int.*, 188:891–907, March 2012. doi: 10.1111/j.1365-246X.2011.05281.x.

K. L. Thomas-Keprta, S. J. Clemett, D. A. Bazylinski, J. L. Kirschvink, D. S. McKay, S. J. Wentworth, H. Vali, E. K. Gibson, Jr., M. F. McKay, and C. S. Romanek. Special Feature: Truncated hexa-octahedral magnetite crystals in ALH84001: Presumptive biosignatures. *Proc. Nat. Acad. Sci.*, 98:2164–2169, February 2001. doi: 10.1073/pnas.051500898.

A. Tilgner. Precession driven dynamos. *Phys. Fluids*, 17(3):034104, March 2005. doi: 10.1063/1.1852576.

D. J. Vaughan and J. A. Tossell. Magnetic Transitions Observed in Sulfide Minerals at Elevated Pressures and Their Geophysical Significance. *Science*, 179:375–377, January 1973. doi: 10.1126/science.179.4071.375.

S. Vennerstrom. Magnetic storms on Mars. *Icarus*, 215:234–241, September 2011. doi: 10.1016/j.icarus.2011.06.030.

F. Vervelidou and E. Thébault. Global maps of the magnetic thickness and magnetization of the Earth's lithosphere. *Earth Planets Space*, 67:173, December 2015. doi: 10.1186/s40623-015-0329-5.

F. J. Vine and D. H. Matthews. Magnetic Anomalies Over Oceanic Ridges. *Nature*, 199: 947–949, September 1963. doi: 10.1038/199947a0.

C. V. Voorhies, T. J. Sabaka, and M. Purucker. On magnetic spectra of Earth and Mars. *J. Geophys. Res.*, 107(E6):5034, June 2002. doi: 10.1029/2001JE001534.

C. V. Voorhies. Thickness of the magnetic crust of Mars. *J. Geopys. Res.*, 113(E4):E04004, April 2008. doi: 10.1029/2007JE002928.

P. J. Wasilewski and M. A. Mayhew. The Moho as a magnetic boundary revisited. *Geophys. Res. Lett.*, 19(22):2259–2262, November 1992. doi: 10.1029/92GL01997.

T. R. Watters, P. J. McGovern, and R. P. Irwin III. Hemispheres Apart: The Crustal Dichotomy on Mars. *Annu. Rev. Earth Pl. Sc.*, 35(1):621–652, May 2007. doi: 10.1146/annurev.earth.35.031306.140220.

A. Wegener. Die Entstehung der Kontinente. *Geologische Rundschau*, 3:276–292, July 1912. doi: 10.1007/BF02202896.

B. P. Weiss, H. Vali, F. J. Baudenbacher, J. L. Kirschvink, S. T. Stewart, and D. L. Shuster. Records of an ancient Martian magnetic field in ALH84001. *Earth Planet. Sci. Lett.*, 201: 449–463, August 2002. doi: 10.1016/S0012-821X(02)00728-8.

S. C. Werner. The early martian evolution - Constraints from basin formation ages. *Icarus*, 195:45–60, May 2008. doi: 10.1016/j.icarus.2007.12.008.

S. C. Werner. The global martian volcanic evolutionary history. *Icarus*, 201:44–68, May 2009. doi: 10.1016/j.icarus.2008.12.019.

K. A. Whaler and R. A. Langel. Minimal crustal magnetizations from satellite data. *Phys. Earth Planet. Int.*, 98:303–319, December 1996. doi: 10.1016/S0031-9201(96)03193-7.

K. A. Whaler and M. Purucker. A spatially continuous magnetization model for Mars. *J. Geophys. Res.*, 110(E9), 2005. doi: 10.1029/2004JE002393.

J. Wicht and A. Tilgner. Theory and Modeling of Planetary Dynamos. *Space Sci. Rev.*, 152: 501–542, May 2010. doi: 10.1007/s11214-010-9638-y.

M. A. Wieczorek and F. J. Simons. Localized spectral analysis on the sphere. *Geophys. J. Int.*, 162:655–675, September 2005. doi: 10.1111/j.1365-246X.2005.02687.x.

D. E. Wilhelms and S. W. Squyres. The martian hemispheric dichotomy may be due to a giant impact. *Nature*, 309:138–140, May 1984. doi: 10.1038/309138a0.

R. J. Willemann. Reorientation of planets with elastic lithospheres. *Icarus*, 60:701–709, December 1984. doi: 10.1016/0019-1035(84)90174-X.

D. A. Williams, R. Greeley, S. C. Werner, G. Michael, D. A. Crown, G. Neukum, and J. Raitala. Tyrrhena Patera: Geologic history derived from Mars Express High Resolution Stereo Camera. *J. Geophys. Res.*, 113:E11005, November 2008. doi: 10.1029/2008JE003104.

D. A. Williams, R. Greeley, R. L. Fergason, R. Kuzmin, T. B. McCord, J.-P. Combe, J. W. Head, L. Xiao, L. Manfredi, F. Poulet, P. Pinet, D. Baratoux, J. J. Plaut, J. Raitala, G. Neukum, and the HRSC Co-Investigator Team. The Circum-Hellas Volcanic Province, Mars: Overview. *Planet. Space Sci.*, 57:895–916, July 2009. doi: 10.1016/j.pss.2008.08.010.

J.-P. Williams and F. Nimmo. Thermal evolution of the Martian core: Implications for an early dynamo. *Geology*, 32:97–100, February 2004. doi: 10.1130/G19975.1.

M. Winklhofer, K. Fabian, and F. Heider. Magnetic blocking temperatures of magnetite calculated with a three-dimensional micromagnetic model. *J. Geophys. Res.*, 102:22695, October 1997. doi: 10.1029/97JB01730.

M. Yoshida and A. Kageyama. Low-degree mantle convection with strongly temperature- and depth-dependent viscosity in a three-dimensional spherical shell. *J. Geophys. Res.*, 111(B3), 2006. doi: 10.1029/2005JB003905.

Y. Yu and J. S. Gee. Spinel in Martian meteorite SaU 008: implications for Martian magnetism. *Earth Planet. Sci. Lett.*, 232:287–294, April 2005. doi: 10.1016/j.epsl.2004.12.015.

S. Zhong and M. T. Zuber. Degree-1 mantle convection and the crustal dichotomy on Mars. *Earth Planet. Sci. Lett.*, 189:75–84, 2001. doi: 10.1016/S0012-821X(01)00345-4.

EIDESSTATTLICHE ERKLÄRUNG

Hiermit versichere ich, dass ich die vorgelegte Dissertation selbst und ohne unerlaubte Hilfe angefertigt, alle in Anspruch genommenen Quellen und Hilfsmittel in der Dissertation angegeben habe und die Dissertation nicht bereits anderweitig als Prüfungsarbeit vorgelegen hat.

Berlin, März 2016

Achim Morschhauser

CURRICULUM VITAE

For reasons of privacy, the CV was removed in the electronic version.